



HAL
open science

Modélisation électro-mécanique multi-échelle des nanocomposites graphène/polymère

Xiaoxin Lu

► **To cite this version:**

Xiaoxin Lu. Modélisation électro-mécanique multi-échelle des nanocomposites graphène/polymère. Autre. Université Paris Saclay (COmUE), 2017. Français. NNT : 2017SACLC058 . tel-01756392v2

HAL Id: tel-01756392

<https://theses.hal.science/tel-01756392v2>

Submitted on 5 Apr 2018

HAL is a multi-disciplinary open access archive for the deposit and dissemination of scientific research documents, whether they are published or not. The documents may come from teaching and research institutions in France or abroad, or from public or private research centers.

L'archive ouverte pluridisciplinaire **HAL**, est destinée au dépôt et à la diffusion de documents scientifiques de niveau recherche, publiés ou non, émanant des établissements d'enseignement et de recherche français ou étrangers, des laboratoires publics ou privés.

Multiscale electro-mechanical modeling of graphene/polymer nanocomposites

Thèse de doctorat de l'Université Paris-Saclay
préparée à Centrale Supélec, Laboratoire Mécanique des Sols,
Structures et Matériaux, UMR 8579 CNRS

École doctorale n°579 SMEMAG
Spécialité de doctorat: Science des Matériaux

Thèse présentée et soutenue à Gif-sur-Yvette, le 13 Nov. 2017, par

Xiaoxin Lu

Composition du Jury :

Gilles LUBINEAU Professeur, King Abdullah University of Science and Technology	Rapporteur
Djimédo KONDO Professeur, Université Pierre et Marie Curie	Rapporteur
Olivier HUBERT Professeur, ENS Paris Saclay	Président
Lionel PICHON Professeur, Laboratoire de Génie Electrique de Paris	Examineur
Fabrice DETREZ Maître de conférences, Université Paris-Est Marne-la-Vallée	Examineur
Jinbo BAI Professeur, Centrale Supélec	Directeur de thèse
Julien YVONNET Professeur, Université Paris-Est Marne-la-Vallée	Co-Directeur de thèse

Acknowledgments

Firstly, I would like to express my most sincere appreciation to my supervisor Professor Jinbo Bai for giving me the opportunity to carry out my doctoral research, and for providing the continuous support of my Ph.D. study and research. He is so patient, motivated, enthusiastic and knowledgeable. It has been an honor to be his Ph.D. student. I also feel very grateful for the financial support from China Scholarship Council for the whole three years research.

Meanwhile, I would also like to take this opportunity to express my deepest gratitude to my co-supervisor and major advisor, Professor Julien Yvonne and Assistant Professor Fabrice Detrez, for their invaluable insights and suggestions. I appreciate all their contributions of time, ideas to make my Ph.D. experience productive and stimulating. I learned a lot from them : hard-working spirit, serious attitude towards research, *etc.*

Besides my supervisors, I would like to thank the rest of my thesis committees : Prof. Gilles Lubineau and Prof. Djimédo Kondo who had the difficult task to make a report on my manuscript, Prof. Olivier Hubert and Prof. Lionel Pichon who made me the honor to examine my work.

Special gratitude is extended to Dr. Florent Pled and Prof. Christian Soize who have helped me to solve problems in numerical modeling. I would also like to thank Prof. Guohua Hu for his encouragement and care for my study and life in France. I am also grateful to all staffs of MSSMat and MSME laboratories for all their assistance.

Additionally, I owe my sincere gratitude to my friends and my fellows in Centrale Supélec who gave me their help, encouragement and confort especially when I was in low spirits : Delong He, Benhui Fan, Hang Zhao, Yang Ma, Yu Liu, Wangshu Chen, Huan Du, Salem Diana, Ahlem Raies, Xue Bai, Shan Feng, Minhao Yang, Yiguo Xu, *etc.* I am also grateful to my friends in Université Paris-Est (Lab. MSME) for their help on my research work and I really treasure the time we have spent together during the past three years in France : Yunmei Luo, Mu He, Yanghao Gong, Yang Xu, Tianyu Zhang, Daicong Da, Dengke Li, Zhou Chen, *etc.* My sincere thanks also go to my best friend Haiyue Li who came to attend my defense from China.

Last but far from least, my deepest gratitude and love belong to my parents for their unconditional love and consistent support through my life.

Table des matières

1	General introduction	1
1.1	Background and motivations	1
1.2	Outline	3
1.3	Notations	4
2	Graphene and graphene nanocomposites	9
2.1	Graphene and graphene nano-platelets	9
2.1.1	Microstructure of graphene and graphene nano-platelet	9
2.1.2	Synthesis method of graphene	10
2.1.3	Electrical properties	13
2.1.4	Mechanical properties	17
2.1.5	Other properties and summary	18
2.2	Graphene reinforced nanocomposites	20
2.2.1	Synthesis of graphene-polymer nanocomposites	20
2.2.2	Electrical properties	22
2.2.3	Mechanical properties	25
2.2.4	Other properties	28
2.2.5	Interfacial properties	28
2.3	Graphene nanocomposites applications	33
2.3.1	Sensors	33
2.3.2	Supercapacitors	35
2.3.3	Photovoltaic material	36
3	Multiscale modeling of electric conductivity in graphene-reinforced nanocomposites	37
3.1	Introduction	37
3.2	Electrical imperfect surface model	40
3.3	Nonlinear conduction mechanisms in polymer/graphene nanocomposites : Tunneling effect	45
3.4	Multiscale Modeling of the electrical behavior of graphene-reinforced composites	48
3.4.1	Microscopic problem	48
3.4.2	Local microscopic constitutive equations	50

3.4.3	Homogenized quantities	50
3.5	Finite element numerical solving procedure	52
3.5.1	Weak forms	52
3.5.2	Linearization	53
3.5.3	Nonlinear finite element discretization and approximation	54
3.5.4	Geometrical modeling of graphene/polymer nanocomposites	56
3.5.5	3D distance function used in the tunneling effect model	58
3.6	Preliminary examples	59
3.6.1	1D benchmark example	59
3.6.2	3D example with two close graphene sheets : identification of the parameter $\alpha(h)$	62
3.7	Numerical analysis of the electrical conductivity of graphene reinforced nanocomposites	65
3.7.1	RVE size analysis	65
3.7.2	Effective electric conductivity and percolation threshold	66
3.7.3	Nonlinear electric behavior of graphene reinforced nanocomposite	72
3.7.4	Effect of barrier height on the percolation threshold . .	75
3.7.5	Effect of graphene aspect ratio on the percolation threshold	76
3.7.6	Effect of alignment of graphene sheets	77
3.8	Comparison between numerical and experimental results . . .	79
3.9	Conclusion	81
4	Modeling of the mechanical behavior of graphene-polymer interphase using molecular dynamics	83
4.1	Introduction	83
4.2	Details of MD simulations	87
4.2.1	Formulations of MD method	87
4.2.2	Potentials	91
4.2.3	The MD algorithm	93
4.2.4	Polymer chain generation	97
4.3	Spatial description of continuum fields in atomistics	100
4.3.1	Murdoch-Hardy procedure	100
4.3.2	Analysis of the molecular configuration	102

4.3.3	Analysis of local mechanical fields	105
4.4	Continuum modeling of thin interphases as imperfect interfaces	107
4.4.1	Imperfect interfaces framework	108
4.4.2	Parameters identification	110
4.5	Numerical results	117
4.5.1	Influence of the polymer thickness	117
4.5.2	Numerical example of random nanocomposite	121
4.6	Conclusion	121
5	Numerical modeling of the mechanical properties of graphene reinforced nanocomposites	125
5.1	Introduction	125
5.2	Elastic imperfect interface model	127
5.3	General introduction of cohesive models	132
5.4	Identification of a nonlinear cohesive model by molecular dynamics	135
5.5	Small deformation analysis of graphene reinforced polymer nanocomposites	137
5.5.1	Governing equations and constitutive relations	137
5.5.2	Computational framework	139
5.5.3	Tension test	144
5.5.4	RVE analysis	145
5.5.5	Mechanical properties of graphene/PE nanocomposites	147
5.5.6	Comparison with analytical solutions	150
5.6	Finite deformation analysis of graphene reinforced polymer nanocomposites	152
5.6.1	General introduction to the finite deformation problems	152
5.6.2	Imperfect interface model at finite strains	157
5.6.3	Computational framework	159
5.7	Weak electromechanic coupling	165
5.7.1	Electrical percolation threshold	166
5.7.2	Distance function at finite deformation	167
5.7.3	Evolution of electrical properties under stretching of the composite	169
5.8	Conclusion	170

6 Conclusion and perspective	173
6.1 General conclusion	173
6.2 Perspectives	174
Bibliographie	177
A Résumé	219

General introduction

1.1 Background and motivations

Graphene/polymer nanocomposites have recently attracted a growing attention due to their interesting electromechanical performances, as shown in recent studies like [Song 2012, Arash 2014, Verdejo 2011, Li 2013]. Even though a large amount of experiments have been carried out to study these new materials, the mechanisms at the nanoscale are still not well understood, and their relation to the effective properties remain an open area. In that context, multiscale methodologies implying simulations from nanoscale up to the macroscale can help tackle this issue. At the atomistic level, numerical simulations allow understanding some phenomena which are not accessible through experiments and analyze the influence of different parameters. Combining these simulations with homogenization methods or multiscale methodology is a step forward to study the influence of the nanoscale constituents on the effective properties [Namilae 2005, Li 2006, Odegard 2005].

It has been evidenced through experiments that the macroscopic properties of the graphene nanocomposites do not originate only from the properties of the proportion and nature of matrix and fillers, but also from physical mechanisms specifically related to the nano-size. One effect, which has been widely studied, is the surface effect related to the presence of unbalanced atoms on surfaces or interfaces and which experience a different equilibrium state than other bulk atoms, creating an additional surface energy (see *e.g.* [Shenoy 2002, Duan 2005b, Gurtin 1975, Yvonnet 2008b, Yvonnet 2011]). A review can be found in [Wang 2011]. In the case of interphase, while linear phenomena have been thoroughly discussed, nonlinear ones are only very recent (see *e.g.* [Brach 2017b]). Another phenomenon, related to the electric conductivity, is purely a quantum effect : coined as “tunneling effect”, which is created through very thin isolating barriers like polymer layers

when the distance between the two conducting phases is very small, lower than several nanometers [Allaoui 2008, Martin-Gallego 2013, Zeng 2011], leading to unexpected values of electrical conductivity for very small volume fractions of fillers. Incorporation of these nanoscale mechanisms into homogenization schemes has been proposed in the case of surface elasticity in [Sharma 2004, Duan 2005b, Duan 2006, Benveniste 2013] and extended to nonlinear phenomena e.g. in [Brach 2017a, Brach 2017b]. However, analytical approaches are usually restricted to some classes of phenomena and to simple geometries, like spheroidal particles [Huang 2007, Le-Quang 2010], or nanofibers [Chen 2007]. For more general shapes and nanoscale distributions of fillers, including the nanoscale effects into more robust, computational homogenization approaches [Yvonnet 2008b, Liu 2015, Farsad 2012] would permit treating more general, possibly nonlinear cases, for arbitrary morphologies of fillers.

In a continuum-based multiscale approach, the parameters of the models must be identified. Usually, these parameters, *e.g.* surface or interface parameters are not accessible through the experiments, but can be evaluated by atomistic simulations [Shenoy 2005, Yvonnet 2011, Yvonnet 2012]. However, only a few works have treated identification of interface properties originating from the nanoscale.

Challenges for predictive, efficient multi-scale models of electro-mechanical properties of graphene nanocomposites, which are studied in this PhD work, are summarized as follows :

- Developing a continuum nonlinear model for the electrical behavior taking into account the nonlinear tunneling effect originating from the nanoscale ;
- Characterizing the mechanical properties of interphases considering atomistic interactions, *i.e.* both linear and nonlinear elastic stiffness of the interphase and the interface ;
- Developing efficient computational homogenization procedures involving the above-mentioned nanoscale phenomena to predict the effective electro-mechanical properties of graphene-reinforced nanocomposites.

The purpose of the present PhD work is to provide contributions to these different scientific issues.

1.2 Outline

The outline of this thesis is as follows :

In Chapter 2, a brief introduction to graphene and graphene-based nanocomposites is provided, including synthesis method, properties and applications.

In Chapter 3, a numerical modeling framework is proposed to evaluate the effective electric conductivity in polymer composites reinforced with graphene sheets, taking into account the electrical tunneling effect, which allows conduction between graphene sheets at small nanometric distances. We introduce a nonlinear Finite Element formulation and a numerical methodology to model the nonlocal and nonlinear effects introduced by the tunneling effect conduction model within the polymer matrix between close graphene sheets. In addition, to avoid meshing in the thickness of the graphene sheets and in view of their very high aspect ratio, a highly conducting surface model is employed. The effective conductivity is then evaluated over representative volume elements containing arbitrary distributed graphene sheets. Finally, the procedure is used to analyze the sensitivity of the effective electric properties with respect to the nanoscale constituents.

In Chapter 4, we present a methodology based on Murdoch-Hardy procedure, which uses the results of atomistic simulations relying on molecular dynamics, to construct the continuum parameters of the interphase in graphene/polymer nanocomposites such as local density distribution, polymer chain orientation, stress distribution, displacement field and effective stiffness. Two continuum models of interface are identified : one contains both the graphene sheet and thick interphases characterizing the observed evolving density of polymer chains around the graphene sheets, and another one where both graphene sheet and interphase are embedded into an imperfect interface model.

In chapter 5, The effective nonlinear mechanical properties of graphene-polymer nanocomposites are evaluated by developing a continuum model incorporating the previous imperfect interface model, extended to the finite strains framework. MD simulations are used to identify the nonlinear behavior of the interface between the graphene and the polymer. The continuum model is used within a computational homogenization framework to evaluate the overall properties of the composite in an incremental scheme. A preliminary

example of weak coupling between the electric and mechanical phenomena is presented.

Finally, conclusions and perspectives are drawn.

1.3 Notations

— Tensors and matrices

a/A	Scalar	\mathbf{a}	Vector
\mathbf{A}	Second order tensor	\mathbb{A}	Fourth order tensor
\mathbf{I}	Second order identity tensor	\mathbb{I}	Fourth order identity tensor
$[A]$	Matrix $n \times m$	\mathbf{n}	Normal vector

— Mathematical symbols

$\mathbf{a} \cdot \mathbf{b} = a_i b_i$	$(\mathbf{A}\mathbf{b})_i = A_{ij} b_j$	$(\mathbf{A}\mathbf{B})_{ij} = A_{ik} B_{kj}$
$\mathbf{A} : \mathbf{B} = A_{ik} B_{ki}$	$(\mathbf{A} : \mathbf{B})_{ij} = A_{ijkl} B_{kl}$	$(\mathbf{A} : \mathbb{B})_{ijkl} = A_{ijmn} B_{mnkl}$
$\mathbf{A} :: \mathbb{B} = A_{ijkl} B_{kl ij}$	$(\mathbf{a} \otimes \mathbf{b})_{ij} = a_i b_j$	
$\llbracket (\cdot) \rrbracket$	Discontinuity of quantity (\cdot) through the interface	
$\langle \cdot \rangle$	Spatial averaging over domain Ω	
$\partial_t \cdot$	Partial derivative with respect to the time	
$\nabla_{\mathbf{x}} \cdot$	Divergence operator with respect to the spatial coordinate \mathbf{x}	
∇	Gradient operator	
$\nabla^s \cdot \{ \cdot \}$	Interface divergence operator	
∇^s	Interface gradient operator	
$\nabla_{\mathbf{X}}$	Gradient operator with respect to initial configuration	

— Notations of electrical part

ϕ	Electrical potential
e	Elementary charge
J	1D electric tunneling current
E	1D electric field
\mathbf{j}, \mathbf{j}^s	Bulk/surface electric current density
\mathbf{K}	Electric conductivity tensor
\mathbf{E}, \mathbf{E}^s	Electric field in bulk/surface
E_c, E_F	Conduction band edge energy and Fermi level
h_p	Planck constant

Φ_0	Barrier height
d	Barrier width (distance between neighbouring graphene sheets)
\overline{W}	Electric power of the domain
w^b, w^s	Electric power density function for the bulk/surface
\mathbf{K}_0^p	Electric conductivity tensor of the polymer
\mathbf{K}^g	Second-order electric conductivity tensor of bulk graphite
\mathbf{K}_*^s	Second-order electric conductivity tensor of graphene surface
d_{cut}	Cut-off distance of the tunneling effect
h	Thickness of multi-layer graphene sheets
$\overline{\mathbf{E}}$	Effective electric field
$\overline{\mathbf{j}}$	Effective current density
\mathbf{P}	Projector operator onto the interface
$\overline{\mathbf{K}}_T(\overline{\mathbf{E}})$	Effective conductivity tensor
[Ne]	Matrix of shape functions
$[\Phi^e]$	Column vector of electric potential in one element
[Be]	Shape functions derivatives matrix
$[\Delta\Phi]$	Column vector of potential increments
η	Graphene aspect ratio
$r_x^{(i)}, r_y^{(i)}, r_z^{(i)}$	Coordinates of the center of i th graphene sheet
$\alpha^{(i)}, \beta^{(i)}, \gamma^{(i)}$	Euler angles of i th graphene sheet
f	Graphene volume fraction in the composites
f_c	Electrical percolation threshold

— Notations of atomistic level

\mathbf{m}_α	Masse of α th atom
$\mathbf{r}_\alpha^{(0)}$	Initial position of α th atom
\mathbf{r}_α	Current position of α th atom
$\mathbf{u}_\alpha = \mathbf{r}_\alpha - \mathbf{r}_\alpha^{(0)}$	Displacement vector of α th atom
$\mathbf{v}_\alpha(t)$	Pseudo velocity of α th atom
$\mathbf{f}_{\alpha\beta}$	Force of β th atom on the α th atom
\mathbf{f}_α	Force on α th atom
$r_{\alpha\beta}$	Inter-atomic distance between α th atom and β th atom
\mathbf{h} and $\mathbf{h}^{(0)}$	Simulation box shape in current/reference configuration
$\tilde{\mathbf{F}}$	Macroscopic deformation gradient tensor
$\tilde{\boldsymbol{\varepsilon}}$	Effective infinitesimal strain tensor
$\mathcal{U}(\{\mathbf{r}_\alpha\}, \tilde{\mathbf{F}})$	System potential energy

$\mathcal{U}^{(vdw)}$	Van der Waals potential
$\mathcal{U}^{(s)}$	Bond stretch potential
$\mathcal{U}^{(b)}$	Bond-angle bend potential
$\mathcal{U}^{(tor)}$	Dihedral angle torsion potential
$w(\mathbf{x})$	Murdoch-Hardy weight function
$b_w(\mathbf{x}, \mathbf{r}_\alpha(t), \mathbf{r}_\beta(t))$	Murdoch-Hardy bond function
$\rho_w(\mathbf{x}, t)$	Murdoch-Hardy mass density
$\mathbf{v}_w(\mathbf{x}, t)$	Murdoch-Hardy Eulerian velocity fields
$\mathbf{u}_w^{(E)}(\mathbf{x}, t)$	Murdoch-Hardy Eulerian displacement field
$\boldsymbol{\sigma}_w(\mathbf{x}, t)$	Murdoch-Hardy Cauchy stress tensor
$s_w(\mathbf{x})$	Murdoch-Hardy nematic order parameter
$\rho_b(\mathbf{x})$	Normalized constant of local bond density at \mathbf{x}
$\mathcal{R}_{Euler}(\mathbf{O}, \mathbf{e}_1, \mathbf{e}_2, \mathbf{e}_3)$	Eulerian frame of reference at origin \mathbf{O}
$\mathbf{n}_{\alpha\beta}$	Covalent bond direction between α and β
$H(x)$	Heaviside step function
f^{Cub}, f^{Sph}	Characteristic function of the cuboid/sphere
L_x, L_y, L_z	Side length of the RVE in molecular dynamics simulation
ϕ and ϕ^s	Bulk/interfacial free energy density
ϕ_0	Bulk free energies at zero strain
ϕ_0^s	Interfacial free energies at zero jump displacement

— Notations of mechanical part

$\mathbf{u}(\mathbf{x})$	Displacement field in the body
$\mathbf{u}^s(\mathbf{x})$	Displacement field inside the interface
\mathbf{u}^g	Displacement field in the graphene sheet
$\boldsymbol{\varepsilon}$	Infinitesimal strain tensor in the bulk
$\boldsymbol{\varepsilon}^s$	Infinitesimal strain tensor on the interface
$\boldsymbol{\sigma}, \boldsymbol{\sigma}^s$	Cauchy stress tensor in the bulk and interface
\mathbf{t}^s	Average traction across the interface
\mathbb{C}	The fourth-order symmetric stiffness tensor
$\bar{\mathbb{C}}$	Effective stiffness tensor
\mathbb{C}^s	The fourth-order symmetric interfacial stiffness tensors
\mathbb{S}	Eshelby's tensor
\mathbf{K}^s	Second-order symmetric cohesive interfacial stiffness tensor
$\Delta \mathbf{u}$	Incremental displacement
$[\boldsymbol{\sigma}], [\boldsymbol{\varepsilon}]$	Vectors of stress/strain

$[\sigma^s], [\varepsilon^s]$	Vectors of surface stress/strain
$[C], [C^s]$	Matrix form of bulk/surface stiffness tensor
τ^s	Surface residual stress
\mathbf{F}	Deformation gradient
$\hat{\mathbf{P}}$	First Piola-Kirchhoff stress tensor
\mathbf{S}	Second Piola-Kirchhoff stress tensor
$\hat{\mathbf{E}}$	Green-Lagrange strain tensor
W	Elastic energy of the domain

— Abbreviations

FEM	Finite element method
MD	Molecular dynamics method
RVE	Representative Volume Element
MT model	Mori-Tanaka model
PCW theory	Ponte Castañeda Willis theory
HS bounding	Hashin-Strikman boundings
STEM	Scanning transmission electron microscopy
EELS	Electron energy-loss spectroscopy
NVE	Microcanonical ensemble
NVT	Canonical ensemble
NpT	Isothermal-isobaric ensemble
PCFF	Polymer consistent force field
CVFF	Consistent valence force field
AQS	Athermal, Quasistatic Simulations
CRSS	Critical Resolved Shear Stress
AC/DC	Alternating/Direct current
HC	High conducting
SG	Single-layer graphene
BG	Bilayer graphene
FG	Few-layer graphene
CNTs	Carbon nanotubes
CMG	Chemical modified graphene
GO	Graphene oxide
RGO	Reduced graphene oxide
GNP	Graphene nanoplatelets
GNS	Graphene nanosheets

SWCNT	Single-walled carbon nanotube
MWCNT	Multi-walled carbon nanotube
GCFs	Graphene-based composite films
CB	Carbon black
CVD	Chemical vapour deposition
AFM	Atomic force microscope
FTIR	Fourier Transform InfraRed spectroscopy
DFT	Density functional theory
HOPG	Highly oriented pyrolytic graphite
SDBS	Sodium dodecylbenzene sulfonate
DMF	Dimethylformamide
PMMA	Poly(methylmethacrylate)
HCB	Hexachlorobenzene
PVA	Poly(vinyl alcohol)
PVF	Polyvinyl fluoride
PE	Polyethylene
PEMA	Poly(ethylmethacrylates)
PU	Polyurethane
PVDF	Poly(vinylidene fluoride)
PS	Polystyrene
PP	Polypropylene
PBT	Poly(butylene terephthalate)
PANI	Polyaniline
PEG	Polyethylene glycol
PPy	Polypyrrole
PEDOT	Poly(3,4-ethylenedioxythiophene)
P3TH	Poly(3-hexylthiophene)
PCBM	Phenyl-C61-butyric acid methylester
ITO	Indium Tin oxide

Graphene and graphene nanocomposites

2.1 Graphene and graphene nano-platelets

2.1.1 Microstructure of graphene and graphene nano-platelet

Graphene, the parent of all graphitic forms (seen in Fig. 2.1 (a)), has become one of the most exciting topics of research in the past decade [Berger 2006, Ohta 2006, Tang 2010]. This two-dimensional material is composed of sp^2 carbon atoms arranged in honeycomb structure. It has been viewed as the building block of all other graphitic carbon allotropes of different dimensionality [Geim 2007]. For example, graphite is made of graphene sheets stacked on top of each other and separated by 3.37Å. The 0-D allotrope carbon, fullerenes, can be regarded as made by wrapping a section of graphene sheet. The 1-D allotrope carbon, carbon nanotubes and nanoribbons, are obtained by rolling and slicing graphene sheets respectively. Ideally graphene is a single-layer material, but graphene samples with two or more layers are being investigated with equal interest. There are three different types of graphenes : single-layer graphene (SG), bilayer graphene (BG), and few-layer graphene (FG, number of layers 10). Although single-layer graphene and bilayer graphene were first obtained by micro-mechanical cleavage [Novoselov 2004], several strategies have since been developed for the synthesis of graphenes [Park 2009c]. In bi- and few-layer graphene, Carbon atoms can be stacked in different ways, generating hexagonal or AA stacking, Bernal or AB stacking and rhombohedral or ABC stacking (Fig. 2.1 (b)).

Hybridized sp^2 bonding of graphene, involves three in-plane σ bonds/atom and π orbital perpendicular to the plane (Fig. 2.1 (c)). Strong σ bonds work

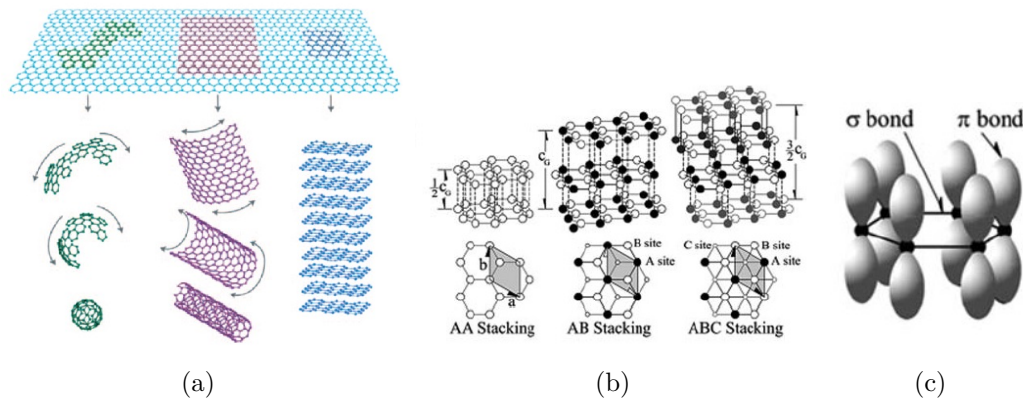


FIGURE 2.1 – (a) Graphene : the parent of all graphitic forms [Geim 2007]; (b) three most common structures and stacking sequences of graphene and (c) Schematic of the in-plane σ bonds and the π orbital perpendicular to the plane of the graphene sheets [Hass 2008].

as the rigid backbone of the hexagonal structure and the out-of-plane π bonds (weak interaction) control interaction between different graphene layers.

2.1.2 Synthesis method of graphene

A number of methods have been established for graphene synthesis, among which chemical vapour deposition (CVD), chemical synthesis and mechanical exfoliation are the most commonly used today.

2.1.2.1 Exfoliation and cleavage

Since graphite involves stacked layers of many graphene sheets bonded together by weak van der Waals force or π bonds, it is possible to produce graphene with a high purity graphite by exfoliation and cleavage method. This method can break the bonds by either mechanical or chemical energy, and produce the separated graphene sheets. Novoselov *et al.* separated a graphene layer from highly oriented pyrolytic graphite (HOPG) using a mechanical exfoliation method in 2004 [Novoselov 2004], and obtained a tiny surface area of single-layer graphene. In order to get large and flat graphene flakes, *e.g.* mm-sized single to few-layer graphene, the bulk graphite was bonded to borosilicate glass following by exfoliation, which left single or few layer of graphene on the substrate [Shukla 2009].

Liquid-phase exfoliation of graphite is also a promising technique to get large-scale graphene sheets. Lotya *et al.* [Lotya 2009] produced single- to few-layer graphene, by making dispersion of graphite powder in sodium dodecylbenzene sulfonate (SDBS), followed by sonication, to exfoliate the graphite into graphene. Zhu *et al.* [Zhu 2013] successfully synthesized large-scale, good-quality graphene nanosheets through the liquid-phase exfoliation of graphite in a solvent of N,N-dimethylformamide (DMF) and water. By using DMF as well, Liu *et al.* [Liu 2012] utilized supercritical DMF to exfoliate expandable graphite into few-layers graphene and then repeated the same procedure to exfoliate the few-layer graphene into monolayer graphene.

2.1.2.2 Chemical vapour deposition (CVD)

Chemical vapour deposition (CVD) is regarded as the most potential way to synthesize high-quality, huge-area and single-layer graphene, and has become the focus of researchers in recent years. The CVD technique applies the decomposition of the carbon source molecules on the metal substrate to synthesize graphene films in which a variety of precursors, including solid, liquid and gas precursors, have been used.

Solid precursors : The first article about the synthesis of graphene using CVD was demonstrated in 2006, where a camphor precursor was decomposed on Ni foils [Somani 2006]. Camphor was first evaporated at 180°C and then pyrolyzed, in another chamber of the CVD furnace, at 700 to 850°C, using argon as the carrier gas. Upon natural cooling to room temperature, few-layer graphene sheets were observed on the Ni foils. Besides, poly(methylmethacrylate)(PMMA) [Sun 2010b] and hexachlorobenzene(HCB) [Gan 2012] were also employed as solid carbon source to grow graphene by CVD methods. What's more interesting is that even the solid waste, food, insects were promoted as carbon precursors to grow graphene films by Ruan *et al.* [Ruan 2011].

Gas precursors : Gas carbon precursors are also very popular in producing the graphene, *e.g.*, methane (CH₄), ethylene (C₂H₄) and acetylene (C₂H₂), in which CH₄ and its mixtures are most common. Generally, a metal substrate such as copper is put into a furnace and heated under low vacuum to around 1000°C. Methane and hydrogen gases are then flowed through the furnace. The hydrogen catalyzes a reaction between

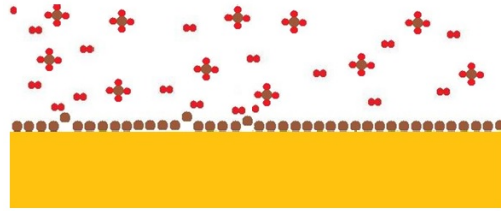


FIGURE 2.2 – Diagram of CVD growth on copper [Prasai 2011].

methane and the surface of the metal substrate, causing carbon atoms from the methane to be deposited onto the surface of the metal through chemical adsorption (see in Fig. 2.2). The furnace is quickly cooled to keep the deposited carbon layer from aggregating into bulk graphite, which crystallizes into a contiguous graphene layer on the surface of the metal.

Liquid precursors : Liquid carbon sources, such as benzene, methanol and ethanol, have also attracted the interest of the scientists due to the friendly economy. And different kinds of alcohols have also been used and compared as liquid carbon sources to produce monolayer graphene by CVD at a process temperature of 850°C for 5 min.

2.1.2.3 Other process and comparison of the synthesis method

TABLE 2.1 – Comparison of the main synthesis method of graphene.

Synthesis Method method	Sample size	Potential application	Quality	Cost
Micromechanical cleavage	<1 mm	Fundamental studies	+++	+++
Direct liquid-phase exfoliation	Potentially infinite volume	Coatings printing, composites, energy, biomedical	+	+
Liquid-phase exfoliation via graphene oxide			+	+
Chemical vapour deposition	Potentially infinite area	Electronics, sensors, biomedical	++	++
Sublimation of silicon carbide	Limited by wafer size (100 mm)	Electronics sensors	++	+++

Apart from the methods above, many other approaches have been recorded to synthesize the monolayer graphene sheet (see [Lee 2017] as review), such as thermal annealing, unzipping of CNTs, solvothermal method, electrochemical method, thermal decomposition, ball-milling exfoliation, calcination, irradiation of highly charged ions and so on.

The comparisons of the main synthesis method of graphene on crystallite size, sample size, quality, price and potential applications are presented in Table. 2.1. In the graphene/polymer nanocomposites, the graphene fillers are mainly produced by the liquid-phase exfoliation method, which requires the least cost and has potential to get large size of graphene sheets sacrificing part of the quality. Besides, the reduction of graphene oxide can also be used to produce graphene in considerable quantities.

2.1.3 Electrical properties

2.1.3.1 Ballistic and diffusive transport

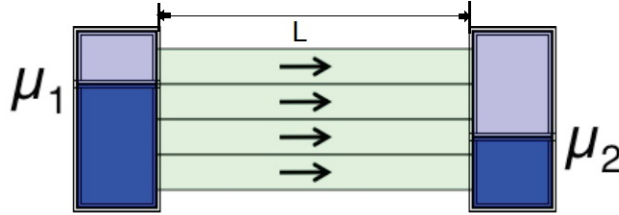


FIGURE 2.3 – A ballistic conductor with length L is connected to two electrodes with Fermi energies μ_1 and μ_2 .

Conductivity is a very important property of the conductor or semiconductor. For an ideal elastic resistor as shown in Fig. 2.3, the electrons travel along the fixed energy channels and the current through the resistor is

$$I = \frac{1}{e} \int_{-\infty}^{+\infty} dE G(E) (f_1(E) - f_2(E)) \quad (2.1)$$

where the conductance function

$$G(E) = \frac{e^2 D(E)}{2t(E)} \quad (2.2)$$

$D(E)$ is the density of state, e is the charge of electron, f_1 and f_2 are the Fermi functions dependent on the energy E for the electrons in 1 and 2 respectively,

μ_1 and μ_2 are chemical potentials, and the voltage difference between them $V = (\mu_1 - \mu_2)/(-e)$. t is the time it takes for an electron to transfer from the source to the drain as described in Fig. 2.4.

Regarding the transfer time t , there are two transport regimes :

- Ballistic transport (Fig. 2.4(a)) : electron goes straight from source to drain, "like a bullet", $t \sim L$.
- Diffusive transport (Fig. 2.4(b)) : electron changes only its momentum and not its energy along the way, $t \sim L^2$.

For 3D case, the Ohm's law should be modified to

$$R = \frac{1}{\sigma A}(L + \lambda) \quad (2.3)$$

where A is the cross sectional area of the sample, $\lambda = v\tau$ is the mean free path of a moving electron, which is the average length that the electron can travel freely, and v is the velocity of the electron, τ is the mean free time. It is obvious that this modification is primarily important for near ballistic conductors ($L \sim \lambda$) and is negligible for conductors that are many mean free paths long ($L \gg \lambda$).

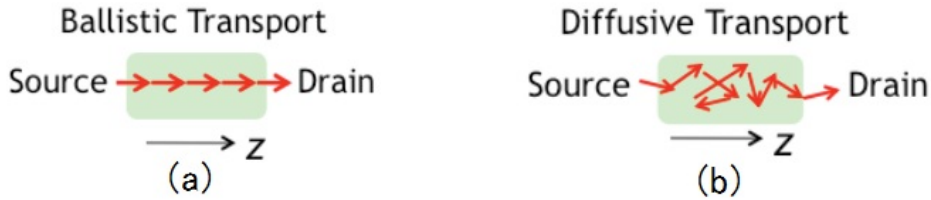


FIGURE 2.4 – Two transport regimes of electrons. (a) Ballistic transport ; (b) Diffusive transport.

For the 2D conductor such as graphene, the conductivity is given as

$$\sigma = G_B \frac{\lambda}{W} \quad (2.4)$$

where W is the width of the sample and the ballistic conductance G_B is

$$G_B = \frac{e^2 D(E) v(E)}{\pi L} \quad (2.5)$$

which is dependent on the band structure of the material.

2.1.3.2 Band structure of graphene

The available energies for electrons allows differentiating insulators, conductors and semiconductors. In free atoms, discrete energy levels are present, but in solid materials (such as insulators, semiconductors and conductors) the available energy states are so close to each other that they form bands. The band gap is an energy range where no electronic states are present. In insulators, the valence band is separated from the conduction band by a large gap. In good conductors such as metals the valence band overlaps the conduction band, whereas in semiconductors there is a small gap between the valence and conduction bands, small enough to allow thermal excitation of electrons from the valence to conduction band. According to the unique crystal structure of mono-layer graphene, the conduction and valence bands meet at the Dirac points on Fermi level (see in Fig. 2.5), which leads to a zero-gap semiconductor.

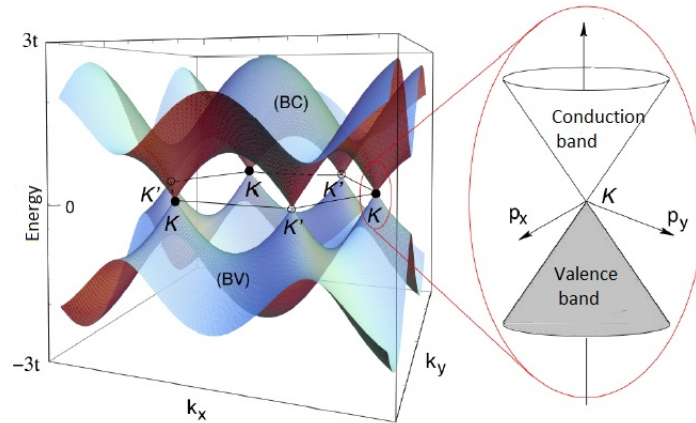


FIGURE 2.5 – The band structure and Brillouin zone of graphene [Fuchs 2013].

The Dirac points are locations in momentum space, on the edge of the Brillouin zone. There are two sets of three Dirac points. Each set is not equivalent with the other set of three. The two sets are labeled K and K' . Near these Dirac points, the electron energy is linearly dependent on the wave vector p ,

$$E = E_c + v_0 p. \quad (2.6)$$

Thus the velocity of the electrons close to Fermi level is independent on the energy ($v = dE/dp = v_0$). This linear dispersion also results in massless

excitons since effective mass is given by the curvature of the energy bands in momentum space. The density of the carrier charge n in graphene is very high $n \sim 10^{11} \text{ cm}^2$. In 2D case, n can be written as

$$n(E) = \frac{N(E)}{WL} \quad (2.7)$$

where $N(E)$ is the total number of states $N(E) = \int_{-\infty}^E D(E)dE$.

These charge carriers travel ballistically over the 2D surface at relativistic speeds, and leads to the better conductivity of pure graphene than metal. It is given by [Bolotin 2008a]

$$\sigma = \frac{4e^2}{h_p} \frac{W p_F}{\pi} \propto \sqrt{n} \quad (2.8)$$

where p_F is the Fermi wave vector and h_p is the Plank constant. At room-temperature, the resistivity ρ ($\rho = 1/\sigma$) of graphene can be on the order of $10^{-6} \Omega \cdot \text{cm}$ [Novoselov 2005]. Besides, the electron mobility in graphene $\mu = \sigma/en$ is remarkably high, which is reported in excess of $200000 \text{ cm}^2 \text{V}^{-1} \text{s}^{-1}$ at carrier density of $2 \times 10^{11} \text{ cm}^2$ for mechanically exfoliated suspended layer of graphene [Bolotin 2008b]. And the mean free path λ can reach 150 nm [Bolotin 2008a].

It should be noted that the number of layers for graphene nanoplatelets can influence their electronic structures, *e.g.*, the electronic structure of bilayer graphene changes with the various microstructures as shown in Fig. 2.6, which would further affect the conductivity of the graphene.

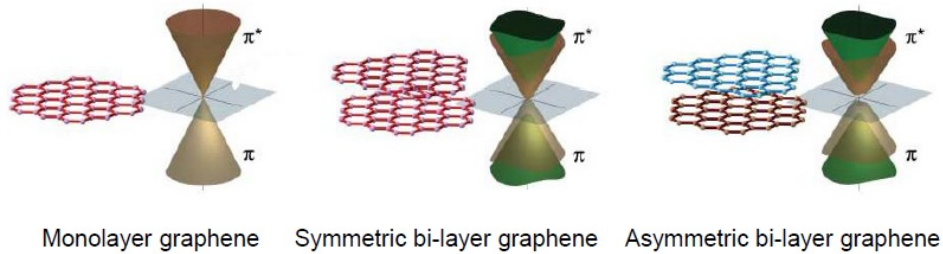


FIGURE 2.6 – The band structure of monolayer and bilayer graphene close to Dirac point. [Ohta 2006].

2.1.3.3 Quantum hall effect

Dirac fermions (electrons or holes) also exhibit very different and unusual properties compared to ordinary electrons, thus leading to new phenomena, such as the anomalous integer quantum Hall effect [Zhang 2005, Novoselov 2007a]. The integer quantum Hall effect refers that when the electrons of a sample are well confined in two dimensions and in the condition of a strong magnetic field and low temperature, the measured Hall resistivity ρ_H or Hall voltage U_H is no longer inversely proportional to the carrier density n or proportional to the magnetic field B . Instead, a series of plateaus appear in the measured curves. This effect was even observed at room temperature [Novoselov 2007b] in the presence of a magnetic field perpendicular to the graphene layer. This gives potential for the application of graphene in quantum storage and computation, calculating the standard resistance and some other physical constants.

2.1.4 Mechanical properties

Numerical methods such as atomistic simulations have been firstly used by researchers to determine the mechanical properties of single-layer graphene [Lier 2000, Reddy 2006], leading to a prediction of Young's modulus higher than 1 TPa. Using density functional theory, an *ab initio* calculation of the stress-strain curve of a graphene single layer has also been obtained [Liu 2007]. The theoretically estimated Young's modulus is 1050 GPa, which is similar to the value of 1020 GPa determined many years ago for the Young's modulus of bulk graphite [Blakslee 1970], and in good agreement with the experimental measures [Lee 2008]. The breaking strength of graphene has been measured to be about 40 N/m by atomic force microscope [Lee 2008].

More recently, the development of atomic force microscope has allowed measuring experimentally the properties of graphene like *e.g.* the Young's modulus. For example, the AFM nanoindentation has been employed for the direct determination of the mechanical properties of monolayer graphene, suspended over holes of 1.0-1.5 μm in diameter on a silicon substrate as shown in Fig. 2.7 [Lee 2008]. They isolated the monolayers through the use of optical microscopy and identified them with Raman spectroscopy, and derived stress-strain curves by assuming that the graphene behaved mechanically as a 2D membrane of thickness 0.335 nm. The Young's modulus and the breaking

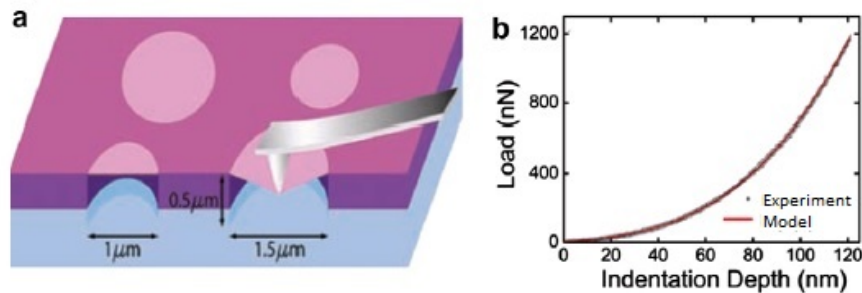


FIGURE 2.7 – Mechanical properties. (a) Schematic of AFM nanoindentation on suspended graphene. (b) Loading/unloading curve for device in (a) with modeling comparison (red line) [Lee 2008].

strength is estimated to be 1.0 TPa and 130 GPa respectively for the defect-free sheet. A similar method is also employed to measure the mechanical properties of chemical modified graphene (CMG), which results in an elasticity modulus of 0.25 TPa [Gómez-Navarro 2008]. The excellent mechanical properties of graphene lead to a significant potential as a filler of reinforcement in composites.

Moreover, Ruoff *et al.* have fabricated graphite-oxide-based thin films via solvent-casting methods and done some research on this kind of paper-like material [Dikin 2007]. It has been shown that the average elasticity modulus can reach 32 GPa and the largest breaking strength is 120 MPa. Some modifications of the graphene oxide paper are applied, including chemical functionalization with divalent ion [Park 2008] or polyacrylamide [Park 2009b] to get cross-linked graphene oxide platelets, which leads to a 10% – 200% improvement of the stiffness and $\sim 50\%$ enhancement of the fracture strength.

2.1.5 Other properties and summary

2.1.5.1 Optical properties

The graphene monolayer is highly transparent as illustrated in Fig. 2.8. The discoverers of graphene, Geim *et al.* [Nair 2008] found that the absorption of visible light of single-layer graphene is only 2.3%, that is to say, the transmittance is up to 97.7%. Indeed, in the visible range, thin graphene films have a transparency that decreases linearly with the film thickness. For 2 nm thick films, the transmittance is higher than 95% and remains above 70% for 10

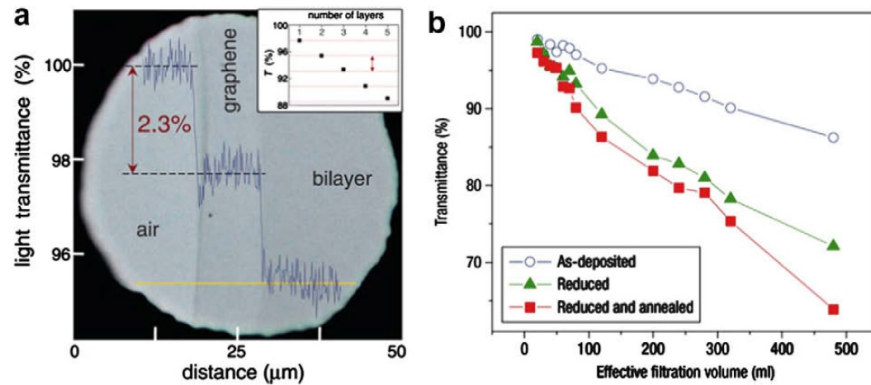


FIGURE 2.8 – (a) Photograph of a $50 \mu\text{m}$ aperture partially covered by graphene and its bilayer. Inset shows the sample design : a $20 \mu\text{m}$ thick metal support structure has apertures 20 , 30 , and $50 \mu\text{m}$ in diameter with graphene flakes deposited over them ; (b) Transmittance at $\lambda \sim 550 \text{ nm}$ as a function of the thickness of reduced GO thin films, assessed indirectly by the total volume of filtered suspension. Plots are shown for thin films with different reduction steps. [Nair 2008]

nm thick films [Blake 2008, Lotya 2009]. The optical characteristic combined with the excellent conductivity of graphene suggests employing graphene as transparent electrode for solar cells or liquid crystal but also as processable transparent flexible electrode material [Blake 2008, Lotya 2009], whose transmittance is over 80% in the spectrum from 400-1800 nm, and the electrical conductivity can still reach 1000 S/m.

2.1.5.2 Thermal properties

The first experimental study of the thermal conductivity of single-layer graphene was performed by Balandin *et al.* [Balandin 2008] (see in Fig. 2.9), who found that a suspended graphene sheet obtained by mechanical exfoliation could exhibit extremely high thermal conductivity values, ranging from $(4.84 \pm 0.44) \times 10^3$ to $(5.30 \pm 0.48) \times 10^3 \text{ W/mK}$. However, the theoretical prediction of the thermal conductivity at room temperature of graphene is more than 6000 W/mK [Berber 2000]. In fact, the thermal conductivities of carbon allotropes are all very high, but that of graphene is the highest of the known materials until now. Therefore, the outstanding thermal conduction

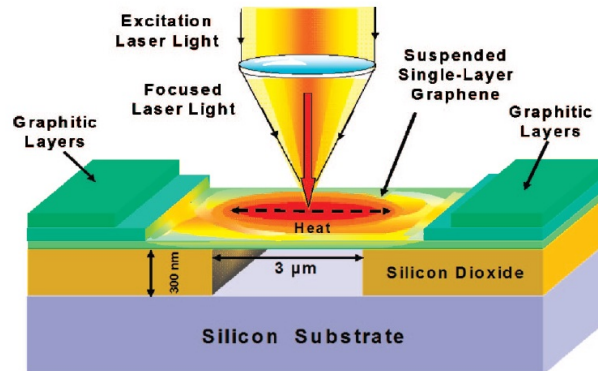


FIGURE 2.9 – Schematic of the experiment showing the excitation laser light focused on a graphene layer suspended across a trench. The focused laser light creates a local hot spot and generates a heat wave inside single-layer graphene propagating toward heat sinks [Balandin 2008].

property of graphene is beneficial for the proposed electronic applications and establishes graphene as an excellent material for thermal evacuation.

2.1.5.3 Summary of the properties of graphene

We summarize the properties of graphene in Table 2.2.

2.2 Graphene reinforced nanocomposites

Due to the discovery of graphene with its combination of extraordinary physical properties and ability to be dispersed in various polymer matrix, a new class of polymer nanocomposites has been created, which exhibits enhancement in mechanical, thermal, electrical, and gas barrier properties of polymers.

2.2.1 Synthesis of graphene-polymer nanocomposites

The most common synthesis strategies of polymer matrix composites are solution mixing, melt blending and *in situ* polymerization [Galpaya 2012, Du 2012]. No matter which strategy is used, improving the dispersion and interfacial interactions between the graphene and polymer matrices are key challenges to obtain property improvements in their composites.

TABLE 2.2 – Properties of graphene

Geometry :
Thinnest material in the world—0.34 nm thick
Highest surface to volume ratio—2630 m ² /g
Lightest continuous film (per unit area)—0.38 mg/m ²
Physical properties :
Highest tensile strength of any material—Young’s modulus of 1 TPa
Large transparency—97.7%
Best conductor of electricity—Resistivity of 10 ⁻⁶ Ωcm
Fastest moving electrons in any material—~ 10 ⁶ m/s
Highest electron mobility of any material—more than 200000 cm ² V ⁻¹ s ⁻¹
Best conductor of heat—thermal conductivity of 5300 W · m ⁻¹ · K ⁻¹
Chemical properties :
Chemically inert
Can be functionalized in a number of specific ways by organic chemistry

2.2.1.1 Solution mixing

Solution mixing is the most straightforward method for the preparation of polymer composites, which can be employed to synthesize the composites with a range of polymer such as poly(vinyl alcohol) (PVA), polyvinyl fluoride (PVF), polyethylene (PE), poly(methylmethacrylate) (PMMA) and polyurethane (PU). The method contains the three steps as :

1. dispersion of graphene in a suitable solvent ;
2. incorporation of polymer ;
3. removal of the solvent by distillation or evaporation.

The solvent compatibility of the polymer and the filler play a critical role in achieving good dispersion, and generally chemical functionalization of graphene can improve the solubility and interaction of the graphene and polymer. Ultrasonication can also help to obtain a homogenize dispersion of graphene sheets.

2.2.1.2 Melt blending

Melt blending is a more practical technique for thermoplastic polymers, such as poly(vinylidene fluoride) (PVDF), polystyrene (PS), polypropylene

(PP). The high temperature is employed to soften the polymer matrix, along with shear force allowing the dispersion of the graphene sheets. The drawback of this technique is the less efficiency in dispersing graphene in the polymer matrix especially at higher filler loadings due to increased viscosity of the composites, and the bucking, rolling of the graphene sheets during the mixing.

2.2.1.3 *In situ* polymerization

In situ polymerization is another popular technique to fabricate graphene polymer nanocomposites such as epoxy, PMMA, Nylon 6, PU, poly(butylene terephthalate) (PBT), polyaniline (PANI), PE, *etc.* In this method, graphene or its derivative is first swollen in the liquid monomer to form a homogeneous mixture. Then the initiator is added and the mixture is exposed to appropriate source of heat, radiation, *etc.* The drawback of this method is the high limitation of the graphene fractions.

Overall, the graphene/polymer nanocomposites with various polymer nanocomposites call for different ways of fabrication in order to get good dispersion and interfacial interactions.

2.2.2 Electrical properties

Graphene sheets can provide percolated pathways for electron transfer, making the composites electrically conductive. Various polymers, such as PMMA, PVA, PVC, PE, PS, PP, *etc.* [Galpaya 2012] have been used as matrix prepare electrically conductive graphene/polymer nanocomposites. The graphene-polymer nanocomposites generally exhibit a non-linear increase of the electrical conductivity as a function of the graphene concentration as shown in Fig. 2.10. The composite showed a very low conductivity at small graphene volume fraction. Increasing the graphene concentration, there is a sudden rise in the electrical conductivity at a certain concentration when the fillers form a network, which realizes a transition from insulator to conductor. This critical filler fraction is the percolation threshold.

According to the large aspect ratio and high conductivity of graphene, it enables the insulator to conductor transition at significantly low loading [Steurer 2009]. The lowest electrical percolation threshold was 0.1 vol% reported by Ruoff *et al.* [Stankovich 2006] for PS solvent blended with isocyanate-treated graphene oxide followed by solution-phase reduction with dimethyl-

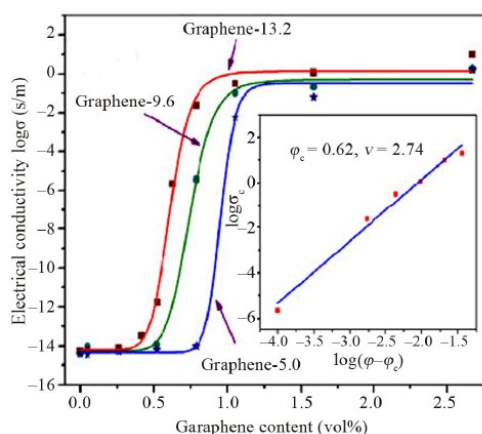


FIGURE 2.10 – Electrical conductivity of graphene/PMMA composites as a function of graphene content [Zhang 2012a].

hydrazine, which is comparable with those of single-walled carbon nanotube (SWCNT). And when the graphene concentration increases to 1 vol%, the electrical conductivity of the composites can reach 1 S/m. The graphitic layers produced by electromechanical exfoliation of graphite in ionic liquids can percolate at 0.13-0.37 vol% as reported [Liu 2008a].

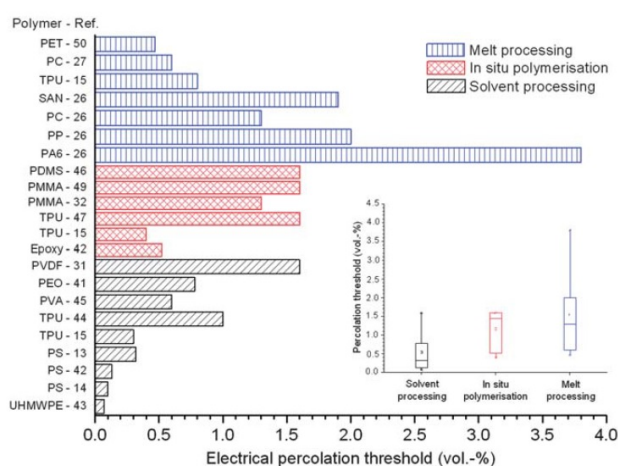


FIGURE 2.11 – Electrical percolation thresholds of graphene/polymer composites according to different processing strategy [Verdejo 2011].

The percolation threshold of graphene reinforced nanocomposites is not only dependent on the surface modification and aspect ratio of graphene, but also associated with the polymer matrix and the fabrication process. In

Fig. 2.11, the electrical percolation thresholds are collected from the literatures according to the production methods : solvent processing [Tkalya 2010, Stankovich 2006, Pang 2010], *in situ* polymerisation [Kim 2010, Jiang 2009b, Kujawski 2010] and melt processing [Kim 2010, Steurer 2009]. It can be seen that the percolation thresholds vary over a wide range of loading fractions which is caused by the different type and functionalisation of graphene and from the degree of dispersion. Low percolation thresholds were achieved with chemically reduced GO, using hydrazine and isocyanate via solvent processing due to a better dispersion of graphene sheets, while the largest was attained with a thermally exfoliated GO via melt processing.

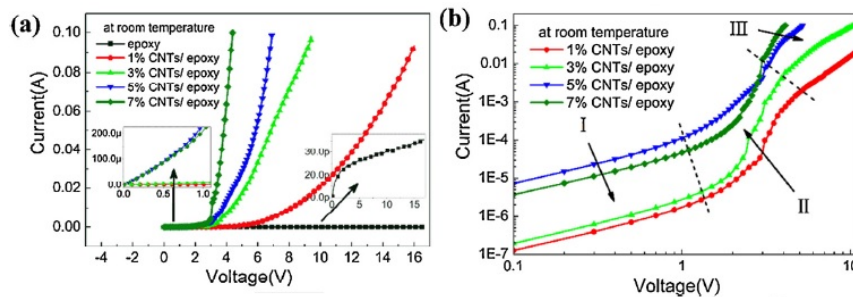


FIGURE 2.12 – I-V curves of the CNTs/epoxy composites under the direct-current voltage at room temperature : (a) in normal scale ; (b) in log-log scale. [Wang 2016].

Wang *et al.* [Wang 2016] demonstrated that the Current-Voltage (I-V) curve of carbon nanotubes (CNTs)/epoxy composites with varied CNTs concentrations measured under direct-current voltage at room temperature exhibited a nonlinear characteristic shown in Fig. 2.12, which is a very typical behavior for the graphene-based material reinforced nanocomposites. Since the range showing the highly non-Ohmic property is wide, the I-V characteristics are expressed logarithmically and are classified into three segments.

Region I : The conduction current changes linearly with voltage and obeys Ohm's law.

Region II : A small increase in the voltage results in a sharp increase of the current.

Region III : The curve remains nonlinear, but the variation of current with the voltage becomes slow.

2.2.3 Mechanical properties

Many research on the CNTs/polymer nanocomposite have been conducted, aiming to develop and make use of the excellent mechanical properties of CNT, as well as introduce some novel functions at the same time, such as electrical and thermal conductivity. However, some problems still exist although many researchers have focused on the CNT/polymer nanocomposites. Compared with CNTs, graphene has advantages for the structural and functional nanocomposites system due to its larger surface area, stronger interface bonding strength and the equally remarkable physical properties [Steurer 2009, Rafiee 2009].

2.2.3.1 Rigidity

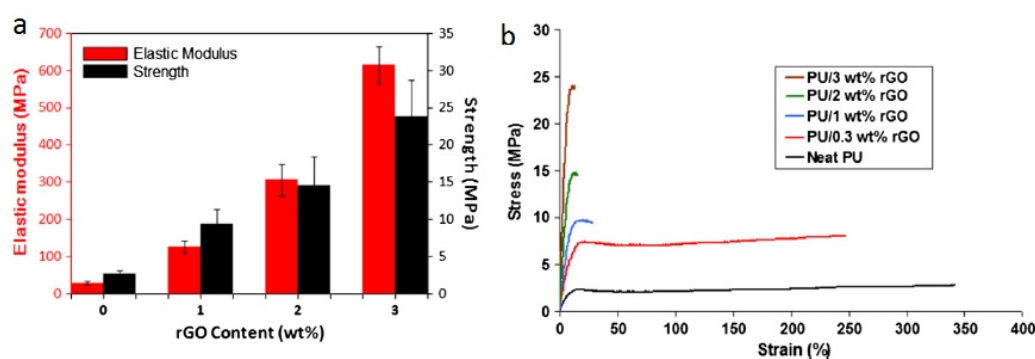


FIGURE 2.13 – (a) Tensile test results for PU/RGO composites as a function of graphene content;(b)Typical tensile stress-strain curves of PU/RGO composites containing different graphene contents [Yousefi 2013].

The studies focusing on the mechanical properties of graphene filled polymer nanocomposites revealed an increase in modulus as a function of loading fraction [Ramanathan 2008, Kim 2010, Das 2009, Fang 2009, Rafiee 2009, Liang 2009c, Verdejo 2008]. For instance, as reported, the modulus increased 31% with the introduction of 0.1 wt% thermally exfoliated graphene into the epoxy matrix [Rafiee 2009], 120% for the graphene/PU composite when the chemically reduce graphene concentration is 1 wt% [Liang 2009c], and 200% for the thermally exfoliated graphene/silicone foam with 0.25 wt% filler fraction [Verdejo 2008].

As expected, the larger improvements can be observed in elastomeric matrices due to their lower intrinsic modulus. Yousefi *et al.* [Yousefi 2013] evaluated the elastic modulus of polyurethane (PU)/reduced graphene oxide(RGO) nanocomposites and strength at different filler concentration as shown in Fig. 2.13 (a), which showed remarkable 21% and 9% increases in tensile modulus and strength due to the addition of 3wt% of RGO compared to neat PU, respectively. It should be noted that the enhancements in these properties were at the expense of ductility or failure strain as the RGO content increased above 1 wt% (Fig. 2.13 (b)).

2.2.3.2 Strength

Though few studies have given details on the strength of the nanocomposites, some experiments proved that graphene filler can improve the strength of the polymer matrix.

Generally, as for the nanoclay/polymer composites, the tensile strength decreases along the content of the filler [Awad 2009], *e.g.*, the tensile strength of PMMA-epoxy-nanoclay composite decreases by 50% with 3.8% nanoclay [Park 2003]. The introduction of graphene-based material, *e.g.*, CNTs, can increase the strength of the composites to some extent. Qian *et al.* [Qian 2000] reported that adding 1 wt% MWCNTs in the PS by solution-evaporation method, results in $\sim 25\%$ improvements in the tensile strength. Xin *et al.* [Xin 2011] found that addition of 1 wt% CNTs into PS increased the tensile strength by about 20%. Compared with other reinforcements, graphene shows great potential in improving the mechanical strength of the polymer matrix. For example, Fang *et al.* [Fang 2010] increased the breaking strength of epoxy by 91.5 % with the introduction of 0.6 wt% graphene. Xu *et al.* [Xu 2010] applied only 0.1 wt% graphene into nylon-6, which led to an increase of 210% for the strength of polymer. The authors ascribed the improvement of the mechanical properties to the larger interfacial area and aspect ratio of graphene as well as the the presence of defects and wrinkles.

Ramanathan *et al.* [Ramanathan 2008] suggested that the presence of the wrinkles may actually lead to nanoscale surface roughness which would likely produce an enhanced mechanical interlocking and adhesion with the polymer chains (see in Fig. 2.14). However, this physical interaction can not efficiently avoid the damage on the interface between graphene and polymer matrix due

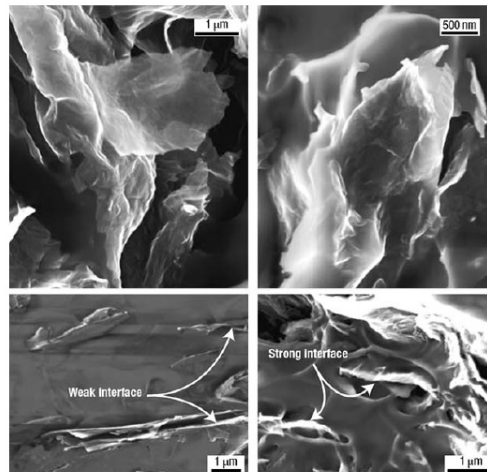


FIGURE 2.14 – (a, b, d) SEM images of thermally reduced graphene/PMMA composites. (c) SEM image of expanded graphite/PMMA composites [Ramanathan 2008].

to the slippage, which limits the maximum strength of the composite.

Some works suggest that using chemical method can improve the interfacial structure of the two phases and can greatly improve the efficiency of the load transfer [Chatterjee 2012, Yan 2012]. Apart from the bonding interface, the distribution [Alexandre 2000] and orientation [Fornes 2003] of the nanofiller can also affect the mechanical properties of the nanocomposites.

2.2.3.3 Toughness and endurance limit

Moreover, graphene filler can also change the toughness of the composites apart from the moduli and strength. The experimental results by Rafiee *et al.* [Rafiee 2010] show that the graphene/epoxy composites exhibit good fracture toughness and the endurance limit, with 65% and 115% increase respectively when the fraction of graphene is 0.125 wt%. Bortz *et al.* [Bortz 2011] proposed that the fracture toughness and the endurance limit under uniaxial tensile of graphene oxide/epoxy composites increased 28-111% and 1580% respectively when the concentration of graphene oxide ≤ 1 wt%. The results are ascribed to the 2D structure and the wrinkles of graphene, which can efficiently prevent cracks from propagating.

2.2.4 Other properties

Improving thermal conductivity using graphene platelets was demonstrated for epoxy [Sun 2010a], PP [Kalaitzidou 2007], PE [Fukushima 2006], PVC [Vadukumpully 2011]. Araby *et al.* [Araby 2014] dispersed cost-effective graphene of hydrophobic surface in the polymer matrix, and obtained a three times enhancement of thermal conductivity at 24 vol%. Gu *et al.* [Gu 2016] fabricated graphene nanoplatelets (GNP)/epoxy nanocomposites via casting method, of which the surface of graphene was functionalized by methanesulfonic acid/ γ -glycidoxypropyltrimethoxysilane. They finally found that the thermal conductivity increased with the increasing graphene addition, and the corresponding thermally conductive coefficient of the functionalized GNPs-epoxy nanocomposites was improved to 1.698 W/mK with 30 wt% functionalized GNPs, 8 times higher than that of original epoxy matrix. A thermal conductivity of 50 W/mK was even obtained by Zhao *et al.* [Zhao 2016] for the poly(ρ -phenylene benzobisoxazole) based nanocomposites with self-alignment graphene sheets whose concentration is less than 5.0 vol% without any assistance of an external magnetic or an electric field.

Apart from the electrical, mechanical and thermal properties introduced above, graphene/polymer nanocomposites also exhibit other functionalities due to the unique 2D structure, excellent physical properties and high aspect ratio. For example :

1. Gas barrier properties [Guo 2012, Liu 2013, Huang 2012]. The compact structure of graphene can hinder the diffusion path of small-molecule gases in the polymer matrix, thus decrease the permeability ;
2. Biocompatibility [Chen 2012] ;
3. Corrosion resistance [Zhang 2013b] ;
4. Optical properties [Loomis 2012] ;
5. Change the crystallization of polymer matrix [Pang 2012, Chiu 2012, Ning 2013] and so on.

2.2.5 Interfacial properties

Interfacial interactions between polymer and graphene plays a key role in the mechanical performance of the corresponding nanocomposites. Generally,

without other heteroatom functionalities of graphene, the interactions between graphene and polymer are controlled by weak van der Waals forces, π - π -stacking, and hydrophobic-hydrophobic interactions [Israelachvili 2015, Adamson 1967].

van der Waals forces are universal attractive interactions between molecules generated by the transient or permanent dipoles of the molecules, and are the major part of the interfacial strength between graphene and common polymers, such as polyethylene, due to the large surface area and intimate contact [Shen 2011, Zhang 2013a].

Hydrophobic-hydrophobic interactions plays an important part in binding graphene in hydrophobic polymer matrices.

π - π **interactions** is dominant acting as strong bonding sites between graphene materials with electron-rich aromatic rings and the matrix with phenyl-ring, like the modified interaction between graphene and polystyrene by melt blending [Shen 2011]. π - π -stacking can adapt to different space organizations and significantly enhance bonding in graphene nanocomposites.

2.2.5.1 Experimental studies

There are several experimental methods to measure the interaction characteristics including wetting, spectroscopy and force microscopy.

Wetting Evaluating the quality of reinforcement wetting is a preliminary measure of adhesion property measurements, and are typically reported in terms of contact angle [Nuriel 2005], surface tension [Dujardin 1998], and Hamaker constant [Maeno 2010]. Different scales measurements of the carbon nanotube wetting by polymer have been reported.

In macroscopic wetting experiments, liquid polymer is placed on top of a carbon nanotube sample to observe whether the polymer is absorbed by the surface or forms a spherical bead. Laplace-Young model is typically used and the results are presented in the form of contact angle [Dujardin 1998].

Microscopic techniques of wetting measurements usually use drop-on-fiber analysis [Tran 2008] and employ optical or electron microscopy to observe the contact angle [Qian 2010]. For example, the contact angle results between car-

bon nanotubes and various polymers such as PP, PMMA, PVDF are reported in the literature [Nuriel 2005, Tran 2008, Qian 2010, Barber 2005].

However, this kind of simple measurement has a number of disadvantages that make it less popular. The main point is that the results of the measurement exhibited a large range even for the same composite system, for instance 25-73° as the contact angle at the polyethylene glycol (PEG) -Multiwall carbon nanotubes (MWCNT) interface [Nuriel 2005, Barber 2005, Barber 2004b].

Spectroscopy Spectroscopy techniques, including Raman and Fourier Transform InfraRed spectroscopy (FTIR) as well as X-ray scattering, are powerful techniques for material characterization. They can not only detect the functionalization but also distinguish different types of functionalization because that the Raman and infrared spectra of pristine and functionalized nanotubes are different. In fact, the Raman spectroscopy can identify the characteristics [Dresselhaus 1996] and dispersion [Bassil 2005] of carbon nanotube in the nanocomposites.

The polymer crystallization affected by the introduction of carbon nanotube can also be tested by X-ray scattering techniques [Zhao 2011]. Since the strength of the spectroscopy techniques for nanocomposites lies in characterization of interfacial properties between filler and matrix, different interaction types, such as van der Waals interaction [Lefrant 2004], hydrogen [Rasheed 2006] and covalent bonds [Baibarac 2009] between carbon nanotube and the surrounding matrix can be characterized by spectroscopy techniques.

The main problem of the spectroscopy technique is that the conclusions are drawn indirectly (e.g., peak shifts indicate load transfer), and therefore insightful analyses are required in order to extract valid conclusions.

Atomic force microscopy Atomic force microscopy (AFM) is a popular technique with high accuracy in atomic force-displacement measurement, and the measurement of the interaction is generally associated with pull-out experiments [Barber 2003] and peeling experiments [Strus 2008].

For instance, Fig. 2.15 shows a typical pull-out force as a function of time during the process of pulling a carbon nanotube out of the solid surrounding polymer matrix. The electron microscope is also used to observe the carbon nanotube to ensure that its original length and diameter have not been changed. The clean pull-out of carbon nanotube is guaranteed by the absence of

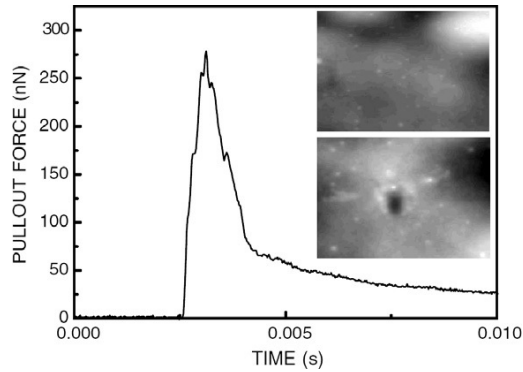


FIGURE 2.15 – Pull-out test of an MWCNT-tip retraction from polyethylene-butene matrix. The insets show the polymer surface before (top) and after (bottom) the pull-out test. The horizontal scan size is $1 \mu\text{m}$ [Barber 2004a]

polymer attached to it, which indicates that the failure occurs at the interface [Barber 2004a].

The peeling force microscopy is another approach to be employed, where a nanotube is attached to a tipless AFM cantilever and is lowered to a substrate to make lateral contact. The nanotube is then peeled off from the surface and the force curve is captured [Strus 2008]. It should be noted that only the normal crack opening is considered in the peel test.

2.2.5.2 Simulation study

Modeling methods are here reported such as molecular dynamics method, coarse grain simulation and density functional theory.

Density functional theory Density functional theory (DFT) studies the electronic structure of atomic scale systems based on quantum mechanics. *ab initio* simulations using DFT, although computationally expensive, provide accurate description of interatomic interactions without assumptions on interatomic force models. This technique has been used in the simulation of carbon nanotube nanocomposites [Li 2009a], which can determine the geometry of the stable state of the system. Moreover, the various interactions between nanotube and polymer have been studied by *ab initio* models, including van der Waals [Simeoni 2005] and chemical functionalization [Mylvaganam 2004]. The results are generally presented in the form of the local density, band structures, and binding energy as a function of distance [Li 2009a, Simeoni 2005].

Molecular dynamics method Molecular dynamics (MD) method can simulate the nanoscale systems based on particle dynamics and interatomic force models (see Chapter 4 for details). The valence and non-bonded interactions between the particles are defined by various force fields. Specifically, the nanotube-polymer interactions have been modeled by molecular dynamics method and the influence of different parameters were investigated.

The pull-out test has been performed by MD simulations [Gou 2005, Li 2011], and the interactions for different nanocomposite systems have been discussed, providing the force-displacement response during the separation and some representative parameters. The studies of the influence of temperature [Wei 2006] and chirality [Chen 2008] on the interaction between carbon nanotube and polymer matrix have also been mentioned.

The normal separation and sliding separation between graphene and PE was also performed by small amount of particles [Awasthi 2008], which provided the peak traction and the energy of separation. The studies to investigate the effect of tension and compression were also carried out on sliding mode separation.

Although the results of molecular dynamics method can be accurate, large numbers of particles and restrictions on time steps require powerful computational facilities.

Coarse grain techniques Coarse grain techniques, such as Monte Carlo simulations, are another method to map atomistic systems onto systems with coarser resolution by bead and spring models [Khounlavong 2010], which exhibits more potential for the larger systems. It bridges atomistic and mesoscopic simulations by applying a trade off between the level of details in the model and computation costs. Although most of the coarse grain simulation works of nanocomposites focus on the polymer systems with nanoparticle inclusions [Khounlavong 2010, Zhang 2004], nanotube-polymer systems [Rahmat 2011] are also investigated.

It has been shown that the polymer morphology at the interface is affected by the inclusion, and the polymer chains at the interface forms a highly ordered and densely packed phase [Zhang 2004] (see in Fig. 2.16), where we can see the tendency of alignment of the elongated polymer chains [Starr 2002]. The density at the interface would finally converge to the bulk polymer density at large distances from interface [Rahmat 2011].

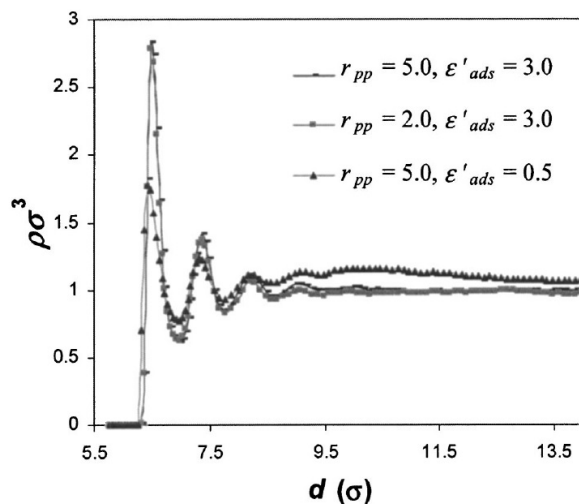


FIGURE 2.16 – Radial distribution of the normalized polymer segment density $\rho\sigma^3$ in the eight-particle system. d is the radial distance to particle surface [Zhang 2004].

2.3 Graphene nanocomposites applications

Generally, even a small fraction of graphene component in the nanocomposites can lead to a dramatic improvement of mechanical and other physical properties, such as electrical conductivity, unique photonic/optical transportation, anisotropic transport and low permeability. Therefore, the introduction of graphene-based nanomaterials has prompted the development of flexible nanocomposites for emerging applications in various fields, including energy conversion [Britnell 2013], energy storage [El-Kady 2013], electronic materials [Kim 2009], low density structural materials [Hu 2013], sensors [Mannoor 2012], chemical screening applications [Guo 2013], and thermal interface materials [Shahil 2012].

2.3.1 Sensors

Firstly, graphene-based nanocomposites have been widely used for sensing applications especially as gas sensors with high sensitivity, selectivity, and stability. For example, Chen *et al.* [Chen 2015] fabricated AgNPs-naphthalene-1-sulphonic acid-RGO composite (Ag-NA-RGO) based sensor where the AgNPs played an important part in the isolation of graphene layers and segregated the graphene layers from a holistic entity to a multi-layer structure. The NO_2

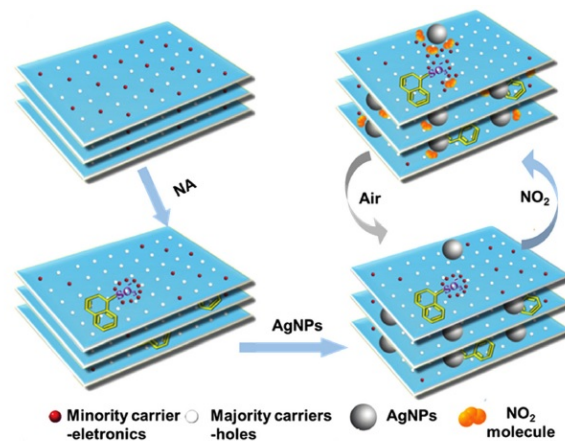


FIGURE 2.17 – The ideal gas sensing mechanism for the gas sensors fabricated based on multilevel hybrid composites. [Chen 2015]

gas molecules can penetrate the structure and be absorbed as shown in Fig. 2.17, and the adsorption of gas molecules results in a conductance change of the device.

Xu *et al.* [Xu 2015] prepared a CO₂ gas surface acoustic wave sensor by using graphene, alanine and Ni NPs to detect, capture and store the CO₂ gas, where the Graphene-Ni Nps-L-alanine sensing layer was fabricated by electrochemical deposition and oscillator circuits. The Ni NPs acted as nuclear sites and a reducing agent in the electrodeposition of G, and may also catalyze the hydrolysis of CO₂, which would enhance the selectivity of this sensor.

Moreover, to detect H₂, the gas sensor with Pd NPs dispersed and anchored on graphene layers was made by microwave method [Martínez-Orozco 2015], where the charge transferring from the gas to graphene composite films leads to a change of the resistance of the sensor.

The graphene-based composite films (GCFs) can also be used as an active layer and an electrode for pressure sensors owing to their superior mechanical and electrical properties. With high sensitivity, such pressure sensors have been used in the continuous recording of pulse, blood pressure and heartbeat for the collection of fundamental health information [Schwartz 2013, Wang 2014a, Zang 2015]. An air pressure sensor based on PDMS-PCA-Graphene films has been produced by An *et al.* [An 2011], where PDMS provides a stable substrate for the macroscopic PCA-G films. The advantage of the graphene-based composite films pressure sensor is low-cost, lightweight and portable,

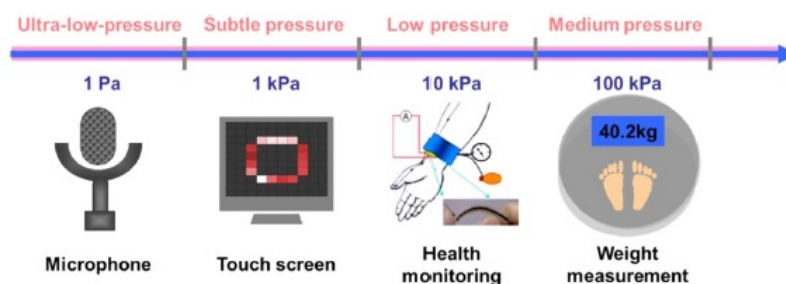


FIGURE 2.18 – The promising applications of the GCFs-based pressure sensor [Zang 2015].

and it is applicable in diverse pressure-dependent applications, from ultra-low pressure to medium pressure as shown in Fig. 2.18.

2.3.2 Supercapacitors

Graphene has also attracted great interest in energy storage applications including supercapacitors and batteries due to the theoretical specific surface area of $2630 \text{ m}^2/\text{g}$. Graphene and graphene derivative materials are often used as the active materials of the supercapacitor electrode, and the polymer binders are used as binders to bind graphene sheets onto the current collector.

PVDF is mainly used as a binder material for graphene-based supercapacitors which can maintain the electrode feature and provide mechanical strength. To form the electrode of the supercapacitor, the graphene nanoplatelets and 10-20 wt% of PVDF are mixed and be kneaded into a paste-like composite, to which some organic solvents are added to adjust the viscosity. The composite slurry is finally coated on to the current collector, following by drying and compressing to form the electrode. To minimize the adverse conductivity effect of PVDF, a certain percentage of conductive carbon (*e.g.*, carbon black) can be introduced to the mixture. For example, [Yan 2010] obtained a specific capacitance of 175 Fg^{-1} and only 9.1% capacitance decrease over 6000 cycles by utilizing the reduced graphene/PVDF/CB supercapacitor electrode.

Nowadays, conducting polymers, such as PANI, polypyrrole(PPy), and poly(3,4-ethylenedioxythiophene) (PEDOT), offer another approach for the supercapacitor applications, which can avoid the disadvantages of not conductive and provide a fast redox reaction with an electrolyte. The GO/PANI

composites have been used as electrode which exhibit a specific capacitance of 320 Fg^{-1} when the fraction of GO is 10 wt% [Zhang 2010b]. Bose *et al.* [Bose 2011] observed that the GNS/PPy composites have almost twice of the specific capacitance and much better cycling performance as supercapacitor electrode compared to pure PPy film. Wen *et al.* [Wen 2014] reported that GO/PEDOT composite electrode has a specific capacitance of 136 Fg^{-1} , and RGO/PEDOT composite electrode has a specific capacitance of 209 Fg^{-1} with 87% capacitance retention over 2000 cycles.

2.3.3 Photovoltaic material

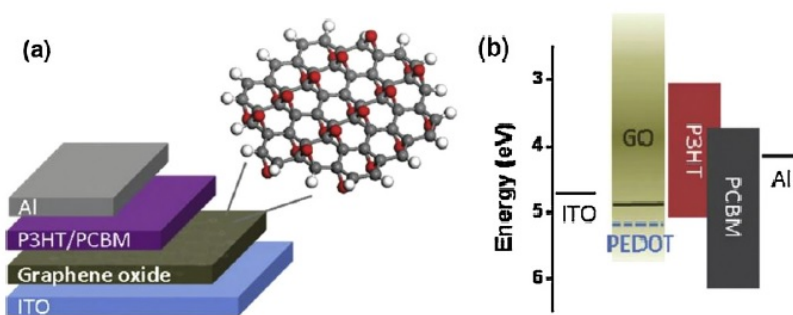


FIGURE 2.19 – (a) Device schematic and (b) energy level diagram of the photovoltaic device structure consisting of ITO/GO/P3HT :PCBM/Al components [Li 2010].

Graphene can be effective in fabricating organic photovoltaic materials as hole transport materials. Chhowalla *et al.* [Li 2010] demonstrated that the graphene oxide can be used as alternative, solution processable hole-transport material in organic photovoltaic films as shown in Fig. 2.19, where the graphene oxide film is located between the photoactive poly(3-hexylthiophene) (P3HT)/ phenyl-C61-butyric acid methylester (PCBM) layer and the Indium Tin oxide (ITO) electrode. This device exhibited great improvement of the photovoltaic efficiency compared to some traditional ones. Moreover, some publications also show a combination of graphene with solid polymer electrolytes and dye-sensitized solar cells [Akhtar 2013, Zheng 2013], as well as the applications of graphene polymer nanocomposites for optoelectronic phenomena [Angmo 2013, Zhang 2013c].

Multiscale modeling of electric conductivity in graphene-reinforced nanocomposites taking into account the tunneling effect

3.1 Introduction

Carbon-based nanofillers (*e.g.*, black carbon, carbon fiber and carbon nanotubes) have been widely used for improving the mechanical, thermal and electric properties of nanocomposites with polymer matrix [Li 2009b, Li 2013, Park 2009a, Tibbetts 2007, Spitalsky 2010]. Graphene, a two dimensional sheet composed of sp^2 carbon atoms arranged in a honeycomb structure, has been recently used as filler in polymer-matrix composites for a wide range of applications, due to its giant electrical and mechanical properties [Xu 2009, Du 2012, Woltornist 2015, Shtein 2015, Zhao 2015]. Even though polymeric materials are considered as electrical insulators due to their extremely low electrical conductivity, the introduction of graphene can lead to a percolation behavior at very low volume fractions and can increase the conductivity of the resulting composites by several orders of magnitude [Wei 2009, Wang 2014b, Vadukumpully 2011]. In recent studies, the percolation threshold for graphene can be as low as 0.07% in volume fraction due to its extremely low aspect ratio [Pang 2010].

In the 2000s, a number of contributions have been proposed for the simulation of the electric conductivity of nanocomposites with carbon-based filler,

mostly with carbon nanotubes (CNTs). A simple model was first set up by Bauhofer and Kovacs [Bauhofer 2009] to describe the electric conductivity in nanocomposites in the form of a power-law. However, such models are empirical and do not allow sensitivity analysis of the effective electric conductivity of the composite with respect to its constituent parameters (microscale).

Experiments to measure the conductivity of composites embedding carbon particles have evidenced two unexpected phenomena : on one hand, the electrical response, *i.e.*, the current-voltage curve can be nonlinear for high applied voltages [Wang 2016, Hu 2008a]. On the other hand, the values of the effective conductivity is much larger than expected, considering that the polymer matrix is almost electrically insulating, even when then percolation threshold is reached [Sandler 2003, He 2009]. To explain these effects, linear models of conductivity are not sufficient. One possible phenomenon to explain these effects is the electric tunneling effect [Allaoui 2008, Martin-Gallego 2013, Zeng 2011] : for small distances between carbon inclusions (of the order of 1 or 2 nm), electrons can cross the energy barrier formed by the polymer layer between both inclusions. In this region, the resulting electric conduction is nonlinear and conduction can be achieved even without perfect contact between inclusions, resulting in small percolation thresholds and increased effective conductivity even at very low volume fractions of inclusions [Gojny 2006, Li 2007, Du 2005].

For design purpose, numerical models of conduction at the scale of a Representative Volume Element (RVE) containing a significant number of graphene sheets is required to fully understand the conditions for percolation and determining optimal configurations and microstructural parameters to increase the performances of these materials. Complete *ab initio* or atomistic simulations including electric conductivity in large systems like polymers-graphene reinforced composites are nowadays not feasible, and classical homogenization methods or Monte Carlo techniques [Bauhofer 2009, Castañeda 1995, Fan 2015, Xia 2017a, Wang 2014c, Grimaldi 2006, Otten 2009] are unable to explain the nonlinear effects and low percolation thresholds in graphene-polymer nanocomposites. Simulations of larger systems require continuum description of fields and related numerical methods. Hu *et al.* [Hu 2008b] and Bao *et al.* [Bao 2012] considered the tunneling effect between CNTs and evaluated the effective electric properties of nanocomposites with randomly distributed CNTs. These authors estimated the tunneling resistance by Sim-

mons' model [Simmons 1963] with the assumption that the electric potential between two tubes is close to zero, and latter introduced the tunneling channels by Landauer-Büttiker(L-B) model [Buldum 2001] and extended the theory to various types of CNTs. Wang *et al.* [Wang 2015] developed a continuum theory considering the factors that affect the overall conductivity of graphene-based nanocomposites, including the dispersion state of graphene, the imperfectly conducting interface and tunneling-assisted interfacial conductivity. Recently, some continuum models are developed to determine the effective AC and DC electrical properties of graphene nanocomposites taking into account their morphological and physical features, which take the effective-medium theory or self-consistent effective medium theory as the backbone [Hashemi 2016, Xia 2017b, Xia 2017a]. A multi-scale multi-physics finite element method is also proposed to predict the electrical response of the graphene/polymer composite under DC loading, in which the representative volume element (RVE) is filled with randomly dispersed nano-platelet conductive inclusions by Monte Carlo model and with the creation of unit cell [Manta 2017].

To our best knowledge, numerical methodologies involving nonlinear tunnelling effect to evaluate the effective electric conductivity in composites are quite few, but are required to better understand the local phenomena and influence of reinforcement parameters on the apparent electric conductivity of the composite and to design materials with higher performances. In the present work, we develop such numerical methodology based on finite elements to study the effective conductivity of graphene-polymer nanocomposites and predict percolation thresholds. A procedure based on numerical calculations on a RVE containing randomly distributed graphene sheets is proposed. A FEM formulation involving the nonlinear electric conduction effects is developed. To take into account the specific non-localities related to the tunneling effect, a distance function map is constructed within the RVE model. In addition, an imperfect surface model (see *e.g.*, [Yvonnet 2008a, Gu 2011]) is introduced to model the graphene sheets as surface within the RVE model and avoid meshing the thickness of graphene sheets, while incorporating the discontinuities in electric current density in the normal direction of graphene sheets. Finally, a procedure is described to compute the effective electric conductivity of the material on the RVE.

This chapter is organized as follows. In section 3.2, we first provide an

introduction to the electrical imperfect surface model. In section 3.3, the tunneling effect model, which characterized the nonlinear conduction mechanisms between the close graphene sheets is described. In section 3.4, the multiscale model of graphene-polymer composite is presented as well as the related homogenization procedure. The FEM discretization of equations to solve the RVE nonlinear problem including the tunnelling effect is described in section 3.5 with related algorithms, along with the geometric modeling of graphene/polymer nanocomposites. Then, we present some examples in section 3.6 to validate the model and the influence of tunneling effect. In section 3.7, apart from the RVE analysis, this model is used to quantitatively analyze the effects of barrier height and configuration of graphene sheets versus electric percolation thresholds in graphene-polymer nanocomposites. Finally, we provide qualitative comparisons between the results provided by the proposed model and some available experimental data. The results of this chapter have been adapted from one published paper [Lu 2017b] and one submitted article [Lu 2017a].

3.2 Electrical imperfect surface model

In our proposed model, the graphene sheets embedded in the polymer matrix are considered as multilayer graphene platelets, and then have a finite thickness. As their aspect ratio can however be very high, we propose to replace the platelets by imperfect interfaces with zero thickness but equivalent energetically. This avoids the meshing of platelets in their thickness for the numerical simulations. In what follows, the theory of imperfect interfaces for electric conduction is reminded.

When two solids are in contact or glued together, there is a thin transition zone between them which behaves as an interphase. Generally, the properties of the interphase are quite different from those of the solids. Since the thickness of the interphase zone is relatively small as compared to the dimensions of the solid, it is possible to replace this zone by an imperfect interface with zero thickness. The modeling of an interphase as an imperfect interface has been first proposed by Sanchez-Palencia [Sanchez-Palencia 1970] and Pham Huy [Huy 1974] using an asymptotic approach in the case of thermal conduction. It was then extended by Klarbring [Klarbring 1991] to the

context of linear elasticity. In this work, the approach we introduced is proposed by Gu [Gu 2011] and Yvonnet [Yvonnet 2008b], which is based on the work of Bövik [Bövik 1994], Hashin [Hashin 2001, Hashin 2002], Benveniste [Benveniste 2006a, Benveniste 2006b, Benveniste 2007]. See a general extension of this framework for multiphysical coupling in [Gu 2011]. This approach has the advantages of being independent of any coordinate system, and not using main curvilinear coordinates.

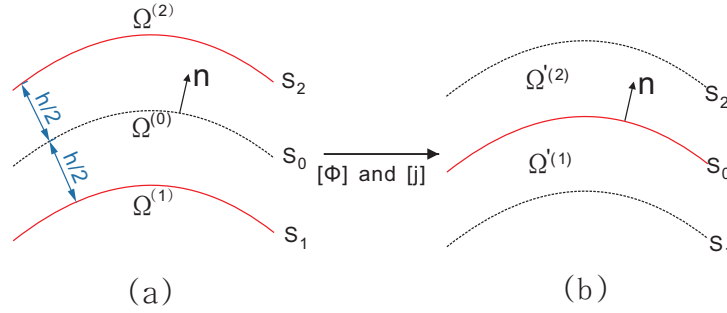


FIGURE 3.1 – Replacement of an interphase by an imperfect interface. (a) Phase 1/interphase 0/Phase 2; (b) Phase 1/imperfect surface S_0 /Phase 2

The following is adapted from the procedure described initially in [Gu 2008].

3 phases Model In Fig. 3.1, an interphase of uniform thickness h , called phase 0, is located between the two materials named by phases 1 and 2. Phase 0 is perfectly bonded to the phases 1 and 2 through the surfaces S_1 and S_2 . As for the electrical conduction, the normal component of the current flux j_n and the electrical potential ϕ are continuous through the perfect surfaces S_1 and S_2 .

$$\begin{aligned} \phi^{(0)}|_{S_1} &= \phi^{(1)}|_{S_1}, & \phi^{(0)}|_{S_2} &= \phi^{(2)}|_{S_2}, \\ j_n^{(0)}|_{S_1} &= j_n^{(1)}|_{S_1}, & j_n^{(0)}|_{S_2} &= j_n^{(2)}|_{S_2}. \end{aligned} \quad (3.1)$$

The three phases 0, 1 and 2 are assumed to be homogeneous and linear. The law of Ohm for electrical conduction in the three phases is then given by

$$\mathbf{j}^{(i)} = \mathbf{K}^{(i)} \mathbf{E}^{(i)}, \quad (3.2)$$

where $\mathbf{K}^{(i)}$ is the electrical conductivity tensor of the phase i which is symmetric and positive, $\mathbf{j}^{(i)}$ corresponds to the electric current flux of the phase i

and $\mathbf{E}^{(i)}$ is the electric field of phase i defined as the negative gradient of the electrical potential, *i.e.*,

$$\mathbf{E}^{(i)} = -\nabla\phi^{(i)}. \quad (3.3)$$

In steady state, the conservation of energy in the absence of a current source is

$$\nabla \cdot \mathbf{j}^{(i)} = 0. \quad (3.4)$$

In Fig. 3.1 (a), the potential $\phi^{(0)}$ on the medium surface S_0 can be expressed as a function of $\phi^{(0)}$ and its derivatives evaluated on the surfaces S_1 and S_2 by Taylor expansion :

$$\phi^{(0)}|_{S_0} = \phi^{(0)}|_{S_1} + \frac{h}{2}\nabla\phi^{(0)} \cdot \mathbf{n}|_{S_1} + O(h^2), \quad (3.5)$$

$$\phi^{(0)}|_{S_0} = \phi^{(0)}|_{S_2} + \frac{h}{2}\nabla\phi^{(0)} \cdot \mathbf{n}|_{S_2} + O(h^2), \quad (3.6)$$

where $\nabla\phi \cdot \mathbf{n} = \nabla^n\phi$.

Subtracting Eq. (3.6) and Eq. (3.5), we obtain

$$\phi^{(0)}|_{S_2} - \phi^{(0)}|_{S_1} = \frac{h}{2}(\nabla\phi^{(0)} \cdot \mathbf{n}|_{S_1} + \nabla\phi^{(0)} \cdot \mathbf{n}|_{S_2}) + O(h^2). \quad (3.7)$$

Considering the conditions of continuity in Eq. (3.1), we obtain

$$\phi^{(0)}|_{S_2} - \phi^{(0)}|_{S_1} = \phi^{(2)}|_{S_2} - \phi^{(1)}|_{S_1}. \quad (3.8)$$

Therefore, the jump of the electrical potential through the interphase $\Omega^{(0)}$ in the configuration of Fig. 3.1 (a) can be deduced as :

$$\phi^{(2)}|_{S_2} - \phi^{(1)}|_{S_1} = \frac{h}{2}(\nabla\phi^{(0)} \cdot \mathbf{n}|_{S_1} + \nabla\phi^{(0)} \cdot \mathbf{n}|_{S_2}) + O(h^2). \quad (3.9)$$

Replacing the interphase by an imperfect interface, the normal derivatives $\nabla\phi^{(0)} \cdot \mathbf{n}|_{S_1}$ and $\nabla\phi^{(0)} \cdot \mathbf{n}|_{S_2}$ should be expressed in terms of certain quantities defined in phase 1 and phase 2. Let $\nabla^n\phi$ be the derivative of the electric potential field in normal direction, and $\nabla^s\phi$ the tangent direction,

$$\nabla^n\phi = \nabla\phi \cdot \mathbf{n} = P_1(\nabla^s\phi, j_n; \mathbf{K}) \quad (3.10)$$

where the function P_1 is defined by

$$P_1(\nabla^s\phi, j_n; \mathbf{K}) = -\frac{j_n}{\mathbf{K} : (\mathbf{n} \otimes \mathbf{n})} - \mathbf{s} \cdot \nabla^s\phi, \quad (3.11)$$

and the vector

$$\mathbf{s} = \frac{\mathbf{K} \cdot \mathbf{n}}{\mathbf{K} : (\mathbf{n} \otimes \mathbf{n})}. \quad (3.12)$$

Due to the fact that j_n and $\nabla^s \phi$ are continuous across a perfect interface, we have

$$\begin{aligned} \nabla \phi^{(0)} \cdot \mathbf{n}|_{S_1} &= P_1(\nabla^s \phi^{(0)}, j_n^{(0)}; \mathbf{K}^{(0)})|_{S_1} = P_1(\nabla^s \phi^{(1)}, j_n^{(1)}; \mathbf{K}^{(0)})|_{S_1}, \\ \nabla \phi^{(0)} \cdot \mathbf{n}|_{S_2} &= P_1(\nabla^s \phi^{(0)}, j_n^{(0)}; \mathbf{K}^{(0)})|_{S_2} = P_1(\nabla^s \phi^{(2)}, j_n^{(2)}; \mathbf{K}^{(0)})|_{S_2}. \end{aligned} \quad (3.13)$$

Introducing Eq. (3.13) to Eq. (3.9), we obtain

$$\phi^{(2)}|_{S_2} - \phi^{(1)}|_{S_1} = \frac{h}{2} \left[P_1(\nabla^s \phi^{(1)}, j_n^{(1)}; \mathbf{K}^{(0)})|_{S_1} + P_1(\nabla^s \phi^{(2)}, j_n^{(2)}; \mathbf{K}^{(0)})|_{S_2} \right] + O(h^2). \quad (3.14)$$

Similarly, as for the current flux, we can get

$$j_n^{(2)}|_{S_2} - j_n^{(1)}|_{S_1} = \frac{h}{2} \left[Q_1(\nabla^s \phi^{(1)}, j_n^{(1)}; \mathbf{K}^{(0)})|_{S_1} + Q_1(\nabla^s \phi^{(2)}, j_n^{(2)}; \mathbf{K}^{(0)})|_{S_2} \right] + O(h^2), \quad (3.15)$$

where Q_1 expresses the normal derivative of the current flux $\nabla^n j_n$ which is given by

$$\nabla^n j_n = Q_1(\nabla^s \phi, j_n; \mathbf{K}) = \nabla^s \cdot (\hat{\mathbf{S}} \cdot \nabla^s \phi) - \nabla^s \cdot (\mathbf{s} j_n) \quad (3.16)$$

and the tensor $\hat{\mathbf{S}}$ is calculated by

$$\hat{\mathbf{S}} = \mathbf{K} - \frac{(\mathbf{K} \cdot \mathbf{n}) \otimes (\mathbf{K} \cdot \mathbf{n})}{\mathbf{K} : (\mathbf{n} \otimes \mathbf{n})}. \quad (3.17)$$

2 phases+imperfect surface Model In the configuration of Fig. 3.1 (b), the interphase zone is replaced by the imperfect surface S_0 , which is geometrically the medium surface of the interphase, and phase i ($i = 1, 2$) is extended from the surface S_i to the surface S_0 . The jumps of the normal component of electrical current flux j_n and the electrical potential ϕ through the interphase in Fig. 3.1 (a) should be identical to the jumps of j_n and ϕ across the limited area by S_1 and S_2 in Fig. 3.1 (b) at a fixed error.

Considering the configuration in Fig. 3.1 (b) where the imperfect surface s_0 separates phase 1 and phase 2, we can define the quantities evaluated on

the surface S_0 but on the side of phase 2 are indicated by an exponent "(+)", while those evaluated on the surface S_0 but on the side of phase 1 by "(-)". Therefore, the Taylor expansion of the potential field is written as

$$\begin{aligned}\phi^{(1)}|_{S_1} &= \phi^{(-)} - \frac{h}{2} \nabla \phi^{(-)} \cdot \mathbf{n} + O(h^2), \\ \phi^{(2)}|_{S_2} &= \phi^{(+)} - \frac{h}{2} \nabla \phi^{(+)} \cdot \mathbf{n} + O(h^2).\end{aligned}\tag{3.18}$$

Due to the relations

$$\begin{aligned}\nabla \phi^{(-)} \cdot \mathbf{n} &= P_1(\nabla^s \Phi^{(-)}, j_n^{(-)}; \mathbf{K}^{(1)}), \\ \nabla \phi^{(+)} \cdot \mathbf{n} &= P_1(\nabla^s \Phi^{(+)}, j_n^{(+)}; \mathbf{K}^{(2)}).\end{aligned}\tag{3.19}$$

we obtain the jump of the electrical potential

$$\begin{aligned}\phi^{(2)}|_{S_2} - \phi^{(1)}|_{S_1} &= \phi^{(+)} - \phi^{(-)} \\ &+ \frac{h}{2} \left[P_1(\nabla^s \phi^{(-)}, j_n^{(-)}; \mathbf{K}^{(1)}) + P_1(\nabla^s \phi^{(+)}, j_n^{(+)}; \mathbf{K}^{(2)}) \right] + O(j^2).\end{aligned}\tag{3.20}$$

Combining Eq. (3.14) and Eq. (3.20), we obtain the jump of the electric potential on the imperfect surface S_0

$$\begin{aligned}[\phi] &= \phi^{(+)} - \phi^{(-)} = \frac{h}{2} \left[P_1(\nabla^s \phi^{(-)}, j_n^{(-)}; \mathbf{K}^{(1)}) + P_1(\nabla^s \phi^{(+)}, j_n^{(+)}; \mathbf{K}^{(2)}) \right] \\ &- \frac{h}{2} \left[P_1(\nabla^s \phi^{(-)}, j_n^{(-)}; \mathbf{K}^{(0)}) + P_1(\nabla^s \phi^{(+)}, j_n^{(+)}; \mathbf{K}^{(0)}) \right] + O(h^2).\end{aligned}\tag{3.21}$$

Similarly, the jump of the current flux on the normal direction of imperfect surface S_0 is given by

$$\begin{aligned}[j_n] &= j_n^{(+)} - j_n^{(-)} = \frac{h}{2} \left[Q_1(\nabla^s \phi^{(-)}, j_n^{(-)}; \mathbf{K}^{(1)}) + Q_1(\nabla^s \phi^{(+)}, j_n^{(+)}; \mathbf{K}^{(2)}) \right] \\ &- \frac{h}{2} \left[Q_1(\nabla^s \phi^{(-)}, j_n^{(-)}; \mathbf{K}^{(0)}) + Q_1(\nabla^s \phi^{(+)}, j_n^{(+)}; \mathbf{K}^{(0)}) \right] + O(h^2).\end{aligned}\tag{3.22}$$

More specifically, in the extreme case where the electrical conductivity of the interphase is much higher than that of each of the phases, we have the expressions to describe the situation as

$$h = \kappa h_0, \quad \mathbf{K}^{(0)} = \frac{1}{\kappa} \mathbf{K}_0^{(0)}, \quad \mathbf{K}^{(1)} = \mathbf{K}_0^{(1)}, \quad \mathbf{K}^{(2)} = \mathbf{K}_0^{(2)},\tag{3.23}$$

where κ is a small dimensionless positive parameter which satisfies $\kappa \ll 1$. h_0 , $\mathbf{K}_0^{(0)}$, $\mathbf{K}_0^{(1)}$ and $\mathbf{K}_0^{(2)}$ are the reference values for the analysis.

Therefore, introduce these equations into Eq. (3.21) and (3.22), we obtain

$$[[\phi]] = O(h^2) \quad (3.24)$$

$$[[j_n]] = \frac{h}{2} \nabla^s \cdot [\hat{\mathbf{S}}^{(0)}(\nabla\phi^{(-)} + \nabla\phi^{(+)})] + O(h^2). \quad (3.25)$$

Neglecting the terms whose order is equal to and greater than $O(h)$, it turns out that

$$[[\phi]] = 0. \quad (3.26)$$

$$[[j_n]] = h \nabla^s \cdot (\hat{\mathbf{S}}^{(0)} \nabla^s \phi). \quad (3.27)$$

3.3 Nonlinear conduction mechanisms in polymer/graphene nanocomposites : Tunneling effect

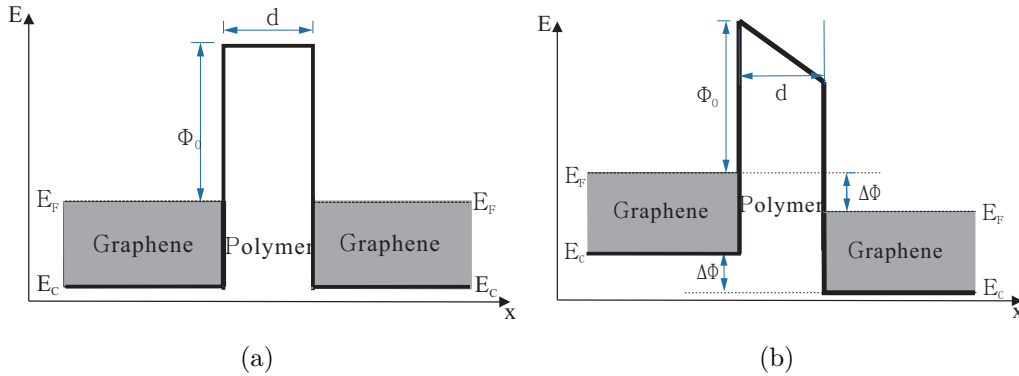


FIGURE 3.2 – Band diagrams of graphene-polymer-graphene unit (a) at equilibrium $V = 0$ (b) with applied voltage V . The grey part indicates filling of energy levels. E_c is the conduction band edge energy and E_F is the Fermi level in graphene (for reasons of clarity in $E_F \neq E_c$ although it is the case in graphene monolayer).

In a first approximation, the polymer/graphene nanocomposite can be seen as a juxtaposition of elementary graphene-polymer-graphene units (see

Figure 3.2(a)). In order to understand the nonlinear electrical behavior of the nanocomposite, we first focus on the conduction mechanism of this unit. When the distance between two graphene sheets is nano-scaled, the polymer matrix can be seen as a dielectric film between two graphene electrodes. There is a strong analogy with a metal-insulator-metal device with tunnel junction. It is known that there are two types of conduction mechanisms in dielectric films [Hamann 1988], which are interface-limited conduction mechanism and bulk-limited conduction mechanism respectively. The former depends on the electric properties at the polymer-graphene interface, while the latter depends on the electric properties of the polymer. In our work, we focus on solving the general problem and neglect the bulk-limited conduction mechanism except Ohm's law in varying polymer.

There are several interface-limited conduction mechanisms [Chiu 2014a] : (1) Schottky emission ; (2) Thermionic-field emission ; (3) Fowler-Nordheim tunneling ; (4) Direct tunneling. Among them, the former two are obvious only at high temperature when the electrons can get enough thermal energy to overcome the barrier so that the electronic current can flow in the conduction band. The latter two occur when the barrier is thin enough to permit its penetration by the quantum tunneling [Simmons 1971]. To simplify the problem, we assume that the system is studied at low temperature so that the thermal current can be neglected, and restrict the electron transportation between electrodes to the tunneling effect.

The tunneling effect is a purely quantum effect. For a 1D model of two close graphene sheets separated by a polymer matrix, the two graphene sheets are considered as source of electrons, and the polymer layer as a potential barrier. Fig. 3.2 depicts the evolution of conduction band edge energy, E_c , which is at equilibrium state across the graphene-polymer-graphene device in Fig. 3.2(a). The potential barrier in polymer corresponding to energy level of conduction band edge is assumed to have a rectangular shape at equilibrium, *i.e.*, the interface effect is neglected in first approximation. The applied electrostatic potential V changes the conduction band edge energy which is shifted from 0 to $\Delta\phi = -eV$ dependent on x (see in Fig. 3.2(b)), where e is the elementary electric charge, that makes the barrier shape become trapezoidal when the graphene sheets have different electrostatic potential. For such 1D model of two close graphene sheets separated by a polymer matrix, the electric

constitutive law is expressed in the polymer in the form

$$J = \mathcal{G}(E, d) E, \quad (3.28)$$

where J denotes the electric current, E is the electric field, and $\mathcal{G}(E, d)$ is a nonlinear function of the electric field E and of the distance between the two graphene sheets d . An explicit formula for the electric tunneling effect through a potential square barrier was first derived by Simmons [Simmons 1963] as :

$$\begin{aligned} \mathcal{G}(E, d) = & \frac{2.2e^3 E^2}{8\pi h_p \Phi_0} \exp\left(-\frac{8\pi}{2.96h_p e E} (2m)^{\frac{1}{2}} \Phi_0^{\frac{3}{2}}\right) \dots \\ & + \left[3 \cdot \frac{(2m\Phi_0)^{\frac{1}{2}}}{2d}\right] (e/h_p)^2 E d \exp\left[-\left(\frac{4\pi d}{h_p}\right) (2m\Phi_0)^{\frac{1}{2}}\right]. \end{aligned} \quad (3.29)$$

Here, the tunneling current J is a nonlinear function of electric field E and depends of three parameters : the height Φ_0 , width d of barrier and the effective mass m of electron in multi-layer graphene. This expression is obtained under the assumptions that the temperature is very low such as $T \approx 0$ K ; the electric field E varies slowly over the width of the potential barrier (*i.e.*, $E \approx V/d$ and the rectangular barrier becomes trapezoidal under the effect of electric field (see. Fig. 3.2b)); the trapezoidal barrier is approximated by rectangular barrier with the same average height. This theory has been used and validated experimentally in the metal-insulator-semiconductor [Maity 2016] and metal-insulator-metal capacitor field [Krishnan 2008]. Note that the current comes only from the electrons which cross the potential barrier. In Simmons' model, the leakage current is not taken into account. This lack of the 1D model can be covered in the 3D extension of the conductivity model (*cf.* Section 3.4.2). However, since we consider the bulk current in addition of tunneling current, the leakage current will not affect the effective current in the composite.

Figure 3.3 shows the evolution of the tunneling current as functions of E and d respectively. Specifically, when d is a constant, the tunneling current increases with electric field E (see in Fig. 3.3 (a)). While with fixed electric field, larger d leads to a sharp decrease of tunneling current (see in Fig. 3.3 (b)).

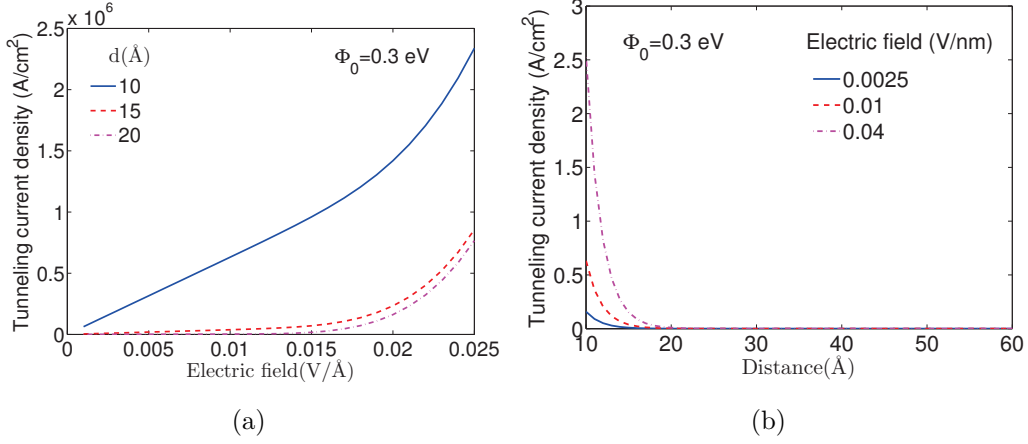


FIGURE 3.3 – Characteristic behaviors of a polymer-graphene-polymer tunnel junction with rectangular barrier : (a) tunneling current density versus Electric field ; (b) tunneling current density versus barrier width.

3.4 Multiscale Modeling of the electrical behavior of graphene-reinforced composites

We consider an RVE defined in a domain Ω whose external boundary is denoted by $\partial\Omega$. The RVE contains N planar graphene sheets associated to surfaces Γ_n $n = 1, 2, \dots, N$, which are distributed randomly inside the polymer matrix, as depicted in Fig. 3.4. The distribution of graphene sheets is assumed to be periodic. We denote collectively the graphene surfaces by $\Gamma = \bigcup_n \Gamma_n$. The homogenization problem defined over the RVE Ω is described in the following.

3.4.1 Microscopic problem

Considering only electrical conduction phenomena, the electric power within the domain Ω is defined by

$$\overline{W} = \int_{\Omega} \omega^b(\mathbf{x}) d\Omega + \int_{\Gamma} \omega^s(\mathbf{x}) d\Gamma, \quad (3.30)$$

where the density functions ω^b and ω^s are defined by

$$\omega^b(\mathbf{x}) = \frac{1}{2} \mathbf{j}(\mathbf{x}) \cdot \mathbf{E}(\mathbf{x}), \quad \omega^s(\mathbf{x}) = \frac{1}{2} \mathbf{j}^s(\mathbf{x}) \cdot \mathbf{E}^s(\mathbf{x}), \quad (3.31)$$

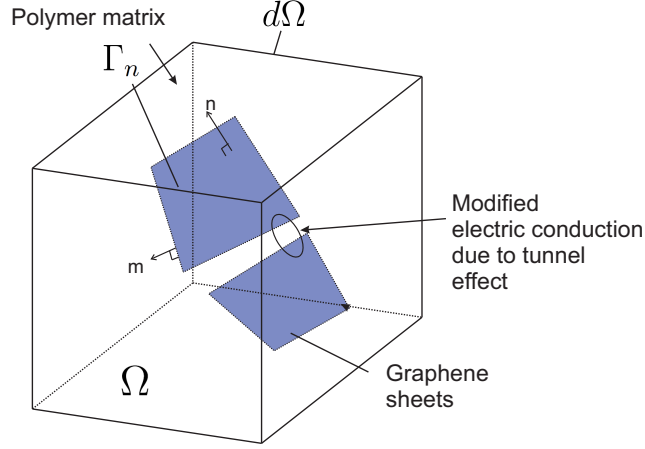


FIGURE 3.4 – RVE model of the graphene-reinforced composite.

where

$$\mathbf{E}(\mathbf{x}) = -\nabla\phi(\mathbf{x}) \quad (3.32)$$

is the electric field, $\mathbf{j}(\mathbf{x})$ is the current density and $\phi(\mathbf{x})$ is the electric potential. In the above, the superscript s denotes surface quantities, *e.g.*, \mathbf{j}^s is the surface current density. The surface electric field is defined with respect to its bulk counterpart as :

$$\mathbf{E}^s = \mathbf{P} \cdot \mathbf{E} = -\mathbf{P} \nabla \phi = -\nabla^s \phi, \quad (3.33)$$

with

$$\mathbf{P}(\mathbf{x}) = \mathbf{I} - \mathbf{n}(\mathbf{x}) \otimes \mathbf{n}(\mathbf{x}) \quad (3.34)$$

is a projector operator characterizing the projection of a vector along the tangent plane to Γ at a point $\mathbf{x} \in \Gamma$ and \mathbf{n} is the unit normal vector to Γ , \mathbf{I} is the second-order identity tensor. The local constitutive relationships relating \mathbf{j} and \mathbf{j}^s with \mathbf{E} are introduced in section 3.4.2. In (3.30) the electric potential is assumed to verify the condition

$$\langle -\nabla\phi(\mathbf{x}) \rangle = \bar{\mathbf{E}} \quad (3.35)$$

where $\langle \cdot \rangle = \frac{1}{V} \int_{\Omega} (\cdot) d\Omega$ is the spatial averaging over Ω , with V the volume of Ω . This condition is verified for the following boundary conditions over $\partial\Omega$:

$$\phi(\mathbf{x}) = -\bar{\mathbf{E}} \cdot \mathbf{x} \quad \text{on } \partial\Omega, \quad (3.36)$$

$$\phi(\mathbf{x}) = -\bar{\mathbf{E}} \cdot \mathbf{x} + \tilde{\phi}(\mathbf{x}) \quad \text{on } \partial\Omega \quad (3.37)$$

where $\tilde{\phi}(\mathbf{x})$ is a periodic function over Ω , such as $\langle \tilde{\phi}(\mathbf{x}) \rangle = 0$. In this study, the second type of boundary conditions has been adopted.

3.4.2 Local microscopic constitutive equations

3.4.2.1 Polymer matrix

In the polymer matrix, the current density \mathbf{j} is related to the electric field through the nonlinear relationship :

$$\mathbf{j} = \begin{cases} \mathbf{K}_0^p \mathbf{E} & \text{if } d(\mathbf{x}) > d_{cut}, \\ \mathcal{G}(\mathbf{E}, d) \frac{\mathbf{E}}{|\mathbf{E}|} & \text{if } d(\mathbf{x}) < d_{cut}, \end{cases} \quad (3.38)$$

where d_{cut} is a cut-off distance above which the tunneling effect can be neglected, and \mathbf{K}_0^p is the electric conductivity tensor of the polymer matrix when neglecting tunneling effect. Here, we make an assumption that the tunneling effect is independent on the thickness of graphene.

3.4.2.2 Graphene sheets

Graphene sheets are composed of several layers of graphene and thus have a finite thickness denoted by h . However, due to the very large aspect ratio of graphene sheets, which can be of the the order of 10^3 between the largest dimension of the sheet and the thickness, it might be cumbersome to model them as volume domains, especially regarding meshing the thickness of the sheets. For this reason, we propose to replace the graphene sheets with finite thickness by highly conducting surfaces (see Fig. 3.5). In that case, the graphene sheets defined in a volume domain Ω^g are modeled by imperfect surfaces Γ where the surface current density \mathbf{j}^s is in that case related to the surface electric field, \mathbf{E}^s through (see *e.g.*, [Yvonnet 2008a, Gu 2011]) :

$$\mathbf{j}^s(\mathbf{x}) = \mathbf{K}_*^s \mathbf{E}^s \quad (3.39)$$

where

$$\mathbf{K}_*^s = h\mathbf{S}^*, \quad \mathbf{S}^* = \mathbf{K}^g - \frac{(\mathbf{K}^g \mathbf{n}) \otimes (\mathbf{K}^g \mathbf{n})}{\mathbf{K}^g : (\mathbf{n} \otimes \mathbf{n})}. \quad (3.40)$$

In (3.40), \mathbf{K}^g denotes the second-order electric conductivity tensor of the bulk graphite, which is here anisotropic.

3.4.3 Homogenized quantities

In this section, we define the effective quantities and their relation to microscopic (local) fields.

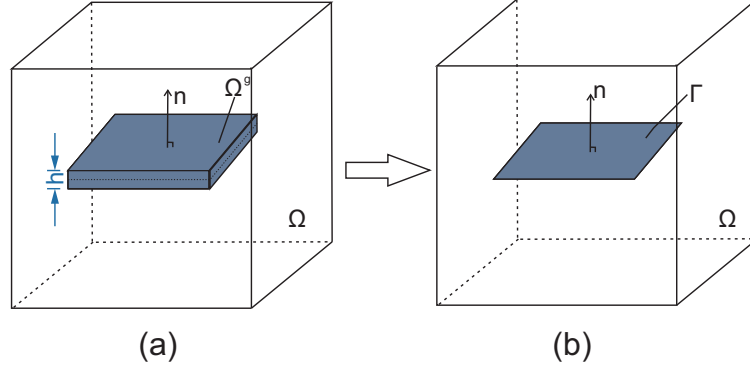


FIGURE 3.5 – Replacement of 3D graphene by a highly conducting surface.

3.4.3.1 Effective electric displacement

From energy consistency, we have :

$$\bar{W} = V \bar{\mathbf{j}} \cdot \bar{\mathbf{E}}, \quad (3.41)$$

where V is the volume of Ω ,

$$\bar{\mathbf{E}} = \frac{1}{V} \int_{\Omega} \mathbf{E}(\mathbf{x}) d\Omega \quad (3.42)$$

is the effective electric field and $\bar{\mathbf{j}}$ is the effective current density defined by

$$\bar{\mathbf{j}} = \frac{1}{V} \frac{\partial \bar{W}}{\partial \bar{\mathbf{E}}}. \quad (3.43)$$

Using (3.30), we have :

$$\begin{aligned} \bar{j}_i &= \frac{1}{V} \int_{\Omega} \frac{\partial \omega^b}{\partial \bar{E}_i} d\Omega + \frac{1}{V} \int_{\Gamma} \frac{\partial \omega^s}{\partial \bar{E}_i} d\Gamma \\ &= \frac{1}{V} \int_{\Omega} \frac{\partial \omega^b}{\partial E_j} \frac{\partial E_j}{\partial \bar{E}_i} d\Omega + \frac{1}{V} \int_{\Gamma} \frac{\partial \omega^s}{\partial E_j^s} \frac{\partial E_j^s}{\partial \bar{E}_i} d\Gamma. \end{aligned} \quad (3.44)$$

Using equation (3.42), we obtain :

$$\frac{\partial \bar{E}_i}{\partial E_j} = \frac{1}{V} \int_{\Omega} \delta_{ij} d\Omega = \delta_{ij} \quad (3.45)$$

and

$$\frac{\partial \omega^s}{\partial E_j^s} \frac{\partial E_j^s}{\partial \bar{E}_i} = j_j^s P_{ij} = j_i^s. \quad (3.46)$$

Thus, we finally obtain using (3.31) :

$$\bar{\mathbf{j}} = \frac{1}{V} \left(\int_{\Omega} \mathbf{j}(\mathbf{x}) d\Omega + \int_{\Gamma} \mathbf{j}^s(\mathbf{x}) d\Gamma \right). \quad (3.47)$$

3.4.3.2 Effective behavior

Due to the nonlinear term (3.38), classical homogenization principles related to the superposition principle do not hold. Nonlinear homogenization problems can be handled *e.g.* by numerical approaches where problems at both scales are concurrently solved (FE²-approaches, see reviews *e.g.* in [Geers 2010, Geers 2016]). In the present case, we restrict the analysis to evaluate the tangent (incremental) effective conductivity tensor, which is defined as :

$$\bar{\mathbf{K}}_T(\bar{\mathbf{E}}) = \frac{\partial \bar{\mathbf{j}}(\bar{\mathbf{E}})}{\partial \bar{\mathbf{E}}}, \quad (3.48)$$

where $\bar{\mathbf{K}}_T(\bar{\mathbf{E}})$ is here evaluated numerically by perturbation.

3.5 Finite element numerical solving procedure

3.5.1 Weak forms

The solution $\phi(\mathbf{x})$ satisfying the periodical boundary conditions in eq.(3.37) and minimizing the dissipated power verifies :

$$D_{\delta\phi} \bar{W}(\phi) = 0 \quad (3.49)$$

where $D_{\delta\phi} \bar{W}(\phi)$ denotes the directional (Gâteaux) derivative defined as :

$$D_{\delta\phi} \bar{W}(\phi) = \left\{ \frac{d}{d\xi} \left[\bar{W}(\phi + \xi\delta\phi) \right] \right\}_{\xi=0}. \quad (3.50)$$

From (3.49) and using (3.30) we obtain :

$$\int_{\Omega} \frac{\partial \omega^b}{\partial \mathbf{E}} \cdot D_{\delta\phi}(\mathbf{E}) d\Omega + \int_{\Gamma} \frac{\partial \omega^s}{\partial \mathbf{E}^s} \cdot D_{\delta\phi}(\mathbf{E}^s) d\Gamma = 0, \quad (3.51)$$

where

$$D_{\delta\phi}(\mathbf{E}) = -\nabla(\delta\phi), \quad (3.52)$$

and

$$D_{\delta\phi}(\mathbf{E}^s) = -\mathbf{P}\nabla(\delta\phi) = -\nabla^s(\delta\phi). \quad (3.53)$$

Using (3.31), we obtain the weak form :

$$\int_{\Omega} \mathbf{j}(\phi) \cdot \nabla(\delta\phi) d\Omega + \int_{\Gamma} \mathbf{j}^s \cdot \nabla^s(\delta\phi) d\Gamma = 0, \quad (3.54)$$

where $\phi \in H^1(\Omega)$, ϕ satisfying the boundary conditions (3.37) over $\partial\Omega$ and $\delta\phi \in H^1(\Omega)$, $\delta\phi = 0$ over $\partial\Omega$. Introducing expressions (3.33) and (3.39) in equation (3.54) yields :

$$\int_{\Omega} \mathbf{j}(\phi) \cdot \nabla(\delta\phi) d\Omega - \int_{\Gamma} \mathbf{P}\nabla\phi \cdot \mathbf{K}_*^s \mathbf{P}\nabla(\delta\phi) d\Gamma = 0. \quad (3.55)$$

3.5.2 Linearization

Due to the term $\mathbf{j}(\phi)$ expressed by (3.38), the weak form (3.55) constitutes a highly nonlinear problem with respect to ϕ . To solve this problem, we employ a Newton-Raphson procedure. For this purpose, the linearization of (3.55) is provided in what follows.

Set

$$\int_{\Omega} \mathbf{j}(\phi) \cdot \nabla(\delta\phi) d\Omega - \int_{\Gamma} \mathbf{P}\nabla\phi \cdot \mathbf{K}_*^s \mathbf{P}\nabla(\delta\phi) d\Gamma = R. \quad (3.56)$$

A first-order Taylor expansion of R gives :

$$R(\phi^k + \Delta\phi^k) \simeq R(\phi^k) + D_{\Delta\phi}R(\phi^k). \quad (3.57)$$

In the above, ϕ^k denotes the electric potential solution field known from a previous iteration k , $\Delta\phi^k$ is the increment of electric potential. Equating the left-hand term of (3.57) to zero gives the linearized problem around the know solution ϕ^k as :

$$D_{\Delta\phi}R(\phi^k) = -R(\phi^k). \quad (3.58)$$

The left-hand term in (3.58) can be expressed by :

$$\int_{\Omega} \frac{\partial \mathbf{j}}{\partial \mathbf{e}} \nabla(\Delta\phi) \cdot \nabla(\delta\phi) d\Omega - \int_{\Gamma} \mathbf{P}\nabla(\Delta\phi) \cdot \mathbf{K}_*^s \mathbf{P}\nabla(\delta\phi) d\Gamma, \quad (3.59)$$

where

$$\frac{\partial \mathbf{j}}{\partial \mathbf{E}} = \mathbf{K}^p(\mathbf{E}) = \begin{cases} \mathbf{K}_0^p & \text{if } d(\mathbf{x}) > d_{cut} \\ \mathcal{G}'(\|\mathbf{E}\|) \cdot \frac{\mathbf{E} \otimes \mathbf{E}}{\|\mathbf{E}\|^2} + \mathcal{G}(\|\mathbf{E}\|) \cdot \frac{\|\mathbf{E}\|^2 \mathbf{I} - \mathbf{E} \otimes \mathbf{E}}{\|\mathbf{E}\|^3} & \text{if } d(\mathbf{x}) \leq d_{cut} \end{cases}, \quad (3.60)$$

where $\mathcal{G}'(\|\mathbf{E}\|)$ is expressed by :

$$\mathcal{G}'(\|\mathbf{E}\|) = 2A\|\mathbf{E}\| \exp\left(-\frac{B}{\|\mathbf{E}\|}\right) + AB \exp\left(-\frac{B}{\|\mathbf{E}\|}\right) + C, \quad (3.61)$$

with

$$A = \frac{2.2e^3}{8\pi h_p \Phi_0}, \quad B = \frac{8\pi}{2.96h_p e} (2m)^{\frac{1}{2}} \Phi_0^{\frac{3}{2}}, \quad (3.62)$$

and

$$C = 3 \cdot \frac{(2m\Phi_0)^{\frac{1}{2}}}{2} (e/h_p)^2 \exp[-(\frac{4\pi d}{h_p})(2m\Phi_0)^{\frac{1}{2}}]. \quad (3.63)$$

3.5.3 Nonlinear finite element discretization and approximation

In the imperfect surface model, the potential is continuous at the graphene surface whereas the normal component of the current density to the graphene surface is discontinuous and the tangential component is continuous. The approximation of the electric potential at a point \mathbf{x} in a volume element Ω^e is expressed as

$$\phi(\mathbf{x}) = \sum_{i=1}^n [\text{Ne}]_i [\Phi^e], \quad (3.64)$$

where $[\text{Ne}]$ is a matrix of shape functions and $[\Phi^e]$ is a column vector containing the nodal values of the electric potential for one element. We introduce the following classical FEM discretizations :

$$\nabla([\Phi_k^e]) = [\text{Be}][\Phi_k^e], \quad \nabla([\Delta\Phi_k^e]) = [\text{Be}][\Delta\Phi_k^e], \quad \nabla([\delta\Phi]) = [\text{Be}][\delta\Phi^e], \quad (3.65)$$

where $[\text{Be}]$ denotes a matrix of shape functions derivatives. Introducing the above discretization in (3.58) gives :

$$\begin{aligned} [\delta\Phi^e]^T & \left(\int_{\Omega} [\text{Be}]^T [K^p(\phi_k)] [\text{Be}] d\Omega \right) [\Delta\Phi_k^e] + [\delta\Phi^e]^T \left(\int_{\Gamma} [\text{Be}]^T [P][K_*^s][P][\text{Be}] d\Gamma \right) [\Delta\Phi_k^e] \\ & = -[\delta\Phi^e]^T \left(\int_{\Omega} [\text{Be}]^T \mathbf{j}(\phi_k) d\Omega \right) - [\delta\Phi^e]^T \left(\int_{\Gamma} [\text{Be}]^T [P][K_*^s][P][\text{Be}][\Phi_k^e] d\Gamma \right). \end{aligned} \quad (3.66)$$

Owing to the arbitrariness of $[\delta\Phi^e]$, we obtain the following system of linear equations :

$$([K_b] + [K_s])[\Delta\Phi_k] = -[R_b] - [R_s], \quad (3.67)$$

where $[K_b]$ and $[K_s]$ denote the bulk and surface tangent matrices, $[R_b]$ and $[R_s]$ are residual terms and $[\Delta\Phi_k]$ is the column vector of potential increments for the whole mesh. The different above matrices and vectors are given by :

$$[K_b] = \int_{\Omega} [\text{Be}]^T [K^p][\text{Be}] d\Omega, \quad [K_s] = \int_{\Gamma^e} [\text{Be}]^T [P][K_*^s][P][\text{Be}] d\Gamma, \quad (3.68)$$

$$[R_b] = \int_{\Omega^e} [Be]^T \mathbf{j}(\phi_k) d\Omega, \quad [R_s] = \int_{\Gamma^e} [Be]^T [P][K_*^s][P][Be][\Phi_k^e] d\Gamma. \quad (3.69)$$

where $[K^p]$ is the matrix of $\mathbf{K}^p(\phi^k)$ which is given by (3.60).

At each iteration, the electric potential field is updated according to :

$$[\Phi_{k+1}] = [\Phi_k] + [\Delta\Phi_k]. \quad (3.70)$$

The process is repeated until the criterion $\|\mathbf{R}\| \leq 10^{-6}$ is reached.

One specificity of the present problem is the presence of the surface electrical energy term in Eq. (3.55) related to the graphene surface. To evaluate the associated surface integral, we first mesh the graphene surface by triangular elements, which then conform with the tetrahedral elements in the volume. Here, a special attention must be paid to the computation of the surface integrals in (3.68) and (3.69). The integrals are evaluated with Gauss points positioned along the graphene surface, then on the centers of triangular elements meshing the surface. It is worth noting that the shape functions $[Be]$ are discontinuous along Γ but that from (3.54), the quantity $[Be(\mathbf{x})]^T [P(\mathbf{x})][K_*^s][P(\mathbf{x})][Be(\mathbf{x})]$ is continuous across Γ . Then, the values of $[Be(\mathbf{x})]$ being constant in each linear element, they can be evaluated in a Gauss point \mathbf{x}' located within neighbor elements, as depicted in Fig. 3.6, according to :

$$[Be(\mathbf{x})]^T [P(\mathbf{x})][K_*^s][P(\mathbf{x})][Be(\mathbf{x})] \simeq [Be(\mathbf{x}')]^T [P(\mathbf{x})][K_*^s][P(\mathbf{x})][Be(\mathbf{x}')]. \quad (3.71)$$

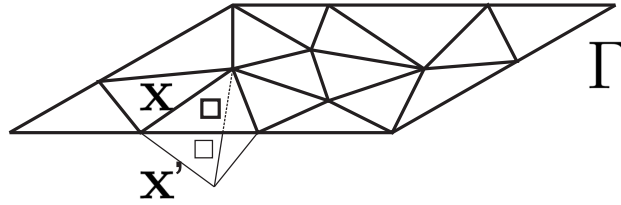


FIGURE 3.6 – Schematic of the mesh for a graphene sheet and one neighbor element for the computation of integral terms.

3.5.4 Geometrical modeling of graphene/polymer nanocomposites

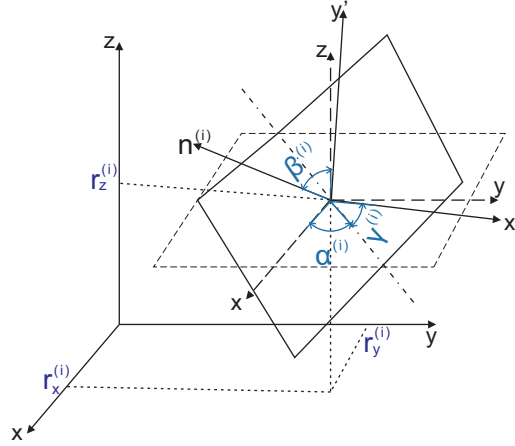


FIGURE 3.7 – Scheme of the position and orientation of graphene sheet in the 3D space.

In the following, the in-plane dimensions of graphene sheets are $15 \times 15 \text{ nm}^2$ and the RVE side length of the cubic domain is 80 nm. We consider multi-layer graphene platelets, also called here sheets, which have a finite thickness. The related aspect ratio $\eta = 15\text{nm}/h$ denotes the ratio between the length of the platelet and its thickness. The position and orientation of i th graphene sheet in RVE are defined by 6 degrees of freedom $\{r_x^{(i)}, r_y^{(i)}, r_z^{(i)}, \alpha^{(i)}, \beta^{(i)}, \gamma^{(i)}\}$ where $r_x^{(i)}, r_y^{(i)}, r_z^{(i)}$ are the coordinates of the center of graphene sheet, and $\alpha^{(i)}, \beta^{(i)}, \gamma^{(i)}$ are the Euler angles. Note that $\alpha^{(i)}, \beta^{(i)}$ give the orientation of the unit normal of graphene sheet, $n^{(i)}$, and $\gamma^{(i)}$ gives the orientation of graphene sheet around the unit normal $n^{(i)}$ (see Figure 3.7). In this study, the graphene sheet are modeled by square plane with the side length $L = 15 \text{ nm}$. This assumption is due to extremely thin thickness of graphene and relies on the imperfect surface model.

The different microstructures are generated by a Markov-chain with hard-inclusion Metropolis algorithm (see [Krauth 2006, Torquato 2013] for review in the case hard-spheres). First, an initial configuration of the system is chosen such the graphene sheet centers are on cubic lattice with random orientation and without overlapping. Then, one randomly chosen graphene sheet

is attempted to move for each step of Metropolis algorithm. A new position for the graphene sheet under consideration is chosen by six random parameters : $(\Delta x, \Delta y, \Delta z) \in [-\delta_x, \delta_x]^3$, $\Delta\alpha \in [-\pi, \pi]$, $\Delta\beta \in [-\delta_\beta, \delta_\beta]$ and $\Delta\gamma \in [-\delta_\gamma, \delta_\gamma]$. The parameter $(\Delta x, \Delta y, \Delta z, \Delta\gamma)$ are generated with an uniform distribution over their definition domains and the couple of increment angles $(\Delta\alpha, \Delta\beta)$ are generate with an uniform distribution on the part of the unit sphere defined by δ_β . The new position of graphene sheet is then $(x^{(i)} + \Delta x, y^{(i)} + \Delta y, z^{(i)} + \Delta z, \alpha^{(i)} + \Delta\alpha, \beta^{(i)} + \Delta\beta, \gamma^{(i)} + \Delta\gamma)$. The parameters δ_x , δ_β and δ_γ are adjusted to give about 50% acceptance of the new position. Periodic boundary conditions are employed throughout the simulation.

Therefore, the acceptance step of this Metropolis algorithm reduces to checking that this displacement does not cause overlap between graphene sheets. To control the overlapping, the graphene sheets are discretized by a compact centered square lattice of small fictitious spherical particles with radius δ . The non-overlapping condition is

$$r_{ij}^2 \geq \delta^2 \quad \forall i, j \quad (3.72)$$

where r_{ij} is a distance between the fictitious spherical particles i and j .

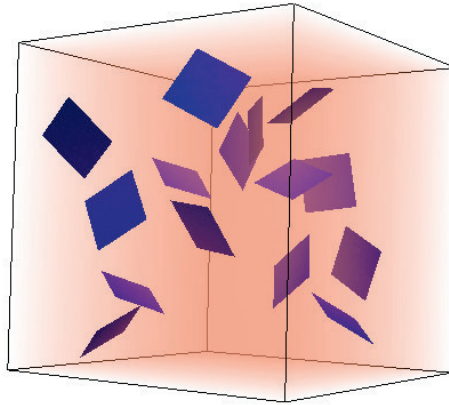


FIGURE 3.8 – RVE for the graphene/polymer nanocomposites involving 25 graphene sheets in a cube of $80 \times 80 \times 80 \text{ nm}^3$

To generate a series of independent isotropic RVE samples as random maps, the position and orientation are saved during a Markov-chain sampling with regular interval to ensure the statistic independence of two RVEs. Note

that the first RVE is saved when the orientation of the unit normal of graphene sheets is isotropic in an average sense. One example of obtained realization of isotropic graphene nanocomposite RVE is illustrated in Fig. 3.8. Finally to generate RVE with aligned graphene sheets, the unit normal of graphene are fixed to be parallel to the z -axis (see Fig. 3.27 (b)). We used GMSH mesh generator [Geuzaine 2009] to create the triangular mesh of surfaces conforming with matrix tetrahedra. All the above FEM developments have been implemented in a house-made code developed at MSME under Matlab.

3.5.5 3D distance function used in the tunneling effect model

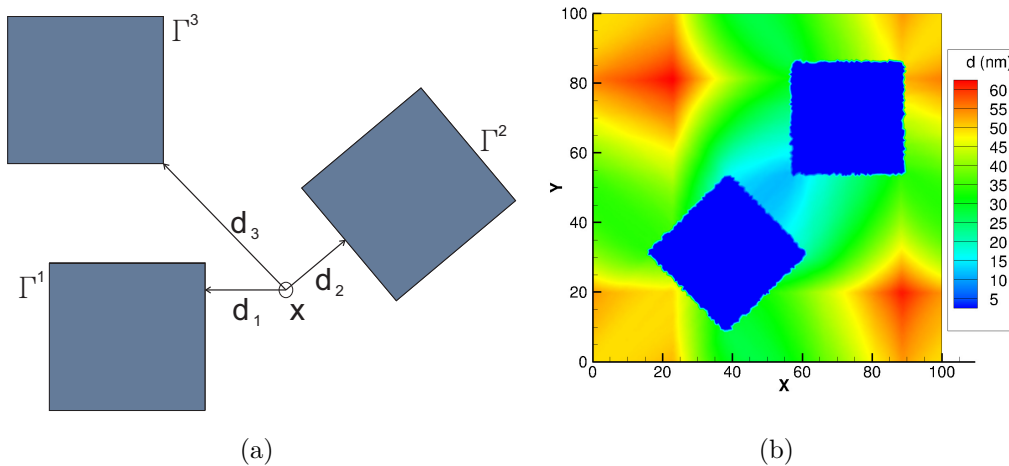


FIGURE 3.9 – a) Distances of a point \mathbf{x} from surrounding graphene sheets to compute the distance $d(\mathbf{x})$. b) Distance function $d(\mathbf{x})$ in 2D RVE with periodic boundary conditions.

We have introduced in section 3.3 a 3D model where the electric conduction is dependent on a distance d between the graphene sheets. Even though this notion is trivial in 1D, many possible choices can be proposed in a full 3D context. In what follows, we propose a simple definition for the distance function $d(\mathbf{x})$ in equation (3.38), which can be computed at all nodes of the mesh once before the calculations for a given distribution of graphene sheets within the RVE. Note that this definition is a possible choice among many others and is part of the model. We consider a point $\mathbf{x} \in \Omega$ and denote by \mathbf{x}^Γ

a point lying on the surface Γ formed by the set of N graphene sheets. We define the distance function $d(\mathbf{x})$ as follows :

$$d(\mathbf{x}) = \min_{\substack{\mathbf{x}^\Gamma \in \Gamma^i \\ i=1,2,\dots,N}} \|\mathbf{x} - \mathbf{x}^\Gamma\| + \min_{\substack{\mathbf{x}^\Gamma \in \Gamma^j \\ j=1,2,\dots,N, j \neq i}} \|\mathbf{x} - \mathbf{x}^\Gamma\|. \quad (3.73)$$

In other words, for a given point \mathbf{x} , we first compute the distance with all N graphene sheets, then the function $d(\mathbf{x})$ is defined as the sum of the two smallest distances between the point and two different neighboring graphene sheets. An illustration of this methodology is schematically depicted in Fig. 3.9 (a) in the 2D context. For one point \mathbf{x} , the distances d_1 , d_2 and d_3 represent the shortest distance with graphene sheets Γ^1 , Γ^2 and Γ^3 . The function $d(\mathbf{x})$ for this point is the sum of d_1 and d_2 , which are the smallest values in the set d_i , $i = 1, 2, 3$. An illustration of the obtained function $d(\mathbf{x})$ for the 2D geometry shown in Fig. 3.9 (b).

3.6 Preliminary examples

3.6.1 1D benchmark example

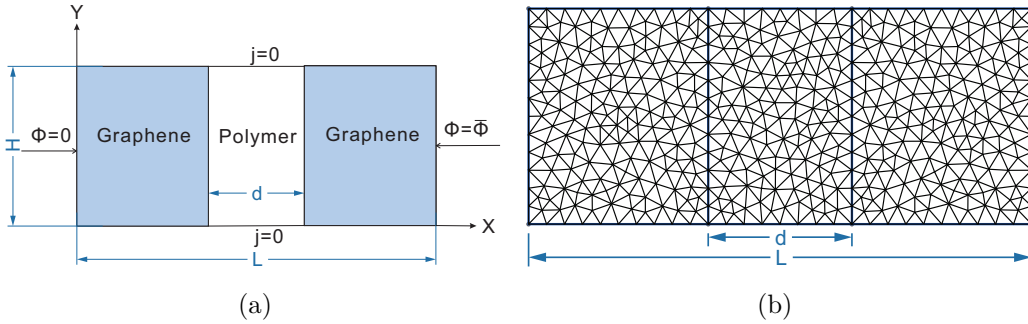


FIGURE 3.10 – Benchmark problem to validate the 1D model : (a) geometry and boundary conditions ; (b) mesh of the 2D domain.

The objective of this first example is to validate the present model on a simple benchmark where an analytical solution can be obtained, and where the tunneling effect can be evidenced. The problem is defined in Fig. 3.10 (a). A domain is composed of two regions associated with graphene and a third one associated with the polymer. The width of the polymer layer (distance between the graphene sheets) is denoted by d . The length of the domain is

$L = d + 2W$, where W denotes the width of graphene sheets, here chosen as $W = 10 \text{ \AA}$. Electric potentials $\phi = 0$ and $\phi = \bar{\phi}$ are prescribed at $(x = 0)$ and $(x = L)$. Whereas the problem is purely 1D, we solve it in a 2D domain meshed with linear triangular elements as shown in Fig. 3.10 (b). To avoid any influence of the y -coordinate and maintain the problem one-dimensional, zero normal current density is prescribed at $(y = 0)$ and $(y = H)$

In all the following examples, the electric conductivity of the polymer is taken as $K_0^p = 1 \times 10^{-10} \text{ S/m}$ and the conductivity tensor is defined by (3.40) with

$$\mathbf{K}^p = \begin{bmatrix} 1 \times 10^{-10} & 0 & 0 \\ 0 & 1 \times 10^{-10} & 0 \\ 0 & 0 & 1 \times 10^{-10} \end{bmatrix} \text{ S/m.} \quad (3.74)$$

Note that in this benchmark example, the conductivity in the direction normal to the graphene sheet is not taken into account. The conductivity of graphene is anisotropic and its in-plane conductivity was adopted from Stankovich *et al.* [Stankovich 2006], who gave a range of $10^{4.92 \pm 0.52} \text{ S/m}$. We then used the value of $10^{4.92} \text{ S/m}$ and therefore take the in-plane conductivity $(K^g)_1 = 8.32 \times 10^4 \text{ S/m}$. The out-plane conductivity of the graphene is taken as $(k_g)_3 = 10^{-3}(k_g)_1$, or :

$$\mathbf{K}^g = \begin{bmatrix} 8.32 \times 10^4 & 0 & 0 \\ 0 & 8.32 \times 10^4 & 0 \\ 0 & 0 & 83.2 \end{bmatrix} \text{ S/m, for 3D examples.} \quad (3.75)$$

The potential difference $\Delta\phi$ between $(x = 0)$ and $(x = L)$ is denoted by $\bar{\phi}$ and the potential difference between both graphene sheets is described by $\Delta\phi_p$. This value is nonlinearly dependent on the value of $\Delta\phi$ and is computed as a result of the FEM computation.

In what follows, we study the effects of both distance d and energy barrier height Φ_0 in Eq. (3.29). The Figures 3.11 present the results of current density as a function of the electric field in the polymer \bar{E}_p ($\bar{E}_p = -\Delta\phi_p/d$) and effective conductivity of the model computed as $\bar{K} = d\bar{J}_1/d\bar{E}_1$ as a function of the effective electric field \bar{E}_1 , where $\bar{E}_1 = -\Delta\phi/L$. First, the barrier height Φ_0 is fixed to 0.17 eV and the distance between the graphene sheets varies from 10 to 50 \AA . We note that the current density increases with the electric field \bar{E}_p , while for a fixed \bar{E}_p , a smaller value of d leads to a larger current density. We compare in Fig. 3.11 (a) our numerical solution of current density

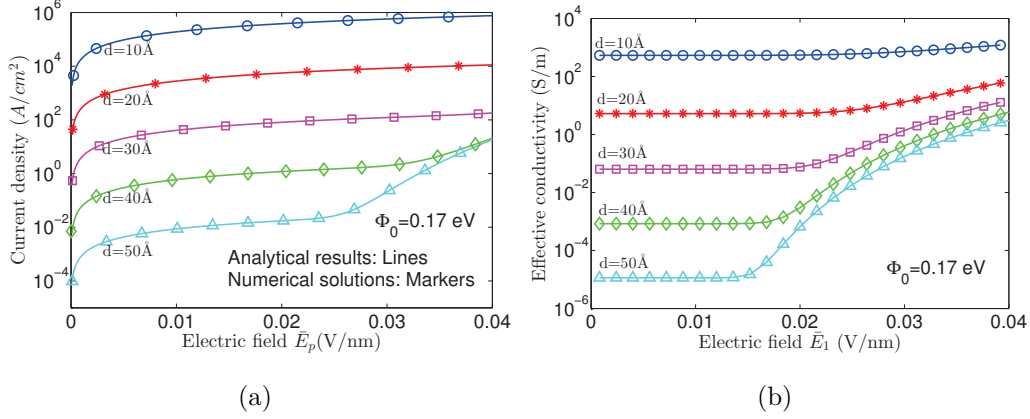


FIGURE 3.11 – (a) Effective current density as a function of \bar{E}_p ; (b) Effective electric conductivity as a function of \bar{E}_1 at different barrier width.

and the analytical estimate provided by Eq. (3.29) for 1D tunneling effect. We note a good agreement between the analytical and the numerical solution. Note that in the case $d = 40$ Å and $d = 50$ Å, the current density increases sharply when \bar{E}_p is over 0.03 V/nm and finally reach the same value. This is because due to the tunneling effect law, when the potential difference between the barrier is large enough, the current density tends to be independent on the barrier width d .

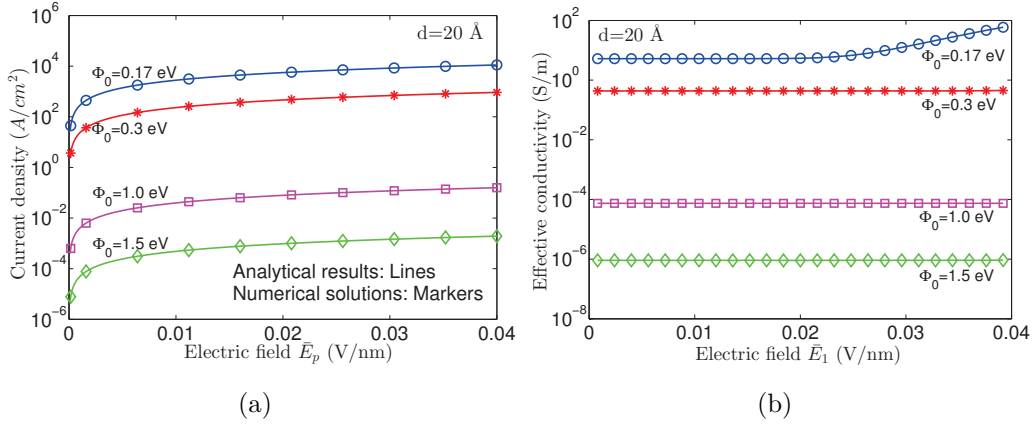


FIGURE 3.12 – (a) Effective current density as a function of \bar{E}_p ; (b) Effective electric conductivity as a function of \bar{E}_1 at different barrier height.

The Figure 3.11(b) indicates that the effective conductivity of this 2D model remains constant at low effective electric field \bar{E}_1 and increases sharply when \bar{E}_1 reaches a threshold, while for the same \bar{E}_1 , the effective conductivity

decreases with an increase of d .

To further investigate the influence of the barrier height Φ_0 , we fix the distance d to 20 Å, and compute the current density and effective conductivity for the same structure as a function of \bar{E}_p and \bar{E}_1 respectively. We observe from Fig. 3.12 that for lower barrier height Φ_0 , we obtain a higher current density and overall electric conductivity for the same electric field.

3.6.2 3D example with two close graphene sheets : identification of the parameter $\alpha(h)$

In the proposed HC surface model, the equivalent 2D surface defined in section 3.4.2.2 was used instead of the actual graphene 3D construction, which also enlarged the region of polymer matrix. Correspondingly, the distance function we compute is larger than in the real configuration which would consequently cause the reduction of the tunneling current as well as the estimated overall electric conductivity. In order to solve this problem, we propose to introduce a correction parameter α to modify the theoretical tunneling effect law in the polymer matrix in the neighborhood of the graphene sheet edges. In this example, we provide a procedure to identify the correction parameter α dependent on the thickness of graphene h for the HC surface model as :

$$\mathbf{j} = \alpha \mathcal{G}(\mathbf{E}, d) \frac{\mathbf{E}}{|\mathbf{E}|}, \quad \text{if } d(\mathbf{x}) < d_{cut}. \quad (3.76)$$

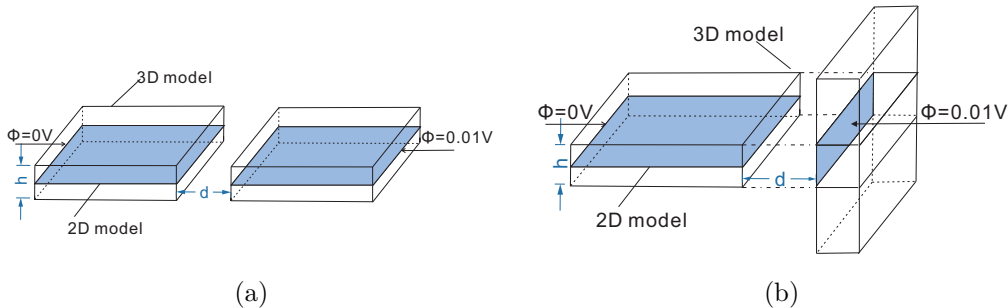


FIGURE 3.13 – Scheme of 3D models with two graphene sheets (a) parallel and (b) perpendicular to each other

With the assumption that the graphene sheets are perfectly flat and cannot overlap, the two extreme locations for each pair of graphene sheets are parallel and perpendicular respectively. Therefore, we consider the models as shown in Fig. 3.13 with Dirichlet boundary condition, where the diameter size of graphene is $15 \times 15 \text{ nm}^2$ and the potential difference between them is 0.01 V . Two methods are used to get the effective electric conductivity of the samples. In the first one, the graphene sheets are modeled as volume parallelepipeds which are meshed with volume elements. In the second one, we employ the introduced surface model where the graphene sheets are modeled as surfaces, meshed with surface triangle elements.

For parallel graphene sheets (see in Fig. 3.13(a)), increase d from 10 to 40 \AA , the calculated results for samples with various thickness are plotted in Fig. 3.14(a). We can note that the effective conductivity is independent on the thickness of graphene. We then replace the graphene volume by a HC surface, the surface parameter \mathbf{K}_*^s is thus given by Eq. (3.40) for the graphene with thickness of 0.2 nm and 0.5 nm respectively,

$$\mathbf{K}_{0.2}^s = \begin{bmatrix} 1.664 & & \\ & 1.664 & \\ & & 0 \end{bmatrix} \times 10^4, \quad \mathbf{K}_{0.5}^s = \begin{bmatrix} 4.16 & & \\ & 4.16 & \\ & & 0 \end{bmatrix} \times 10^4. \quad (3.77)$$

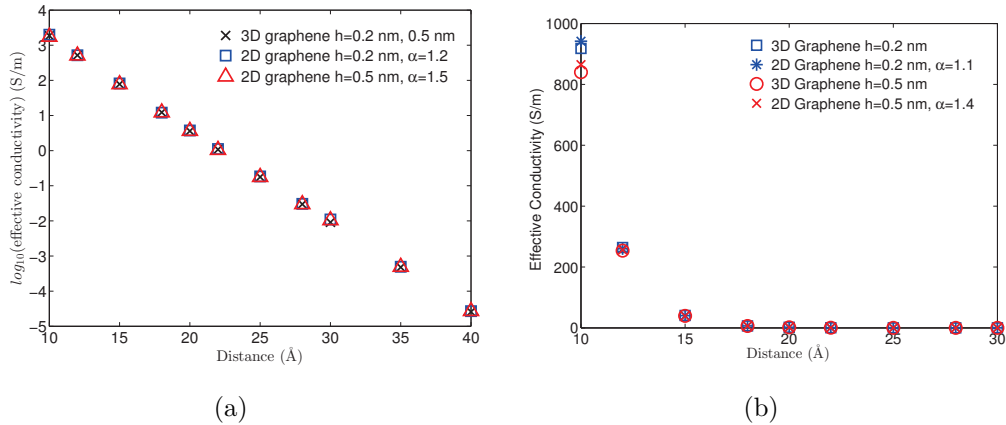


FIGURE 3.14 – Comparison of the results by two methods with the model of two (a) parallel and (b) perpendicular graphene sheets

It could be noted that the methodology we propose is in excellent agreement with the 3D graphene FEM estimation when α is chosen to be 1.2 for

the 0.2 nm thick graphene and 1.5 for the 0.5 nm thickness.

Using this procedure, we can fit the curve by choosing the modified parameter $\alpha_{//}$ for configuration with two parallel graphene sheets as :

$$\alpha_{//}(h) = 1 + h. \quad (3.78)$$

As for perpendicular graphene sheets (see in Fig. 3.13(b)), we cut the configuration from the middle part vertical to Z axis as RVE. Fig. 3.14(b) shows the computed overall conductivities for models with different graphene thickness (0.2 nm and 0.5 nm) as a function of distance d from 10 to 30 Å. It is shown that larger the d is, the smaller is the influence of graphene thickness on the effective conductivity. For the graphene with $h = 0.2$ nm, we introduce the HC surface in place of it with the surface conductivity :

$$\mathbf{K}_{//}^s = \begin{bmatrix} 1.664 & & \\ & 1.664 & \\ & & 0 \end{bmatrix} \times 10^4, \quad \mathbf{K}_{\perp}^s = \begin{bmatrix} 1.664 & & \\ & 0 & \\ & & 1.664 \end{bmatrix} \times 10^4. \quad (3.79)$$

In that case, α is obtained as 1.1. Similarly, when $h = 0.5$ nm, α is obtained as 1.4. The parameter α_{\perp} for the configuration with two perpendicular graphene sheets can then be approximated as :

$$\alpha_{\perp}(h) = 0.9 + h. \quad (3.80)$$

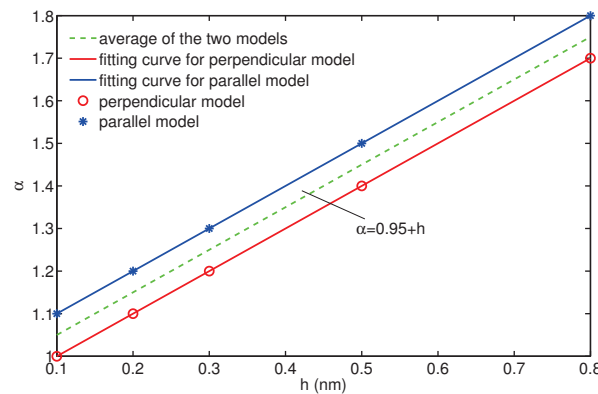


FIGURE 3.15 – Fitting curve for the parameter α

Finally, for graphene sheets with thickness of h (nm), we defined the tunneling current modified parameter α as the average of these two extreme conditions as shown by green dashed line in Fig. 3.15 as :

$$\alpha(h) = 0.95 + h. \quad (3.81)$$

3.7 Numerical analysis of the electrical conductivity of graphene reinforced nanocomposites

Experimental works have evidenced that electrical properties of graphene or nanotube-reinforced nanocomposites are significantly dependent on the microstructure parameters such as the size [Bryning 2005], the orientation of fillers [Yousefi 2012, Du 2005], as well as the inherent characteristics of polymer matrix [Bauhofer 2009, Haggenueller 2007]. In this section, we employ the proposed continuum numerical tunneling model framework to quantitatively analyze the effects of barrier height and configuration of graphene sheets versus electric percolation thresholds in graphene-polymer nanocomposites.

3.7.1 RVE size analysis

We first analyze the convergence of the apparent (effective) conductivity of the composite as a function of the size of the RVE. Periodic boundary conditions are prescribed. For each size of the cubic domain defining the RVE, 30 realizations of random microstructures with the same graphene volume fraction (1.05 vol%) and the same applied electric field (1.25×10^{-3} V/nm), are computed to determine the apparent electric conductivity according to Eq. (3.48). Samples with side length ranging from 30 to 80 nm are analyzed. Graphene sheets are still modeled as square domains with dimensions 15×15 nm² and a thickness of 0.3 nm, which is taken into account through the surface model in Eq. (3.40). Fig. 3.16 (a-c) provides the effective conductivities tensor components $(\overline{K}_T)_{11}$, $(\overline{K}_T)_{22}$, $(\overline{K}_T)_{33}$ as a function of the domain size. It is shown that the dispersion of results decreases when the size of the volume increases. In Fig. 3.16 (d), we can see that the mean values of electric conductivities along the three axes (x, y and z) are close to each other in the case of

random structures, leading to an isotropic behavior.

The mean values converge when the side length of the RVE is roughly 80 nm, which is the value we use in the following analysis.

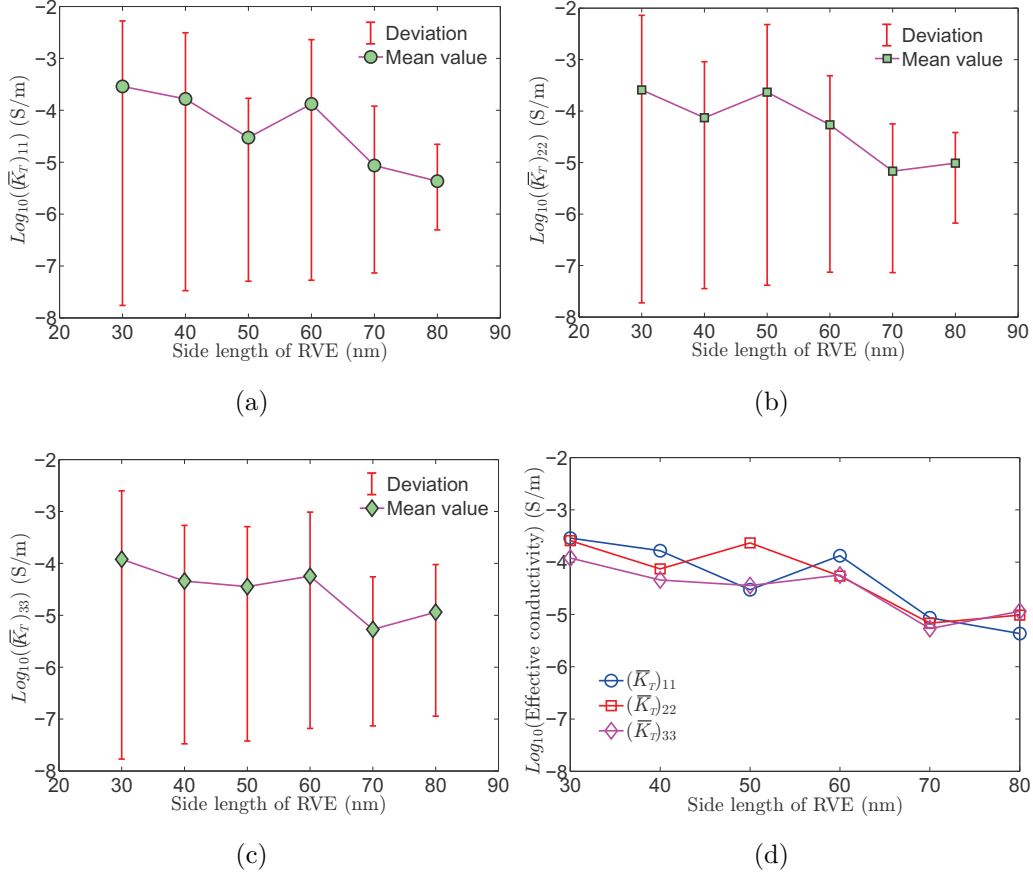


FIGURE 3.16 – Effective conductivities tensor components as a function of RVE size, $f=1.05$ vol%, $\overline{E}=1.25 \times 10^{-3}$ V/nm. (a) $(\overline{K}_T)_{11}$ (b) $(\overline{K}_T)_{22}$ (c) $(\overline{K}_T)_{33}$ (d) Comparison of the three components.

3.7.2 Effective electric conductivity and percolation threshold

Next, we use the proposed methodology to investigate the influence of graphene volume fraction on the effective electric conductivity of graphene/polymer nanocomposites. The polymer matrix is made of PMMA. The length of the cubic RVE is 80 nm. The volume fraction is increased by accounting

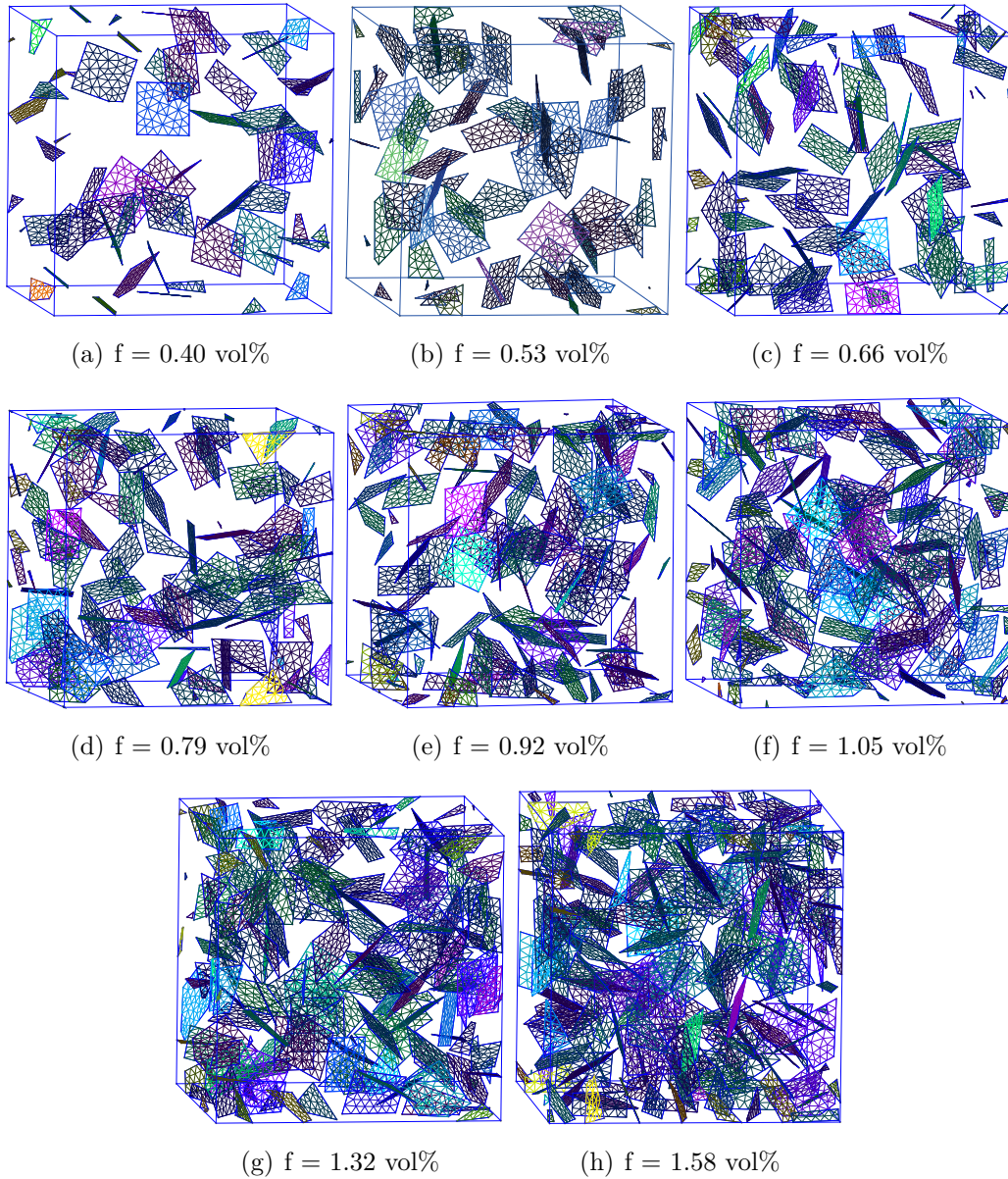


FIGURE 3.17 – Realizations of microstructures for different graphene volume fractions. For visualization purpose, only the mesh of graphene sheets is depicted.

for the thickness of graphene sheets through Eq. (3.40) and by increasing the number of introduced graphene sheets in the domain. The graphene sheets are still square surfaces with a fixed size $15 \times 15 \text{ nm}^2$ and a thickness of 0.3 nm. The aspect ratio of graphene is 50. The sheets are distributed randomly using a Markov-chain hard-plate algorithm (see in Section 3.5.4). Several realizations of microstructures are shown in Fig. 3.17, where only the mesh of the graphene surfaces is shown.

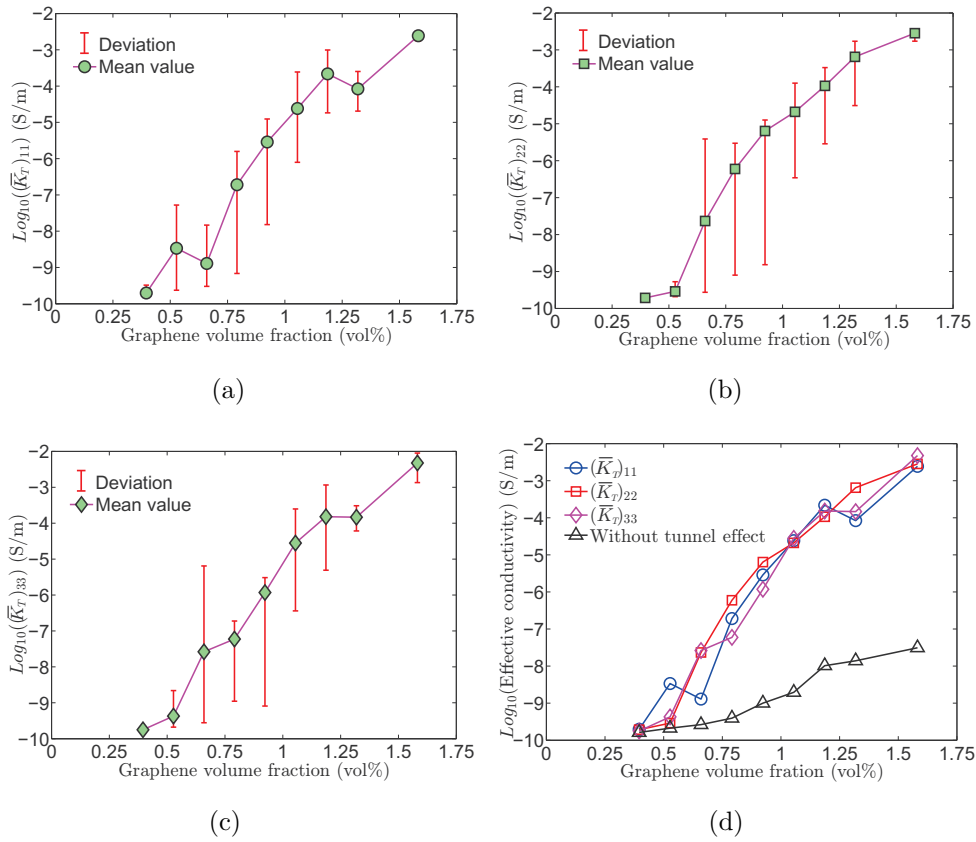


FIGURE 3.18 – Effective conductivities tensor components as a function of the graphene volume fraction, $\overline{E}=1.25 \times 10^{-3} \text{ V/nm}$, $\Phi_0 = 0.17 \text{ eV}$. (a) $(\overline{K}_T)_{11}$ (b) $(\overline{K}_T)_{22}$ (c) $(\overline{K}_T)_{33}$ (d) Comparison with the case in which tunneling effect is neglected.

The barrier height between graphene and PMMA is taken as $\Phi_0 = 0.17 \text{ eV}$ [Rahman 2012]. Periodic boundary conditions defined in Eq. (3.37) are prescribed. The problem being nonlinear, the effective conductivity is the incremental one as defined in Eq. (3.48), and depends on the intensity and

history of the applied electric field. The examples are given for a fixed value $\bar{E} = 0.0025$ V/nm for each direction respectively. The associated potential difference is $\Delta\phi = 0.2$ V.

The numerical results are provided in Fig. 3.18 for PMMA/graphene nanocomposite with varying graphene volume fractions. Taking into account the tunneling effect, the numerical values of $(\bar{K}_T)_{11}$, $(\bar{K}_T)_{22}$ and $(\bar{K}_T)_{33}$ are plotted for each volume fraction as shown in Fig. 3.18 (a-c), where the average values are obtained for 30 realizations. It indicates that the electric conductivity of the graphene-reinforced nanocomposites increases with the graphene volume fraction, and a sharp rise of conductivity can be noticed at about 0.8 vol% where the mean value turns to be over 10^{-8} S/m. Meanwhile, we can see that the deviation of the conductivities corresponding to each 30 realizations whose graphene volume fraction is around 0.8 vol% is much larger.

For better comparison, we have superimposed the mean values of $(\bar{K}_T)_{11}$, $(\bar{K}_T)_{22}$ and $(\bar{K}_T)_{33}$ in Fig. 3.18 (d) and also plotted the average value $\frac{1}{3}[(\bar{K}_T)_{11} + (\bar{K}_T)_{22} + (\bar{K}_T)_{33}]$ when the tunneling effect is neglected. It can be shown that the tunneling effect is responsible of an increase in the apparent conductivity of several orders of magnitude, which is expected as the polymer matrix alone is almost isolating and that in our model, the graphene sheets are not in contact with each other. This insulator-to-conductor transition in composites made of a conductive filler and an insulating matrix is frequently described by percolation theory. And percolation threshold is the minimum filler content in the matrix which is characterised by a sharp rise of several magnitude in conductivity due to the formation of conductive network. We estimate the percolation threshold around about 0.8 vol% which indicates that a very small volume fraction of graphene can leads to a giant increase in the effective conductivity of the composite. These theoretical predictions are in good qualitative agreement with those available in [Tkalya 2014].

We examined the results both with and without tunneling effect obtained from our present work along with the two conventional homogenization theory, *i.e.* Mori-Tanaka (MT) theory [Weng 1990, Weng 1984], and Ponte Castañeda Willis (PCW) theory [Castañeda 1995, Pan 2011]. The Hashin-Strikman (HS) boundings [Hashin 1963] are also presented as a theoretical footing. Assuming that the graphene is ellipsoidal, the MT and PCW theories for the effective electrical conductivity of graphene-polymer nanocomposite can be written as

a function of graphene volume fraction f :

$$K_e^{MT} = K^p \left(1 + \frac{f\bar{T}}{1 - f[1 - K^p\bar{T}/(K^g - K^p)]} \right), \quad (3.82)$$

$$K_e^{PCW} = K^p \left(1 + \frac{f\bar{T}}{1 - f\bar{T}/3} \right). \quad (3.83)$$

Due to the extremely high contrast ration of conductivity between graphene and polymer matrix, \bar{T} can be estimated by :

$$\bar{T} \simeq \frac{1}{3} \left(\frac{1}{S_{11}} + \frac{1}{S_{22}} + \frac{1}{S_{33}} \right), \quad (3.84)$$

where S is the Eshelby tensor [Eshelby 1957] associated with the shape of the graphene.

The upper and lower HS bounds are given by :

$$K_e^{HS(+)} = K^g \left(1 + \frac{(1-f)(K^p - K^g)}{f(K^p - K^g)/3 + K^g} \right), \quad (3.85)$$

$$K_e^{HS(-)} = K^p \left(1 + \frac{f(K^g - K^p)}{(1-f)(K^g - K^p)/3 + K^p} \right). \quad (3.86)$$

We have plotted the effective conductivity by MT and PCW theory, as well as our present work by FEM in Fig. 3.19, with the graphene aspect ratio of $\eta = 50$ and electric conductivities of polymer and graphene being $K^p = 1 \times 10^{-10}$ S/m and $K^g = 8.32 \times 10^4$ S/m respectively. It shows that the PCW theory increases sharply at the graphene volume fraction $f = 6.8$ vol% and rapidly goes out of the HS upper bound. Both our FEM results and the MT curve reside between the HS bounds, but the numerical results with tunneling effect show a sharp increase at 0.8 vol%. It is clear that our present work has more potential to explain the numerous experimental results which demonstrate extremely low percolation threshold for graphene-reinforced nanocomposites ranging from 0.1 vol% to 1 vol% [Stankovich 2006, Zhang 2010a, Kim 2015].

In order to better understand the importance of tunneling effect on the percolation behavior, the current density field in the polymer matrix of a random microstructure is presented in Fig. 3.20 when with and without considering tunneling effect respectively. The side length of the RVE cube is 40 nm, and the graphene volume fraction is 1.05 vol%. It is shown in Fig. 3.20 (a) that if tunneling effect is neglected, the maximum current density in the matrix

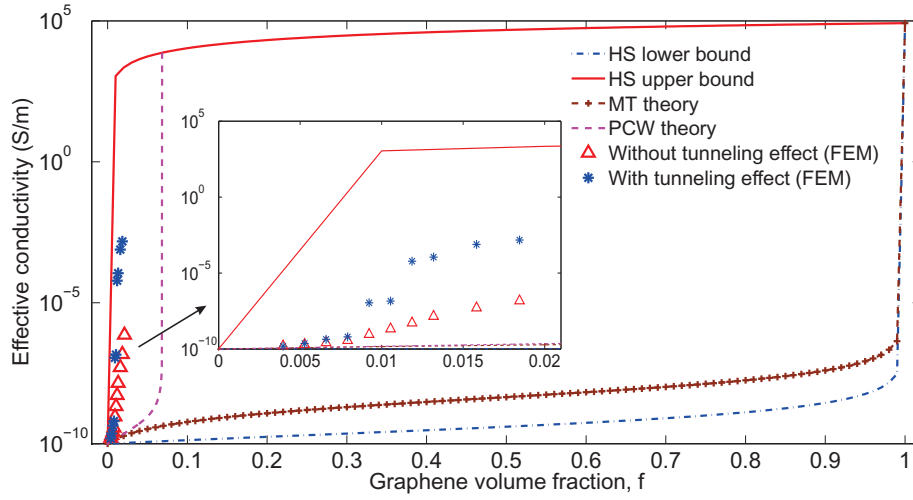


FIGURE 3.19 – The effective electrical conductivity calculated by FEM due to our present work, as well as the estimations by MT and PCW theory. The graphene aspect ratio $\eta = 50$, the electrical conductivity of polymer matrix and graphene are taken to be 1×10^{-10} S/m and 8.32×10^4 S/m respectively. The HS upper and lower bounds are also shown.

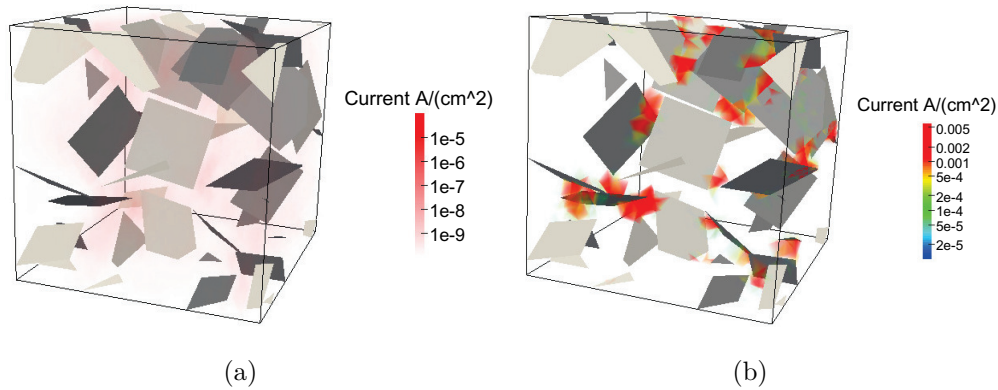


FIGURE 3.20 – Current density in the polymer matrix of microstructure with graphene volume fraction $f = 1.05$ vol%, side length of RVE $l = 40$ nm. (a) Without tunneling effect, (b) Considering tunneling effect. The values below the minimum of scale bar are set to transparency. (By ParaView [Ayachit 2015])

is about 10^{-9} A/cm², which indicates that the composite is insulating. While with the introduction of tunnel effect, we can see the tunneling current in the local matrix between graphene sheets in Fig. 3.20 (b), which is 10^7 times larger than in Fig. 3.20 (a). Therefore, a current path can be formed due to the tunneling current and leads to a insulator-conductor transition of the nanocomposite.

3.7.3 Nonlinear electric behavior of graphene reinforced nanocomposite

We can then use our simulation model to investigate the influence of the tunneling effect for explaining the nonlinear electric behavior of graphene reinforced nanocomposites. An RVE containing randomly distributed graphene sheets is considered with 1.05 vol% and $\eta = 50$. The barrier height between graphene and PMMA is $\Phi_0 = 0.17$ eV [Rahman 2012]. Fig 3.21 shows the current-density curve, which exhibits a linear (Ohmic) behavior for low applied electric fields, and a nonlinear behavior for higher electric fields. The numerical simulations are in good agreement with the experimental results reported in [Wang 2016].

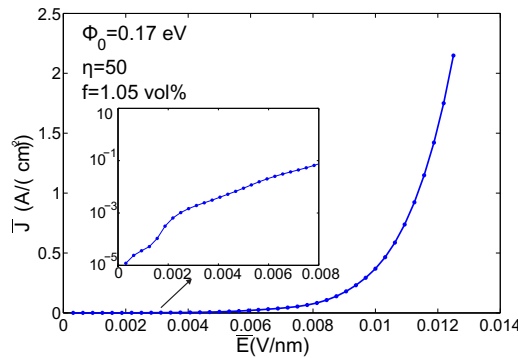


FIGURE 3.21 – Current density-electric field curve of a Nanocomposite with 1.05 vol% graphene, $\Phi_0 = 0.17$ eV, $\eta = 50$.

For a series samples with various graphene volume fraction which is above the percolation threshold, we present the relation between $\ln(\bar{J})$ and \bar{E} as shown in Fig. 3.22.

In generally, the conduction mechanisms in the conductor-insulator-conductor system include the interface-limited mechanism and the bulk-limited mecha-

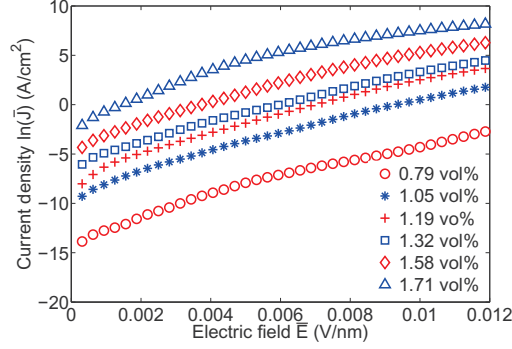


FIGURE 3.22 – Nonlinear behavior of the graphene nanocomposite with various graphene volume fraction, $\ln(\bar{J})$ versus \bar{E} .

nism. Sze [Sze 2006] summarized all the basic conduction processes in insulators, such as Schottky emission, Frankel-Poole emission, tunneling/field emission. Cashell *et al.* [Cashell 1981] has also proposed a model to describe the macroscopic electrical behavior in carbon black/polymer composites. Therefore, we propose to fit the $\bar{J}-\bar{E}$ behaviors in Fig. 3.22 by four expressions based on various conduction mechanisms and the proposed model in this work :

Schottky emission

$$\bar{J} = a \exp(b\sqrt{\bar{E}}), \text{ for simplicity written as, } \ln(\bar{J}) = A\sqrt{\bar{E}} + B. \quad (3.87)$$

Tunneling emission

$$\bar{J} = a' \bar{E}^2 \exp(-b'/\bar{E}), \text{ written as, } \ln(\bar{J}/\bar{E}^2) = -A'/\bar{E} + B'. \quad (3.88)$$

Frenkel-Poole emission

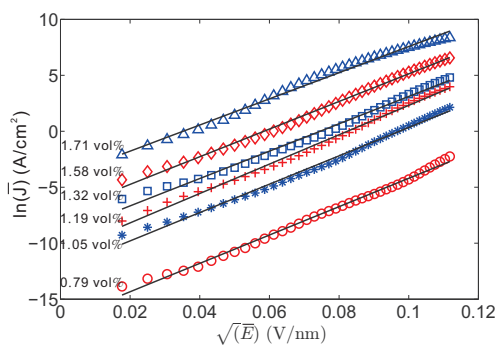
$$\bar{J} = a'' \bar{E} \exp(b''\sqrt{\bar{E}}), \text{ written as, } \ln(\bar{J}/\bar{E}) = A''\sqrt{\bar{E}} + B''. \quad (3.89)$$

Cashell's model

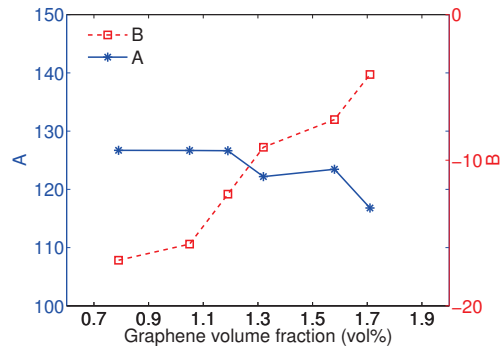
$$\bar{J} = a''' \bar{E} \exp(b''' \bar{E}), \text{ written as, } \ln(\bar{J}/\bar{E}) = A''' \bar{E} + B'''. \quad (3.90)$$

The fitting curves and the corresponding fitting parameters for the numerical results by the four equations above are shown in Fig. 3.23 respectively, where (a) and (b) denote to the Schottky emission expression in Eq. (3.87), (c) and (d) refer to the tunneling emission mechanism as Eq. (3.88), (e) and

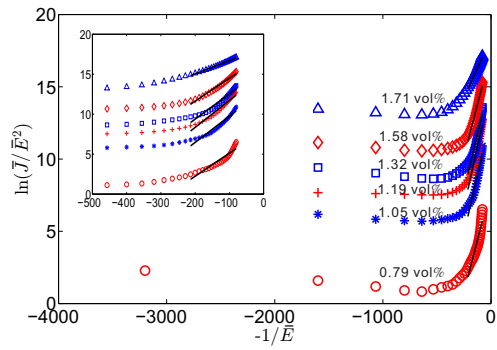
(f) base on the Frenkel-Poole emission equation as (3.89), (g) and (h) are for Cashell's model (3.90). It can be seen that both Schottky emission expression and Cashell's model can fit the nonlinear electrical behavior well when the graphene volume fraction in the nanocomposites is above the percolation threshold, but below 1.7 vol%. That is because the graphene/polymer nanocomposites are insulators below the percolation threshold, and above a certain high graphene concentration, the conduction mechanism of the composites changes. Seen in Fig. 3.23 (b) and (h), the tangents of the linear fitting curve A and A''' fluctuate within a narrow range, B and B''' keep on increasing along with the graphene concentration. However, we can also notice that the tunneling emission model and the Frenkel-Poole emission equation only work at high electrical field as shown in Fig. 3.23 (c) and (e).



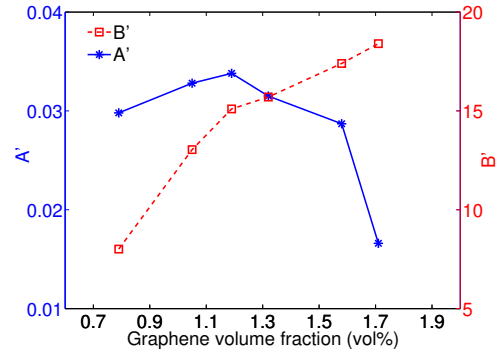
(a)



(b)



(c)



(d)

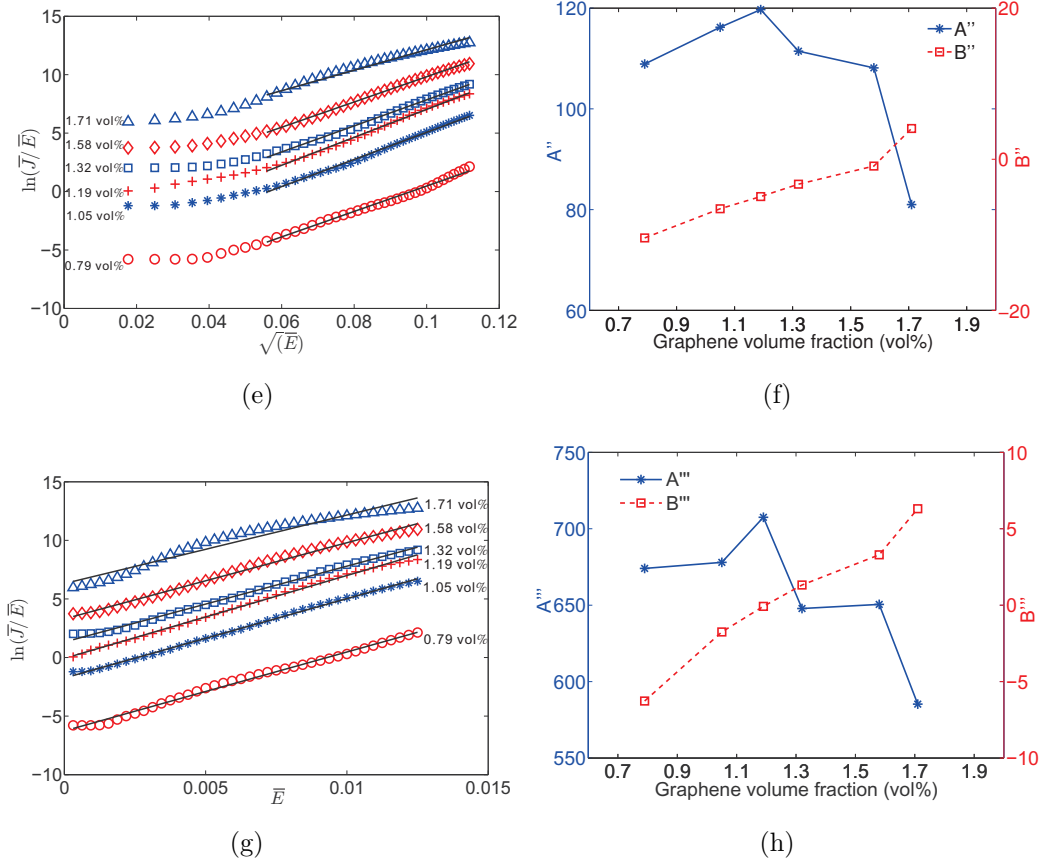


FIGURE 3.23 – Fitting curves and fitting parameters correspond to the four expressions. (a-b) Schottky emission ; (c-d) Tunneling emission ; (e-f) Frenkel-Poole emission ; (g-h) Cashell’s model.

3.7.4 Effect of barrier height on the percolation threshold

In the following, we study the effects of barrier height between graphene and various polymers on the nonlinear response of the nanocomposite. In our simulations, we have considered that the percolation threshold corresponds to a sharp variation of the effective conductivity above 10^{-8} S/m. In Fig. 3.24, the effective conductivity component $(\bar{K}_T)_{11}$ is plotted as a function of the graphene volume fraction for the values $\Phi_0 = 0.17$ eV, 0.3 eV, 1.0 eV and without tunneling effect. The aspect ratio is $\eta = 50$ and applied electric field $\bar{E} = 1.25 \times 10^{-3}$ V/nm. It should also be noted that for small barrier height (0.17 eV and 0.3 eV), the computation results of electric conductivity taking

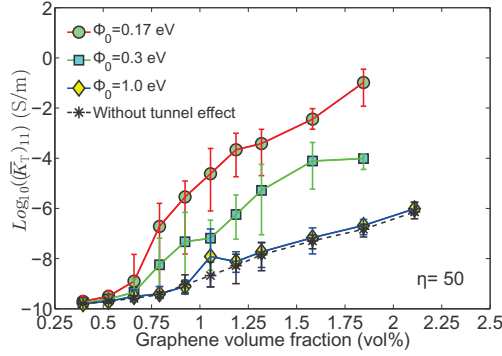


FIGURE 3.24 – Effective conductivity versus graphene sheets volume fraction for several barrier heights Φ_0 , $\bar{E}=1.25 \times 10^{-3}$ V/nm, $\eta = 50$.

into account the tunneling effect are much larger than the predictions without tunneling effect, while for $\Phi_0 = 1.0$ eV, the effective conductivity characteristics exhibit no obvious difference either with or without tunneling effect. We can see from these simulations that the lower the barrier height is, the lower the percolation threshold. Experimental results reporting percolation thresholds for different polymer matrices and graphene types can be found in [Stankovich 2006, Jiang 2009b, Ansari 2009, Liang 2009b].

3.7.5 Effect of graphene aspect ratio on the percolation threshold

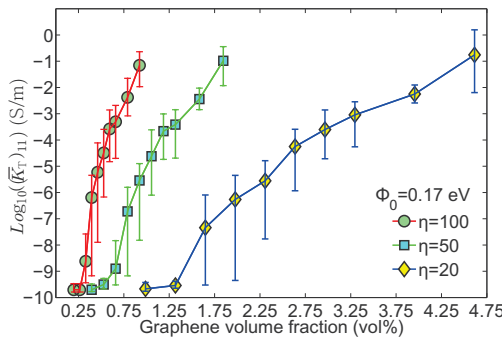


FIGURE 3.25 – Effective conductivity $(\bar{K}_T)_{11}$ as a function of the graphene volume fraction for several graphene aspect ratios η .

Next, we use our numerical model to estimate the percolation threshold f_c of the nanocomposite as a function of the graphene volume fraction and

aspect ratio for graphene sheets. In Fig. 3.25, the effective conductivity tensor component $(\overline{K}_T)_{11}$ is computed for different aspect ratios $\eta = 20, 50$ and 100 as a function of volume fraction. The side length of the graphene is fixed, and the various aspect ratios are obtained by changing the thickness of the graphene sheets. For each case, the values are averaged over 30 realizations of random distributions of graphene sheets within the RVE. As the behavior of the composite is nonlinear, the results of conductivity are presented for a fixed electric field $\overline{E} = 1.25 \times 10^{-3}$ V/nm. The barrier height is $\Phi_0 = 0.17$ eV. According to our numerical simulations, the effective conductivity clearly depends on the aspect ratio, a larger η provides lower percolation threshold. The obtained percolation thresholds for $\eta = 20, 50$, and 100 are 1.65 vol%, 0.79 vol%, and 0.33 vol% respectively.

3.7.6 Effect of alignment of graphene sheets

Next, we evaluate the effect of alignment of graphene sheets on the effective conductivity of the composite. For this purpose, we consider on one hand a microstructure with graphene sheets whose both positions and orientations are randomly distributed, and on the other hand a microstructure where positions of graphene sheets are randomly distributed but the orientation is fixed. Each point corresponds to the mean value over 30 realizations. Results are presented in Fig. 3.26. To clearly evidence the anisotropy, we have plotted the three components of the effective conductivity tensor. The parameters are $\overline{E} = 1.25 \times 10^{-3}$ V/nm, $\Phi_0 = 0.17$ eV and $\eta = 50$.

As expected, the numerical model clearly captures the anisotropic behavior of aligned graphene sheets (see Fig. 3.26 (b)). Another conclusion is that aligning the graphene sheets does not significantly increase either the maximum effective conductivity in the direction normal to the graphene sheets or the percolation threshold, as compared to randomly oriented sheets. However, the increase in conductivity after the percolation threshold is sharper in the case of aligned graphene sheets.

Finally, we depict in Fig. 3.27 the current density field in the polymer matrix when tunneling effect is taken into account for aligned and randomly oriented graphene sheets, to show the percolation path of electric current in both these configurations. The parameters are $\eta = 50$ and $\Phi_0 = 0.17$ eV, $f = 1.05$ vol%. The electrical field is applied on the X-direction.

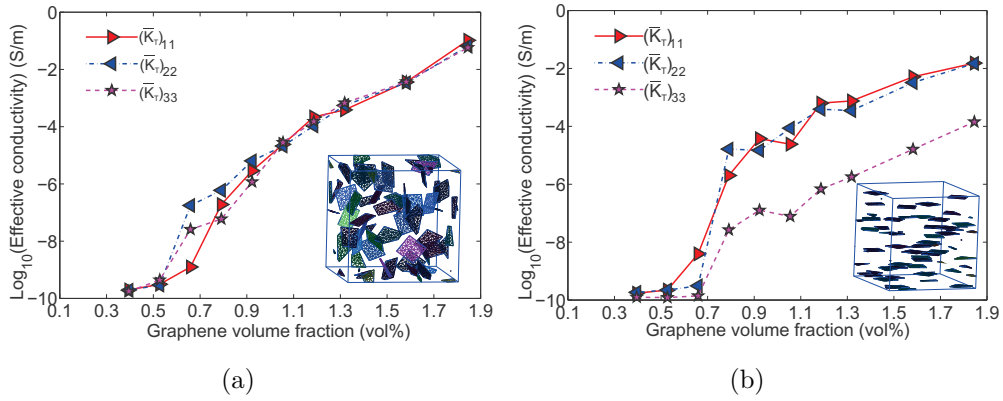


FIGURE 3.26 – Effective conductivity tensor components as a function of the graphene volume fraction : (a) random positions and orientations of graphene ; (b) random positions and direction of graphene normal to Z-axis.

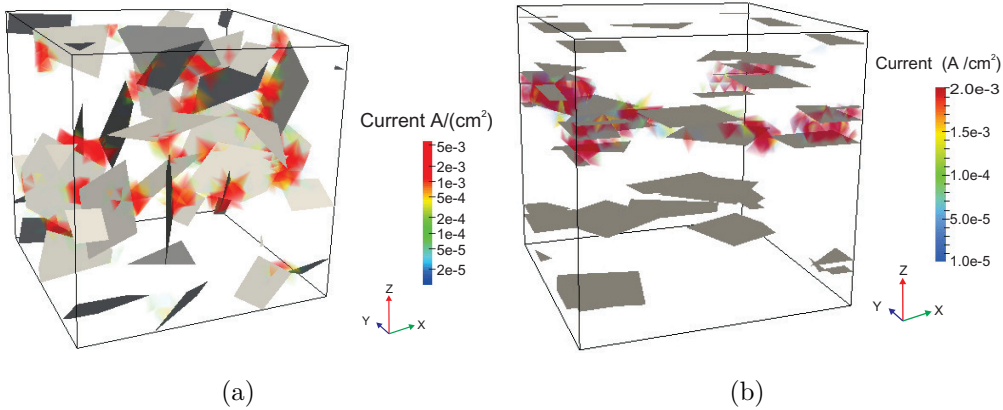


FIGURE 3.27 – Current density in the polymer matrix of microstructure with graphene volume fraction $f = 1.05 \text{ vol\%}$: (a) random positions and orientations of graphene ; (b) random positions and direction of graphene normal to Z-axis.

3.8 Comparison between numerical and experimental results

In the following, the obtained numerical results are compared with available experimental data reported by Stankovich [Stankovich 2006] and Zhang [Zhang 2010a] respectively. In these works, the percolation threshold and electric conductivities of graphene reinforced nanocomposites were measured as a function of graphene volume fraction.

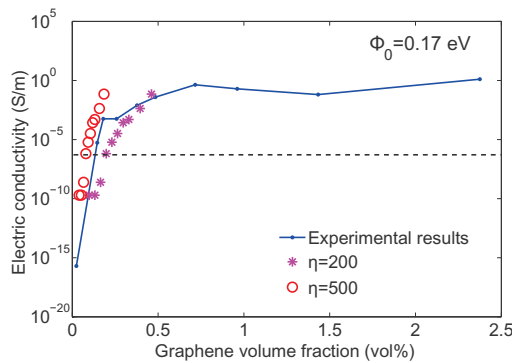


FIGURE 3.28 – Experimentally measured [Stankovich 2006] and predicted electric conductivities of polystyrene-graphene composites with various aspect ratio of graphene sheets ($\eta = 200, 500$).

Fig. 3.28 shows the experimental results of electric conductivity of polystyrene/graphene composites as a function of graphene volume fraction measured in [Stankovich 2006], where the graphene was prepared by complete exfoliation of graphite and the dispersion of individual graphene sheets at molecular-level. The percolation threshold is exhibited to be 0.1 vol%. The estimated electric conductivities of the composites containing two different aspect ratios of graphene platelets, 200 and 500, obtained from the numerical simulation in our study are also plotted in Fig. 3.28. Assuming the barrier height to be 0.17 eV, we can see that the percolation threshold for composites containing graphene sheets with $\eta = 200$ occurred at relatively higher graphene volume fraction, $f_c = 0.2$ vol%, than that of the composites containing graphene with $\eta = 500$, where $f_c = 0.08$ vol%. In general, the graphene platelets in the matrix have various aspect ratio due to the preparation method and their possible aggregation during the synthesis. The proposed numerical

estimations considering the aspect ratio range of 200 – 500 are in reasonable agreement with the experimental data for low graphene volume fraction.

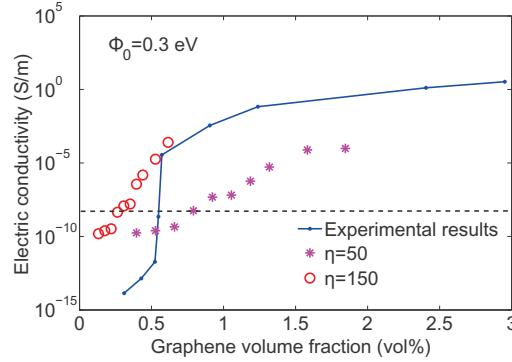


FIGURE 3.29 – Experimentally measured [Zhang 2010a] and predicted electric conductivities of polyethylene terephthalate/graphene nanocomposites with various aspect ratio of graphene sheets ($\eta = 50, 150$).

Fig. 3.29 plots the electric conductivities of polyethylene terephthalate-graphene nanocomposites as a function of graphene volume fraction. A high aspect ratio of $\eta = 146$ is obtained for graphene sheets from laser granularity analyzer. The experimental measured percolation threshold [Zhang 2010a] is about 0.5 vol%. Similarly, two different aspect ratios of graphene sheets, 50 and 150, were considered in the numerical modeling with the barrier height of 0.3 eV, leading to a range of percolation threshold from 0.25 vol% to 0.8 vol%. The experimentally measured electric conductivities roughly lie between the two numerical curves for the two considered aspect ratios. It should be noted that due to the computational limitations, the contrast of conductivities between graphene and polymer matrix cannot be higher than 10^{16} . Therefore, we have to take the electric conductivity of polymer matrix as 10^{-10} S/m, which may be one reason of discrepancy between experimental and numerical results for low graphene volume fraction. There are some other reasons which may also bring this discrepancy.

Firstly, the dispersion state of graphene is hard to control in the experimental preparation, and the aggregation of graphene in the microstructure may lead to the heterogeneity of the macroscopic property. However, in our present work, the numerical simulation is based on randomly distributed graphene sheets. Moreover, the numerical simulation ignores the defects in the nanocomposites especially the ones on the interface.

3.9 Conclusion

In this chapter, we have proposed a numerical modeling framework for predicting the effective electric conductivity in polymer/graphene nanocomposites, taking into account tunnelling effect. A computational homogenization method has been developed, and the following features were introduced.

First, a 3D tunneling effect model of electric conduction for close graphene sheets has been proposed, by extending the 1D model to 3D and by defining an appropriate distance map function. Then, the related nonlinear equations of the electrical problem have been introduced. The nonlinear equations have been solved by a FEM technique, where the graphene sheets have been modeled using imperfect interfaces with high conductivity, which avoids meshing them along their thickness. Appropriate linearization have been introduced and the effective conductivity has been evaluated numerically by appropriate definitions of effective quantities through homogenization.

The method has been validated for benchmarks and applied to RVE computations of polymer/graphene nanocomposites. Such procedure allows analyzing the effects of microstructural parameters, and percolation thresholds have been predicted in good agreement with available experimental data. From the numerical analysis, we can conclude that the tunnelling effect might be the cause of experimentally observed nonlinear electric response in nanocomposites and an unexpected very low percolation thresholds. The electric behaviors of the composites with various graphene concentration, which are obtained by the numerical simulation, can be fitted by various nonlinear equations. Although tunneling emission and Frenkel-Poole equations only work at high electrical field, the expressions based on Schottky emission and Cashell's model can fit the nonlinear $\bar{J} - \bar{E}$ behavior quite well. We can also observe from the numerical results that the lower percolation thresholds can be obtained for lower barrier height between the polymer and the graphene sheets and for higher aspect ratios of graphene platelets. Furthermore, the proposed numerical predictions show that aligning the graphene sheets leads to a sharper increase of the effective electric conductivity after the percolation threshold as compared to randomly oriented sheets, but without significant enhancement of percolation thresholds and maximum effective conductivity.

Modeling of the mechanical behavior of graphene-polymer interphase using molecular dynamics

4.1 Introduction

Graphene, as one of the stiffest known materials, whose Young's modulus is around 1 TPa [Lee 2008, Lier 2000, Jiang 2009a], is an attractive candidate for use in high-performance polymer-based composites. From 2000s, a significant amount of research has been carried out on graphene-polymer nanocomposites due to their potential for large increases in strength and stiffness [Satti 2010, Cai 2009, Rafiee 2009, Arash 2014, Verdejo 2011]. The enhanced mechanical properties of the nanocomposites have been found to depend on various factors including the graphene-polymer bonding, the concentration of graphene, and the uniformity of dispersion [Tang 2013, Terrones 2011, Zhao 2010]. Among these, the graphene-polymer interphase and the interfacial region between the filler and the matrix phases are recognized as key factors influencing the effective mechanical properties of the nanocomposites [Zaman 2011].

Many experimental attempts have been endowed to understand the interfacial behavior between graphene and polymer, aiming to improve the interactions and achieve better performance of nanocomposites, *i.e.* [Ma 2013, Wan 2012]. Some measurement means for the interfacial strength have been provided, assuming the existence of interface between the filler and matrix. For example, Gong *et al.* [Gong 2010] explored the interfacial behavior by monitoring the stress transfer with the help of Raman spectroscopy. The AFM probe, associated with nanopullout process, is also a controllable approach to

get the interfacial strength in the graphene reinforced polymer nanocomposites [Zhang 2012b, Nie 2017, Barber 2003, Barber 2004a].

In the report of Seidel *et al.* [Seidel 2006], it was shown that the surface of graphene is highly attractive and causes the polymer to attain higher density near the interface, which creates an interphase region of certain thickness, whose mechanical properties are neither the one of graphene nor of the polymer matrix. However, the quantitative characterization of the interphase, such as the property of the microstructure and the local mechanical properties have not been reported so far by many researchers. Currently, only Liu *et al.* [Liu 2016] provided a modern tool to determine the thickness of the interphase by combining the scanning transmission electron microscopy (STEM) and electron energy-loss spectroscopy (EELS), by which an interphase thickness of 13 and 12.5 nm was measured for GNPs/epoxy and GO/epoxy, respectively.

The success of several studies has demonstrated that continuum modeling is a powerful tool to investigate the mechanical behavior of nanocomposites and overcome the limitation of atomistic methods [Srivastava 2017, Tserpes 2017, Yang 2013]. There have been mainly two approaches to model the interfacial effects due the interface in the continuum model : the introduction of a third body, called interphase, or the use of a model with imperfect interfaces.

On the one hand, most of the works using a nanocomposite model with an interphase were performed on the CNT/polymer nanocomposites. Wan *et al.* [Wan 2005] studied the load transfer and effective moduli of CNT/polymer nanocomposites. They assumed that the elastic moduli of interphase are constants and they studied the effect of both soft and hard interphases on effective behavior. Hernández-Pérez *et al.* [Hernández-Pérez 2010] proposed that the interphase moduli are assumed to range continuously from those of CNT to those of polymer. They concluded that an exponential variation may be more suitable than a linear one to represent the effective elastic properties of CNT/polymer nanocomposites.

On the other hand, the interfacial interaction can be modeled by imperfect interface which may be regarded as coherent or non-coherent interface [Chatzigeorgiou 2017]. The non-coherent imperfect interfaces are modelled as a zero-thickness boundary layer instead of a thin interphase, by spring-layer imperfect interface model [Benveniste 1985, Achenbach 1989, Hashin 1992,

[Hashin 2002] where the traction vector is continuous across an interface and proportional to the displacement vector jump across the same interface. For the coherent or the membrane-type imperfect interface model [Shenoy 2002, Sharma 2003, Duan 2005b, Yvonnet 2008b, Yvonnet 2011], the displacement vector is continuous across an interface but the traction vector suffers a jump across the same interface. Some works to predict the elastic property of composites with random microstructures have been addressed, considering the normal and tangential stiffness parameter of interface [Lee 2007, Guessasma 2010, Wang 2014d].

The difficulty here is the identification of specific properties of the interface and interphase. To obtain a reliable prediction of the macroscopic mechanical properties of graphene reinforced nanocomposites, we need to better understand the microscopic mechanisms of the interfacial interaction between graphene and polymer matrix. Therefore, the aim of this chapter is to identify the local mechanical properties of the interface as well as the interphase. The final goal is to define the most simplest and the most efficient continuum model with the consideration of the interfacial interaction for the computation of the effective stiffness of graphene reinforced nanocomposites.

In this chapter, we propose a numerical methodology to characterize the organization and elastic properties of the interphase via molecular dynamics method. The information of each particle in the atomistic system (*i.e.*, masses, positions, stresses and velocities) has to be transposed to the continuum notions as the density, velocity, stress and displacement field. Since many works have been presented for the identification of local stress field [Admal 2016b, Admal 2016a], the main innovation for the identification of the elastic property is the choice of an appropriate definition of displacement fields. Besides, the stiffness parameters of the imperfect interface are also identified via atomistic simulations by monitoring the variation of free energy during the motion of graphene layer. The local interfacial properties are further introduced by two continuum models : one contains both interface and interphase layers, the other replaces the graphene sheet, interface region and interphase region by an equivalent imperfect surface. Compared with MD results, we provide a simplified model which can be easily used to study random composites efficiently.

Atomistic modeling is a useful tool to provide a view of the elastic property of a system containing the potential of all the atomic interactions. Shenoy

[Shenoy 2005] developed an atomistic method to calculate the surface elastic properties in the nanostructures accounting for additional surface relaxations engendered by the applied strain. Yvonnet *et al.* [Yvonnet 2011, Yvonnet 2012] employed *ab initio* calculations to extract elastic coefficients of general anisotropic surfaces, and compared the mechanic properties of nanowires obtained by the continuum model incorporating the surface energy and the complete *ab initio* models respectively. It was shown that the multiscale simulation combining the atomistic and continuum methods show significant potential for nanoscale modeling [Namilae 2005, Li 2006, Odegard 2005]. To the best of our knowledge, it is the first time that the choice of a fully non-coherent imperfect interface model is justified and identified by atomistic simulations.

One approach for defining the continuum stress and density field from the atomistic level was pioneered by Irving and Kirkwood by the principles of non-equilibrium classical statistical mechanics, and further substantiated by Noll [Irving 1950, Noll 1955]. There have been many literatures related to the discussion and application of this procedure [Lutsko 1988, Cormier 2001, Admal 2010, Torres-Sánchez 2016]. Recently, Murdoch and Hardy [Hardy 1982, Murdoch 1993, Murdoch 2007] developed a new approach, defining the continuum fields by spatial averaging of the discrete motions using weight function instead of statistical mechanics. The so called Murdoch-Hardy procedure was further extended for the multiscale analysis [Admal 2010, Zhang 2015, Admal 2016b, Admal 2016a]. Apart from the stress field, the displacement field in the composite system is also required for the identification of the stiffness of the interphase region. To link the deformation of the lattice vectors of crystal to that of a continuum deformation field, Cauchy-Born rule [Born 1940, Weiner 1981] is a fundamental assumption, and it is suitable for the linkage of 3D multiscale deformations of bulk materials such as space-filling crystals [Arroyo 2002, Arroyo 2004]. However, for the amorphous body such as the polymer matrix, it is no longer applicable [Tanguy 2002, Wittmer 2002, Maloney 2004, Maloney 2006, Lemaitre 2006]. To overcome this difficulty, we extended the Murdoch-Hardy procedure to estimate the displacement field in Eulerian coordinate.

The chapter is organized as follows. First, in section 4.2, we provide a general introduction of the molecular dynamics (MD) method including the fundamental equations and the atomistic potentials, and present our methodology to generate the molecular RVE containing the single layer graphene

sheets in the middle of polyethylene (PE) bulk. Section 4.3 describes atomistic model for analysis, and gives the molecular topology and Eulerian mechanical field obtained by Murdoch-Hardy procedure. In section 4.4, the imperfect surfaces framework for the continuum model is established, and the macroscopic elastic parameters for the interface, interphase and the polymer bulk are identified from the atomistic information. Finally, in section 4.5, the numerical estimations obtained by the continuum models are compared with the MD results, demonstrating the influence of the polymer thickness on the effective elastic tensor components. Finally, the simplified imperfect surface model is employed to analyze the mechanical characteristics of the polymer based nanocomposites with randomly distributed graphene filler.

4.2 Details of MD simulations

Molecular Dynamics simulation is a technique for computing the equilibrium and transport properties of a classical many-body system. It is a computational tool to understand the properties of assemblies of molecules in terms of their structure and the microscopic interactions between them. The accuracy of the atomistic predictions depends on the initial molecular structure, the force field used to describe the atomic interactions and the procedure to cure the material.

In this section, a general introduction of MD formulation is first given. Then we provide a description of interatomic potentials used in this study. The common MD algorithms are also presented, which are followed by the methodology of generation process for graphene-PE sandwich structure.

4.2.1 Formulations of MD method

In statistical mechanics experiments and simulations can be performed in different ensembles, *e.g.*, Microcanonical ensemble (NVE, or NVU), Canonical ensemble (NVT) and Isothermal-isobaric ensemble (NpT), as shown in Fig. 4.1. An ensemble is a collection of individual systems that can be studied to yield macroscopic properties of the entire collection. Every equilibrium configuration generated via MD represents a unique microstate of the considerate statistical ensemble.

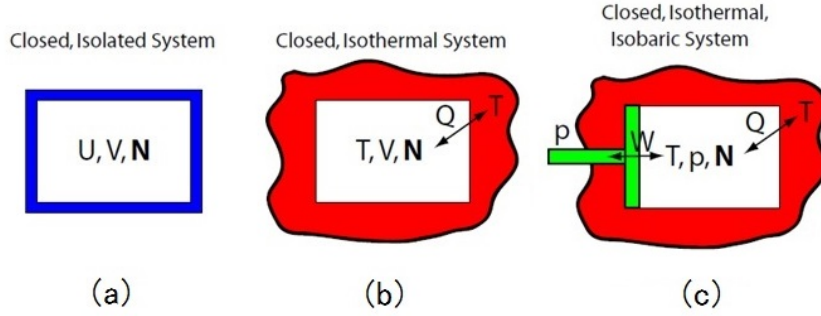


FIGURE 4.1 – Scheme of the statistical ensemble. (a) NVE ; (b) NVT ; (c) NpT.

Microcanonical ensemble (NVE) Generally, if the simulation system is sufficiently large, the small part of it may be considered as a canonical system. In the microcanonical (NVE) ensemble, the system has constant number of particles (N), constant volume (V) and constant energy (E), as shown in Fig. 4.1 (a). Considering the isolated system of atoms or molecules, the total energy E is the sum of the kinetic and potential energies of the molecules. It is constant in time and identified as the Hamiltonian $\mathcal{H} = E$, given as

$$\mathcal{H}(\mathbf{r}_1(t), \mathbf{r}_2(t), \dots, \mathbf{p}_1(t), \mathbf{p}_2(t), \dots) = \sum_{\alpha=1}^1 \frac{1}{2m_{\alpha}} \mathbf{p}_{\alpha} \cdot \mathbf{p}_{\alpha} + \mathcal{U}_{total}(\mathbf{r}_1(t), \dots), \quad (4.1)$$

where m_{α} and \mathbf{r}_{α} denote mass and position of atom α , respectively, and \mathcal{U}_{total} is the potential energy defined as the sum of energies due to all the force fields, such as pair-wise interaction of the atoms, bond potentials, three-body potentials or others, which we will further discuss in section 4.2.2. \mathbf{p}_{α} is the momentum defined by

$$\mathbf{p}_{\alpha} = m_{\alpha} \dot{\mathbf{r}}_{\alpha}. \quad (4.2)$$

In Eq. (4.2), the dot indicates derivative with respect to time. Then the Hamilton's equations for the system are given by

$$\dot{\mathbf{r}}_{\alpha} = \frac{\partial \mathcal{H}}{\partial \mathbf{p}_{\alpha}}, \quad (4.3)$$

$$\dot{\mathbf{p}}_{\alpha} = -\frac{\partial \mathcal{H}}{\partial \mathbf{r}_{\alpha}}. \quad (4.4)$$

The replacement of Newtonian formulation of mechanics by Hamiltonian's equation for a system of particles is a straightforward procedure when there

are no geometrical constraints and therefore the particle positions may be described by their rectangular Cartesian coordinates.

The Newtonian dynamics is used to calculate the motion of the atoms to determine the net force and acceleration experience by each atom. The solution of the classical equations of motion is written as

$$m_\alpha \ddot{\mathbf{r}}_\alpha = \mathbf{f}_\alpha. \quad (4.5)$$

The atomistic displacement vector is defined by

$$\mathbf{u}_\alpha(t) = \mathbf{r}_\alpha(t) - \mathbf{r}_\alpha^{(0)}, \quad (4.6)$$

where $\mathbf{r}_\alpha^{(0)}$ is the initial position of α th atom.

Canonical ensemble (NVT) In the canonical ensemble, the amount of substance (N), volume (V) and temperature (T) are constant (see in Fig. 4.1 (b)). Since T and E are dual variables, the control of the system temperature T can be realized by the exchange of the energy E.

The evolution equations are given by

$$\dot{\mathbf{r}}_\alpha = \nabla_{\mathbf{p}_\alpha} \mathcal{H}(\mathbf{r}, \mathbf{p}), \quad (4.7)$$

$$\dot{\mathbf{p}}_\alpha = \nabla_{\mathbf{r}_\alpha} \mathcal{H}(\mathbf{r}, \mathbf{p}) + \mathbf{f}_\alpha^{th}(\mathbf{p}; T). \quad (4.8)$$

In this ensemble, the energy of endothermic and exothermic processes is exchanged with the help of a variety of thermostat algorithms, which contributes to the term $\mathbf{f}_\alpha^{th}(\mathbf{p}; T)$. Two types of thermostat have been provided : one is deterministic such as Evans thermostat [Evans 1983, Evans 1984], Berendsen thermostat [Berendsen 1984], and Nosé-Hoover thermostat [Nosé 1984, Hoover 1985]; the other is stochastic such as Langevin thermostat [Grest 1986] and Nosé-Hoover-Langevin thermostat [Leimkuhler 2009, Samoletov 2007].

Isothermal-isobaric ensemble (NpT) In the isothermal-isobaric ensemble, the number of the particles (N), pressure (p) and temperature (T) maintains constant as in Fig. 4.1 (c). It requires both a thermostat (control T) and barostat (control p), and is the closest to 'laboratory conditions'. Correcting the pressure in a simulation can be achieved by scaling the inter particle distances, *i.e.*, changing the size and shape of the simulation box.

The macroscopic deformation gradient tensor $\tilde{\mathbf{F}}$ of the simulation box is defined by

$$\tilde{\mathbf{F}} = \mathbf{h} \cdot (\mathbf{h}^{(0)})^{-1} \quad (4.9)$$

where $\mathbf{h}^{(0)}$ and $\mathbf{h} = \{\mathbf{a}, \mathbf{b}, \mathbf{c}\}$ are defined as the box simulation shape in the reference and current configuration respectively. Basis vectors $\mathbf{a}, \mathbf{b}, \mathbf{c}$ represent the three edges that meet at one vertex of the parallelepiped (see in Fig. 4.2).

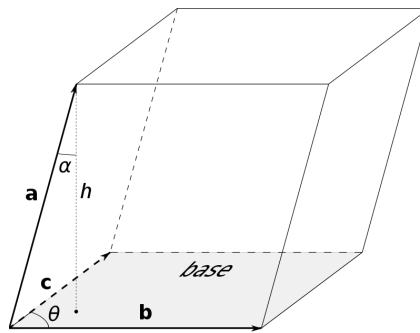


FIGURE 4.2 – Basis vectors of a parallelepiped.

Several barostat have been presented to control the pressure of the system. Berendsen barostat [Berendsen 1984] and Andersen barostat [Andersen 1980, Martyna 1994] allow the box size to fluctuate but not change its shape. Rahman-Parrinello Barostat [Parrinello 1980, Parrinello 1981] which is used only for solids, allows both the size and shape of the box to change.

Periodical boundary conditions In all the ensembles, periodical boundary condition usually need to be employed due to the small sample size unless surface effects are of particular interest. Considering for example the two dimensional box surrounding the 2D box with replicas of itself as shown in Fig. 4.3, we can adopt the minimum image convention that each atom interacts with the nearest atom or image in the periodic array. During the simulation, if an atom leaves the basic simulation box then its replica in a surrounding box will go into the box as shown in Fig. 4.3. The cutoff is chosen such that a particle in the primary box does not see its image in the surrounding boxes.

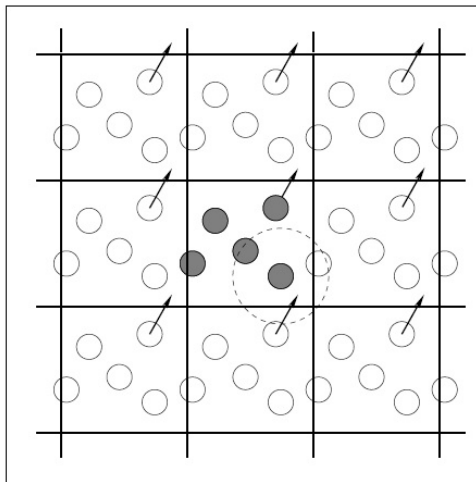


FIGURE 4.3 – Periodic boundary conditions. As a particle moves out of the simulation box, an image particle moves in to replace it. In calculating particle interactions within the cutoff range, both real and image neighbours are included.

4.2.2 Potentials

Several force fields have been used in the molecular modeling to describe the potentials between different atoms or atom groups, including polymer consistent force field (PCFF) [Heinz 2005], consistent valence force field (CVFF) [Dauber-Osguthorpe 1988], Compass [Sun 1998], and Dreiding [Mayo 1990].

In the current study, the Dreiding potential is employed which consists of the valence interactions and the nonbonded interactions of the atoms since it is well validated for polymer chemistry. The electrostatic contribution are neglected for simplicity reasons in this work. The system potential energy of the system, $\mathcal{U}(\{\mathbf{r}_\alpha\})$ via the Dreiding potential, is represented by the sum of the contributions of all the interactions above :

$$\mathcal{U}(\{\mathbf{r}_\alpha\}) = \mathcal{U}^{(vdw)}(\{\mathbf{r}_\alpha\}) + \mathcal{U}^{(s)}(\{\mathbf{r}_\alpha\}) + \mathcal{U}^{(b)}(\{\mathbf{r}_\alpha\}) + \mathcal{U}^{(tor)}(\{\mathbf{r}_\alpha\}) \quad (4.10)$$

The forces \mathbf{f}_α acting on the atoms are usually derived from a potential energy $\mathcal{U}(\{\mathbf{r}_\alpha\})$ as

$$\mathbf{f}_\alpha = -\partial_{\mathbf{r}_\alpha} \mathcal{U}(\{\mathbf{r}_\alpha\}). \quad (4.11)$$

Since the potentials used are conservative, a set of central forces between the pairs of atoms, $\mathbf{f}_{\alpha\beta}$, can be expressed in terms of the set of inter-atomic distances $r_{\alpha\beta}$ between the α th and β th atoms [Admal 2010, Tadmor 2011], which are defined by

$$\mathbf{f}_{\alpha\beta} = -\partial_{r_{\alpha\beta}}\mathcal{U}(\{\mathbf{r}_\alpha\}) \frac{\mathbf{r}_\alpha - \mathbf{r}_\beta}{r_{\alpha\beta}}. \quad (4.12)$$

Here $\mathbf{f}_{\alpha\beta}$ is the force of β th atom on the α th atom. It is interesting to note that this definition assures that

$$\mathbf{f}_{\alpha\beta} = -\mathbf{f}_{\beta\alpha}, \quad \text{and} \quad \mathbf{f}_\alpha = \sum_{\beta \neq \alpha} \mathbf{f}_{\alpha\beta} \quad (4.13)$$

For convenient reasons, we consider only the van der Waals interactions in the nonbonded part of Dreiding potential, which is modeled by the Lennard-Jones 12-6 type expression

$$\mathcal{U}^{(vdw)}(\{\mathbf{r}_\alpha\}) = \sum_{\alpha} \sum_{\substack{\beta \neq \alpha, \\ r_{\alpha\beta} < r_c}} 4\varepsilon_{\alpha\beta} \left[\left(\frac{\sigma_{\alpha\beta}}{r_{\alpha\beta}} \right)^{12} - \left(\frac{\sigma_{\alpha\beta}}{r_{\alpha\beta}} \right)^6 \right] \quad (4.14)$$

where $\varepsilon_{\alpha\beta}$ and $\sigma_{\alpha\beta}$ are parameters which depend on the atom types. For computational reasons, we use a cutoff radius $r_c = 14.0\text{\AA}$.

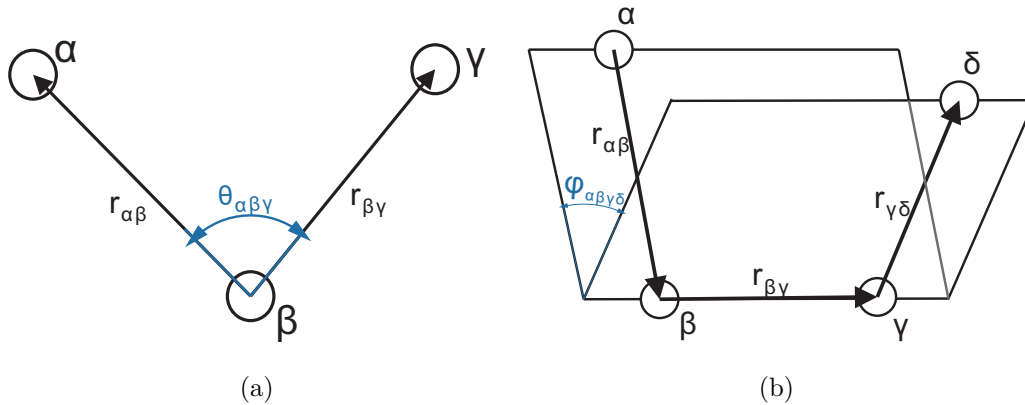


FIGURE 4.4 – Profiles for the potentials. (a) The valence angle and associated vectors, (b) The dihedral angle and associated vectors.

We assume that the valence interactions consist of bond stretch ($\mathcal{U}^{(s)}$, two-body), bond-angle bend ($\mathcal{U}^{(b)}$, three-body), dihedral angle torsion ($\mathcal{U}^{(tor)}$,

four-body). In the case of coarse-grain PE and graphene, these potentials are written as :

$$\mathcal{U}^{(s)}(\{\mathbf{r}_\alpha\}) = \sum_{\text{Bond}} \frac{k_{\alpha\beta}^{(s)}}{2} (r_{\alpha\beta} - r_{\alpha\beta}^0)^2 \quad (4.15)$$

$$\mathcal{U}^{(b)}(\{\mathbf{r}_\alpha\}) = \sum_{\text{Bending}} \frac{k_{\alpha\beta\gamma}^{(b)}}{2} (\cos(\theta_{\alpha\beta\gamma}) - \cos(\theta_{\alpha\beta\gamma}^0))^2 \quad (4.16)$$

$$\mathcal{U}^{(tor)}(\{\mathbf{r}_\alpha\}) = \sum_{\text{Dihedral}} \left(\sum_{n=1}^5 A_n \cos^{n-1}(\theta_{\alpha\beta\gamma\delta}) \right) \quad (4.17)$$

where $k_{\alpha\beta}^{(s)}$, $r_{\alpha\beta}^0$, $k_{\alpha\beta\gamma}^{(b)}$, $\theta_{\alpha\beta\gamma}^0$ and $k_{\beta\gamma}^{(tor)}$ are parameters which depend on the atom types. The bending angle $\theta_{\alpha\beta\gamma}$ and the dihedral angle $\phi_{\alpha\beta\gamma\delta}$ are defined in Fig. 4.4 and they can be computed using interatomic distances [Glusker 1994] :

$$\cos(\theta_{\alpha\beta\gamma}) = \frac{\mathbf{r}_{\beta\alpha} \cdot \mathbf{r}_{\beta\gamma}}{r_{\alpha\beta} r_{\beta\gamma}} = \frac{r_{\alpha\beta}^2 + r_{\beta\gamma}^2 - r_{\alpha\gamma}^2}{2r_{\alpha\beta} r_{\beta\gamma}} \quad (4.18)$$

$$\cos(\theta_{\alpha\beta\gamma\delta}) = \frac{(\mathbf{r}_{\alpha\beta} \times \mathbf{r}_{\beta\gamma}) \cdot (\mathbf{r}_{\beta\gamma} \times \mathbf{r}_{\gamma\delta})}{|\mathbf{r}_{\alpha\beta} \times \mathbf{r}_{\beta\gamma}| |\mathbf{r}_{\beta\gamma} \times \mathbf{r}_{\gamma\delta}|} \quad (4.19)$$

$$= \frac{(r_{\alpha\beta}^2 + r_{\beta\gamma}^2 - r_{\alpha\gamma}^2)(r_{\beta\gamma}^2 + r_{\gamma\delta}^2 - r_{\beta\delta}^2) - 2r_{\beta\gamma}^2(r_{\beta\gamma}^2 - r_{\alpha\gamma}^2 - r_{\beta\delta}^2 + r_{\alpha\delta}^2)}{4\sqrt{r_{\alpha\beta}^2 r_{\beta\gamma}^2 - \frac{1}{4}(r_{\alpha\beta}^2 + r_{\beta\gamma}^2 - r_{\alpha\gamma}^2)^2} \sqrt{r_{\gamma\delta}^2 r_{\beta\gamma}^2 - \frac{1}{4}(r_{\gamma\delta}^2 + r_{\beta\gamma}^2 - r_{\beta\delta}^2)^2}} \quad (4.20)$$

The parameters in Dreiding used to represent the interactions between the atoms used in this work are given in Table 1. It should be noted that the Van der Waals potential parameters between C of graphene and -CH₂- of PE can be obtained by the mixing rule such as

$$\varepsilon_{\alpha\beta} = \sqrt{\varepsilon_{\alpha\alpha} \varepsilon_{\beta\beta}}, \quad (4.21)$$

$$\sigma_{\alpha\beta} = \sqrt{\sigma_{\alpha\alpha} \sigma_{\beta\beta}}. \quad (4.22)$$

$$(4.23)$$

4.2.3 The MD algorithm

4.2.3.1 The Verlet algorithm

The Verlet method (also known as leapfrog or Störmer-Verlet) is a popular time-discretization scheme for molecular simulation. It is specialized to the

TABLE 4.1 – Dreiding potential used in the graphene/PE system

<i>Masses</i>					
Atom	Atomic mass (g/mole)				
C	12.00				
H	1.01				
<i>Bond stretching parameters</i>					
Bond type	$r_0(\text{\AA})$	$k_s(\text{Kcal/mole})$			
CH ₂ – CH ₂	1.54	700			
C-C	1.40	934			
<i>Angle bending parameters</i>					
Angle type	θ_0 (degree)	k_b (Kcal/mole)			
CH ₂ – CH ₂ – CH ₂	109.5	100			
C-C-C	120.0	100			
<i>Torsion parameters</i>					
Angle type	A_1	A_2	A_3	A_4	A_5
–CH ₂ – CH ₂ –	1.0	-3.0	0.0	4.0	0.0
-C-C-	25.0	0.0	-25.0	0.0	0.0
<i>Van der Waals parameters</i>					
Atom type	ε (Kcal/mole)	σ (\AA)			
CH ₂	0.1984	4.0677			
C	0.0950	3.8800			
Cut-off distance for all the pair potential is 14 \AA					

problems expressed by the classical equations of motion :

$$\dot{\mathbf{r}}_\alpha = \mathbf{v}_\alpha, \quad \text{and} \quad m\dot{\mathbf{v}}_\alpha = \mathbf{f}_\alpha, \quad (4.24)$$

and verifies certain conservation principles associated to the continuous time ordinary differential equations.

Starting from Taylor expansions, we have

$$\mathbf{r}(t + \delta t) = \mathbf{r}(t) + \delta t\mathbf{v}(t) + \frac{1}{2}\delta t^2\dot{\mathbf{v}}(t) + \frac{1}{6}\delta t^3\ddot{\mathbf{v}}(t) + O(\delta t^4) \quad (4.25)$$

$$\mathbf{r}(t - \delta t) = \mathbf{r}(t) - \delta t\mathbf{v}(t) + \frac{1}{2}\delta t^2\dot{\mathbf{v}}(t) - \frac{1}{6}\delta t^3\ddot{\mathbf{v}}(t) + O(\delta t^4) \quad (4.26)$$

where the superscript $t - \delta t$, t , $t + \delta t$ denote the physical quantity at a series of time steps. Adding these two equations gives

$$\mathbf{r}(t + \delta t) = 2\mathbf{r}(t) - \mathbf{r}(t - \delta t) + \delta t^2\dot{\mathbf{v}}(t) + O(\delta t^4) \quad (4.27)$$

which is called the Verlet algorithm. The Verlet algorithm uses positions and accelerations at time t and the positions from time $t - \delta t$ to calculate new positions at time $t + \delta t$, and uses no explicit velocities. The advantages of the Verlet algorithm are : i) it is straightforward, and ii) the storage requirements are modest. The disadvantage is that the algorithm is moderately accurate.

Therefore, the scheme is usually given in an alternative “velocity Verlet” form that takes a step from a given vector $\mathbf{r}(t)$, $\mathbf{v}(t)$ to $\mathbf{r}(t + \delta t)$, $\mathbf{v}(t + \delta t)$ by the sequence of operations where there is no compromise on precision. :

$$\mathbf{v}(t + \frac{1}{2}\delta t) = \mathbf{v}(t) + \frac{1}{2}\delta t\dot{\mathbf{v}}(t) \quad (4.28)$$

$$\mathbf{r}(t + \delta t) = \mathbf{r}(t) + \delta t\mathbf{v}(t + \frac{1}{2}\delta t) \quad (4.29)$$

$$\mathbf{v}(t + \delta t) = \mathbf{v}(t + \frac{1}{2}\delta t) + \frac{1}{2}\delta t\dot{\mathbf{v}}(t + \delta t). \quad (4.30)$$

4.2.3.2 Athermal, Quasistatic Simulation (AQS)

The Athermal, Quasistatic Simulation (AQS) techniques have been introduced by [Maeda 1978, Kobayashi 1980, Maeda 1981] and used to determine the elastic constants of amorphous glasses materials by [Tanguy 2002,

Wittmer 2002, Maloney 2004, Lemaitre 2006, Maloney 2006]. In the current work, the AQS algorithm is used to assure that the system follows equilibrium trajectories. For each small pseudo time increment, δt , this algorithm consists to move affinely the atoms from previous state, and then to perform a minimization to find the nearest local minimum. Specifically, based on an equilibrium system, the AQS algorithm consists of the repeated alternating steps as follows :

- 1) Application of a small, homogeneous strain to all particles and simulation cell boundaries.

In our study, we suppose that the tensor $\mathbf{h}(t) = \{\mathbf{a}(t), \mathbf{b}(t), \mathbf{c}(t)\}$ is parameterized by a scalar, t , called pseudo time. The coordinates of all the atoms in the system as well as the simulation cell are changed by the deformation gradient tensor $\tilde{\mathbf{F}}(t)$ as $\mathbf{r}'_\alpha = \mathbf{r}_\alpha \tilde{\mathbf{F}}(t)$. The system potential energy, $\mathcal{U}(\{\mathbf{r}_\alpha\}, \tilde{\mathbf{F}})$ depends on the current position of particles, $\{\mathbf{r}_\alpha\}$, via the DREIDING potential but also on the shape of simulation box via the macroscopic deformation gradient tensor $\tilde{\mathbf{F}}$. In the initial reference configuration, the system are in equilibrium state, that means that potential energy, $\mathcal{U}(\{\mathbf{r}_\alpha^{(0)}\}, \tilde{\mathbf{F}} = \mathbf{I})$, is in a local minimum.

- 2) Minimization of the potential energy of all the particles in the simulation cell.

The conjugate gradient algorithm is utilized to realize the minimization process. The total potential energy can be reduced by moving each atom towards the direction of the force applied on it by the surrounding atoms. The relaxation iteration is repeated until both the average energy per atom \mathcal{U} and the maximum atom displacement $|\mathbf{u}_{max}| = \max |\mathbf{u}_\alpha|$ in each iteration step converge simultaneously within sufficient accuracy. Then the actual potential energy, $\mathcal{U}(\{\mathbf{r}_\alpha\}, \tilde{\mathbf{F}}(t))$ in the state of equilibrium, is in a local minimum.

The equilibrium trajectory imposes that force on particle α is always zero

$$\mathbf{f}_\alpha = -\partial_{\mathbf{r}_\alpha} \mathcal{U}(\{\mathbf{r}_\alpha\}, \tilde{\mathbf{F}}(t)) = \sum_{\beta \neq \alpha} \mathbf{f}_{\alpha\beta} = 0. \quad (4.31)$$

The pseudo velocity of α -th atom is estimated by backward finite difference approximation :

$$\mathbf{v}_\alpha(t) \approx \frac{\mathbf{r}_\alpha(t) - \mathbf{r}_\alpha(t - \delta t)}{\delta t}. \quad (4.32)$$

The AQS algorithm relies on the idea that in the absence of external loss, amorphous solids remain close to a mechanically stable state in a complex potential energy landscape. For molecular or metallic glasses, this assumption is reasonable as soon as the bath temperature is low compared to the glass transition temperature T_g . And another limitation of the AQS is that the strain rate must be small, which is far less than $1/\tau$, where τ characterizes the thermally activated escape of the system from a local minimum.

4.2.4 Polymer chain generation

There are many algorithms for generating the initial configuration of the polymer system, for example :

- Monte Carlo methods and its variants [Vacatello 2001], where the distributions of the states are sampled and the new state are given by Metropolis algorithm. It is the most relevant approach, but proved to be delicate for large systems.

- Random walk methods [Hossain 2010], which generally produce the configurations out of equilibrium, and are then combined with the relaxation techniques (*i.e.* Molecular dynamics) to obtain the equilibrated configuration.

- Hybrid method [Karayiannis 2002], where the Monte Carlo method is used first to explore the modifications for the conformation following with the relaxation algorithm by molecular dynamics.

Many algorithms for the preparation of initial system of polymer chain have been proposed on the basis of random walk method. The push off methods [Auhl 2003, Kremer 1990], based on two steps process : random Gaussian chain generation and equilibration, are very classical for polymerization. Since the chains are generated randomly in the simulation box without considering the interactions, which leads to a system far from the equilibrium, it will require long time to reach equilibrium. To bypass this difficulty, self avoiding random walk [Binder 1995, Sommer 2010] has been widely used in the literatures to generate the initial systems. The advantage of this method is the introduction of Lennard-Jones interactions which can avoid the spatially overlapping of the chains. Radical like polymerisation [Gao 1995, Perez 2008] has also been proved to be a very efficient tool to build the more complex polymer samples, which is divided in three stages : nucleation of the radicals, growth of the chains within a solvent of monomers and the termination.

Since the chains are progressively built in an interacting molecular dynamics solvent, the system can be equilibrated during the growth. Recently, a hierarchical backmapping strategy has been developed by Zhang *et al.* [Zhang 2014] to generate equilibrated high molecular weight polymer melts.

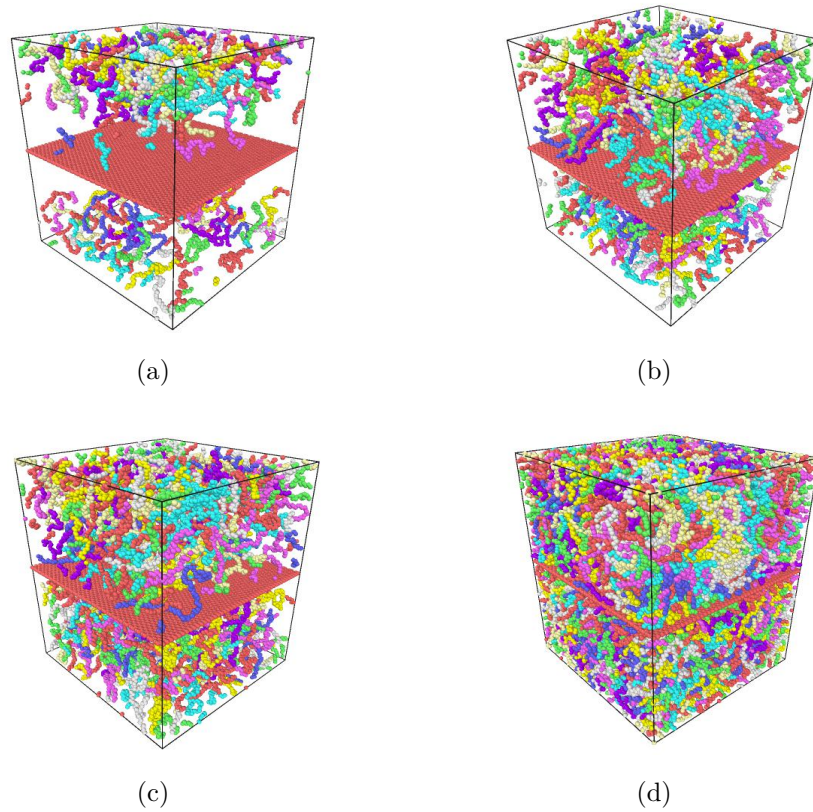


FIGURE 4.5 – Generation strategy of polymer chains of graphene reinforced nanocomposites. (a) 50 monomers have grown on each chain by self avoiding walk method, following by a relaxation by MD. (b) The growth of 50 more monomers on each chain based on the equilibrated system is shown. (c)-(d) Repeat the growth process until the equilibrated system of the nanocomposites is obtained. Colors are randomly chosen for different chains to get good visibility, and the layer of red points in the middle of the box is graphene platelet.

Based on the simple chemical structure of PE, the coarse-grained model [Arash 2015] is used in our work and the amorphous PE matrix is represented by the beads of united atom $-\text{CH}_2-$ units. The initial system is prepared from the self-avoiding random walk (see, *e.g.*, [Binder 1995] for review) combining

the molecular dynamics relaxation steps as introduced by [Gao 1995] and used by [Perez 2008] to generate homopolymer and copolymers, as shown in Fig. 4.5. Other methods may be used to construct an amorphous polymer (see, *e.g.*, [Baschnagel 2000, Haley 2015]).

The different steps of the algorithm are :

- (i) **Initialization** : the atoms inside the graphene sheet are arranged on the median plane ($z = 0$) of the simulation box.
- (ii) **Chain nucleation** : the first atom of each chain is randomly placed with a uniform probability density inside the box deprived of a layer of thickness of 2\AA and centered on the graphene sheet.
- (iii) **Chain growth** : all chains grow at each step of the random walk with the random order. The degrees of freedom associated with the hardest potentials are maintained at their equilibrium position, *i.e.* the distance between two atoms and the flexion angle between two bonds are fixed. Under these constraints, the possible positions of the next atoms are on a circle. The set of N_t trial positions $\{\mathbf{r}_{\alpha+1}\} = \{\mathbf{r}_{\alpha+1}^{(1)}, \dots, \mathbf{r}_{\alpha+1}^{(N_t)}\}$ are chosen with uniform distribution on this circle. The potential energy, $\mathcal{U}(\mathbf{r}_1, \dots, \mathbf{r}_\alpha, \mathbf{r}_{\alpha+1}^{(i)})$, for each trial position is computed. The position is randomly chosen with a probability distribution according to the Boltzmann weight

$$p(\mathbf{r}_{\alpha+1}^{(i)}) \propto \exp\left(-\frac{\mathcal{U}(\mathbf{r}_1, \dots, \mathbf{r}_\alpha, \mathbf{r}_{\alpha+1}^{(i)})}{k_b T}\right) \quad (4.33)$$

where k_b is the Boltzmann constant and the temperature $T = 300$ K. It interesting to note that the chains can grow from both extremities.

- (iv) **Chain relaxation** : an annealing is performed by a molecular dynamics simulation with Berendsen thermostat [Berendsen 1984] at the temperature of 700 K during 20 ps. The position of atoms in graphene sheet are freezed at the same position.

This relaxation step is performed when the chains are 50, 100, 150, 200, 250, 300, 350, 400, 450, 500 monomers after the algorithm come back to step (iii).

- (v) **Final relaxations and quenching** : after the chain growth, the system is then first relaxed at NpT ensemble via Nosé-Hoover [Martyna 1994, Shinoda 2004] at $T=700$ K and $p=0$ atm for 10000 fs and followed by

a cooling from 700 K to 200 K during 40000 fs. Then, a second NpT relaxation at T=200 K and p=0 atm for 20000 fs. An other relaxation during 20000 fs is performed at NVE ensemble. The last step is the quenching at 0 K by a minimization of the system potential energy.

4.3 Spatial description of continuum fields in atomistics

4.3.1 Murdoch-Hardy procedure

In this work, the Murdoch-Hardy procedure [Hardy 1982, Murdoch 1993, Hardy 2002] is described. The main point here is to identify the properties of continuum fields (*i.e.* mass density, stress, velocity) with local space averages of microscopic quantities (*i.e.* molecular masses, molecular stresses, molecular velocity). A physical interpretation of the Murdoch-Hardy procedure is that a measuring device with a finite size measures the quantities of interest at a point \mathbf{x} in Eulerian coordinate. This device is modeled by a scalar-valued weighting function $w(\mathbf{x})$ which defines a spatial averaging and satisfies the normalization condition

$$\int_{\mathbb{R}^3} w(\mathbf{x}) d\mathbf{x} = 1. \quad (4.34)$$

The masse density $\rho_w(\mathbf{x}, t)$ is defined as

$$\rho_w(\mathbf{x}, t) = \sum_{\alpha} m_{\alpha} w(\mathbf{r}_{\alpha}(t) - \mathbf{x}). \quad (4.35)$$

Here, the masse density $\rho_w(\mathbf{x}, t)$ must verify the continuity equation (conservation of mass) in the current configuration

$$\partial_t \rho_w + \nabla_{\mathbf{x}} \cdot (\rho_w \mathbf{v}_w) = 0, \quad (4.36)$$

where ∂_t . and $\nabla_{\mathbf{x}}$. denote the partial derivative with respect the time and the divergence operator with respect the spatial coordinate \mathbf{x} , respectively.

To satisfy the continuity equation (4.36), the velocity fields in the Eulerien description $\mathbf{v}_w(\mathbf{x}, t)$ is defined by [Murdoch 2012]

$$\mathbf{v}_w(\mathbf{x}, t) = \begin{cases} \frac{1}{\rho_w} \sum_{\alpha} m_{\alpha} \mathbf{v}_{\alpha}(t) w(\mathbf{r}_{\alpha}(t) - \mathbf{x}) & \text{if } \rho_w(\mathbf{x}, t) \neq 0 \\ \mathbf{0} & \text{otherwise.} \end{cases} \quad (4.37)$$

Following [Gremaud 2016], we introduce the displacement field defined in Eulerian coordinate, $\mathbf{u}_w(\mathbf{x}, t)$, which allows to rebuild the solid as it was at time $t = 0$, before the various translations, rotations and deformations it underwent, both in the absolute frame and in the mobile frame. The relation between the Eulerian displacement and velocity fields is

$$\mathbf{v}_w(\mathbf{x}, t) = -\frac{d\mathbf{u}_w}{dt}, \quad \text{or} \quad \partial_t \mathbf{u}_w = -\mathbf{v}_w \cdot (\mathbf{I} + \nabla_{\mathbf{x}} \mathbf{u}_w) \quad (4.38)$$

where \mathbf{I} is the unit second order tensor and $\nabla_{\mathbf{x}}$ the gradient operator with respect the spatial coordinate \mathbf{x} . The displacement field can be estimated by a finite difference approximation

$$\mathbf{u}_w(\mathbf{x}, t + \delta t) \approx \mathbf{u}_w(\mathbf{x}, t) - \delta t \mathbf{v}_w(\mathbf{x}, t + \delta t) \cdot (\mathbf{I} + \nabla_{\mathbf{x}} \mathbf{u}_w(\mathbf{x}, t)). \quad (4.39)$$

To the best of our knowledge, this is the first time in this work that the displacement field in Eulerian coordinate, $\mathbf{u}_w(\mathbf{x}, t)$ is used for the Murdoch-Hardy procedure.

Following [Admal 2010, Admal 2016b, Admal 2016a] the atomistic Cauchy stress tensor is decomposed in two terms the kinematics contribution, $\boldsymbol{\sigma}_{w,k}$, and the potential contribution, $\boldsymbol{\sigma}_{w,v}$, such as

$$\boldsymbol{\sigma}_w(\mathbf{x}, t) = \boldsymbol{\sigma}_{w,k}(\mathbf{x}, t) + \boldsymbol{\sigma}_{w,v}(\mathbf{x}, t) \quad (4.40)$$

where

$$\boldsymbol{\sigma}_{w,k}(\mathbf{x}, t) = -\sum_{\alpha} (\mathbf{v}_{\alpha}(t) - \mathbf{v}_w(\mathbf{x}, t)) \otimes (\mathbf{v}_{\alpha}(t) - \mathbf{v}_w(\mathbf{x}, t)) w(\mathbf{r}_{\alpha}(t) - \mathbf{x}). \quad (4.41)$$

Here, the kinematics contribution will be consider null because we assume that the stress measurement is carried out when the box shape does not change, *i.e.* for an instant t such as $\dot{\mathbf{h}}(t) = 0$, which implies $\mathbf{v}_w(\mathbf{x}, t) = \mathbf{0}$ for all \mathbf{x} and $\mathbf{v}_{\alpha} = \mathbf{0}$ for all α .

The potential contribution of atomistic Cauchy stress, $\boldsymbol{\sigma}_{w,v}$ satisfies the balance equation

$$\nabla_{\mathbf{x}} \cdot \boldsymbol{\sigma}_{w,v}(\mathbf{x}, t) = \sum_{\alpha} \mathbf{f}_{\alpha}(t) w(\mathbf{r}_{\alpha}(t) - \mathbf{x}). \quad (4.42)$$

The expression of $\boldsymbol{\sigma}_{v,w}$ is not unique, the most common one being

$$\boldsymbol{\sigma}_{v,w}(\mathbf{x}, t) = \frac{1}{2} \sum_{\alpha, \beta} \mathbf{f}_{\alpha\beta}(t) \otimes (\mathbf{r}_{\beta}(t) - \mathbf{r}_{\alpha}(t)) b_w(\mathbf{x}; \mathbf{r}_{\alpha}(t), \mathbf{r}_{\beta}(t)), \quad (4.43)$$

where $b_w(\mathbf{x}, \mathbf{r}_\alpha(t), \mathbf{r}_\beta(t))$ is the bond function expressed by

$$b_w(\mathbf{x}; \mathbf{r}_\alpha(t), \mathbf{r}_\beta(t)) = \int_0^1 w((1-s)\mathbf{r}_\alpha + s\mathbf{r}_\beta - \mathbf{x}) ds. \quad (4.44)$$

To assess the local conformation of polymer chains in the normal direction of graphene, the nematic order parameter s_w is defined by

$$s_w(\mathbf{x}) = \frac{1}{\rho_b(\mathbf{x})} \sum_{\text{Bond}^{(PE)}} \left(\frac{3(\mathbf{n}_{\alpha\beta} \cdot \mathbf{e}_z)^2 - 1}{2} \right) b_w(\mathbf{x}; \mathbf{r}_\alpha(t), \mathbf{r}_\beta(t)) \quad (4.45)$$

where $\text{Bond}^{(PE)}$ is the set of covalent bond in the polymer; \mathbf{e}_z is the unit normal of graphene; $\mathbf{n}_{\alpha\beta} = (\mathbf{r}_\alpha - \mathbf{r}_\beta)/r_{\alpha\beta}$ is the unit vector which defines the covalent bond direction between two CH_2 atom group α and β along the polymer chain and $\rho_b(\mathbf{x}) = \sum_{\text{Bond}^{(PE)}} b_w(\mathbf{x}; \mathbf{r}_\alpha(t), \mathbf{r}_\beta(t))$ is a normalization constant which corresponds to the local bond density at \mathbf{x} .

4.3.2 Analysis of the molecular configuration

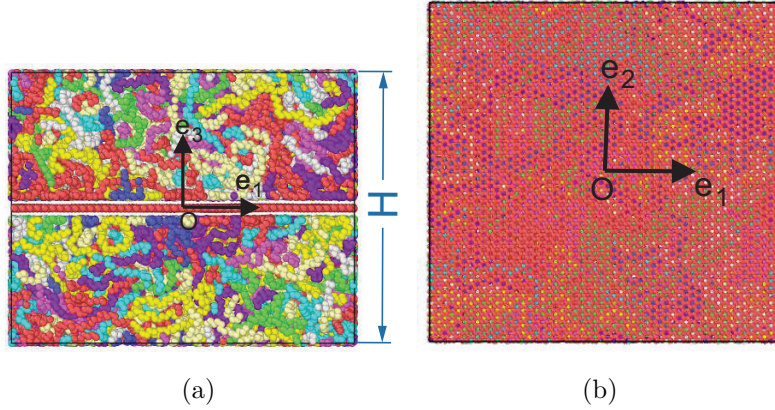


FIGURE 4.6 – Graphene/PE nanocomposite with sandwich structure under periodical boundary condition, single layer graphene is located in the middle of the box.

We have generated a sandwich structure in rectangular box under periodical boundary condition with 40 PE chains. Each PE chain contains 500 CH_2 units. The length, $L_x = 100.8\text{\AA}$, and width, $L_y = 94.57\text{\AA}$, of box is fixed to have 25×38 crystal lattice in graphene sheet, the thickness H depends on the number of PE chains. The origin of absolute referential, $\mathcal{R}_{Euler}(O, \mathbf{e}_1, \mathbf{e}_2, \mathbf{e}_3)$,

in the Eulerian specification is the center of the graphene sheet and its orientation is defined such that \mathbf{e}_3 is normal to the graphene and the triangles in the graphene hexagonal lattice pointing along the \mathbf{e}_1 direction (see Fig. 4.6).

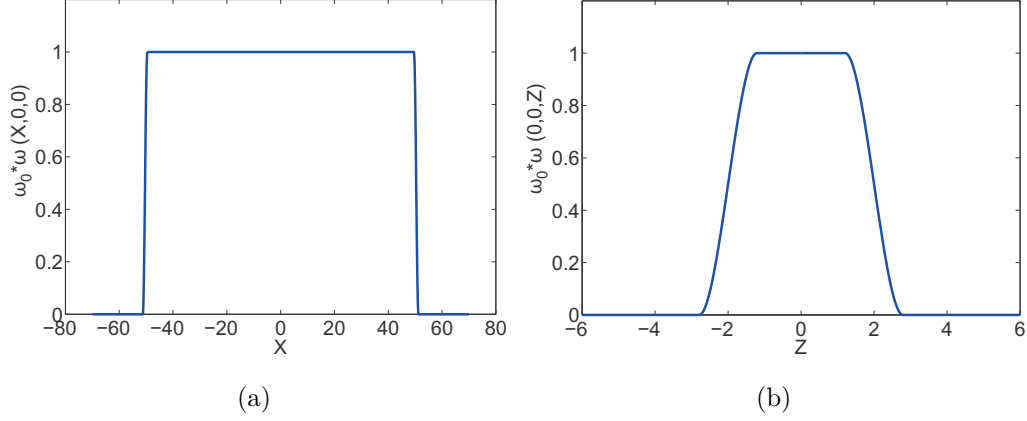


FIGURE 4.7 – Profiles for weighting function a) along \mathbf{e}_1 and b) along \mathbf{e}_3

Here, we want to probe the topological and mechanical properties as a function of the z distance from the graphene sheet. For that reason an anisotropic measuring device with rectangular cuboid shape is used such with lengths $l_1^w = L_x$, $l_2^w = L_y$ and $l_3^w = 4\text{\AA}$. We assume that the measure is uniform for all points in the cuboid and that the atoms occupy a small sphere of radius $r^w = 0.79\text{\AA}$ to regularize the weighting function $w(\mathbf{x})$. Under these assumptions, the weighting function is defined by a convolution product

$$w(\mathbf{x}) = \frac{1}{w_0} \int_{\Omega} f^{(Cub)}(\mathbf{x} - \mathbf{x}') f^{(Sph)}(\mathbf{x} - \mathbf{x}') d\mathbf{x}' \quad (4.46)$$

where w_0 is the normalization constant given by equation (4.34) and $f^{(Cub)}$ and $f^{(Sph)}$ are the characteristic function of the cuboid and sphere respectively given by

$$f^{(Sph)}(\mathbf{x}) = 1 - H(|\mathbf{x}| - r^w) \quad (4.47)$$

$$f^{(Cub)}(\mathbf{x}) = \prod_{i=1}^3 \left(1 - H\left(\left|\mathbf{x} \cdot \mathbf{e}_i - \frac{l_i^w}{2}\right|\right) \right) \quad (4.48)$$

where $H(x)$ denotes the Heaviside step function. The representation of weighting function along \mathbf{e}_1 and \mathbf{e}_3 is shown in Fig. 4.7.

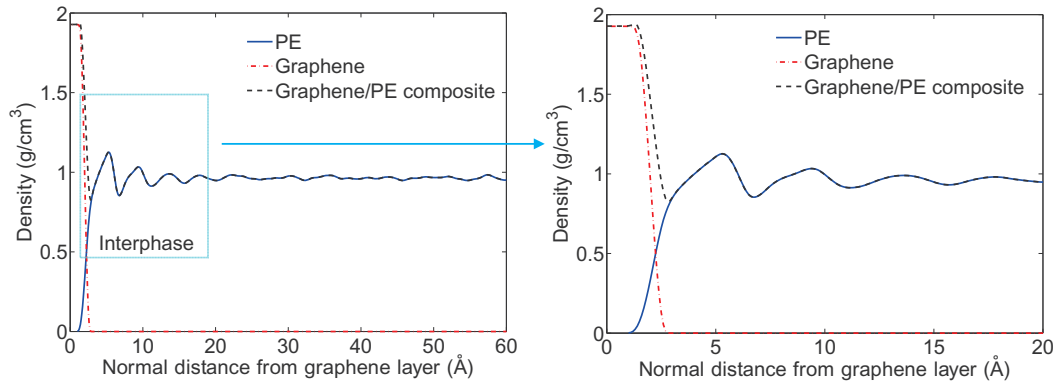


FIGURE 4.8 – Local mass density normal to a graphene sheets of a fully relaxed graphene/PE sandwich structure nanocomposites at undeformed state.

Fig. 4.8 shows the local density of graphene, PE and composite system for a sandwich structure with $h = 106\text{\AA}$ as a function of the z distance from the graphene sheet. We can see a dense packing of PE mass close to graphene layer called interphase zone, which is due to the adsorption of the PE chains on both the two faces of graphene sheets. On each side of graphene, the thickness of the interphase is around 2 nm. The density of the graphene/PE composite with sandwich structure is dominated by the density of graphene in the midplane and by the density of polymer for the rest part.

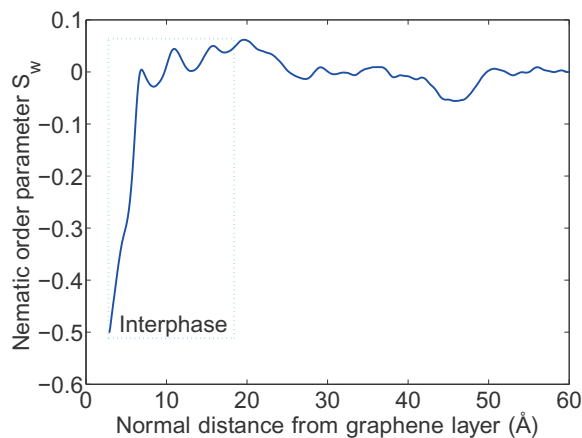


FIGURE 4.9 – Nematic order parameter of the polymer as a function of the normal distance from graphene layer.

Fig. 4.9 represents the nematic order parameter s_w for polymer bond. We can see a decrease in the interphase part which also presents a thickness of

around 2 nm. Generally, the nematic order s is used to describe the orientational order of a nematic liquid crystal. For a completely random and isotropic sample, $s=0$, whereas for a perfectly aligned sample along z axis, $s=1$. In addition, $s = -1/2$ denotes that all the bonds are in the plane perpendicular to z . Therefore, it indicates that in the interfacial zone next to the graphene sheets, the chains of the polymer can not fully extended and turn to be more paralleled to the graphene layer.

4.3.3 Analysis of local mechanical fields

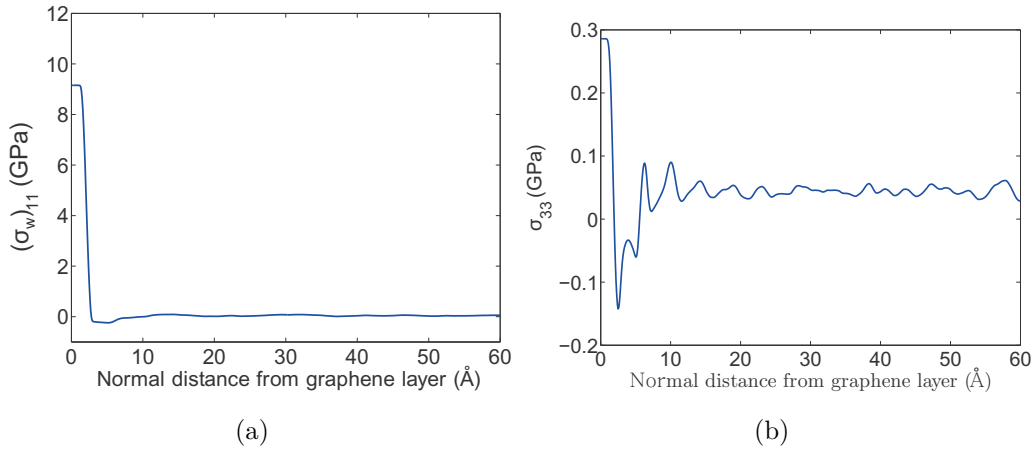


FIGURE 4.10 – Evolution of initial Cauchy stress fields components along the normal of graphene layer \mathbf{e}_3 . (a) $(\sigma_w)_{11}$ (b) $(\sigma_w)_{33}$ vs z for an elongation along \mathbf{e}_1 .

The initial Cauchy stress fields components of the sandwich structure, $(\sigma_w)_{11}$ and $(\sigma_w)_{33}$, are shown in Fig. 4.10 as a function of z -distance from the middle-layer graphene sheet. It can be noticed that for both components of the stress field, the stress concentration occurs close to the graphene layer, and that the local stress presents a decrease at the interphase region and finally converges to a certain value in the polymer matrix region. The residual stress comes from the quenching from 200K to 0K during the sample processing.

Fig. 4.11 represents the normal component of displacement fields along the normal of graphene layer at an elongation of 0.3% along \mathbf{e}_3 , where the left and right figures denote to $\mathbf{u}_w^{(2)} \cdot \mathbf{e}_3$ obtained by the averaging of the displacements of each atom and to $\mathbf{u}_w \cdot \mathbf{e}_3$ obtained by our new estimation in Eq. (4.38),

respectively. The displacement $\mathbf{u}_w^{(2)}$ is given by

$$\mathbf{u}_w^{(2)}(\mathbf{x}, t) = \frac{1}{N^w} \sum_{\alpha} (\mathbf{r}_{\alpha}(t) - \mathbf{r}_{\alpha}^{(0)}), \quad N^w \text{ is the number of atoms in each slice.} \quad (4.49)$$

It is obvious that the simple displacement averaging can not lead to the proper displacement fields. As in the left figure of Fig. 4.11, the magnitude of the displacement is not in good agreement with actual deformation, and the opposite number of the curve tangent which corresponds to the strain tensor component ε_{33} is 0.0054%, far from the effective strain of 0.3%, while the estimation of displacement by Eq. (4.38) shows a good agreement. As shown in the right figure of Fig. 4.11, at an elongating of 0.3% along \mathbf{e}_3 , the local strain along \mathbf{e}_3 , ε_{33} , is estimated as the opposite of the tangent of the curve, which is about 0.23% at the interphase region, and turns to 0.32% for the polymer matrix part.

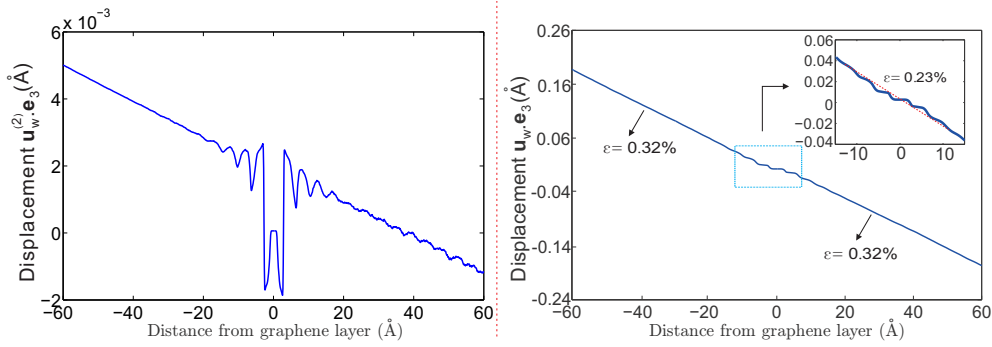


FIGURE 4.11 – Component of the Eulerian displacement $\mathbf{u}_w \cdot \mathbf{e}_3$ along the normal of graphene layer \mathbf{e}_3 for an elongation along \mathbf{e}_3 . The left figure represents the results by simple averaging the displacements of each atom, and the right figure shows the results obtained by Eq. 4.38.

In addition, in the shear elongation case in the plane of \mathbf{e}_1 and \mathbf{e}_3 at $\varepsilon_{13} = 3\%$, local displacement fields component $\mathbf{u}_w \cdot \mathbf{e}_1$ along the normal distance from graphene layer is shown in Fig. 4.12. A sharp decrease of $\mathbf{u}_w \cdot \mathbf{e}_1$ can be seen at the middle layer, which indicates the slipping at the interface between graphene and polymer and thus demonstrates that the shear strength between graphene and polymer matrix is extremely low.

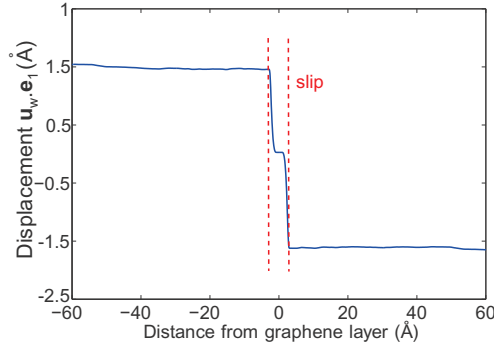


FIGURE 4.12 – Component of the Eulerian displacement $\mathbf{u}_w \cdot \mathbf{e}_1$ along the normal of graphene layer \mathbf{e}_3 for a simple shear elongation along $\varepsilon_{13} = 3\%$.

4.4 Continuum modeling of thin interphases as imperfect interfaces

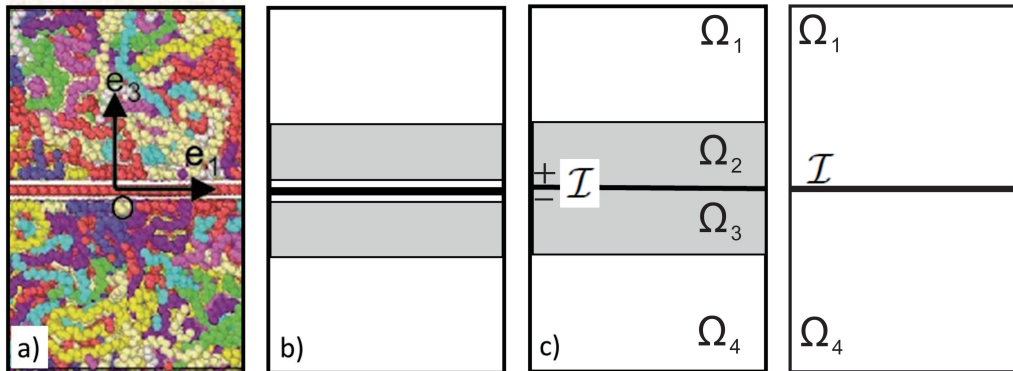


FIGURE 4.13 – a) Atomistic configuration; b) 7 layer continuum model; c) Continuum model with imperfect interface and interphases (Model I); d) Continuum model with single equivalent imperfect interface (Model II).

For the continuum point of view, the polymer/graphene nanocomposite can be modeled by a seven layer composite : the central layer for graphene, two thin layer for the interfacial part between graphene and polymer; two layers for interphase and two layer for polymer bulk see Fig. 4.13 (b). The thickness of the three central layers suggest that they can be replaced by one imperfect interface to take into account the elasticity of graphene and the jump displacement that we have shown in the previous section 4.3.3. This model is

denoted by model I (see in Fig. 4.13 (c)). Making use of an equivalent imperfect interface to replace the graphene sheet, the interface region and the interphase region, Model II is proposed as shown in Fig. 4.13 (d). Another naive model is also proposed in which the interphase and interface are neglected and only the stiffnesses of pure polymer and graphene sheet are included, denoted by Model III (see in Fig. 4.13 (d) when \mathcal{I} represents only the graphene layer). In the first part of this section, the imperfect interfaces framework is presented. Then, the identification procedure of the elastic properties of bulk polymer, interphase and interface is discussed.

4.4.1 Imperfect interfaces framework

The purpose of this section is to establish the equations governing continua embedding general interface for the model I (see Figure 4.13c). In this section, we assume infinitesimal displacement and linear behavior for the sake of simplicity. The interface unit normal of the interface \mathcal{I} is \mathbf{e}_3 .

The displacement in the body is denoted by $\mathbf{u}(\mathbf{x})$ and the displacement jump, $[[\mathbf{u}]]$, across the interface \mathcal{I} is defined by

$$[[\mathbf{u}]] = \mathbf{u}|_{\mathcal{I}}^+ - \mathbf{u}|_{\mathcal{I}}^-, \quad (4.50)$$

where $\mathbf{u}|_{\mathcal{I}}^+$ and $\mathbf{u}|_{\mathcal{I}}^-$ are the values of displacement in the upper and lower surfaces of interface \mathcal{I} respectively .

The displacement field, \mathbf{u}^s , inside the interface \mathcal{I} is defined as the median value

$$\mathbf{u}^s(\mathbf{x}) = \frac{1}{2} \left(\mathbf{u}|_{\mathcal{I}}^+ + \mathbf{u}|_{\mathcal{I}}^- \right), \quad \forall \mathbf{x} \in \mathcal{I}. \quad (4.51)$$

The infinitesimal strain tensor in the bulk is defined by

$$\boldsymbol{\varepsilon}(\mathbf{x}) = \frac{1}{2} \left(\nabla \mathbf{u}(\mathbf{x}) + \nabla \mathbf{u}^T(\mathbf{x}) \right), \quad \forall \mathbf{x} \in \Omega_{(i)}, \quad (4.52)$$

and the infinitesimal strain tensor on the interface is defined by

$$\boldsymbol{\varepsilon}^s(\mathbf{x}) = \mathbf{P} \boldsymbol{\varepsilon} \mathbf{P}, \quad \forall \mathbf{x} \in \mathcal{I} \quad (4.53)$$

where ∇ is the gradient operator and $\nabla^s = \mathbf{P} \cdot \nabla$ is the interface gradient operator and $\mathbf{P} = \mathbf{I} - \mathbf{e}_3 \otimes \mathbf{e}_3$ is the projector onto the interface \mathcal{I} .

In absence of external force densities in bulk and in interface, the balance equation are

$$\nabla \cdot \boldsymbol{\sigma} = \mathbf{0} \quad \forall \mathbf{x} \in \Omega_{(i)} \quad (4.54)$$

$$\nabla^s \cdot \boldsymbol{\sigma}^s + \llbracket \mathbf{t} \rrbracket = \mathbf{0} \quad \forall \mathbf{x} \in \mathcal{I} \quad (4.55)$$

where $\nabla \cdot$ is the divergence operator; $\nabla^s \cdot \{ \cdot \} = \nabla \{ \cdot \} : \mathbf{P}$ is the interface divergence operator; $\boldsymbol{\sigma}^s$ the interfacial stress and $\llbracket \mathbf{t} \rrbracket$ is the traction vector jump across the interface defined by

$$\llbracket \mathbf{t} \rrbracket = \llbracket \boldsymbol{\sigma} \cdot \mathbf{e}_3 \rrbracket = \left(\boldsymbol{\sigma}|_{\mathcal{I}}^+ - \boldsymbol{\sigma}|_{\mathcal{I}}^- \right) \cdot \mathbf{e}_3. \quad (4.56)$$

We assume the existence of a bulk free energy densities $\phi(\boldsymbol{\varepsilon})$ and an interfacial free energy density $\phi^s(\boldsymbol{\varepsilon}^s, \llbracket \mathbf{u} \rrbracket)$ in the bulk and the interface respectively, such as the behavior laws derive from them

$$\boldsymbol{\sigma} = \partial_{\boldsymbol{\varepsilon}} \phi \quad \forall \mathbf{x} \in \Omega_{(i)} \quad (4.57)$$

$$\boldsymbol{\sigma}^s = \partial_{\boldsymbol{\varepsilon}^s} \phi^s \quad \forall \mathbf{x} \in \mathcal{I} \quad (4.58)$$

$$\mathbf{t}^s = \partial_{\llbracket \mathbf{u} \rrbracket} \phi^s \quad \forall \mathbf{x} \in \mathcal{I} \quad (4.59)$$

where \mathbf{t}^s denotes the average traction across the interface, defined by

$$\mathbf{t}^s = \frac{1}{2} \left(\boldsymbol{\sigma}|_{\mathcal{I}}^+ + \boldsymbol{\sigma}|_{\mathcal{I}}^- \right) \cdot \mathbf{e}_3 \quad (4.60)$$

Under the assumptions of standard linear elastic behavior with internal stresses, the both free energy are given by

$$\phi(\boldsymbol{\varepsilon}) = \frac{1}{2} \boldsymbol{\varepsilon} : \mathbb{C}_{(i)} : \boldsymbol{\varepsilon} + \boldsymbol{\tau}(\mathbf{x}) : \boldsymbol{\varepsilon} + \phi_0 \quad \forall \mathbf{x} \in \Omega_{(i)} \quad (4.61)$$

$$\phi^s(\boldsymbol{\varepsilon}^s, \llbracket \mathbf{u} \rrbracket) = \frac{1}{2} \boldsymbol{\varepsilon}^s : \mathbb{C}^s : \boldsymbol{\varepsilon}^s + \boldsymbol{\tau}^s : \boldsymbol{\varepsilon}^s + \frac{1}{2} \llbracket \mathbf{u} \rrbracket \cdot \mathbf{K}^s \cdot \llbracket \mathbf{u} \rrbracket + \phi_0^s \quad \forall \mathbf{x} \in \mathcal{I} \quad (4.62)$$

where $\mathbb{C}_{(i)}$ is the fourth-order symmetric stiffness tensor of layer $\Omega_{(i)}$; \mathbb{C}^s is the fourth-order symmetric interfacial stiffness tensors; $\boldsymbol{\tau}$ is the internal stresses in the bulk and $\boldsymbol{\tau}^s$ is the internal surface stress; ϕ_0 and ϕ_0^s are the free energies of bulk and interface under zero strain and zero jump displacement; and \mathbf{K}^s is the second-order positive symmetric tensor which corresponds to the cohesive stiffness of interface.

4.4.2 Parameters identification

4.4.2.1 Identification of local elastic parameters in polymer bulk

Using the Murdoch-Hardy procedure which was presented in section 4.3.1, a Cauchy stress field, $\boldsymbol{\sigma}_w$, and a continuous displacement field $\mathbf{u}_w^{(E)}$ can be defined. Under infinitesimal displacement assumption, the initial and final configuration can be considered as the same, therefore a displacement field $\mathbf{u}_w = -\mathbf{u}_w^{(E)}(\mathbf{x})$ can be defined as the opposite of the Eulerian displacement field. An infinitesimal strain tensor, $\boldsymbol{\varepsilon}_w$, is defined using the following centered finite difference approximation of the spatial derivative of displacement field

$$\partial_{x_i} \mathbf{u}_w(\mathbf{x}) \approx \frac{\mathbf{u}_w(\mathbf{x} + \delta x \mathbf{e}_i) - \mathbf{u}_w(\mathbf{x} - \delta x \mathbf{e}_i)}{2\delta x}, \quad \text{for } i \in \{1, 2, 3\}. \quad (4.63)$$

Elongation and simple shear are prescribed to the molecular box to identify the elastic tensor $\mathbb{C}(\mathbf{x})$ on each point of polymer. Under infinitesimal strain assumption, the box shape is defined by the effective infinitesimal strain tensor $\tilde{\boldsymbol{\varepsilon}}$. The displacement on the boundary of the box is given by

$$\mathbf{u} = \tilde{\boldsymbol{\varepsilon}} \mathbf{x}, \quad \text{for } \mathbf{x} \in \partial\Omega. \quad (4.64)$$

The choice of an anisotropic weight function impose that the stress field and strain field for these deformations of molecular box depend only of the coordinate z along \mathbf{e}_3 axis. Moreover, the components of local infinitesimal strain into the plan $(\mathbf{e}_1, \mathbf{e}_2)$, are equal to the corresponding components of the effective infinitesimal strain tensor

$$\mathbf{P} \cdot \boldsymbol{\varepsilon}_w(\mathbf{x}) \cdot \mathbf{P} = \mathbf{P} \cdot \tilde{\boldsymbol{\varepsilon}} \cdot \mathbf{P}, \quad \forall \mathbf{x} \in \Omega_{(i)} \quad (4.65)$$

For an elongation along \mathbf{e}_1 , $\tilde{\boldsymbol{\varepsilon}} = \tilde{\varepsilon}_1 \mathbf{e}_1 \otimes \mathbf{e}_1$, the local strain deformation which is orthogonal to the plan $(\mathbf{e}_1, \mathbf{e}_2)$ is negligible $(\boldsymbol{\varepsilon}_w)_{i3} \ll (\boldsymbol{\varepsilon}_w)_{11} = \tilde{\varepsilon}_1$ for $i = \{1, 2, 3\}$. Moreover, the equation (4.65) imposes that $(\boldsymbol{\varepsilon}_w)_{22} = (\boldsymbol{\varepsilon}_w)_{12} = \tilde{\varepsilon}_6 = 0$, so that the local stress increment is given by

$$\Delta \boldsymbol{\sigma}_w(\mathbf{x}) = \boldsymbol{\sigma}_w(\mathbf{x}) - \boldsymbol{\sigma}_w^{(0)}(\mathbf{x}) = \mathbb{C}(\mathbf{x}) : \tilde{\varepsilon}_1 \mathbf{e}_1 \otimes \mathbf{e}_1 \quad (4.66)$$

where $\boldsymbol{\sigma}_w^{(0)}(\mathbf{x})$ is the internal stresses which are computed on the undeformed molecular box ($\tilde{\boldsymbol{\varepsilon}} = \mathbf{0}$). Then, the following components of the stiffness tensor in a classical Voigt notation are obtained by

$$\mathbb{C}_{I1}(\mathbf{x}) = \frac{(\Delta \boldsymbol{\sigma}_w)_I(\mathbf{x})}{\tilde{\varepsilon}_1} \quad (4.67)$$

The results are similar for the other effective deformations into the plan ($\mathbf{e}_1, \mathbf{e}_2$)

$$\mathbb{C}_{I2}(\mathbf{x}) = \frac{(\Delta\boldsymbol{\sigma}_w)_I(\mathbf{x})}{\tilde{\varepsilon}_2} \quad \text{for } \tilde{\boldsymbol{\varepsilon}} = \tilde{\varepsilon}_2 \mathbf{e}_2 \otimes \mathbf{e}_2 \quad (4.68)$$

$$\mathbb{C}_{I6}(\mathbf{x}) = \frac{(\Delta\boldsymbol{\sigma}_w)_I(\mathbf{x})}{\tilde{\varepsilon}_6} \quad \text{for } \tilde{\boldsymbol{\varepsilon}} = \tilde{\varepsilon}_6 \frac{1}{2} (\mathbf{e}_1 \otimes \mathbf{e}_2 + \mathbf{e}_2 \otimes \mathbf{e}_1) \quad (4.69)$$

This post processing have shown that $\forall \mathbf{x} \mathbb{C}_{11}(\mathbf{x}) \approx \mathbb{C}_{22}(\mathbf{x})$, $\mathbb{C}_{31}(\mathbf{x}) \approx \mathbb{C}_{32}(\mathbf{x})$, $\mathbb{C}_{21}(\mathbf{x}) \approx \mathbb{C}_{12}(\mathbf{x})$ and $\forall I \geq 4 \mathbb{C}_{I1}(\mathbf{x}) \approx \mathbb{C}_{I2}(\mathbf{x}) \approx 0$; and $\forall I < 6 \mathbb{C}_{I6}(\mathbf{x}) \approx 0$. The Figures 4.14 show the evolution of \mathbb{C}_{11} , \mathbb{C}_{12} , \mathbb{C}_{13} and \mathbb{C}_{66} with the distance to the graphene z . A substantial increase of stiffness components is shown for $z < 2\text{\AA}$ due to graphene sheet. In the interphase area, $2\text{\AA} \leq z \leq 12\text{\AA}$ where $s_w < 0$, the stiffness components is 40% higher than in the bulk part $z \geq 12\text{\AA}$ where $s_w \approx 0$.

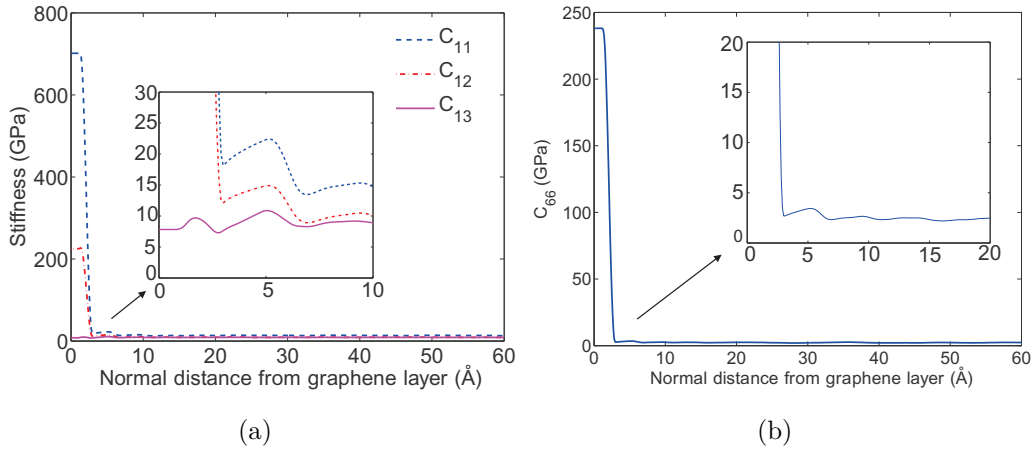


FIGURE 4.14 – Evolution of stiffness tensor components along the normal of graphene layer \mathbf{e}_3 . (a) \mathbb{C}_{11} , \mathbb{C}_{12} , \mathbb{C}_{13} vs z ; (b) \mathbb{C}_{66} vs z .

For an elongation normal to \mathbf{e}_3 , $\tilde{\boldsymbol{\varepsilon}} = \tilde{\varepsilon}_3 \mathbf{e}_3 \otimes \mathbf{e}_3$, only the strain ε_{33} has a significant value so that the components \mathbb{C}_{I3} of the stiffness tensor are given by

$$\mathbb{C}_{I3}(\mathbf{x}) = \frac{(\Delta\boldsymbol{\sigma}_w)_I(\mathbf{x})}{\tilde{\varepsilon}_3}. \quad (4.70)$$

Fig. 4.15 shows the evolution of \mathbb{C}_{33} with the distance to the graphene z . It shows that in the interphase area, $2\text{\AA} \leq z \leq 12\text{\AA}$, \mathbb{C}_{33} is almost 1.5 times higher than in the polymer matrix area where $z \geq 12\text{\AA}$. Overall, the thickness of the interphase region which has various stiffness from the pure polymer is

supposed to be 12 Å, smaller than the one we defined from the view of local density which is around 2 nm.

Due to the slip at the polymer/graphene interface, the local strain, $\boldsymbol{\varepsilon}_w(\mathbf{x})$ and the local stress increment, $\Delta\boldsymbol{\sigma}_w(\mathbf{x})$, in the polymer remains zero for all shears in the graphene plane. It is therefore impossible to identify with this method the stiffness tensor components C_{I4} and C_{I5} . For convenient reasons, we assume that $C_{44}(\mathbf{x}) = C_{55}(\mathbf{x}) = C_{66}(\mathbf{x})$. In the polymer, other components $C_{I4}(\mathbf{x}) = C_{I5}(\mathbf{x}) = 0$.

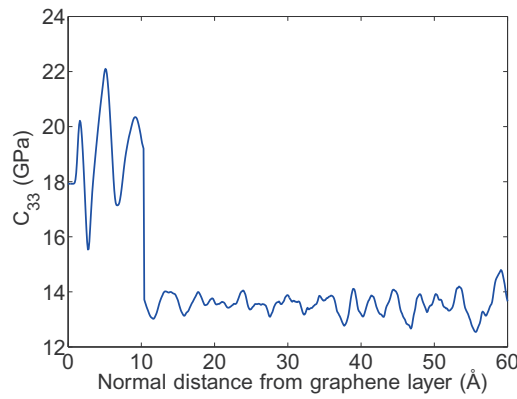


FIGURE 4.15 – Evolution of the stiffness tensor component C_{33} along the normal of graphene layer \mathbf{e}_3 .

4.4.2.2 Identification of interface parameters

Interfaces can be categorized into four models according to their kinematic or kinetic characteristics as shown in Fig. 4.16.

For the identification of interface parameters, we write the surface free energy ϕ^s as the sum of three contributions as shown in Fig. 4.17 : one for the graphene and two for the interfaces polymer/graphene. Therefore, the three layers description of the imperfect interface is used. Following the classification in above, the graphene layer can be considered like an elastic interface, denoted by $s2$, *i.e.* it is kinematically coherent ($[[\mathbf{u}]]|_{s2} = \mathbf{0}$) but kinetically non-coherent ($[[\mathbf{t}]]|_{s2} \neq \mathbf{0}$). The free energy of $s2$ is defined by

$$\phi^{s2} = \frac{1}{2} \boldsymbol{\varepsilon}^{s2} : \mathbb{C}^{s2} : \boldsymbol{\varepsilon}^{s2} + \boldsymbol{\tau}^{s2} : \boldsymbol{\varepsilon}^{s2} + \phi_0^{s2} \quad (4.71)$$

where \mathbb{C}^{s2} is the fourth order surface stiffness tensor of graphene, $\boldsymbol{\tau}^{s2}$ is the internal surface stress and $\boldsymbol{\varepsilon}^{s2}$ is the surface strain tensor into the graphene

sheet.

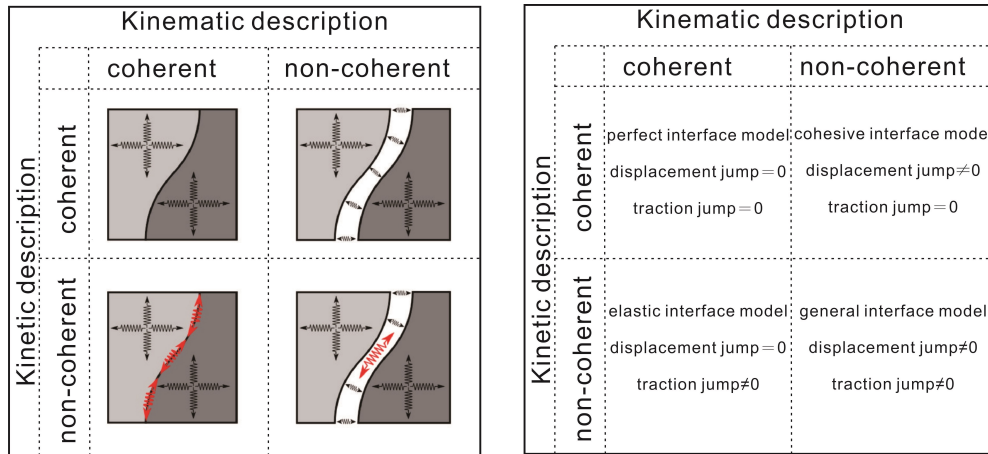


FIGURE 4.16 – An overview of interface models. Graphical illustration (left) and mathematical explanation (right). From the viewpoint of continuum mechanics, interfaces can be divided into four categories depending on their kinematic or kinetic characteristics. The elastic interface model does not allow for the displacement jump, but the traction may suffer a jump across the interface. The cohesive interface model on the contrary, allows for the displacement jump but assumes the continuity of the traction field across the interface. The intersection of elastic and cohesive interface model is the perfect interface model for which both the traction and displacement across the interface are continuous. This contribution formulates the general interface model which encompasses all other interface types. Reproduced from [Chatzigeorgiou 2017].

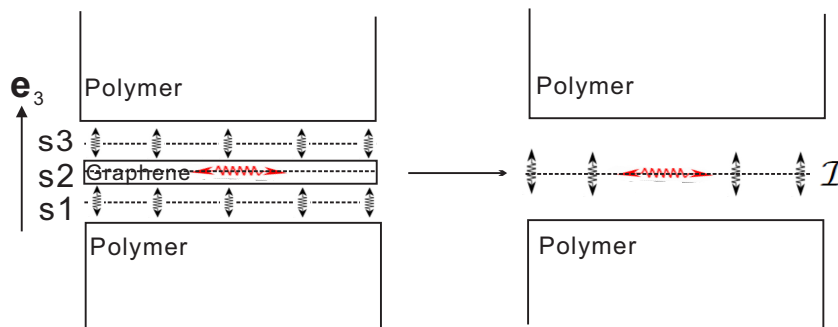


FIGURE 4.17 – Scheme of the three layers of the imperfect interface \mathcal{I} .

The graphene/polymer interfacial regions can be considered like cohesive interfaces, denoted $s1$ and $s3$, *i.e.* it is kinematically non-coherent ($[[\mathbf{u}]]|_{s1} \neq \mathbf{0}$

and $[[\mathbf{u}]]|_{s3} \neq \mathbf{0}$) but kinetically coherent ($[[\mathbf{t}]]|_{s1} = [[\mathbf{t}]]|_{s3} = \mathbf{0}$). The cohesive laws for interface $s1$ and $s3$ is

$$\boldsymbol{\sigma}|_{s1} \cdot \mathbf{e}_3 = \mathbf{K}^{s1} [[\mathbf{u}]]|_{s1}, \quad \boldsymbol{\sigma}|_{s3} \cdot \mathbf{e}_3 = \mathbf{K}^{s3} [[\mathbf{u}]]|_{s3} \quad (4.72)$$

where \mathbf{K}^{s1} and \mathbf{K}^{s3} are the second order cohesive stiffness matrix of the interface $s1$ and $s3$. The free energy of $s1$ and $s3$ are defined by

$$\phi^{s1} = \frac{1}{2} [[\mathbf{u}]]|_{s1} \cdot \mathbf{K}^{s1} \cdot [[\mathbf{u}]]|_{s1} + \phi_0^{s1}, \quad \phi^{s3} = \frac{1}{2} [[\mathbf{u}]]|_{s3} \cdot \mathbf{K}^{s3} \cdot [[\mathbf{u}]]|_{s3} + \phi_0^{s3} \quad (4.73)$$

where $\phi_0^s = \phi_0^{s1} + \phi_0^{s2} + \phi_0^{s3}$.

The kinematic compatibility across the graphene sheet $s2$ enforces that the jump of displacement field in the equivalent imperfect interface are

$$[[\mathbf{u}]] = \mathbf{u}|_{s3}^+ - \mathbf{u}|_{s1}^- = (\mathbf{u}|_{s3}^+ - \mathbf{u}^g) + (\mathbf{u}^g - \mathbf{u}|_{s1}^-) = [[\mathbf{u}]]|_{s1} + [[\mathbf{u}]]|_{s3}. \quad (4.74)$$

‘+’ and ‘-’ correspond to the upper and lower surface of the interface with respect to the normal direction \mathbf{e}_3 . The results of atomistic simulations suggest that the displacement jumps across interface $s1$ and $s3$ are equal. For the sake of simplicity, we assume that $[[\mathbf{u}]]|_{s1} = [[\mathbf{u}]]|_{s3} = [[\mathbf{u}]]/2$, which implies that the displacement field, \mathbf{u}^g ($\mathbf{u}^g = \mathbf{u}|_{s2}^+ = \mathbf{u}|_{s2}^- = \mathbf{u}|_{s1}^+ = \mathbf{u}|_{s3}^-$), and the strain fields, $\boldsymbol{\varepsilon}^{s2}$, on the graphene sheet are given by

$$\mathbf{u}^g = \frac{\mathbf{u}|_{s3}^+ + \mathbf{u}|_{s1}^-}{2}, \quad \boldsymbol{\varepsilon}^{s2}(\mathbf{x}) = \frac{1}{2} \left(\nabla^s \mathbf{u}^g(\mathbf{x}) + (\nabla^s \mathbf{u}^g)^T(\mathbf{x}) \right). \quad (4.75)$$

Remind that the cohesive law for the equivalent imperfect interface

$$\mathbf{K}^s [[\mathbf{u}]] = \mathbf{t}^s = \frac{(\boldsymbol{\sigma}|_{s1} + \boldsymbol{\sigma}|_{s3}) \cdot \mathbf{e}_3}{2}, \quad (4.76)$$

introducing the cohesive laws of the interface $s1$ and $s3$ and using the equality of jump displacement across $s1$ and $s3$, we obtain

$$\mathbf{K}^s = \frac{1}{4} (\mathbf{K}^{s1} + \mathbf{K}^{s3}) = \frac{1}{2} \mathbf{K}^{s1} = \frac{1}{2} \mathbf{K}^{s3}. \quad (4.77)$$

The two last equality come from the mirror symmetry of the system with respect to the graphene plane which implies that $\mathbf{K}^{s1} = \mathbf{K}^{s3}$.

The additivity of specific free energy and the equation (4.77) gives

$$\phi^s = \phi^{s1} + \phi^{s2} + \phi^{s3} \quad (4.78)$$

$$\phi^s = [[\mathbf{u}]]|_{s1} \cdot \mathbf{K}^s \cdot [[\mathbf{u}]]|_{s1} + \frac{1}{2} \boldsymbol{\varepsilon}^s : \mathbb{C}^{s2} : \boldsymbol{\varepsilon}^s + [[\mathbf{u}]]|_{s3} \mathbf{K}^s \cdot [[\mathbf{u}]]|_{s3} + \phi_0^s. \quad (4.79)$$

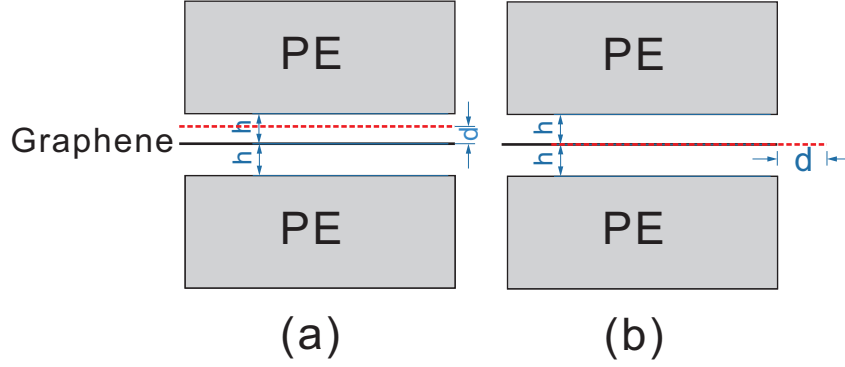


FIGURE 4.18 – a) Scheme of graphene sheet translation along \mathbf{e}_3 ; b) Graphene sheet translation along \mathbf{e}_1 .

After establishing the new expression of specific free energy of the imperfect interface, ϕ^s , the identification of stiffness tensor \mathbf{K}^s is detailed. At atomic scale we impose elementary rigid body motions of graphene sheet, d , along the direction \mathbf{e}_i (see Fig. 4.18). The polymer atoms displacements are kept fixed so that the variation of potential energy is only due to the displacement discontinuity at the interface. Assuming that the temperature is 0 K in our simulations, the variation of free energy for a translation $d\mathbf{e}_i$ of graphene is given by the variation of potential energy

$$\Delta\mathcal{U} = \langle \phi - \phi^{(0)} \rangle = \int_{\Omega} \phi - \phi_0 \, d\Omega + \int_{\mathcal{I}} \phi^s - \phi_0^s \, dS \quad (4.80)$$

$$= S \left(\llbracket \mathbf{u} \rrbracket |_{s1} \cdot \mathbf{K}^s \cdot \llbracket \mathbf{u} \rrbracket |_{s1} + \llbracket \mathbf{u} \rrbracket |_{s3} \mathbf{K}^s \cdot \llbracket \mathbf{u} \rrbracket |_{s3} \right) \quad (4.81)$$

$$= S (d\mathbf{e}_i \cdot \mathbf{K}^s \cdot d\mathbf{e}_i + (-d\mathbf{e}_i) \mathbf{K}^s \cdot (-d\mathbf{e}_i)) \quad (4.82)$$

$$= 2Sd^2(\mathbf{K}^s)_{ii} \quad (4.83)$$

where S is the graphene sheet surface. The last equation shows that the potential energy is a quadratic function of d and its curvature is proportional to the diagonal component $(\mathbf{K}^s)_{ii}$. For this reason, the potential energy is computed for 7 values of d (see Fig. 4.19). The fitting of this curves gives $(\mathbf{K}^s)_{11} = (\mathbf{K}^s)_{22} = 0.0085 \text{ GPa}\cdot\text{nm}^{-1}$ and $(\mathbf{K}^s)_{33} = 52.96 \text{ GPa}\cdot\text{nm}^{-1}$. To obtain, the non-diagonal components of \mathbf{K}^s , the graphene sheet is moved simultaneously along two directions, such as $\llbracket \mathbf{u} \rrbracket |_{s1} = -\llbracket \mathbf{u} \rrbracket |_{s2} = d(\mathbf{e}_i + \mathbf{e}_j)$ for $i \neq j$. A second order polynomial fit allows to determine $(\mathbf{K}^s)_{21} = (\mathbf{K}^s)_{12} = 0.0219 \text{ GPa}\cdot\text{nm}^{-1}$ and $(\mathbf{K}^s)_{23} = (\mathbf{K}^s)_{32} = (\mathbf{K}^s)_{31} = (\mathbf{K}^s)_{13} = 0.0283 \text{ GPa}\cdot\text{nm}^{-1}$.

This identification method allows to identify the Critical Resolved Shear Stress (CRSS) associated to the slip in the graphene plane by computation

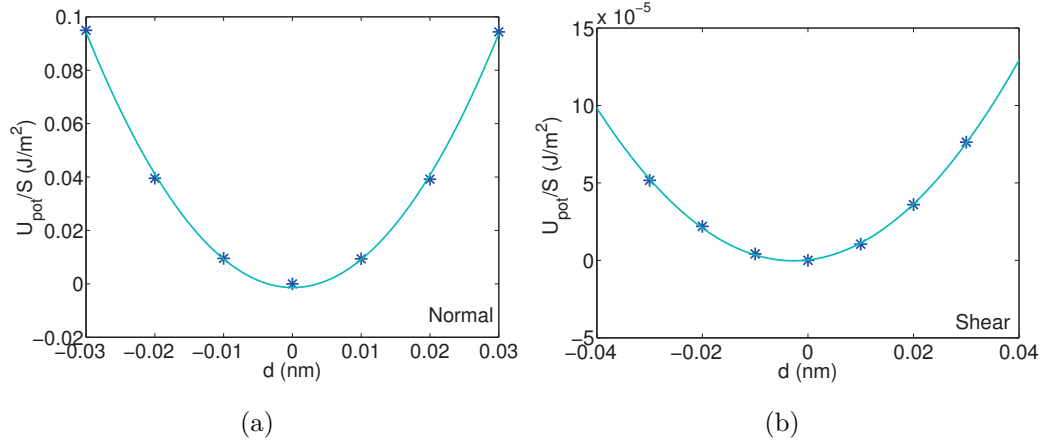


FIGURE 4.19 – a) Evolution of potential energy as function of d ; a) for translation of graphene along \mathbf{e}_3 ; b) along \mathbf{e}_1 .

of the local shear stress increments. Fig. 4.20 shows the evolution of the local shear stress increments $(\Delta\sigma_{(w)})_{13}$ as function d for a translation of graphene sheet along \mathbf{e}_3 . The curve has a periodicity which is the same as the lattice of graphene. There are two maxima in one period, the value of CRSS, $\tau^* \approx 17$ MPa is the smaller.

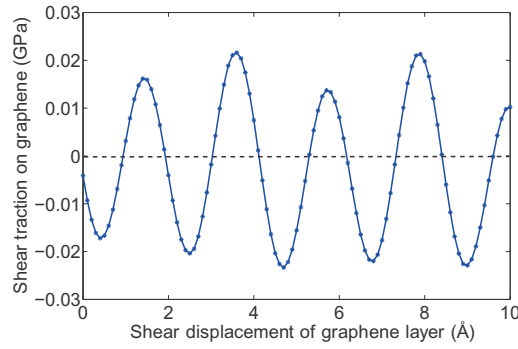


FIGURE 4.20 – Evolution of shear stress in a graphene plane for a translation along \mathbf{e}_1 .

The surface elasticity tensor is identified by the method used for the bulk. Indeed, the fourth-order stiffness tensor \mathbb{C} is identified on the graphene sheet. Then, \mathbb{C}^s , is deduced from (see *e.g.* [Gu 2011]).

$$\mathbb{C}^s = h \left(\mathbb{C} - \frac{(\mathbb{C} : \mathbf{N}) \otimes (\mathbb{C} : \mathbf{N})}{\mathbf{N} : \mathbb{C} : \mathbf{N}} \right) \quad (4.84)$$

where $\mathbf{N} = \mathbf{e}_3 \otimes \mathbf{e}_3$ and $h = 4\text{\AA}$ is the graphene sheet thickness. The h value is chosen as the double of the characteristic size of the repulsive part of the potential between the graphene and the polymer. In this work, \mathbb{C}^s is identified to be

$$[\mathbb{C}^s] = \begin{bmatrix} 281840 & 0 & 0 & 0 & 0 & 0 \\ 0 & 281840 & 0 & 0 & 0 & 0 \\ 0 & 0 & 0 & 0 & 0 & 0 \\ 0 & 0 & 0 & 93400 & 0 & 0 \\ 0 & 0 & 0 & 0 & 0 & 0 \\ 0 & 0 & 0 & 0 & 0 & 0 \end{bmatrix} \text{MPa.nm.} \quad (4.85)$$

4.5 Numerical results

4.5.1 Influence of the polymer thickness

The effective stiffness tensor components of the sandwich structural composite can be directly estimated by molecular dynamics method [Zhu 2007, Frankland 2003]. Due to the identification of the local stiffness along the normal distance to graphene layer, we can also achieve the effective stiffness of the samples by the continuum model consisting of imperfect interface and interphase (Model I mentioned in section 4.4) through a homogenization process. In this part, to simplify the numerical method, we also consider an equivalent model, denoted by Model II (see in section 4.4), where we use only one equivalent imperfect interface to replace the graphene sheet, the interface regions and interphase region. From the numerical point of view, the Model II is advantageous because it does not require to refine the mesh inside the interphases. Besides, the numerical results can also be obtained by the naive model (Model III) without considering the interfacial interactions.

Accounting for the sandwich structural samples of a series of thickness, we compared the effective stiffness components $\bar{\mathbb{C}}_{11}$, $\bar{\mathbb{C}}_{33}$ and $\bar{\mathbb{C}}_{66}$ estimated by the « imperfect interface+interphase » model (Model I), Model II and Model III with the results of atomistic simulations respectively as shown in Fig. 4.22 (a-c). Remaining the density of polymer and the length of the polymer chain, the thickness of the samples are changed by altering the number of the chains.

In the continuum model, the identified stiffness tensor components of the

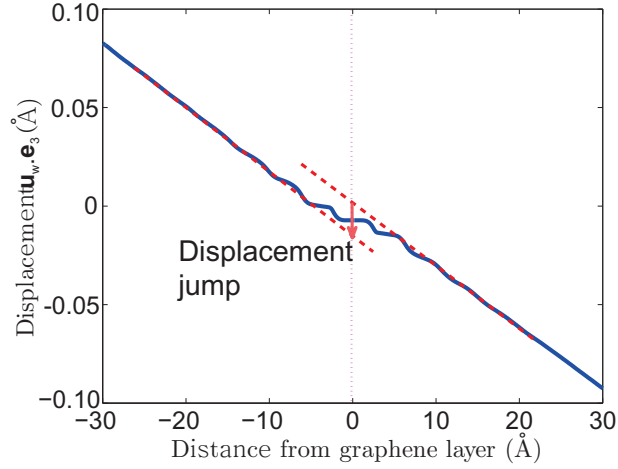


FIGURE 4.21 – Displacement field component $\mathbf{u}_w \cdot \mathbf{e}_3$ along with the normal distance from graphene at 0.3% elongation on \mathbf{e}_3 , where the displacement jump through the graphene layer is pointed out.

pure polymer region in the samples with various thickness are presented in Table. 4.2. For each sample, the stiffness tensor components C_{11} , C_{33} , C_{12} of the interphase region is 40% higher than the corresponding ones of pure polymer, and the other components C_{13} and C_{66} can be regarded equal to the ones of pure polymer. Besides, in model I, the cohesive interface stiffness tensor components are identified in section 4.4.2.2.

TABLE 4.2 – Identified stiffness tensor components of the pure polymer region

Thickness (nm)	$C_{11}=C_{22}$ (GPa)	C_{33} (GPa)	$C_{12}=C_{21}=C_{13}=C_{31}=C_{23}=C_{32}$ (GPa)	$C_{44}=C_{55}=C_{66}$ (GPa)
7.72	17.4	18	11.92	2.74
8.71	16.23	16.40	10.83	2.70
9.62	16.20	16.17	10.92	2.64
10.62	15.50	15.47	10.20	2.65
11.53	15.50	15.55	10.70	2.40
13.51	14.50	14.43	9.32	2.59

Furthermore in model II, the equivalent interface is modeled by the combination of an imperfect surface of graphene sheet and a cohesive interface with a negative stiffness $\tilde{\mathbf{K}}_{33}^s$. $\tilde{\mathbf{K}}_{33}^s$ is identified by the introduction of 0.3% elongation along \mathbf{e}_3 to the sandwich structural sample, as the ratio between the variation of stress after deformation on graphene surface $\Delta\sigma_{33}^s$ and the

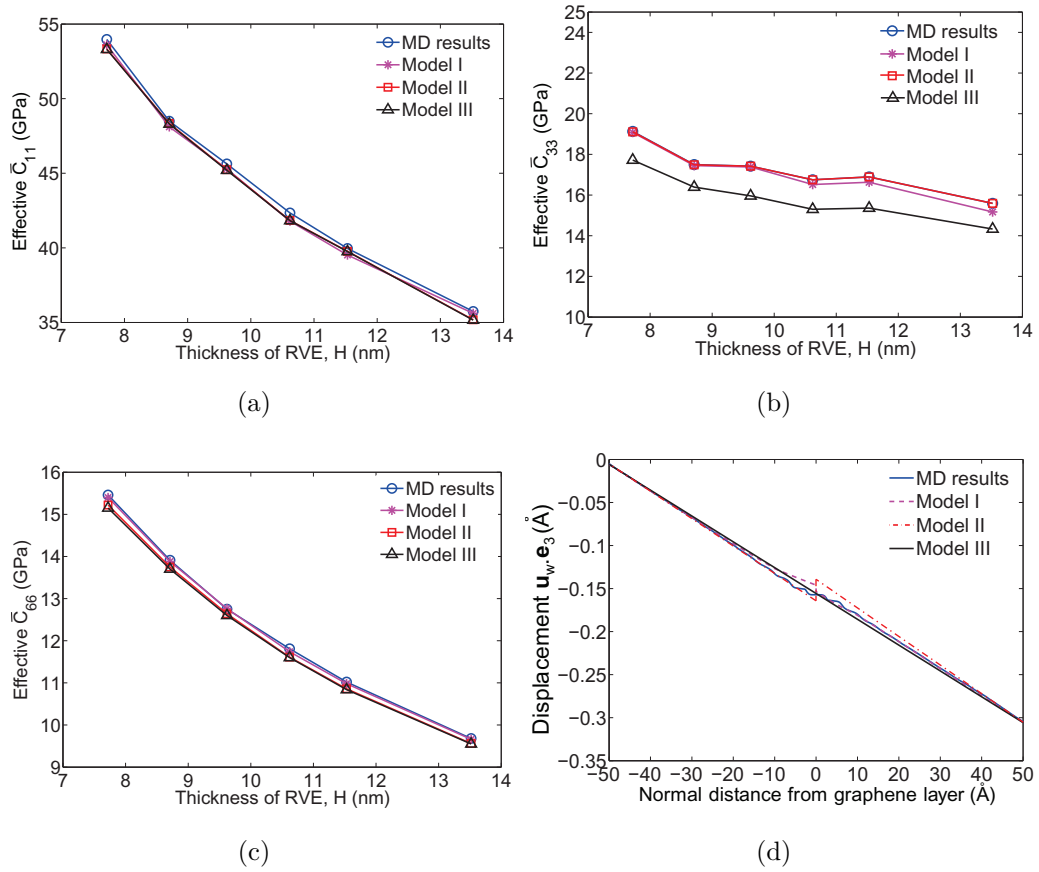


FIGURE 4.22 – Effective stiffness components (a) \bar{C}_{11} , (b) \bar{C}_{33} , (c) \bar{C}_{66} as a function of the thickness of sandwich structure computed by molecular dynamics method, continuum model with imperfect interface and interphase, and Model II with imperfect surface, and Model III respectively. (d) Comparison of the displacement fields component $\mathbf{u}_w \cdot \mathbf{e}_3$ vs z along z for an elongation of 0.3% along \mathbf{e}_3 obtained by these three methods. The thickness of the sample is 10.38 nm.

displacement jump through graphene sheet $[[\mathbf{u}]] \cdot \mathbf{e}_3$ (assume to be negative, see in Fig. 4.21). The identified surface stiffness tensor components $\tilde{\mathbf{K}}_{33}^s$ for the samples with different thickness are presented in Table. 4.3, to fit the effective stiffnesses obtained by Model II with MD results. The appearance of the negative values for $\tilde{\mathbf{K}}_{33}^s$ can be explained as follows. From the MD results, we have evidenced that the effective $\bar{\mathbf{C}}_{33}$ was larger than that of the pure polymer, *i.e.* was enhanced by the interface. However, introducing an interface stiffness component with any positive value can only reduce the effective stiffness, and the stiffing effect associated with the interface can only occur with a negative value of the interface stiffness component $\tilde{\mathbf{K}}_{33}^s$. The negative values for the interface stiffness components have been reported in some literatures [Miller 2000, Shenoy 2005, Hoang 2015]. The tangent stiffness of the cohesive interface can be neglected in the model since it is orders of magnitude smaller than the normal direction.

TABLE 4.3 – Identified $\tilde{\mathbf{K}}_{33}^s$ of the equivalent imperfect interface

Thickness (nm)	7.72	8.71	9.62	10.62	11.53	13.51
$\tilde{\mathbf{K}}_{33}^s$ (GPa.nm ⁻¹)	-40	-30	-23.5	-19	-17	-14.4

It can be seen in Fig. 4.22 (a-c) that for all of these three components, the estimations by Model I and Model II are in good agreement with the molecular dynamics results. With the assumptions of Model III, we can obtain the effective $\bar{\mathbf{C}}_{11}$ and $\bar{\mathbf{C}}_{66}$ which also agree well with the molecular dynamics method. Since the surface stiffness components \mathbf{C}_{11}^s and \mathbf{C}_{66}^s of graphene are much larger than the stiffness components \mathbf{C}_{11} and \mathbf{C}_{66} of the interphase and the polymer matrix, the effect of the interphase region especially at high thickness has been weakened along these directions. However, the effective $\bar{\mathbf{C}}_{33}$ component calculated by Model III exhibits 5-7% error compared with the actual situation as shown in Fig. 4.22 (b), which indicates the important role of interphase in the normal direction. Among all the provided models, Model II is the most advantageous because it can be easily used to study random structures with good accuracy and requires less computation cost related to meshing procedure. Moreover, we make a comparison of the displacement fields component $\mathbf{u}_w \cdot \mathbf{e}_3$ vs z for an elongation of 0.3% along e_3 obtained by these three models with MD simulation, which is shown in Fig. 4.22 (d). The thickness of the sample is 10.38 nm. Different from the stepped shape of displacement in the

interphase region obtained by MD simulation, the displacement jump at the imperfect interface can be observed in Model I and Model II, being positive and negative respectively.

4.5.2 Numerical example of random nanocomposite

As an illustration, we introduce the Model II in a finite element analysis to analyze the mechanical characteristics of a nanocomposites RVE with graphene randomly dispersed in the matrix. The coefficients of the interface model have been identified by the procedure described in the former section. The microstructure of the sample is shown in Fig. 4.23 (a), where the side length of the representative volume element (RVE) is 40 nm, and 10 graphene sheets with the size $15 \times 15 \times 0.2 \text{ nm}^3$ are randomly distributed inside the RVE. At the elongation of 3% along \mathbf{e}_3 , the numerical results of the displacement fields, pressure fields and the Von Mises stress fields are presented in Fig. 4.23 (b-d). The displacement jump through the graphene platelets can be observed in Fig. 4.23 (b). In Fig. 4.23 (c), stress concentration is observed around the graphene sheets, from which we can infer that the damages of the graphene nanocomposites are more likely to occur in the interface. Finally, the Von Mises stress around the interface region appears to be nearly 100 times larger than in the polymer bulk as shown in Fig. 4.23 (d), suggesting that the interfacial region suffers a larger deformation.

4.6 Conclusion

In this chapter, we have employed the Murdoch-Hardy procedure to study the mechanical properties of the graphene/polymer sandwich microstructures, whose systems are prepared from the self-avoiding random walk combining the molecular dynamics relaxation steps. The local density of the system and the nematic order parameter s_w for the polymer bond are obtained which illustrate the existence and the special microstructure of the interphase layer. The Cauchy stress fields components and the displacement fields have also been identified for the sandwich structure as a function of the normal distance from graphene sheet.

A continuum model has been proposed to describe the complex interfaces in the graphene/polymer nanocomposites. For the bulk polymer and inter-

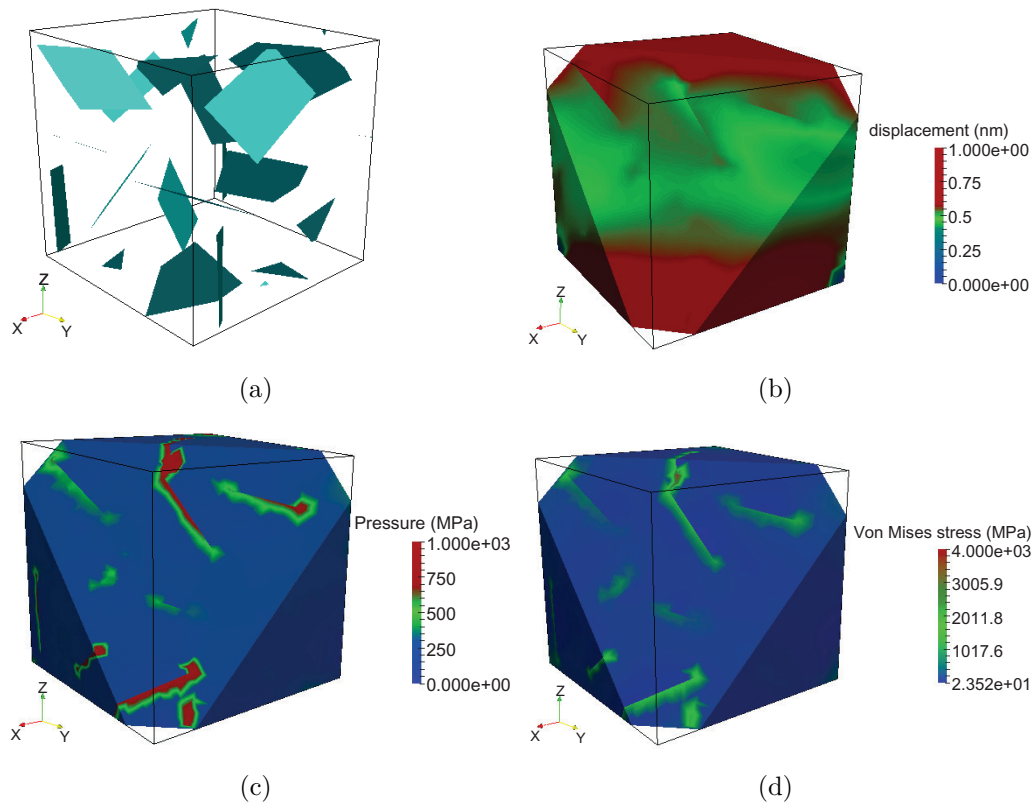


FIGURE 4.23 – (a) Microstructure (b) displacement field, (c) pressure, (d) Von Mises stress of the random nanocomposites with the employment of imperfect surface model denoted Model II with elongation of 3% along \mathbf{e}_3 . (by ParaView)

phase regions, the local elastic parameters have been identified by combining the Cauchy stress field and displacement field obtained from Murdoch-Hardy procedure. We have reported that the interphase between graphene and polymer is stiffer than the pure polymer bulk. The thickness of interphase is evaluated to be about 2 nm, which is much thinner than the experimental results of around 12 nm [Liu 2016]. That is because in our simulation, the graphene is a perfect monolayer and the polymer matrix is PE. However, in the experiments, the filler is multi-layer graphene nanoplatelets and the polymer matrix is epoxy. Considering the interfacial region as a cohesive interface, the elastic properties of the interface have been identified by monitoring the variation of free energy of the system along with the displacement of the graphene layer. The elastic stiffness of the interface is extremely anisotropic, since the shear strength between graphene and polymer is quite small compared with the tensile strength. The normal component of the surface elastic stiffness is $(\mathbf{K}^s)_{33} = 52.96 \text{ GPa}\cdot\text{nm}^{-1}$, which is much more larger than $(\mathbf{K}^s)_{11} = (\mathbf{K}^s)_{22} = 0.0085 \text{ GPa}\cdot\text{nm}^{-1}$.

Three continuum models, named Model I, Model II and Model III, have been proposed to estimate the effective elasticity properties of the graphene/polymer interphases with a series of polymer thickness. Model I contains the information of the specific property of interphase extracted from atomistic level, and the interface is modeled as imperfect surface. In Model II, the graphene sheet, interface region and interphase region are replaced by a single equivalent imperfect intersurface with negative normal surface stiffness component $(\tilde{\mathbf{K}}^s)_{33}$. Model III is a naive model without considering the interfacial interaction between graphene and polymer matrix. The results show that the elasticity properties obtained by Model I and Model II present a good agreement with the MD simulation but Model III exhibits errors in the calculated effective properties, which indicates the significance of the nano-scaled interphase. Among these models, Model II presents to be both simple and accurate and has been employed into the Finite element calculations of a 3D RVE, containing randomly distributed graphene sheets and embedding the identified model for the imperfect interfaces.

Numerical modeling of the mechanical properties of graphene reinforced nanocomposites

5.1 Introduction

Due to its exceptional mechanical properties, graphene is a very attractive candidate for reinforcement in composites as shown in [Potts 2011, Ramanathan 2008].

For instance, Rafiee *et al.* [Rafiee 2009] dispersed 0.1% graphene platelets into the epoxy matrix, leading to a 31% improvement of the Young's modulus and 40% increase of the tensile strength compared with the pristine epoxy. By functionalizing graphene nanosheets, the polystyrene nanocomposites with 0.9% graphene nanosheets can also reveal around 70% and 57% increases in tensile strength and Young's modulus [Fang 2009].

The enhancement in mechanical properties of graphene reinforced nanocomposites is mainly governed by the interfacial interactions between the filler and the matrix apart from the properties of the constituent phases themselves. Generally, the control of stress transfer across the interface can be achieved by means of covalent bonding, electrostatic interactions, hydrogen bonding or van der Waals interactions [Giannelis 1996, Vaia 1995, Moniruzzaman 2006]. The cracks and delamination usually occur at the interface due to weak interactions. To explore the influence of interfacial interaction between graphene and polymer on the microscopic mechanical properties, numerical tools need to be employed. Since the interfacial behavior is mainly governed by atomistic level interactions, the atomistic simulations can potentially provide information about the interfacial interactions. Pullout tests have been performed

by atomistic simulations to evaluate the shear strength of the interface between carbon nanotube and polymer [Liao 2001, Chowdhury 2007, Gou 2004, Namilae 2005], which provided the force versus displacement response. The simulated shear characteristics of the interface have also been incorporated into multiscale modeling [Namilae 2005, Liu 2008b]. Moreover, the characteristics of normal separation or combined loading separation between graphene and polymer have been discussed by Awasthi *et al.* [Awasthi 2008]. The cohesive law of separation has been evaluated for graphene planes using the van der Waals potential, and has been extended to multi-walled CNTs by incorporating curvature effects in [Lu 2007].

In the field of polycrystals, atomistic simulations have been performed to evaluate the interfacial behavior, and the obtained results have been utilized as separation laws for cohesive zone models. The degradation of interfaces can be studied and analyzed conveniently with cohesive zone models [den Bosch 2007]. Cohesive zone models proposed by Barenblatt [Barenblatt 1962] and Dugdale [Dugdale 1960] assume a generic relation between forces and displacements occurring at the interface during the separation. The models have been embedded in finite element analysis by Needleman [Needleman 1987], Hutchinson and Tvergaard [Tvergaard 1993], or have been modeled by cohesive elements like in Camacho and Ortiz [Camacho 1996], Xu and Needleman [Xu 1994]. These elements are surface-like and are compatible with general bulk finite element discretization of the solid, including those which account for plasticity and large deformations.

In this chapter, we develop a finite element model at small deformation to predict the mechanical properties of graphene reinforced nanocomposites. The computations are based on the RVEs with randomly distributed graphene sheets. The cohesive zone model which accounts for interface elasticity is introduced into the FEM formulation. The cohesive law of the interface is identified by molecular dynamics, in which we model the separation process between graphene and polyethylene (PE) film at the atomistic level. In addition, an imperfect surface model is employed to model the graphene sheets as surfaces which incorporates the discontinuity of stress in the normal direction of graphene sheets. The general model of imperfect interface introduced and identified in the previous section is used. We extend the model to finite deformations. Incorporating the electrical model described in Chapter. 3, we provide a preliminary coupling of the electro-mechanical properties of gra-

phene reinforced nanocomposites. The purpose is to observe the variation of electrical conductivity and percolation threshold of the nanocomposites with various graphene volume fraction at a series of finite deformations.

The chapter is organized as following : First, in section 5.2, we make a general introduction of the elastic imperfect surface model. In section 5.3, a general introduction of cohesive zone model is provided. Section 5.4 provides the details on the identification process of cohesive laws by molecular dynamics method, for the interfacial elasticity of graphene reinforced nanocomposites. The fitting function is presented which can be incorporated into the continuum finite element model. In section 5.5, the multiscale model of graphene-reinforced nanocomposites at small deformation is described as well as the FEM discretization of the equations to solve the nonlinear problem. The RVE analysis and the effective stiffness of the nanocomposites as a function of the graphene volume fraction are presented. Then, in section 5.6, the mechanical modeling at finite strains is developed, followed by the computational framework for the graphene reinforced nanocomposites at finite deformation. The framework includes the weak formulation of the governing equations, and the corresponding finite element linearization and discretization. Finally, the numerical examples of the electro-mechanic coupling, based on the finite element models in section 5.6 and section 3.4, are presented in section 5.7

5.2 Elastic imperfect interface model

Imperfect interfaces have important effects on the effective mechanical properties of the composite materials. The most common models are the linear spring model and the coherent interface model. In the linear spring model, the assumption is made that through the interface, the stress vector is continuous while the displacement vector undergoes a jump which is proportional to the stress vector. In the coherent interface model, the displacement through the interface is continuous, while the stress is discontinuous due to the presence of surface stresses in the interface, which is proportional to the surface strain and satisfies the Young-Laplace equations. The two models were initially proposed and formulated on the basis of phenomenological considerations [Gurtin 1975, Hashin 1990, Hashin 1991, Murdoch 1976]. They were then justified by an asymptotic approach [Klarbring 1991, Benveniste 2006a,

Benveniste 2001, Gu 2011]. The interphase between the two solids can be modeled as an imperfect interface, which is developed on the basis of the work of Bövik [Bövik 1994] and Benveniste [Benveniste 2006a].

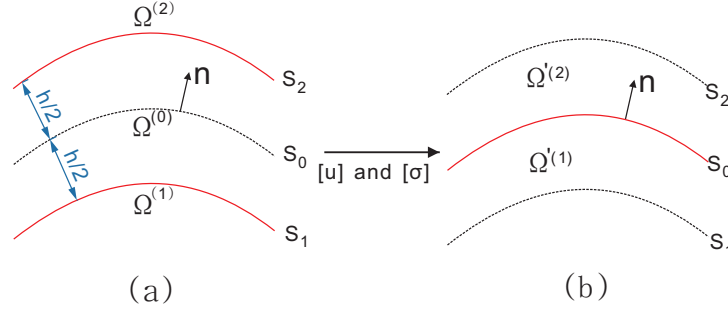


FIGURE 5.1 – Scheme of the interface model. (a) Phase 1/interphase 0/Phase 2; (b) Phase 1/ imperfect interface S_0 /Phase 2

The scheme of the model is similar to the one for the electrical imperfect surface models in Chapter. 3. In the configuration of Fig. 5.1, the interface S_1 which is between the Phase 1 and the interphase 0, and the interface S_2 which is between the phase 2 and the interphase 0 are perfect. Thus, we have the continuity of the displacement vector \mathbf{u} and the continuity of the normal vector of stress $\boldsymbol{\sigma}_n$ ($\boldsymbol{\sigma}_n = \boldsymbol{\sigma} \cdot \mathbf{n}$) through S_1 and S_2 :

$$\begin{aligned} \mathbf{u}^{(0)}|_{S_1} &= \mathbf{u}^{(1)}|_{S_1}, & \mathbf{u}^{(0)}|_{S_2} &= \mathbf{u}^{(2)}|_{S_2}, \\ \boldsymbol{\sigma}_n^{(0)}|_{S_1} &= \boldsymbol{\sigma}_n^{(1)}|_{S_1}, & \boldsymbol{\sigma}_n^{(0)}|_{S_2} &= \boldsymbol{\sigma}_n^{(2)}|_{S_2}. \end{aligned} \quad (5.1)$$

Phase 1, Phase 2 and the interphase 0 are linearly elastic and generally anisotropic. The behavior is characterized by the Hooke's law :

$$\boldsymbol{\sigma}^{(i)} = \mathbb{C}^{(i)} : \boldsymbol{\varepsilon}^{(i)} \quad (5.2)$$

where $\mathbb{C}^{(i)}$ ($i=0,1,2$) is the stiffness tensor and $\boldsymbol{\varepsilon}^{(i)}$ is the infinitesimal strain tensor defined by :

$$\boldsymbol{\varepsilon}^{(i)} = \frac{1}{2}[\nabla \mathbf{u}^{(i)} + (\nabla \mathbf{u}^{(i)})^T]. \quad (5.3)$$

In the absence of volume forces, the equations of equilibrium take the form :

$$\nabla \cdot \boldsymbol{\sigma}^{(i)} = \mathbf{0}. \quad (5.4)$$

In the configuration described in Fig. 5.1, the interphase $\Omega^{(0)}$ is eliminated and replaced by an imperfect interface S_0 . The main problem to solve is to determine the conditions through the imperfect interface model in order that the imperfect interface is equivalent to the interphase at a fixed error.

With the similar process as in the electrical imperfect interface model, two functions \mathbf{f}_1 and \mathbf{g}_1 are introduced to calculate the normal derivatives of the displacement and stress :

$$\begin{aligned}\nabla^n \mathbf{u} &= \nabla \mathbf{u} \cdot \mathbf{n} = \mathbf{f}_1(\nabla^s \mathbf{u}, \boldsymbol{\sigma}_n; \mathbb{C}), \\ \nabla^n \boldsymbol{\sigma}_n &= \nabla \boldsymbol{\sigma}_n \cdot \mathbf{n} = \mathbf{g}_1(\nabla^s \mathbf{u}, \boldsymbol{\sigma}_n; \mathbb{C}).\end{aligned}\quad (5.5)$$

The arguments of \mathbf{f}_1 and \mathbf{g}_1 are the tangential derivative of the displacement $\nabla^s \mathbf{u}$, and the stress vector $\boldsymbol{\sigma}_n$, which are continuous across the perfect interface S_1 and S_2 . The stiffness tensor \mathbb{C} plays a role of the parameter and is evaluated in the phase or interphase. Then the elastic imperfect interface model of order $O(h^2)$ is characterized by

$$\begin{aligned}[[\mathbf{u}]] &= \frac{h}{2} \left[\mathbf{f}_1(\nabla^s \mathbf{u}^{(+)}, \boldsymbol{\sigma}_n^{(+)}; \mathbb{C}^{(0)}) + \mathbf{f}_1(\nabla^s \mathbf{u}^{(-)}, \boldsymbol{\sigma}_n^{(-)}; \mathbb{C}^{(0)}) \right] - \\ &\frac{h}{2} \left[\mathbf{f}_1(\nabla^s \mathbf{u}^{(+)}, \boldsymbol{\sigma}_n^{(+)}; \mathbb{C}^{(2)}) + \mathbf{f}_1(\nabla^s \mathbf{u}^{(-)}, \boldsymbol{\sigma}_n^{(-)}; \mathbb{C}^{(1)}) \right] + O(h^2).\end{aligned}\quad (5.6)$$

$$\begin{aligned}[[\boldsymbol{\sigma}_n]] &= \frac{h}{2} \left[\mathbf{g}_1(\nabla^s \mathbf{u}^{(+)}, \boldsymbol{\sigma}_n^{(+)}; \mathbb{C}^{(0)}) + \mathbf{g}_1(\nabla^s \mathbf{u}^{(-)}, \boldsymbol{\sigma}_n^{(-)}; \mathbb{C}^{(0)}) \right] - \\ &\frac{h}{2} \left[\mathbf{g}_1(\nabla^s \mathbf{u}^{(+)}, \boldsymbol{\sigma}_n^{(+)}; \mathbb{C}^{(2)}) + \mathbf{g}_1(\nabla^s \mathbf{u}^{(-)}, \boldsymbol{\sigma}_n^{(-)}; \mathbb{C}^{(1)}) \right] + O(h^2),\end{aligned}\quad (5.7)$$

where $[[\bullet]] = \bullet^{(+)} - \bullet^{(-)}$ represents the jump through the imperfect surface S_0 in Fig. 5.1 (b).

The gradient of displacement vector can be decomposed as

$$\nabla \mathbf{u} = \nabla \mathbf{u} \cdot \mathbf{P} + \nabla \mathbf{u} \cdot \mathbf{P}^\perp = \nabla^s \mathbf{u} + \nabla^n \mathbf{u} \otimes \mathbf{n} \quad (5.8)$$

where \mathbf{P} and \mathbf{P}^\perp are the project tensor

$$\mathbf{P}^\perp = \mathbf{n} \otimes \mathbf{n}, \quad \mathbf{P} = \mathbf{I} - \mathbf{n} \otimes \mathbf{n} \quad (5.9)$$

and thus

$$\nabla^s \mathbf{u} = \nabla \mathbf{u} \cdot \mathbf{P}, \quad \nabla^n \mathbf{u} = \nabla \mathbf{u} \cdot \mathbf{n}. \quad (5.10)$$

Taking into account Hooke's law, the stress vector is expressed by

$$\boldsymbol{\sigma}_n = \boldsymbol{\sigma} \cdot \mathbf{n} = (\mathbb{C} : \nabla \mathbf{u}) \cdot \mathbf{n} = [\mathbb{C} : (\nabla \mathbf{u} \cdot \mathbf{P}^\perp)] \cdot \mathbf{n} + [\mathbb{C} : \nabla^s \mathbf{u}] \cdot \mathbf{n}. \quad (5.11)$$

In this equation,

$$[\mathbb{C} : (\nabla \mathbf{u} \cdot \mathbf{P}^\perp)] \cdot \mathbf{n} = (\mathbf{n} \cdot \mathbb{C} \cdot \mathbf{n}) \cdot \nabla^n \mathbf{u} = \hat{\mathbf{Q}} \cdot \nabla^n \mathbf{u} \quad (5.12)$$

where $\hat{\mathbf{Q}} = \mathbf{n} \cdot \mathbb{C} \cdot \mathbf{n}$ is the acoustic tensor, and the inverse of $\hat{\mathbf{Q}}$ is denoted by $\hat{\mathbf{F}}$,

$$\hat{\mathbf{F}} = \hat{\mathbf{Q}}^{-1}. \quad (5.13)$$

Introducing Eq. (5.12) to Eq. (5.11), it turns out that

$$\nabla^n \mathbf{u} = \mathbf{f}_1(\nabla^s \mathbf{u}, \boldsymbol{\sigma}_n; \mathbb{C}) = \hat{\mathbf{F}} \cdot \boldsymbol{\sigma}_n - \Lambda : \nabla^s \mathbf{u} \quad (5.14)$$

where the third-order tensor

$$\Lambda_{ijk} = F_{ip} C_{pqjk} n_q. \quad (5.15)$$

Using the expression of \mathbf{f}_1 in Eq. (5.14) in Eq. (5.6), we can obtain that

$$\begin{aligned} \llbracket \mathbf{u} \rrbracket &= \frac{h}{2} [(\hat{\mathbf{F}}^{(0)} - \hat{\mathbf{F}}^{(1)}) \cdot \boldsymbol{\sigma}_n^{(-)} - (\Lambda^{(0)} - \Lambda^{(1)}) : \nabla^s \mathbf{u}^{(-)}] + \dots \\ &\dots + \frac{h}{2} [(\hat{\mathbf{F}}^{(0)} - \hat{\mathbf{F}}^{(2)}) \cdot \boldsymbol{\sigma}_n^{(+)} - (\Lambda^{(0)} - \Lambda^{(2)}) : \nabla^s \mathbf{u}^{(+)}] + O(h^2). \end{aligned} \quad (5.16)$$

Then, the divergence of the stress tensor is decomposed as

$$\nabla \cdot \boldsymbol{\sigma} = \nabla \boldsymbol{\sigma} : \mathbf{P} + \nabla \boldsymbol{\sigma} : \mathbf{P}^\perp. \quad (5.17)$$

It should be noted that

$$\nabla^n \boldsymbol{\sigma}_n = \nabla \boldsymbol{\sigma}_n \cdot \mathbf{n} = \nabla (\boldsymbol{\sigma} \cdot \mathbf{n}) \cdot \mathbf{n} = \nabla \boldsymbol{\sigma} : \mathbf{P}^\perp. \quad (5.18)$$

Combining with the relations that $\nabla \mathbf{n} \cdot \mathbf{n} = 0$ and $\nabla \cdot \boldsymbol{\sigma} = 0$, we can obtain

$$\nabla^n \boldsymbol{\sigma}_n = -\nabla \boldsymbol{\sigma} : \mathbf{P} = -\nabla^s \cdot \boldsymbol{\sigma}. \quad (5.19)$$

Introducing the constitutive law (5.19) we obtain

$$\nabla^n \boldsymbol{\sigma}_n = -\nabla^s \cdot [\mathbb{C} : (\nabla \mathbf{u} \cdot \mathbf{P})] - \nabla^s \cdot [\mathbb{C} : (\nabla \mathbf{u} \cdot \mathbf{P}^\perp)] \quad (5.20)$$

where

$$\nabla^s \cdot [\mathbb{C} : (\nabla \mathbf{u} \cdot \mathbf{P}^\perp)] = \nabla^s \cdot [(\mathbb{C} \cdot \mathbf{n}) \cdot (\nabla^n \mathbf{u})] = \nabla^s \cdot [(\mathbb{C} \cdot \mathbf{n}) \cdot \mathbf{f}_1]. \quad (5.21)$$

Finally, we have :

$$\nabla^n \boldsymbol{\sigma}_n = \mathbf{g}_1(\nabla^s \mathbf{u}, \boldsymbol{\sigma}_n; \mathbb{C}) = -\nabla^s \cdot (\mathbb{C} : \nabla^s \mathbf{u}) - \nabla^s \cdot [(\mathbb{C} \cdot \mathbf{n}) \cdot \mathbf{f}_1]. \quad (5.22)$$

Considering the expression of \mathbf{f}_1 in Eq. (5.14), and introducing it into Eq. (5.22), we have

$$\mathbf{g}_1(\nabla^s \mathbf{u}, \boldsymbol{\sigma}_n; \mathbb{C}) = -\nabla^s \cdot (\mathbb{A} : \nabla^s \mathbf{u}) - \nabla^s \cdot (\boldsymbol{\Theta} \cdot \boldsymbol{\sigma}_n), \quad (5.23)$$

where \mathbb{A} is a fourth-order tensor and $\boldsymbol{\Theta}$ is a third-order tensor defined by

$$\mathbb{A} = \mathbb{C} - (\mathbb{C} \cdot \mathbf{n}) \cdot \boldsymbol{\Lambda}, \quad \boldsymbol{\Theta} = (\mathbb{C} \cdot \mathbf{n}) \cdot \hat{\mathbf{F}}. \quad (5.24)$$

Therefore, introducing Eq. (5.23) into Eq. (5.7), the jump of the stress vector can be written as

$$\begin{aligned} \llbracket \boldsymbol{\sigma}_n \rrbracket &= \frac{h}{2} \left\{ \nabla^s \cdot [(\mathbb{A}^{(1)} - \mathbb{A}^{(0)}) : \nabla^s \mathbf{u}^{(-)}] + \nabla^s \cdot [(\boldsymbol{\Theta}^{(1)} - \boldsymbol{\Theta}^{(0)}) \cdot \boldsymbol{\sigma}_n^{(-)}] \right\} \\ &+ \frac{h}{2} \left\{ \nabla^s \cdot [(\mathbb{A}^{(2)} - \mathbb{A}^{(0)}) : \nabla^s \mathbf{u}^{(+)}] + \nabla^s \cdot [(\boldsymbol{\Theta}^{(2)} - \boldsymbol{\Theta}^{(0)}) \cdot \boldsymbol{\sigma}_n^{(+)}] \right\} + O(h^2). \end{aligned} \quad (5.25)$$

In our work, the stiffness of the interphase is much higher than the phases, which can be described as

$$h = \kappa h_0, \quad \mathbb{C}^{(0)} = \frac{1}{\kappa} \mathbb{C}_0^{(0)}, \quad \mathbb{C}^{(1)} = \mathbb{C}_0^{(1)}, \quad \mathbb{C}^{(2)} = \mathbb{C}_0^{(2)}, \quad (5.26)$$

where κ is a very small dimensionless positive parameter which satisfies that $\kappa \ll 1$, h_0 , $\mathbb{C}_0^{(0)}$, $\mathbb{C}_0^{(1)}$ and $\mathbb{C}_0^{(2)}$ are the reference values.

Therefore, we can get

$$\begin{aligned}\hat{\mathbf{F}}^{(0)} &= \kappa \hat{\mathbf{F}}_0^{(0)}, \quad \mathbf{\Lambda}^{(0)} = \mathbf{\Lambda}_0^{(0)}, \quad \mathbf{\Theta}^{(0)} = \mathbf{\Theta}_0^{(0)}, \quad \mathbb{A}^{(0)} = \frac{1}{\kappa} \mathbb{A}_0^{(0)}, \\ \hat{\mathbf{F}}^{(i)} &= \hat{\mathbf{F}}_0^{(i)}, \quad \mathbf{\Lambda}^{(i)} = \mathbf{\Lambda}_0^{(i)}, \quad \mathbf{\Theta}^{(i)} = \mathbf{\Theta}_0^{(i)}, \quad \mathbb{A}^{(i)} = \frac{1}{\kappa} \mathbb{A}_0^{(i)},\end{aligned}\tag{5.27}$$

where $i=1,2$. Introduce these equations to Eq. (5.16) and (5.25), and neglect the terms whose orders are equal and higher than $O(h)$, we can finally obtain the conditions on the imperfect interface as

$$[[\mathbf{u}]] = \mathbf{0},\tag{5.28}$$

$$[[\boldsymbol{\sigma}_n]] = -h \nabla^s \cdot (\mathbb{A}^{(0)} : \nabla^s \mathbf{u}).\tag{5.29}$$

These two equations are widely used to describe the effects of surface and interface in nanometric materials [Duan 2005a, Duan 2005b].

5.3 General introduction of cohesive models

Cohesive zone models have been introduced by Dugdale [Dugdale 1960] and Barenblatt [Barenblatt 1962] and have attracted a growing interest in the scientific community to describe failure processes and delamination. The basic idea of the cohesive model is to split the material behavior in deformation and separation respectively, the former being modeled by continuum elements and the latter embedded within the interface elements, as shown in Fig. 5.2 [den Bosch 2007]. The model relates the relative displacement ($[[\mathbf{u}]]$) of two associated points of the interface to the force per unit of area (\mathbf{t}) needed for separation. In the cohesive elements, the opening traction is controlled by a separation dependent law, which is called cohesive law. The separation can occur in normal (\mathbf{n}) or tangential (\mathbf{t}) direction, and generally, the parameters of the cohesive law are different in these two directions. So the cohesive zone law comprises the two relations \mathbf{t}_n and \mathbf{t}_t .

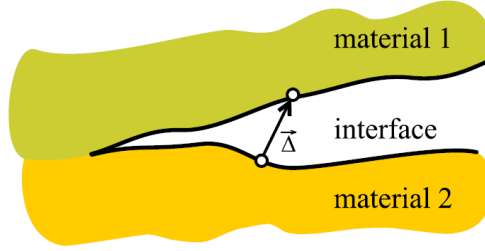


FIGURE 5.2 – An interface between two materials with an opening displacement between two points initially matching.

Cohesive zone laws can involve coupling between tangential and normal components of the traction forces and discontinuity of displacement components. In the uncoupled case, the normal and tangential tractions are independent of the tangential and normal opening as

$$t_n = f_n(\llbracket u_n \rrbracket), \quad t_t = f_t(\llbracket u_t \rrbracket). \quad (5.30)$$

Both normal and tangential tractions generally depend on both the normal and tangential opening displacement as

$$t_n = f_n(\llbracket u_n \rrbracket, \llbracket u_t \rrbracket), \quad t_t = f_t(\llbracket u_n \rrbracket, \llbracket u_t \rrbracket). \quad (5.31)$$

A large variety of cohesive zone laws has been described in literature. Most of them can be categorized into the following groups : (a) polynomial [Needleman 1987], (b) piece-wise linear [Tvergaard 1992], (c) exponential [Needleman 1990] and (d) rigid-linear [Camacho 1996], as shown in Fig. 5.3. These four cohesive zone laws are depicted schematically in the lower figures of Fig. 5.3, where in the upper row the normal traction is given as a function of the normal opening and in the lower row the tangential traction as a function of the tangential opening. The maximum normal traction and the maximum tangential traction are indicated by $t_{n,max}$ and $t_{t,max}$, respectively, and δ_n and δ_t are characteristic opening lengths for normal and tangential direction. The areas below the curves represent the normal and tangential work-of-separation ϕ_n and ϕ_t .

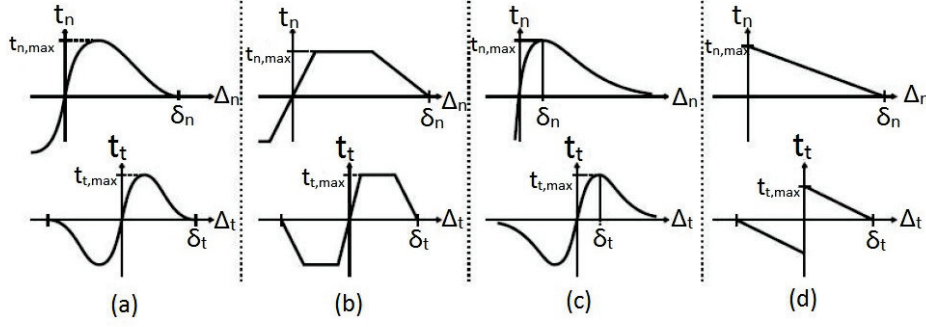


FIGURE 5.3 – Some examples of the cohesive law ($\Delta_n = \llbracket u_n \rrbracket$, $\Delta_t = \llbracket u_t \rrbracket$) [den Bosch 2006]. (a) polynomial, (b) piece-wise linear, (c) exponential, (d) rigid-linear.

Among them, the exponential cohesive zone law is the most popular, which presents some advantages as compared to other laws. First of all, a phenomenological description of contact is achieved in normal compression. Secondly, the tractions and their derivatives are continuous, which is attractive from a computational point of view. The exponential cohesive zone law originates from the universal relationship between binding energies and atomic separation of interfaces. The exponential cohesive law is based on a potential ϕ , which is a function of both the normal and the tangential opening. The potential incorporates four independent parameters : the work of separation for pure normal opening, ϕ_n , the work of separation for pure tangential opening, ϕ_t , the characteristic opening δ_n in normal direction, and the characteristic opening δ_t in tangential direction. For pure normal and tangential opening, the tractions are expressed by [den Bosch 2006] :

$$\begin{aligned} t_n &= \frac{\phi_n}{\delta_n} \left(\frac{\Delta_n}{\delta_n} \right) \exp\left(-\frac{\Delta_n}{\delta_n}\right) \exp\left(-\frac{\Delta_t^2}{\delta_t^2}\right), \\ t_t &= 2 \frac{\phi_t}{\delta_t} \left(\frac{\Delta_t}{\delta_t} \right) \left(1 + \frac{\Delta_n}{\delta_n} \right) \exp\left(-\frac{\Delta_n}{\delta_n}\right) \exp\left(-\frac{\Delta_t^2}{\delta_t^2}\right), \end{aligned} \quad (5.32)$$

and the characteristic lengths δ_n and δ_t can be expressed as a function of the maximum traction :

$$\begin{aligned} \delta_n &= \frac{\phi_n}{t_{n,max} \exp(1)}, \\ \delta_t &= \frac{\phi_t}{t_{t,max} \sqrt{\frac{1}{2} \exp(1)}}. \end{aligned} \quad (5.33)$$

For large deformation, it is no longer physical to discriminate between normal and tangential openings. A large displacement formulation is therefore proposed later in this chapter to resolve the ambiguity induced by the choice of a local basis, whereby no distinction will be made between normal and tangential loadings. Instead of defining two separate constitutive relations for the normal and tangential direction, only one constitutive relation between the traction \mathbf{t} and the opening displacement Δ is used. The cohesive zone law is based on the normal traction relation of the exponential cohesive zone law discussed before as [Roy 2001, den Bosch 2006, Tang 2005] :

$$t = \frac{\phi}{\delta} \left(\frac{\Delta}{\delta} \right) \exp\left(-\frac{\Delta}{\delta}\right) \quad (5.34)$$

where ϕ is the work of separation and δ is a characteristic opening length. The maximum traction t_{max} is related to ϕ and δ by :

$$t_{max} = \frac{\phi}{\delta \exp(1)}. \quad (5.35)$$

5.4 Identification of a nonlinear cohesive model by molecular dynamics

In the present work, a nonlinear model for the interface between graphene and polymer is identified by MD. For this purpose, a sample as described in Fig. 5.4 (a) is considered, where a graphene layer is placed on the PE matrix and the system is at equilibrium state where the graphene experienced zero average force due to the polymer layer. To obtain this structure, the initial system is prepared by the self-avoiding random walk [Binder 1995, Sommer 2010] combining the simultaneously molecular dynamics relaxation and using the LAMMPS (<http://lammmps.sandia.gov>). The system contains 80 PE chains, with 500 -CH₂- for each chain, and 4860 carbon atoms of graphene. The structure is periodical on X-Y plane and non-periodical on Z direction. Dreiding potential [Mayo 1990] is employed in the simulation. To study the separation in opening mode, graphene was moved along the Z direction in steps of 0.5 Å, while the graphene atoms and bottom layer of the polymer were kept fixed. The separation process is depicted in Figs. 5.4 (a-d). The polymer chains undergoes stretch at the beginning, and then a void appears when the graphene moves further due to the separation of certain polymer chains. The size of the

void grows along with the separation and finally the chains of the polymer slide along each others, leading to the complete separation. It should be noted that the separation is based on the sliding of the polymer chains dominated by van der Waals forces, and no chemical bond break are modeled.

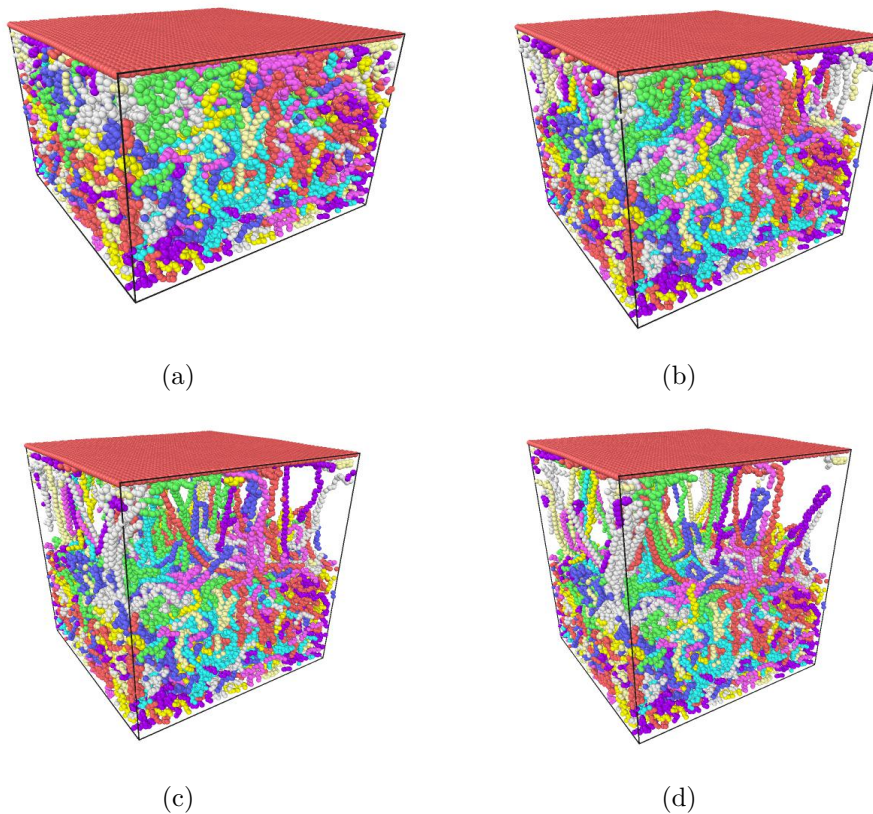


FIGURE 5.4 – Evolution of the MD model during the normal separation. The model contains 44860 atoms, and the graphene is moved with a step of 0.5 Å. The graphene atoms and the bottom layer of the polymer are fixed during the relaxation.

The interaction force between graphene and polymer was monitored, as from which we can get the normal traction of cohesive zone as a function of the displacement of graphene layer as shown in Fig. 5.5. The normal traction of the graphene/polymer interface shows a sharp decrease at 0.7 nm and then drops to zero when the displacement reaches 5 nm. The MD results are fitted

with the following empirical model :

$$t_n = \begin{cases} -1529[[u_n]]^2 + 2150[[u_n]], & \text{if } 0 \leq [[u_n]] < 0.7 \\ \frac{65}{[[u_n]]^8} - \frac{4.31}{[[u_n]]^{14}} + A, & \text{if } 0.7 \leq [[u_n]] \leq 1.15 \\ 360 \exp(-0.16[[u_n]]) + B, & \text{if } [[u_n]] > 1.15 \end{cases} \quad (5.36)$$

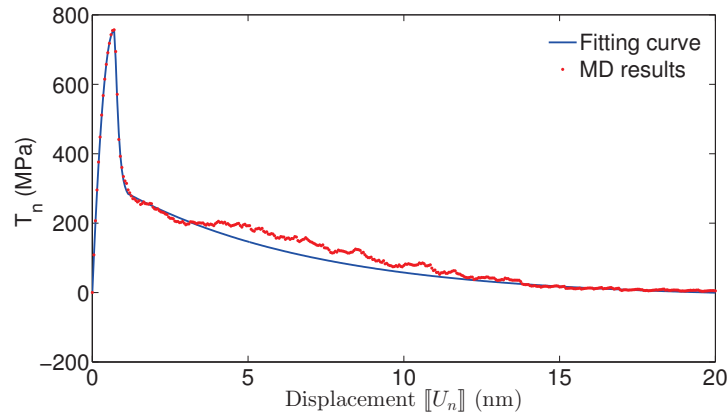


FIGURE 5.5 – Traction-displacement response of the separation process. The points denote the MD results and the line is the fitting curve.

5.5 Small deformation analysis of graphene reinforced polymer nanocomposites

In the following, we present the main equations describing the mechanical model of graphene-reinforced polymer nanocomposite.

5.5.1 Governing equations and constitutive relations

Let us consider a bounded domain $\Omega \in \mathbb{R}^3$, whose external boundary is denoted by $\partial\Omega$. N planar graphene sheets are distributed randomly inside the domain of polymer matrix and are associated with the internal discontinuities Γ_n ($n=1,2,\dots,N$), as shown in Fig. 5.6. The graphene surfaces are collectively denoted by $\Gamma = \cup_n \Gamma_n$. Taking into account the interface between graphene surface and polymer matrix, the two sides of the surface Γ_n are denoted by Γ_n^+ and Γ_n^- . The graphene surface and its surrounding polymer environment

is modeled as an imperfect interface where displacements on normal traction are discontinuous (see previous section).

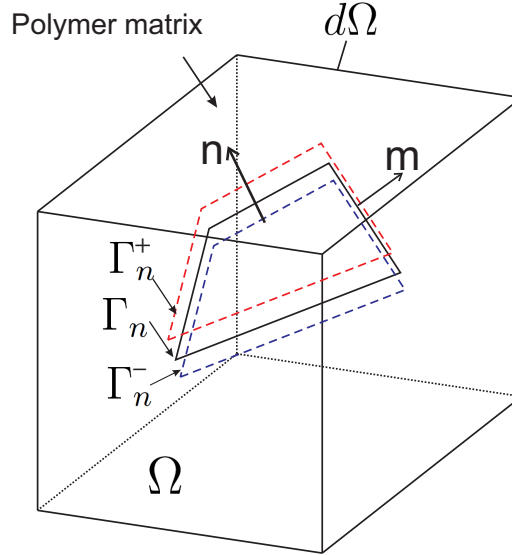


FIGURE 5.6 – RVE model of the graphene-reinforced nanocomposite.

The equilibrium equations of the problem are then given by Eq. (4.54), (4.55). The linearized strain tensor $\boldsymbol{\varepsilon}$ and surface strain tensor were defined in Eq. (4.51), (4.52).

Periodic boundary condition are prescribed as :

$$\mathbf{u} = \bar{\boldsymbol{\varepsilon}} \cdot \mathbf{x} + \tilde{\mathbf{u}} \text{ on } \partial\Omega \quad (5.37)$$

where $\tilde{\mathbf{u}}$ is periodic on Ω , and $\bar{\boldsymbol{\varepsilon}}$ is a constant macroscopic strain field.

In the linear elastic model, the bulk constitutive law is given by :

$$\boldsymbol{\sigma} = \mathbb{C} : \boldsymbol{\varepsilon} \text{ on } \Omega \quad (5.38)$$

where \mathbb{C} is the Hooke's tensor. The surface stress $\boldsymbol{\sigma}^s$ is related to the surface strain by surface elasticity of graphene \mathbb{C}^s :

$$\boldsymbol{\sigma}^s = \mathbb{C}^s : \boldsymbol{\varepsilon}^s + \boldsymbol{\tau}^s \text{ on } \Gamma. \quad (5.39)$$

The constitutive relations on the interface Γ_n is generally written as

$$\mathbf{t} = \mathbf{t}([\mathbf{u}]) \text{ on } \Gamma_n \quad (5.40)$$

where

$$[[\mathbf{u}]] = (\mathbf{u}^- - \mathbf{u}^+) \text{ on } \Gamma_n \quad (5.41)$$

The traction can be decomposed into rectangular components, as one normal direction \mathbf{n} and two tangent directions \mathbf{m} , \mathbf{b} .

$$\mathbf{t} = t_n \cdot \mathbf{n} + t_m \cdot \mathbf{m} + t_b \cdot \mathbf{b} \quad (5.42)$$

Due to the extremely low value of shear stiffness compared to the normal direction, the last two terms in Eq. (5.42) corresponding to the shear traction can be ignored in this case. In the directions normal to the interface, the relation between the normal traction and normal displacement jump $[[u_n]]$ in the interface is described in Eq. (5.36).

5.5.2 Computational framework

5.5.2.1 Weak form

To apply the framework to finite element method, we express the potential energy of the system and minimize it with respect to the displacement field in order to get the weak form of the equations. Thus, the potential energy of the system is given by :

$$W = W^b(\boldsymbol{\varepsilon}) + W^s(\boldsymbol{\varepsilon}^s) + W^c([[\mathbf{u}]]) \quad (5.43)$$

where $W^b(\boldsymbol{\varepsilon})$ is the bulk elastic strain energy given by

$$W^b(\boldsymbol{\varepsilon}) = \int_{\Omega} \frac{1}{2} \boldsymbol{\varepsilon} : \mathbb{C} : \boldsymbol{\varepsilon} d\Omega \quad (5.44)$$

and $W^s(\boldsymbol{\varepsilon}^s)$ is the surface elastic energy provided by

$$W^s(\boldsymbol{\varepsilon}^s) = \int_{\Gamma} (\boldsymbol{\tau}^s : \boldsymbol{\varepsilon}^s + \frac{1}{2} \boldsymbol{\varepsilon}^s : \mathbb{C}^s : \boldsymbol{\varepsilon}^s) dS \quad (5.45)$$

$\boldsymbol{\tau}^s$ is the surface residual stress, and $W^c([[\mathbf{u}]])$ is the cohesive energy expressed by

$$W^c([[\mathbf{u}]]) = \int_{\Gamma} [[\mathbf{u}]] \cdot \mathbf{t}([[\mathbf{u}]]) dS. \quad (5.46)$$

Stationarity is obtained by the condition of vanishing Gâteaux (directional) derivative of W in the direction $\delta \mathbf{u}$:

$$D_{\delta \mathbf{u}} W = 0. \quad (5.47)$$

Therefore, we can obtain the weak form as :

$$\int_{\Omega} \boldsymbol{\varepsilon}(\mathbf{u}) : \mathbf{C} : \boldsymbol{\varepsilon}(\delta \mathbf{u}) d\Omega + \int_{\Gamma} \boldsymbol{\varepsilon}^s(\mathbf{u}) : \mathbf{C}^s : \boldsymbol{\varepsilon}^s(\delta \mathbf{u}) dS \quad (5.48)$$

$$+ \int_{\Gamma} \llbracket \delta \mathbf{u} \rrbracket \cdot \mathbf{t}(\llbracket \mathbf{u} \rrbracket) dS = - \int_{\Gamma} \boldsymbol{\tau}^s(\mathbf{u}) : \delta \boldsymbol{\varepsilon}^s(\delta \mathbf{u}) dS, \quad (5.49)$$

where $\mathbf{u} \in H^1(\Omega)$, \mathbf{u} satisfying the boundary condition (5.37) over $\partial\Omega$ and $\delta \mathbf{u} \in H_0^1(\Omega)$, $\delta \mathbf{u} = 0$ over $\partial\Omega$, $\llbracket \delta \mathbf{u} \rrbracket = \delta \mathbf{u}^- - \delta \mathbf{u}^+$ on the cohesive zone.

5.5.2.2 Linearization

It is worth noting that the above problem is nonlinear due to the term $(\mathbf{t}(\llbracket \mathbf{u} \rrbracket))$. To solve this problem, we employ a Newton-Raphson procedure. For this purpose, the linearization of Eq. (5.49) is provided in what follows.

From now on, we assume that $\boldsymbol{\tau}^s = \mathbf{0}$. Setting

$$R = \int_{\Omega} \boldsymbol{\varepsilon}(\mathbf{u}) : \mathbf{C} : \boldsymbol{\varepsilon}(\delta \mathbf{u}) d\Omega + \int_{\Gamma} \boldsymbol{\varepsilon}^s(\mathbf{u}) : \mathbf{C}^s : \boldsymbol{\varepsilon}^s(\delta \mathbf{u}) dS + \int_{\Gamma} \llbracket \delta \mathbf{u} \rrbracket \cdot \mathbf{t}(\llbracket \mathbf{u} \rrbracket) dS, \quad (5.50)$$

a first-order Taylor expansion of R gives :

$$R(\mathbf{u}_k + \Delta \mathbf{u}_k) \simeq R(\mathbf{u}_k) + D_{\Delta \mathbf{u}} R(\mathbf{u}_k). \quad (5.51)$$

where \mathbf{u}_k denotes the displacement field known from a previous iteration k , $\Delta \mathbf{u}_k$ is the increment of displacement. Then linearized problem around the know solution \mathbf{u}_k is given as :

$$D_{\Delta \mathbf{u}} R(\mathbf{u}_k) + R(\mathbf{u}_k) = 0. \quad (5.52)$$

The left-hand term in (5.52) can be expressed as :

$$D_{\Delta \mathbf{u}} R(\mathbf{u}_k) = \int_{\Omega} \boldsymbol{\varepsilon}(\delta \mathbf{u}) : \mathbf{C} : \boldsymbol{\varepsilon}(\Delta \mathbf{u}_k) dv + \int_{\Gamma} \boldsymbol{\varepsilon}^s(\delta \mathbf{u}) : \mathbf{C}^s : \boldsymbol{\varepsilon}^s(\Delta \mathbf{u}_k) dS + \dots \\ + \int_{\Gamma} \llbracket \delta \mathbf{u} \rrbracket \cdot \frac{\partial \mathbf{t}(\llbracket \mathbf{u} \rrbracket)}{\partial \llbracket \mathbf{u} \rrbracket} \Delta \llbracket \mathbf{u}_k \rrbracket dS \quad (5.53)$$

where

$$\frac{\partial \mathbf{t}(\llbracket \mathbf{u} \rrbracket)}{\partial \llbracket \mathbf{u} \rrbracket} = \mathbf{T} = T_n \mathbf{n} \otimes \mathbf{n} \quad (5.54)$$

and

$$T_n = \begin{cases} -3058 \llbracket u_n \rrbracket + 2150, & \text{if } 0 \leq \llbracket u_n \rrbracket < 0.7 \\ -\frac{520}{\llbracket u_n \rrbracket^9} + \frac{60.34}{\llbracket u_n \rrbracket^{15}}, & \text{if } 0.7 \leq \llbracket u_n \rrbracket \leq 1.15 \\ -57.6 \exp(-0.16 \llbracket u_n \rrbracket), & \text{if } \llbracket u_n \rrbracket > 1.15. \end{cases} \quad (5.55)$$

5.5.2.3 Discretization

In the following, the bulk strain and stress tensors are expressed by the vectors $[\sigma] = \{\sigma_{11}, \sigma_{22}, \sigma_{33}, \sigma_{23}, \sigma_{13}, \sigma_{12}\}$ and $[\varepsilon] = \{\varepsilon_{11}, \varepsilon_{22}, \varepsilon_{33}, 2\varepsilon_{23}, 2\varepsilon_{13}, 2\varepsilon_{12}\}$ respectively.

According to the constitutive relations in Eqs. (5.38) and (5.39), the matrix form of the polymer elastic tensor $[C]$ is given by

$$[C] = \begin{bmatrix} \lambda + 2\mu & \lambda & \lambda & 0 & 0 & 0 \\ \lambda & \lambda + 2\mu & \lambda & 0 & 0 & 0 \\ \lambda & \lambda & \lambda + 2\mu & 0 & 0 & 0 \\ 0 & 0 & 0 & \mu & 0 & 0 \\ 0 & 0 & 0 & 0 & \mu & 0 \\ 0 & 0 & 0 & 0 & 0 & \mu \end{bmatrix} \quad (5.56)$$

where λ and μ are the Lamé's constants of polymer matrix, and $[\sigma] = [C][\varepsilon]$.

Similarly, defining the surface stress and strain tensors as vectors $[\sigma]^s = \{\sigma_{11}^s, \sigma_{22}^s, \sigma_{33}^s, \sigma_{23}^s, \sigma_{13}^s, \sigma_{12}^s\}$ and $[\varepsilon]^s = \{\varepsilon_{11}^s, \varepsilon_{22}^s, \varepsilon_{33}^s, 2\varepsilon_{23}^s, 2\varepsilon_{13}^s, 2\varepsilon_{12}^s\}$ respectively, the surface stiffness matrix $[C^s]$ is expressed as :

$$[C^s] = \begin{bmatrix} (\lambda^s + 2\mu^s)P_{11}^2 & \lambda^s P_{11}P_{22} + 2\mu^s P_{12}^2 & \lambda^s P_{11}P_{33} + 2\mu^s P_{13}^2 \\ \lambda^s P_{11}P_{22} + 2\mu^s P_{12}^2 & (\lambda^s + 2\mu^s)P_{22}^2 & \lambda^s P_{22}P_{33} + 2\mu^s P_{23}^2 \\ \lambda^s P_{11}P_{33} + 2\mu^s P_{13}^2 & \lambda^s P_{22}P_{33} + 2\mu^s P_{23}^2 & (\lambda^s + 2\mu^s)P_{33}^2 \\ \lambda^s P_{11}P_{23} + 2\mu^s P_{12}P_{13} & (\lambda^s + 2\mu^s)P_{22}P_{23} & (\lambda^s + 2\mu^s)P_{23}P_{33} \\ (\lambda^s + 2\mu^s)P_{11}P_{13} & \lambda^s P_{13}P_{22} + 2\mu^s P_{12}P_{23} & (\lambda^s + 2\mu^s)P_{13}P_{33} \\ (\lambda^s + 2\mu^s)P_{11}P_{12} & (\lambda^s + 2\mu^s)P_{12}P_{22} & \lambda^s P_{12}P_{33} + 2\mu^s P_{13}P_{23} \\ \lambda^s P_{11}P_{23} + 2\mu^s P_{12}P_{13} & (\lambda^s + 2\mu^s)P_{11}P_{13} & (\lambda^s + 2\mu^s)P_{11}P_{12} \\ (\lambda^s + 2\mu^s)P_{22}P_{23} & \lambda^s P_{13}P_{22} + 2\mu^s P_{12}P_{23} & (\lambda^s + 2\mu^s)P_{12}P_{22} \\ (\lambda^s + 2\mu^s)P_{23}P_{33} & (\lambda^s + 2\mu^s)P_{13}P_{33} & \lambda^s P_{12}P_{33} + 2\mu^s P_{13}P_{23} \\ \lambda^s P_{23}^2 + \mu^s (P_{22}P_{33} + P_{23}^2) & \lambda^s P_{13}P_{23} + \mu^s (P_{13}P_{23} + P_{12}P_{33}) & \lambda^s P_{12}P_{23} + \mu^s (P_{13}P_{22} + P_{12}P_{23}) \\ \lambda^s P_{13}P_{23} + \mu^s (P_{13}P_{23} + P_{12}P_{33}) & \lambda^s P_{13}^2 + \mu^s (P_{11}P_{33} + P_{13}^2) & \lambda^s P_{12}P_{13} + \mu^s (P_{11}P_{23} + P_{12}P_{13}) \\ \lambda^s P_{12}P_{23} + \mu^s (P_{13}P_{22} + P_{12}P_{23}) & \lambda^s P_{12}P_{13} + \mu^s (P_{11}P_{23} + P_{12}P_{13}) & \lambda^s P_{12}^2 + \mu^s (P_{11}P_{22} + P_{12}^2) \end{bmatrix} \quad (5.57)$$

where λ^s and μ^s are the surface Lamé's constants of graphene and satisfying $[\sigma^s] = [C^s][\varepsilon^s]$. The surface strain matrix is related to the bulk strain matrix through matrix $[Q]$, with the equation $[\varepsilon^s] = [Q][\varepsilon]$, and the matrix $[Q]$ is defined as

$$[Q] = \begin{bmatrix} P_{11}^2 & P_{12}^2 & P_{13}^2 & P_{12}P_{13} & P_{11}P_{13} & P_{11}P_{12} \\ P_{12}^2 & P_{22}^2 & P_{23}^2 & P_{22}P_{23} & P_{12}P_{23} & P_{12}P_{22} \\ P_{13}^2 & P_{23}^2 & P_{33}^2 & P_{23}P_{33} & P_{13}P_{33} & P_{13}P_{23} \\ 2P_{12}P_{13} & 2P_{22}P_{23} & 2P_{23}P_{33} & P_{23}^2 + P_{22}P_{33} & P_{12}P_{33} + P_{13}P_{23} & P_{12}P_{23} + P_{13}P_{22} \\ 2P_{11}P_{13} & 2P_{12}P_{23} & 2P_{13}P_{33} & P_{12}P_{33} + P_{13}P_{23} & P_{13}^2 + P_{11}P_{33} & P_{11}P_{23} + P_{13}P_{12} \\ 2P_{11}P_{12} & 2P_{12}P_{22} & 2P_{13}P_{23} & P_{12}P_{23} + P_{13}P_{22} & P_{11}P_{23} + P_{12}P_{13} & P_{12}^2 + P_{11}P_{22} \end{bmatrix} \quad (5.58)$$

The domain Ω is discretized into a mesh of n_{el} element whose shape functions are denoted by \mathbf{N}^i . The unknown displacement field \mathbf{u} is interpolated on the element level with the same shape functions in terms of the nodal displacement values \mathbf{u}_i . These shape functions are also used to interpolate the test function $\delta\mathbf{u}$.

$$\mathbf{u}(\mathbf{x})|_{\Omega^e} = \sum_{i=1}^{n_{en}} \mathbf{N}^i(\mathbf{x}) \cdot \mathbf{u}_i, \quad \delta\mathbf{u}(\mathbf{x})|_{\Omega^e} = \sum_{i=1}^{n_{en}} \mathbf{N}^i(\mathbf{x}) \cdot \delta\mathbf{u}_i \quad (5.59)$$

The approximation of the jump in the displacement field can be described by the approximation of displacements on the corresponding elements on the crack surface Γ_n^+ and Γ_n^- .

$$[[\mathbf{u}]]|_{\Gamma_n^e} = \sum_{i=1}^{n_{en}} \mathbf{N}^i|_{\Gamma_n^{e-}} \mathbf{u}_{i-} - \sum_{i=1}^{n_{en}} \mathbf{N}^i|_{\Gamma_n^{e+}} \mathbf{u}_{i+} = \sum_{p=1}^{2n_{en}} [M^p] \mathbf{u}_p \quad (5.60)$$

$$[[\delta\mathbf{u}]]|_{\Gamma_n^e} = \sum_{i=1}^{n_{en}} \mathbf{N}^i|_{\Gamma_n^{e-}} \delta\mathbf{u}_{i-} - \sum_{i=1}^{n_{en}} \mathbf{N}^i|_{\Gamma_n^{e+}} \delta\mathbf{u}_{i+} = \sum_{p=1}^{2n_{en}} [M^p] \delta\mathbf{u}_p \quad (5.61)$$

$$[[\Delta\mathbf{u}]]|_{\Gamma_n^e} = \sum_{i=1}^{n_{en}} \mathbf{N}^i|_{\Gamma_n^{e-}} \Delta\mathbf{u}_{i-} - \sum_{i=1}^{n_{en}} \mathbf{N}^i|_{\Gamma_n^{e+}} \Delta\mathbf{u}_{i+} = \sum_{p=1}^{2n_{en}} [M^p] \Delta\mathbf{u}_p \quad (5.62)$$

Thereby, \mathbf{u}_{i-} and \mathbf{u}_{i+} denote the displacements at the element nodes, belonging to Γ_n^- and Γ_n^+ , respectively. The newly introduced term $[M]$ comprises the shape function \mathbf{N} evaluated on Γ_n^- and Γ_n^+ , and associated with the sign '-' for the degrees of freedom belonging to Γ_n^- and '+' for those to Γ_n^+ .

Introducing Eqs. (5.53)-(5.62) into Eq. (5.52), with

$$\boldsymbol{\varepsilon}(\Delta\mathbf{u}) = [B] \cdot \Delta\mathbf{u} \quad (5.63)$$

$$\boldsymbol{\varepsilon}(\delta \mathbf{u}) = [B] \cdot \delta \mathbf{u} \quad (5.64)$$

where $[B]$ is the derivative of the shape function, the following discrete system of linear equation is obtained

$$([K^b] + [K^s] + [K^c])\Delta \mathbf{u} = [R^b] + [R^s] + [R^c] \quad (5.65)$$

where $[K^b]$, $[K^s]$ and $[K^c]$ denote the bulk, graphene surface and crack surface stiffness matrix. $[R^b]$, $[R^s]$ and $[R^c]$ are the corresponding residual terms, and $\Delta \mathbf{u}$ is the incremental displacement field. The matrices $[K^b]$, $[K^s]$, $[K^c]$, $[R^b]$, $[R^s]$ and $[R^c]$ are defined by :

$$[K^b] = \int_{\Omega} [B]^T [C] [B] dV \quad (5.66)$$

$$[K^s] = \int_{\Gamma} [B]^T [Q]^T [C^s] [Q] [B] dS \quad (5.67)$$

$$[K^c] = \int_{\Gamma} [M^e]^T [T] [M^e] dS \quad (5.68)$$

$$[R^b] = - \int_{\Omega} [B]^T \boldsymbol{\sigma}(\mathbf{u}_k) dV \quad (5.69)$$

$$[R^s] = - \int_{\Gamma} [B]^T [Q]^T [C^s] [\boldsymbol{\varepsilon}^s] dS \quad (5.70)$$

$$[R^c] = - \int_{\Gamma} [M^e]^T \mathbf{t}(\llbracket \mathbf{u}_k \rrbracket) dS. \quad (5.71)$$

where

$$[B] = \begin{bmatrix} \frac{\partial N_1}{\partial X_1} & 0 & 0 & \frac{\partial N_2}{\partial X_1} & 0 & 0 & \frac{\partial N_3}{\partial X_1} & 0 & 0 & \frac{\partial N_4}{\partial X_1} & 0 & 0 \\ 0 & \frac{\partial N_1}{\partial X_2} & 0 & 0 & \frac{\partial N_2}{\partial X_2} & 0 & 0 & \frac{\partial N_3}{\partial X_2} & 0 & 0 & \frac{\partial N_4}{\partial X_2} & 0 \\ 0 & 0 & \frac{\partial N_1}{\partial X_3} & 0 & 0 & \frac{\partial N_2}{\partial X_3} & 0 & 0 & \frac{\partial N_3}{\partial X_3} & 0 & 0 & \frac{\partial N_4}{\partial X_3} \\ \frac{\partial N_1}{\partial X_2} & \frac{\partial N_1}{\partial X_1} & 0 & \frac{\partial N_2}{\partial X_2} & \frac{\partial N_2}{\partial X_1} & 0 & \frac{\partial N_3}{\partial X_2} & \frac{\partial N_3}{\partial X_1} & 0 & \frac{\partial N_4}{\partial X_2} & \frac{\partial N_4}{\partial X_1} & 0 \\ \frac{\partial N_1}{\partial X_3} & 0 & \frac{\partial N_1}{\partial X_1} & \frac{\partial N_2}{\partial X_3} & 0 & \frac{\partial N_2}{\partial X_1} & \frac{\partial N_3}{\partial X_3} & 0 & \frac{\partial N_3}{\partial X_1} & \frac{\partial N_4}{\partial X_3} & 0 & \frac{\partial N_4}{\partial X_1} \\ 0 & \frac{\partial N_1}{\partial X_3} & \frac{\partial N_1}{\partial X_2} & 0 & \frac{\partial N_2}{\partial X_3} & \frac{\partial N_2}{\partial X_2} & 0 & \frac{\partial N_3}{\partial X_3} & \frac{\partial N_3}{\partial X_2} & 0 & \frac{\partial N_4}{\partial X_3} & \frac{\partial N_4}{\partial X_2} \end{bmatrix} \quad (5.72)$$

5.5.3 Tension test

In the following numerical examples, the Lamé constants of the polymer matrix (PE) are $\lambda = 6890$ MPa, and $\mu = 820$ MPa. The surface Lamé constants of the single layer graphene are $\lambda^s = 95.04$ GPa, and $\mu^s = 93.4$ GPa. The cohesive law is written in Eq. (5.36). The parameters have been identified by the molecular dynamics procedure described in section 5.4 under the assumption of Dreiding potential.

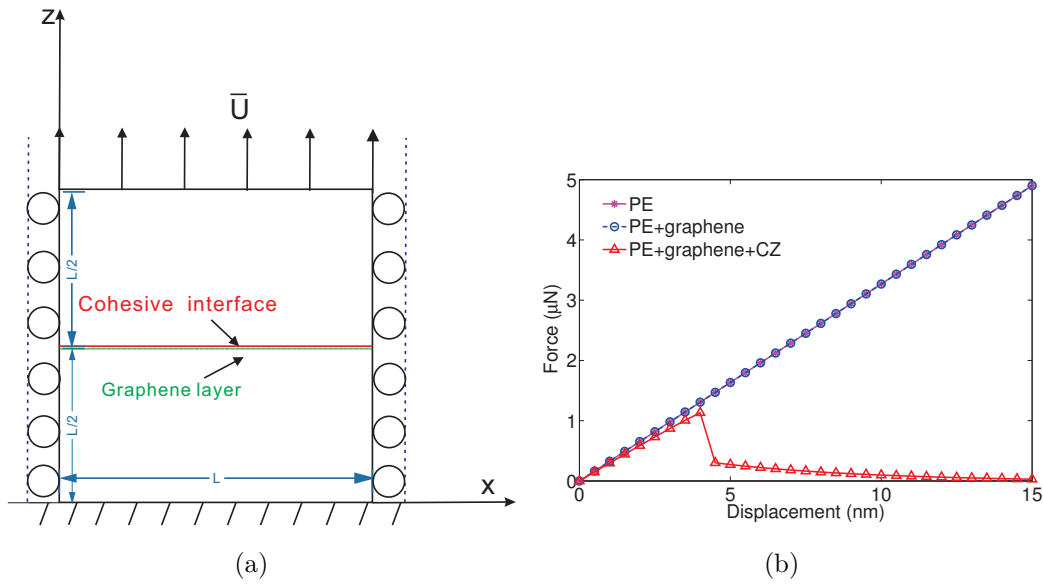


FIGURE 5.7 – Tension test example. (a) Geometry and boundary conditions. (b) Load-displacement response.

In this first example, we consider a cubic structure with a single layer graphene in the middle of the domain including a cohesive zone to check the influence of the interface. A uniform displacement is loaded as $u_z(z) = \bar{\epsilon}_{33}z$, and the displacement on the bottom surface is fixed. The geometry and the loading conditions are provided in Fig. 5.7 (a). The length of the cubic domain is $L = 40$ nm.

The computed load-displacement responses are depicted in Fig. 5.7 (b). Assuming that the domain is pure PE, a linear load-displacement behavior is obtained. The introduction of single graphene layer without normal damage does not influence the response as the imperfect interface model of the Gurtin-Murdoch type only implies an additional stiffness in the tangential direction. However, taking into account the cohesive zone model along the normal di-

rection, we observe a decrease of load when the displacement exceeds 4.5 nm, and the load finally drops to zero for a displacement of 15 nm.

5.5.4 RVE analysis

To determine a proper size of representative volume element (RVE), we analyze the convergence of the effective Young's moduli and shear moduli of the composite as a function of the size of the RVE. Periodic boundary conditions are prescribed. For each size of the cubic domain defining the RVE, 30 realizations of random microstructures with the same graphene volume fraction (1.05 vol%) are computed to determine the effective stiffness tensor by classical computational homogenization, for overall strain components of 0.01 %. Samples with side length ranging from 30 to 80 nm are analyzed. Graphene sheets are modeled as square domains with dimensions $15 \times 15 \text{ nm}^2$ and a thickness of 0.2 nm, which is taken into account through the surface model. Fig. 5.8 (a-f) provides the effective Young's moduli and E_{11} , E_{22} , E_{33} , and shear moduli G_{11} , G_{22} , G_{33} as a function of the domain size. It shows that the dispersion of results decreases when the size of the volume increases, and the results converge at large size of RVE. In the following computation, we take the side length of RVE to be 70 nm.

We then define an isotropy error parameter to further discuss this problem. All the symmetric fourth-order tensors can be expressed as the combination of the fourth-order identity tensor \mathbb{I} ($2I_{ijkl} = \delta_{ik}\delta_{jl} + \delta_{il}\delta_{jk}$) and $\mathbf{I} \otimes \mathbf{I}$, where \mathbf{I} is the second-order identity tensor. Generally, we choose to express a tensor as a combination of the following two tensors :

$$\mathbb{J} = \frac{1}{3}\mathbf{I} \otimes \mathbf{I} \tag{5.73}$$

and

$$\mathbb{K} = \mathbb{I} - \mathbb{J} \tag{5.74}$$

which satisfy the properties as

$$\mathbb{J} : \mathbb{J} = \mathbb{J}, \quad \mathbb{K} : \mathbb{K} = \mathbb{K}, \quad \mathbb{J} : \mathbb{K} = \mathbb{K} : \mathbb{J} = \mathbf{0}. \tag{5.75}$$

Since \mathbb{J} and \mathbb{K} are the projection tensors in space, for any averaged computed effective stiffness tensor of the graphene nanocomposite $\overline{\mathbb{C}}$, we can get

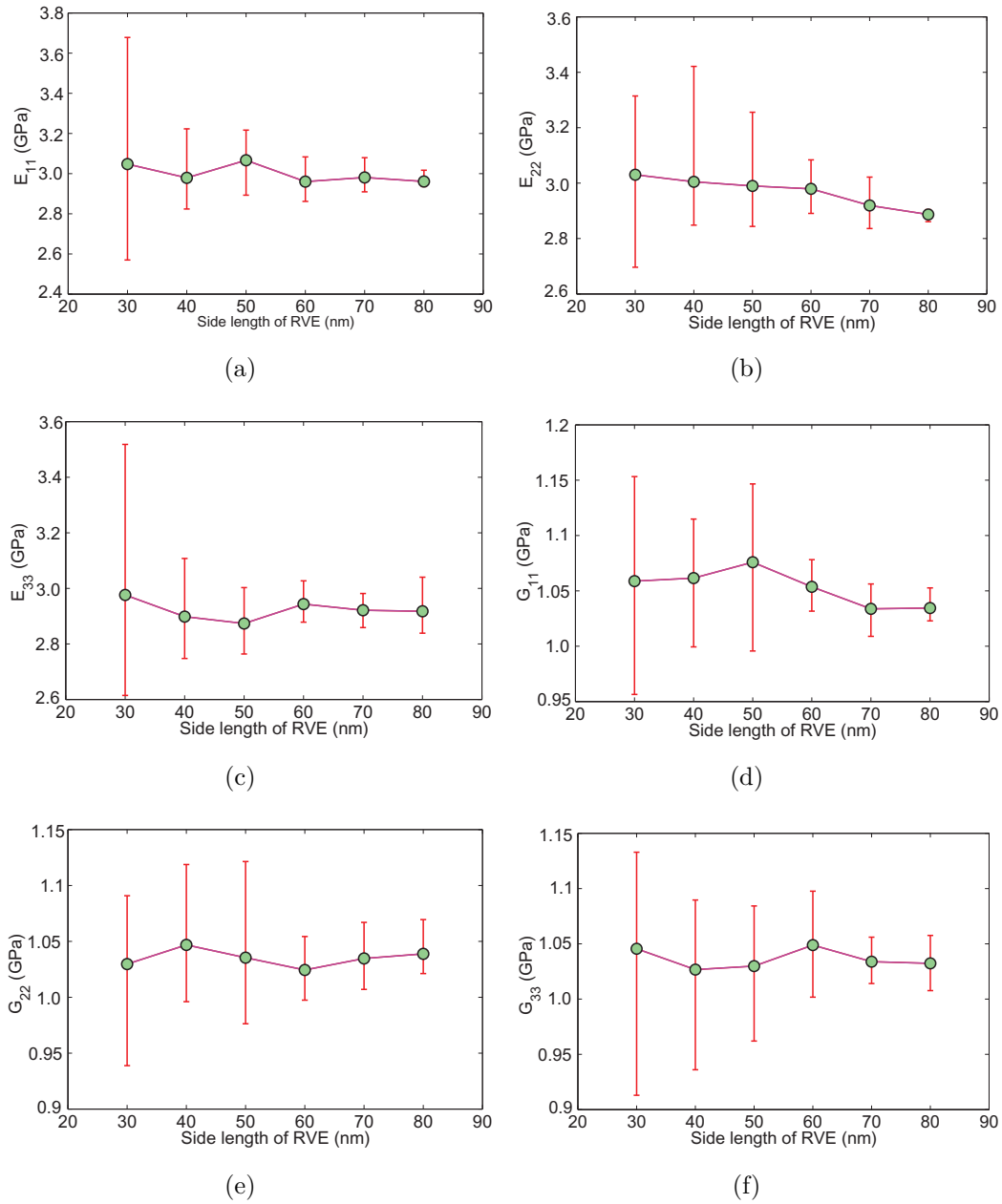


FIGURE 5.8 – Effective Young's moduli and shear moduli along the RVE size. The dimension of graphene sheets is $15 \times 15 \times 0.2 \text{ nm}^3$, and the graphene volume fraction is 1.05 vol%.

the symmetric isotropic tensor as :

$$\bar{\mathbb{C}}_{iso} = (\mathbb{J} :: \bar{\mathbb{C}})\mathbb{J} + \frac{1}{5}(\mathbb{K} :: \bar{\mathbb{C}})\mathbb{K}. \quad (5.76)$$

Then the isotropy error is given by

$$ERR = \frac{\|\bar{\mathbb{C}} - \bar{\mathbb{C}}_{iso}\|}{\|\bar{\mathbb{C}}_{iso}\|}. \quad (5.77)$$

It is obvious that $ERR = 0$ for the isotropic material, and it increases along with the anisotropy properties of the material. We then take two different sizes of RVE, with side length of 30 nm and 70 nm respectively, and analyze the isotropy error as a function of the number of the samples provided (see in Fig. 5.9). It shows that the ERR values for small RVE ($L = 30$ nm) converges when the number of the samples is about 40, while for the larger RVE ($L = 70$ nm), the ERR value becomes steady when the number of the samples is over 10. That is to say, at the case of $L = 30$ nm, the results of the calculated effective stiffness of the graphene nanocomposites is reliable only if we take the average value of more than 40 samples. However, as for the case of $L = 70$ nm, 10 numerical samples with independent microstructures can present a good estimation of the mechanical properties.

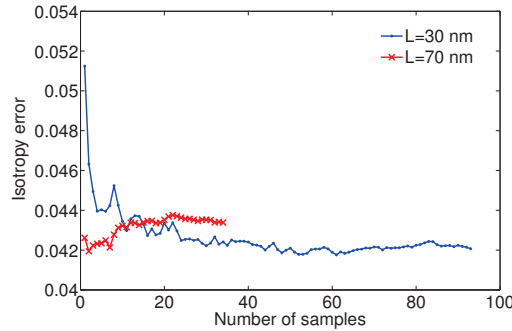


FIGURE 5.9 – Isotropy error as a function of various numbers of samples for the RVEs with side length $L=30$ nm, 70 nm respectively.

5.5.5 Mechanical properties of graphene/PE nanocomposites

Then we can use this methodology taking into account the interfacial behavior to investigate the effective Young's moduli and shear moduli of graphene

reinforced nanocomposites with various graphene volume fraction. The graphene sheets are still defined as square surfaces with the size $15 \times 15 \text{ nm}^2$, and a fixed thickness of 0.2 nm, which are randomly distributed in the RVE with the size of 70 nm. The volume fraction is obtained by increasing the number of introduced graphene sheets in the domain. The examples are given for small deformations $\bar{\epsilon}_{ij} = 0.01\%$, and periodical boundary conditions are prescribed.

The numerical results are provided in Fig. 5.10 for graphene/PE nanocomposite with varying graphene volume fractions. Taking into account the cohesive interface between inclusion and matrix, the numerical values of E_{ii} and G_{ii} ($i=1,2,3$) are plotted for each volume fraction as shown in Fig.5.10 (a-f), where the average values are obtained for 10 realizations, as a comparison of the estimations neglecting the interfacial behavior. It indicates that the elastic moduli of the graphene-reinforced nanocomposites increases with the graphene volume fraction. As expected, as compared with the computational results without the cohesive interface, the introduction of interface decreases the stiffness of the composites, and plays an important role especially at large graphene volume fraction. An increase of around 30% of the moduli is exhibited when the graphene volume fraction reaches 1.5 vol%. The experimental results in some literatures [Liang 2009a, Martin-Gallego 2013] show 50% and 62% improvement of Young's modulus by the addition of 1.5 wt% functionalized graphene sheets and 0.7 wt% graphene oxide respectively. There are several reasons for the higher experimental results compared to our numerical results : firstly, the aspect ratio of graphene in the experiments can be larger than our assumption in the numerical example ; secondly, the functionalized graphene sheets and graphene oxide show enhancement of the interfacial interaction with the polymer matrix ; moreover, the Young's modulus of the graphene nanocomposites also depends on the microstructures of the samples, where the aggregation or alignment of the graphene sheets has big influence of the results.

We also compute the isotropy error values for the composites with a series of graphene volume fraction as shown in Fig. 5.11. Each point in the figure is calculated on the basis of 10 samples of independent microstructures. The ascending curve indicates that the addition of graphene can increase the anisotropy level of the nanocomposites at small graphene concentration.

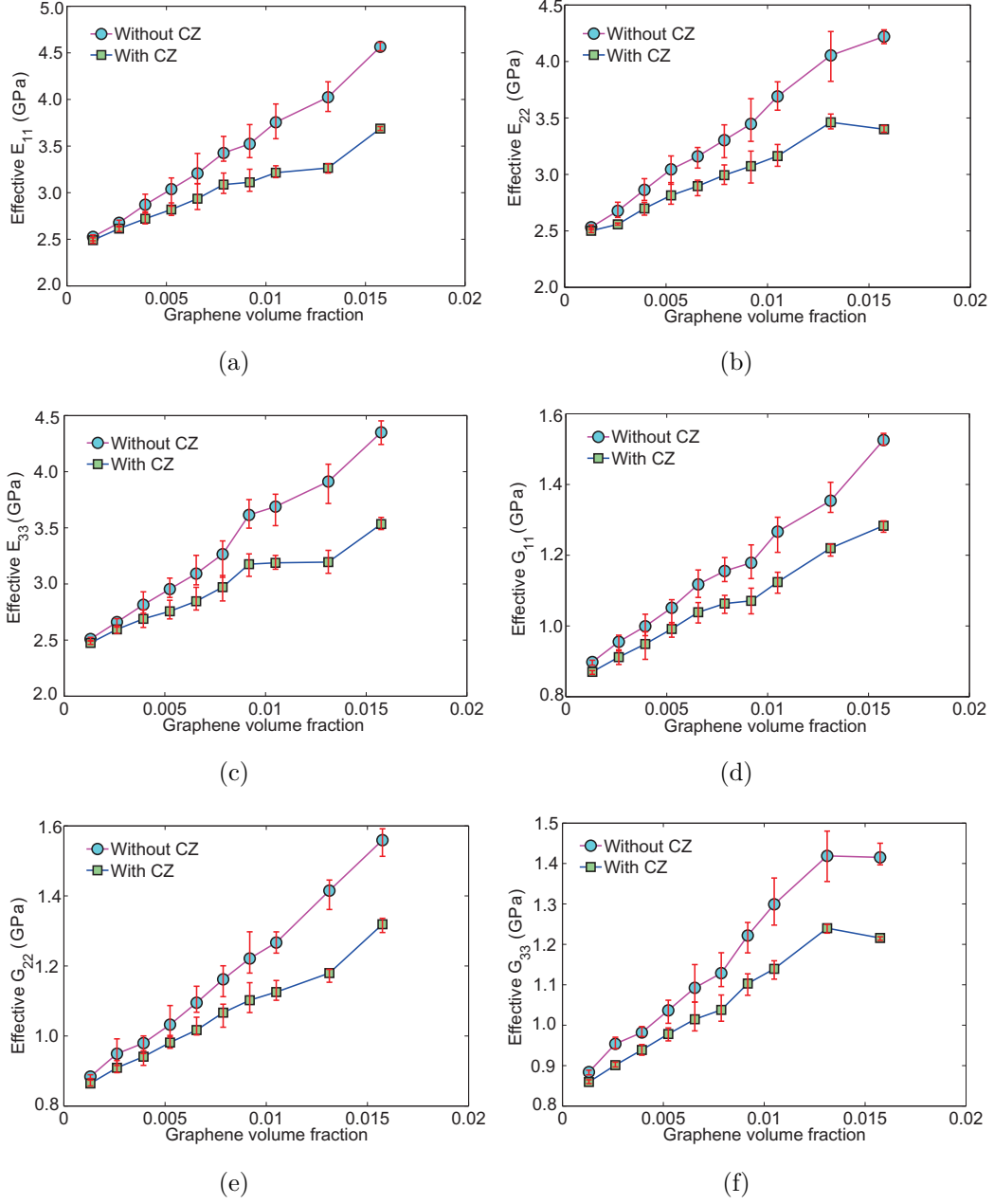


FIGURE 5.10 – Effective Young’s moduli and shear moduli along with the increase of graphene volume fraction. Graphene sheets are randomly distributed in the RVE, which has the side length of 70 nm. The dimensions of graphene sheets are $15 \times 15 \times 0.2 \text{ nm}^3$.

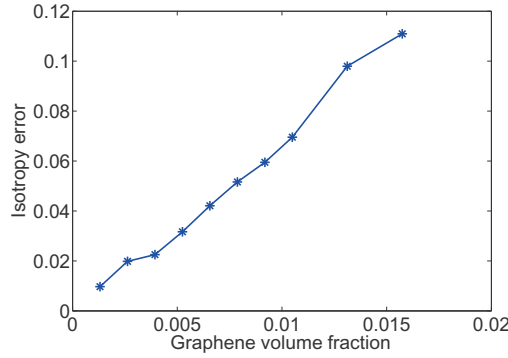


FIGURE 5.11 – Isotropy error of the graphene reinforced nanocomposites as a function of graphene volume fraction.

5.5.6 Comparison with analytical solutions

We examined the results obtained from our present work along with the two conventional homogenization theory, *i.e.* Mori-Tanaka (MT) theory [Weng 1990, Weng 1984, Benveniste 1987], and Lielens theory [Lielens 1999]. And the Hashin-Strikman (HS) boundings [Hashin 1963] are also presented as a theoretical footing. Assuming that the the graphene is ellipsoidal, the MT theory for the effective stiffness tensor of graphene-polymer nanocomposite can be written as a function of graphene volume fraction f :

$$\mathbb{C}_{MT} = \mathbb{C}_p + f(\mathbb{C}_g - \mathbb{C}_p) : \mathbb{A}_{MT} \quad (5.78)$$

where \mathbb{C}_p and \mathbb{C}_g are the stiffness tensors for polymer matrix and graphene inclusion respectively, and \mathbb{A}_{MT} is the Mori-Tanaka stress concentration tensor for the inclusion expressed as

$$\mathbb{A}_{MT} = \mathbb{A}_{dil} : [(1 - f)\mathbb{I} + f\mathbb{A}_{dil}]^{-1} \quad (5.79)$$

where \mathbb{I} is the fourth order identity tensor. The dilute inclusion concentration tensor, \mathbb{A}_{dil} , is given by

$$\mathbb{A}_{dil} = [\mathbb{I} + \mathbb{S} : \mathbb{C}_p^{-1} : (\mathbb{C}_g - \mathbb{C}_p)] \quad (5.80)$$

where \mathbb{S} is the Eshelby tensor [Eshelby 1957] associated with the shape of the graphene. Assuming that the inclusion is isotropic, the Eshelby's tensor for an ellipsoidal inclusion with semi-axes a , b , c can be expressed in terms of

elliptic integrals. In the case of flat ellipsoid with penny shape ($a = b \gg c$), the Eshelby's tensor reduces to

$$\begin{aligned}
 \mathbb{S}_{1111} = \mathbb{S}_{2222} &= \frac{\pi(13 - 8\nu) c}{32(1 - \nu) a}, \\
 \mathbb{S}_{3333} &= 1 - \frac{\pi(1 - 2\nu) c}{4(1 - \nu) a}, \\
 \mathbb{S}_{1122} = \mathbb{S}_{2211} &= \frac{\pi(8\nu - 1) c}{32(1 - \nu) a}, \\
 \mathbb{S}_{1133} = \mathbb{S}_{2233} &= \frac{\pi(2\nu - 1) c}{8(1 - \nu) a}, \\
 \mathbb{S}_{3311} = \mathbb{S}_{3322} &= \frac{\nu}{1 - \nu} \left(1 - \frac{\pi(4\nu + 1) c}{8\nu a} \right), \\
 \mathbb{S}_{1212} &= \frac{\pi(7 - 8\nu) c}{32(1 - \nu) a}, \\
 \mathbb{S}_{3131} = \mathbb{S}_{2323} &= \frac{1}{2} \left(1 + \frac{\pi(\nu - 2) c}{4(1 - \nu) a} \right), \\
 \mathbb{S}_{1112} = \mathbb{S}_{1223} = \mathbb{S}_{1232} &= 0,
 \end{aligned} \tag{5.81}$$

where ν is the Poisson's ratio of the matrix.

The upper and lower Hashin-Shtrikman bounds of the elasticity tensor are given by :

$$\mathbb{C}_{HS(+)} = \mathbb{C}_g + (1 - f) \left[(\mathbb{C}_p - \mathbb{C}_g)^{-1} + f \mathbb{S}_g : \mathbb{C}_g^{-1} \right]^{-1}, \tag{5.82}$$

$$\mathbb{C}_{HS(-)} = \mathbb{C}_p + f \left[(\mathbb{C}_g - \mathbb{C}_p)^{-1} + (1 - f) \mathbb{S}_p : \mathbb{C}_p^{-1} \right]^{-1}. \tag{5.83}$$

Furthermore, the elastic moduli of polymer composites are also predicted by Lielens method, given by

$$\mathbb{C}_{LIL} = \left[\left(1 - \frac{f + f^2}{2} \right) \mathbb{C}_{MT^{-1}}^{-1} + \frac{f + f^2}{2} \mathbb{C}_{MT}^{-1} \right]^{-1} \tag{5.84}$$

in which \mathbb{C}_{MT} is the estimation for the effective elasticity from the Mori-Tanaka method. $\mathbb{C}_{MT^{-1}}$ is the effective elasticity tensor following from the inverse Mori-Tanaka approximation in which, for a two-phase material, the inclusion part becomes matrix material and vice versa.

We have plotted the effective Young's moduli by MT and Lielens theory, as well as our present work by FEM in Fig. 5.12, with the graphene aspect ratio of $\gamma = 75$. It should be noted that lower HS bound corresponds to the

Mori-Tanaka result, and both our FEM results and the Lielens curve reside between the HS bounds. Zoom in the initial section of the curves (see in Fig. 5.12 (b)), we can see that the numerical results quite agree with the MT model at small graphene volume fraction.

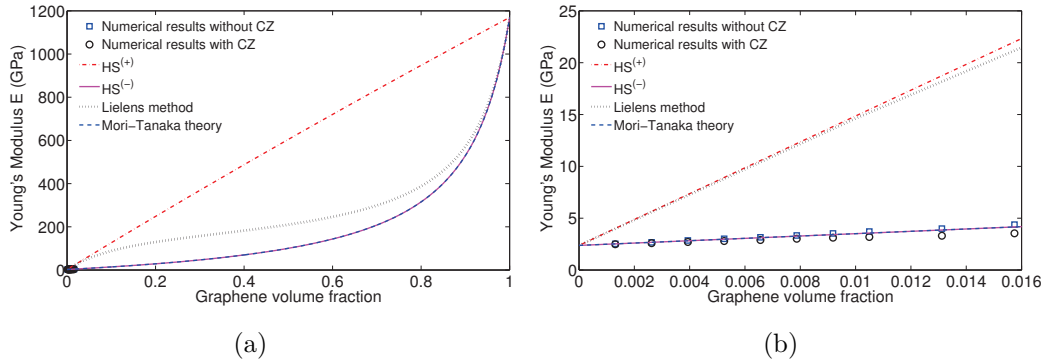


FIGURE 5.12 – The effective Young's modulus calculated by FEM due to our present work, as well as the estimations by MT and Lielens theory. The graphene aspect ratio $\gamma = 75$. The Hashin-Shtrikman upper and lower bounds are also shown. (a) Graphene volume fraction from 0 to 1, (b) Zoom in the small graphene volume fraction part.

5.6 Finite deformation analysis of graphene reinforced polymer nanocomposites

5.6.1 General introduction to the finite deformation problems

5.6.1.1 Kinematic

We consider a deformable solid \mathcal{B} which occupies an open domain $\Omega_0 \subset \mathbb{R}^3$ with boundary $\partial\Omega_0$ at the initial instant, as indicated in Fig. 5.13. The state Ω_0 supposed to be nature, *i.e.* free of constraints, refers to the reference (or initial) configuration. Applying the external forces or displacements on the boundary of the solid, it occupies a new domain $\Omega \subset \mathbb{R}^3$ with boundary $\partial\Omega$ after the displacement and deformation. This new domain Ω corresponds to the current (or deformed) configuration.

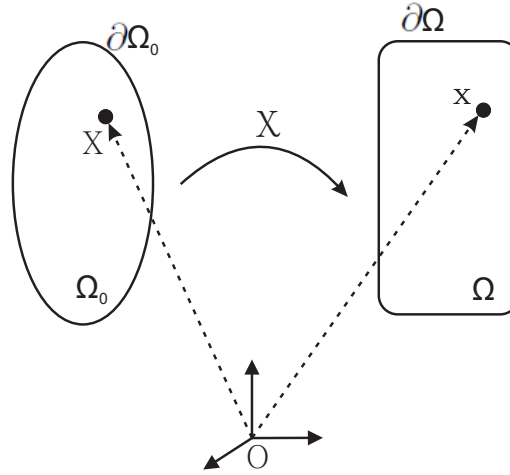


FIGURE 5.13 – Configuration and motion of a continuum body.

Each material point P_0 in domain Ω_0 is localized by the position vector \mathbf{X} in a fixed orthogonal frame. After the deformation, the particle occupies the point P in Ω localized by the vector \mathbf{x} . The Lagrangian description of the motion of particle P from vector \mathbf{X} to vector \mathbf{x} is given by the transformation χ

$$\mathbf{x} = \chi(\mathbf{X}, t) \quad (5.85)$$

where χ is a vector field which is uniquely invertible called the motion of the body \mathcal{B} , thus

$$\mathbf{X} = \chi^{-1}(\mathbf{x}, t). \quad (5.86)$$

The displacement field \mathbf{u} in the spatial description is a function of the current position \mathbf{x} and time t

$$\mathbf{u}(\mathbf{x}, t) = \mathbf{x} - \mathbf{X}(\mathbf{x}, t). \quad (5.87)$$

The deformation gradient \mathbf{F} is defined as :

$$\mathbf{F} = \frac{\partial \mathbf{x}}{\partial \mathbf{X}} = \nabla_{\mathbf{X}} \mathbf{x} \quad (5.88)$$

where $\nabla_{\mathbf{X}}$ is the gradient operator with regard to the initial configuration, and \mathbf{F} is a second-order tensor defining the transformation from the vector $d\mathbf{X}$ to $d\mathbf{x}$.

To combine the deformation gradient with the displacement vector, we deduce from Eq. (5.87) and Eq. (5.88) that

$$\nabla_{\mathbf{x}}\mathbf{u} = \mathbf{F} - \mathbf{I}. \quad (5.89)$$

and $\nabla_{\mathbf{x}}\mathbf{u}$ is a second-order tensor, and \mathbf{I} is a second-order identity tensor..

The change of the volume element between reference and current configuration at time t is given as

$$dv = JdV \quad (5.90)$$

where $J = \det \mathbf{F} > 0$, known as the Jacobian determinant. If there is no motion, we can obtain the consistency condition $J = 1$. dV and dv denote infinitesimal volume elements defined in the reference and current configurations respectively. Moreover, the vector elements of the infinitesimally small areas ds and dS on the current and reference configuration are related by Nanson's formula expressed as

$$\mathbf{n}ds = J\mathbf{F}^{-T}\mathbf{N}dS \quad (5.91)$$

where \mathbf{n} and \mathbf{N} are the normal vector of the surface element ds of Ω , and that of the surface element dS of Ω_0 , respectively.

The right Cauchy-Green tensor \mathbf{C} is defined as :

$$\mathbf{C} = \mathbf{F}^T\mathbf{F}. \quad (5.92)$$

\mathbf{C} is a symmetric and positive definition satisfying

$$\begin{aligned} \mathbf{C} &= \mathbf{C}^T, \\ \det \mathbf{C} &= (\det \mathbf{F})^2 = J^2 > 0. \end{aligned} \quad (5.93)$$

The left Cauchy-Green tensor, $\hat{\mathbf{B}}$, is defined by :

$$\hat{\mathbf{B}} = \mathbf{F}\mathbf{F}^T \quad (5.94)$$

which is an important strain measure in terms of spatial coordinates. The commonly used strain tensor, Green-Lagrange strain tensor, $\hat{\mathbf{E}}$ is expressed as

$$\hat{\mathbf{E}} = \frac{1}{2}(\mathbf{F}^T\mathbf{F} - \mathbf{I}). \quad (5.95)$$

Let a surface locally plane at a given point $\mathbf{x} \in \Omega$ at time t , and \mathbf{n} is the unit vector at \mathbf{x} directed along the outward normal to an infinitesimal spatial surface element $ds \in \partial\Omega$ corresponding to the quantities \mathbf{x} , \mathbf{n} and ds which are associated with the current configuration, we also define the notations \mathbf{X} , \mathbf{N} and dS referring to the reference configuration. Therefore, for every surface elements, we have

$$d\mathbf{f} = \boldsymbol{\sigma} \mathbf{n} ds., \quad (5.96)$$

where $\boldsymbol{\sigma}$ is the Cauchy stress tensor.

According to the Nanson's formula in Eq. (5.91), we can transfer the surface element from Ω to Ω_0 :

$$d\mathbf{f} = \boldsymbol{\sigma} J \mathbf{F}^{-T} \mathbf{N} dS = \hat{\mathbf{P}} \mathbf{N} dS \quad (5.97)$$

where $\hat{\mathbf{P}} = J \boldsymbol{\sigma} \mathbf{F}^{-T}$ denotes the first Piola-Kirchhoff tensor. Generally, $\hat{\mathbf{P}}$ is not symmetric and satisfies the properties $\hat{\mathbf{P}} \mathbf{F}^T = \mathbf{F} \hat{\mathbf{P}}^T$. The second way to realize this transformation from Ω to Ω_0 is that

$$d\mathbf{f}_0 = \mathbf{F}^{-1} d\mathbf{f} = \mathbf{S} \mathbf{N} dS \quad (5.98)$$

where $\mathbf{S} = J \mathbf{F}^{-1} \boldsymbol{\sigma} \mathbf{F}^{-T}$ denotes the second Piola-Kirchhoff stress tensor. \mathbf{S} is a symmetric second-order tensor and has the relation with the first Piola-Kirchhoff tensor $\hat{\mathbf{P}}$ as

$$\hat{\mathbf{P}} = \mathbf{F} \mathbf{S}. \quad (5.99)$$

5.6.1.2 Constitutive equations of hyperelastic materials

The hyperelastic material postulates the existence of a strain energy function W , which is defined per unit reference volume

$$W = W(\mathbf{F}). \quad (5.100)$$

The strain energy W should satisfy the objective principle, which means that the amount of the energy is unchanged after a translation and rotation of the reference object. Therefore, W is not an arbitrary function of \mathbf{F} and must obey the restriction for all tensors \mathbf{F}

$$W(\mathbf{F}) = W(\mathbf{Q}\mathbf{F}) \quad (5.101)$$

where \mathbf{Q} is a orthogonal tensor satisfying $\mathbf{Q}^{-1} = \mathbf{Q}^T$ and $\det \mathbf{Q} = 1$. Therefore, making use of the right polar decomposition of \mathbf{F} , which is to say $\mathbf{F} = \mathbf{R}\mathbf{U}$, and taking a special choice of \mathbf{Q} , for instance $\mathbf{Q} = \mathbf{R}^T$, we can find from Eq. (5.101) that for arbitrary \mathbf{F} :

$$W(\mathbf{F}) = W(\mathbf{R}^T\mathbf{F}) = W(\mathbf{R}^T\mathbf{R}\mathbf{U}) = W(\mathbf{U}) = W(\mathbf{C}) = W(\mathbf{E}). \quad (5.102)$$

Another condition which the function W must satisfy for the behavior at finite strains is the growth conditions, implies that W tends to infinity if the determinant of \mathbf{F} approaches to zero or infinity.

$$\begin{aligned} W(\mathbf{F}) &\rightarrow +\infty \text{ as } \det \mathbf{F} \rightarrow +\infty \\ W(\mathbf{F}) &\rightarrow +\infty \text{ as } \det \mathbf{F} \rightarrow 0 \end{aligned} \quad (5.103)$$

Moreover, the strain energy function vanishes in the reference configuration where $\mathbf{F} = \mathbf{I}$, which gives

$$W(\mathbf{I}) = 0. \quad (5.104)$$

The Piola-Kirchhoff stress tensors $\hat{\mathbf{P}}$ and \mathbf{S} for the hyperelastic materials at finite strain are expressed as

$$\begin{aligned} \hat{\mathbf{P}} &= 2\mathbf{F} \frac{\partial W(\mathbf{C})}{\partial \mathbf{C}}, \\ \mathbf{S} &= 2 \frac{\partial W(\mathbf{C})}{\partial \mathbf{C}} = \frac{\partial W(\mathbf{E})}{\partial \mathbf{E}}. \end{aligned} \quad (5.105)$$

More specifically, for isotropic hyperelastic materials, the strain energy W may be expressed as a set of independent strain invariants of the right Cauchy-Green tensor \mathbf{C} , through $I_a(\mathbf{C})$ ($a=1,2,3$) :

$$W = W(I_1(\mathbf{C}), I_2(\mathbf{C}), I_3(\mathbf{C})) \quad (5.106)$$

where

$$\begin{aligned} I_1(\mathbf{C}) &= \text{tr} \mathbf{C}, \\ I_2(\mathbf{C}) &= \frac{1}{2}[(\text{tr} \mathbf{C})^2 - \text{tr} \mathbf{C}^2], \\ I_3(\mathbf{C}) &= \det \mathbf{C}. \end{aligned} \quad (5.107)$$

Therefore, the variation of the function W with respect to \mathbf{C} is given by

$$\frac{\partial W}{\partial \mathbf{C}} = \frac{\partial W}{\partial I_1} \frac{\partial I_1}{\partial \mathbf{C}} + \frac{\partial W}{\partial I_2} \frac{\partial I_2}{\partial \mathbf{C}} + \frac{\partial W}{\partial I_3} \frac{\partial I_3}{\partial \mathbf{C}} \quad (5.108)$$

with

$$\frac{\partial I_1}{\partial \mathbf{C}} = \mathbf{I}, \quad \frac{\partial I_2}{\partial \mathbf{C}} = I_1 \mathbf{I} - \mathbf{C}, \quad \frac{\partial I_3}{\partial \mathbf{C}} = I_3 \mathbf{C}^{-1}. \quad (5.109)$$

Substituting (5.108) and (5.109) to (5.105), we can obtain the general form of a stress relation in terms of the three strain invariants, which characterizes isotropic hyperelastic materials at finite strain as

$$\mathbf{S} = 2 \frac{\partial W(\mathbf{C})}{\partial \mathbf{C}} = 2 \left(\frac{\partial W}{\partial I_1} + I_1 \frac{\partial W}{\partial I_2} \right) \mathbf{I} - 2 \frac{\partial W}{\partial I_2} \mathbf{C} + 2 \frac{\partial W}{\partial I_3} I_3 \mathbf{C}^{-1}. \quad (5.110)$$

The most classical models for the hyperelastic materials include the Saint Venant-Kirchhoff model, Mooney-Rivlin model, Ogden model, Yeoh model, Gent model and so on (see *e.g.* [Holzapfel 2000]). Each of the model has the unique description of the strain energy function W , and suitable for different cases.

5.6.2 Imperfect interface model at finite strains

Consider a continuum body Ω in the reference configuration $\Omega_0 \subset \mathbb{R}^3$, and the spatial configuration $\Omega_t \subset \mathbb{R}^3$. In the reference configuration, the graphene sheets are distributed randomly in the domain as the internal discontinuity Γ_n ($n=1,2,\dots,N$), as shown in Fig. 5.6. The graphene surfaces are collectively denoted by $\Gamma_0 = \cup_n \Gamma_n$. The two sides of the interface are denoted by Γ_0^+ and Γ_0^- . And the unit vector normal to the interface in the reference configuration is $\mathbf{n}(\mathbf{X})$. The displacement of the bulk, and the two sides of the interface are \mathbf{u} , \mathbf{u}^- and \mathbf{u}^+ respectively. Due to the assumption that the graphene sheets are attached to one side of the interface, the displacement jump at the interface is defined by the displacements of nodes on each side of the interface \mathbf{u}^- and \mathbf{u}^+ . The current positions of the material particles are defined by \mathbf{x} for the bulk, \mathbf{x}^- and \mathbf{x}^+ for the two sides of interface. As for the non-coherent interface, $[[\mathbf{u}]] = [[\mathbf{u}^+]] - [[\mathbf{u}^-]] \neq 0$ and $[[\mathbf{x}]] \neq 0$.

Apart from the bulk deformation gradient \mathbf{F} defined in Eq. (5.88), the surface deformation gradient \mathbf{F}_s is given by

$$\mathbf{F}^s = \mathbf{F} \cdot \mathbf{P}(\mathbf{X}) \quad (5.111)$$

where $\mathbf{P}(\mathbf{X})$ is the projection matrix denoted by

$$\mathbf{P}(\mathbf{X}) = \mathbf{I} - \mathbf{n}(\mathbf{X}) \otimes \mathbf{n}(\mathbf{X}). \quad (5.112)$$

Similarly, the surface Green strain $\hat{\mathbf{E}}^s$ is expressed by

$$\hat{\mathbf{E}}^s = \mathbf{P}(\mathbf{X})\hat{\mathbf{E}}\mathbf{P}(\mathbf{X}) \quad (5.113)$$

where $\hat{\mathbf{E}}$ has been given in Eq. (5.95).

The equilibrium equations for the bulk and the graphene surface are given as :

$$\nabla_{\mathbf{X}} \cdot \mathbf{S} = 0, \text{ on } \Omega \quad (5.114)$$

$$\nabla_{\mathbf{X}}^s \cdot \mathbf{S}^s = \llbracket \mathbf{S} \rrbracket \cdot \mathbf{n}, \text{ on } \Gamma \quad (5.115)$$

where \mathbf{S} and \mathbf{S}^s the second Piola-Kirchhoff stress tensor for bulk and graphene surface respectively. $\nabla_{\mathbf{X}}^s \cdot (\cdot)$ denotes the surface divergence with respect to the initial configuration defined by

$$\nabla_{\mathbf{X}}^s \cdot (\cdot) = \nabla_{\mathbf{X}} \cdot (\cdot) : \mathbf{P}(\mathbf{X}). \quad (5.116)$$

We also define the surface gradient $\nabla_{\mathbf{X}}^s(\cdot)$ as

$$\nabla_{\mathbf{X}}^s(\cdot) = \nabla_{\mathbf{X}}(\cdot) \cdot \mathbf{P}(\mathbf{X}). \quad (5.117)$$

As for the constitutive relation, we choose the simplest hyperelastic material model, the Saint Venant-Kirchhoff model, which is just an extension of the linear elastic material model to the nonlinear regime. Therefore, have :

$$\mathbf{S} = \mathbb{C} : \hat{\mathbf{E}} \text{ on } \Omega \quad (5.118)$$

and

$$\mathbf{S}^s = \mathbb{C}^s : \hat{\mathbf{E}}^s \text{ on } \Gamma \quad (5.119)$$

where \mathbb{C} and \mathbb{C}^s are the stiffness tensors for polymer bulk and graphene surface.

As for the behavior of the cohesive interface, the expression of the normal traction to the interface, neglecting the tangential traction is given by

$$\mathbf{t}_n(\llbracket \mathbf{u} \rrbracket) = t_n \frac{\llbracket \mathbf{u} \rrbracket}{\|\llbracket \mathbf{u} \rrbracket\|} \quad (5.120)$$

where t_n is referred in (5.36) and periodical boundary condition is applied as the description in Eq. (5.37).

5.6.3 Computational framework

5.6.3.1 Weak form

To derive the mechanical weak form, we use the principle of virtual work in this work. The internal virtual work δW_{int} is given by the contributions of the polymer bulk, graphene surface and cohesive interface as :

$$\delta W_{int}(\delta \mathbf{u}, \mathbf{u}) = \delta W_{int}^b + \delta W_{int}^s + \delta W_{int}^c \quad (5.121)$$

where

$$\delta W_{int}^b = \int_{\Omega_0} \mathbf{S}(\hat{\mathbf{E}}(\mathbf{u})) : \delta \hat{\mathbf{E}}(\mathbf{u}) dV \quad (5.122)$$

$$\delta W_{int}^s = \int_{\Gamma_0} \mathbf{S}^s(\hat{\mathbf{E}}(\mathbf{u})) : \delta \hat{\mathbf{E}}^s(\mathbf{u}) dS \quad (5.123)$$

$$\delta W_{int}^c = \int_{\Gamma_0} [[\delta \mathbf{u}]] \cdot \mathbf{t}([[\mathbf{u}]]) dS \quad (5.124)$$

where $\delta \mathbf{u}$ is the virtual displacement field, and $\delta \hat{\mathbf{E}} = \text{sym}(\mathbf{F}^T \Delta \delta \mathbf{u})$. The surface Green-Lagrange strain tensor is defined as $\delta \hat{\mathbf{E}}^s = \mathbf{P}^T \delta \hat{\mathbf{E}} \mathbf{P}$. Considering the periodical boundary conditions or displacement boundary conditions, the weak form of the finite strain problem for the graphene reinforced nanocomposites is given by

$$\int_{\Omega_0} \mathbf{S}(\hat{\mathbf{E}}(\mathbf{u})) : \delta \hat{\mathbf{E}}(\mathbf{u}) dV + \int_{\Gamma_0} \mathbf{S}^s(\hat{\mathbf{E}}(\mathbf{u})) : \delta \hat{\mathbf{E}}^s(\mathbf{u}) dS + \int_{\Gamma_0} [[\delta \mathbf{u}]] \cdot \mathbf{t}([[\mathbf{u}]]) dS = 0 \quad (5.125)$$

where $\mathbf{u} \in H^1(\Omega_0)$, \mathbf{u} satisfying the boundary condition (5.37) over $\partial\Omega_0$ and $\delta \mathbf{u} \in H^1(\Omega_0)$, $\delta \mathbf{u} = 0$ over $\partial\Omega_0$, $[[\delta \mathbf{u}]] = \delta \mathbf{u}^- - \delta \mathbf{u}^+$ on the cohesive zone.

5.6.3.2 Linearization

Here again, we use the Newton Raphson method to solve the above non-linear equations. Setting

$$R = \int_{\Omega_0} \mathbf{S}(\hat{\mathbf{E}}(\mathbf{u})) : \delta \hat{\mathbf{E}}(\mathbf{u}) dV + \int_{\Gamma_0} \mathbf{S}^s(\hat{\mathbf{E}}(\mathbf{u})) : \delta \hat{\mathbf{E}}^s(\mathbf{u}) dS + \int_{\Gamma_0} [[\delta \mathbf{u}]] \cdot \mathbf{t}([[\mathbf{u}]]) dS \quad (5.126)$$

the first-order Taylor expansion of R gives :

$$R(\mathbf{u}_k + \Delta \mathbf{u}_k) \simeq R(\mathbf{u}_k) + D_{\Delta \mathbf{u}} R(\mathbf{u}_k) \quad (5.127)$$

where \mathbf{u}_k denotes the displacement field known from a previous iteration k, $\Delta \mathbf{u}_k$ is the increment of displacement. The linearized problem around the know solution \mathbf{u}_k is given as :

$$D_{\Delta \mathbf{u}} R(\mathbf{u}_k) = -R(\mathbf{u}_k). \quad (5.128)$$

The left-hand term in (5.52) can be expressed as :

$$D_{\Delta \mathbf{u}} R(\mathbf{u}_k) = \frac{d}{d\xi} R(\mathbf{u}_k + \xi \Delta \mathbf{u})|_{\xi=0}. \quad (5.129)$$

Due to the relations that

$$D_{\Delta \mathbf{u}} \mathbf{F} = \nabla_{\mathbf{X}}(\Delta \mathbf{u}), \quad (5.130)$$

$$D_{\Delta \mathbf{u}} \mathbf{E} = \text{sym}(\mathbf{F}^T \nabla_{\mathbf{X}}(\Delta \mathbf{u})), \quad (5.131)$$

we can obtain the directional derivative of the first term of R as

$$\begin{aligned} D_{\Delta \mathbf{u}} \int_{\Omega_0} \mathbf{S}(\hat{\mathbf{E}}(\mathbf{u})) : \delta \hat{\mathbf{E}}(\mathbf{u}) dV &= \int_{\Omega_0} D_{\Delta \mathbf{u}}(\delta \hat{\mathbf{E}}) : \mathbf{S} dV + \int_{\Omega_0} \frac{\partial \mathbf{S}}{\partial \hat{\mathbf{E}}} D_{\Delta \mathbf{u}} \hat{\mathbf{E}} : \delta \hat{\mathbf{E}} dV \\ &= \int_{\Omega_0} \nabla_{\mathbf{X}} \delta \mathbf{u} : \nabla_{\mathbf{X}}(\Delta \mathbf{u}) \mathbf{S} dV + \int_{\Omega_0} \mathbf{F}^T \nabla_{\mathbf{X}} \delta \mathbf{u} : \mathbb{C} : \mathbf{F}^T \nabla_{\mathbf{X}}(\Delta \mathbf{u}) dV \end{aligned} \quad (5.132)$$

and the directional derivative of the second term of R as

$$\begin{aligned} D_{\Delta \mathbf{u}} \int_{\Gamma_0} \mathbf{S}^s(\hat{\mathbf{E}}(\mathbf{u})) : \delta \hat{\mathbf{E}}^s(\mathbf{u}) dS &= \int_{\Gamma_0} D_{\Delta \mathbf{u}}(\delta \hat{\mathbf{E}}^s) : \mathbf{S}^s dS + \int_{\Gamma_0} \frac{\partial \mathbf{S}^s}{\partial \hat{\mathbf{E}}^s} D_{\Delta \mathbf{u}} \hat{\mathbf{E}}^s : \delta \hat{\mathbf{E}}^s dS \\ &= \int_{\Gamma_0} \nabla_{\mathbf{X}}^s \delta \mathbf{u} : \nabla_{\mathbf{X}}^s(\Delta \mathbf{u}) \mathbf{S}^s dS + \int_{\Gamma_0} (\mathbf{F}^s)^T \nabla_{\mathbf{X}}^s \delta \mathbf{u} : \mathbb{C}^s : (\mathbf{F}^s)^T \nabla_{\mathbf{X}}^s(\Delta \mathbf{u}) dS. \end{aligned} \quad (5.133)$$

Finally, the directional derivative of the third term of R is obtained as

$$\int_{\Gamma_0} \llbracket \delta \mathbf{u} \rrbracket \cdot \mathbf{t}(\llbracket \mathbf{u} \rrbracket) dS = \int_{\Gamma_0} \llbracket \delta \mathbf{u} \rrbracket \cdot \frac{\partial \mathbf{t}(\llbracket \mathbf{u} \rrbracket)}{\partial \llbracket \mathbf{u} \rrbracket} \Delta \llbracket \mathbf{u}_k \rrbracket dS \quad (5.134)$$

where

$$\frac{\partial \mathbf{t}(\llbracket \mathbf{u} \rrbracket)}{\partial \llbracket \mathbf{u} \rrbracket} = \mathbf{T} = T_n \mathbf{n}_u \otimes \mathbf{n}_u + \frac{t_n}{\|\llbracket \mathbf{u} \rrbracket\|} (\mathbf{I} - \mathbf{n}_u \otimes \mathbf{n}_u). \quad (5.135)$$

In the above equation, T_n has been given in (5.55) and $\mathbf{n}_u = \llbracket \mathbf{u} \rrbracket / \|\llbracket \mathbf{u} \rrbracket\|$.

Therefore, the linearized equation as shown in Eq. (5.128) is expressed in details as :

$$\begin{aligned} & \int_{\Omega_0} \nabla_{\mathbf{X}} \delta \mathbf{u} : \nabla_{\mathbf{X}} (\Delta \mathbf{u}) \mathbf{S} dV + \int_{\Omega_0} \mathbf{F}^T \nabla_{\mathbf{X}} \delta \mathbf{u} : \mathbb{C} : \mathbf{F}^T \nabla_{\mathbf{X}} (\Delta \mathbf{u}) dV + \\ & \int_{\Gamma_0} \nabla_{\mathbf{X}}^s \delta \mathbf{u} : \nabla_{\mathbf{X}}^s (\Delta \mathbf{u}) \mathbf{S}^s dS + \int_{\Gamma_0} (\mathbf{F}^s)^T \nabla_{\mathbf{X}}^s \delta \mathbf{u} : \mathbb{C}^s : (\mathbf{F}^s)^T \nabla_{\mathbf{X}}^s (\Delta \mathbf{u}) dS \\ & + \int_{\Gamma_0} \llbracket \delta \mathbf{u} \rrbracket \cdot \frac{\partial \mathbf{t}(\llbracket \mathbf{u} \rrbracket)}{\partial \llbracket \mathbf{u} \rrbracket} \Delta \llbracket \mathbf{u}_k \rrbracket dS = - \int_{\Omega_0} \nabla_{\mathbf{X}} \delta \mathbf{u} : \mathbf{F} \mathbf{S} dV \\ & - \int_{\Gamma_0} \nabla_{\mathbf{X}}^s \delta \mathbf{u} : \mathbf{F}^s \mathbf{S}^s dS - \int_{\Gamma_0} \llbracket \delta \mathbf{u} \rrbracket \mathbf{t}(\llbracket \delta \mathbf{u} \rrbracket) dS. \end{aligned} \quad (5.136)$$

5.6.3.3 Discretization

The discretization of displacements, their variation \mathbf{u} , $\delta \mathbf{u}$, and related jumps $\llbracket \mathbf{u} \rrbracket|_{\Gamma_n^e}$, $\llbracket \delta \mathbf{u} \rrbracket|_{\Gamma_n^e}$ and $\llbracket \Delta \mathbf{u} \rrbracket|_{\Gamma_n^e}$ is identical as in section 5.5.2.3.

In the following, the second Piola-Kirchhoff stress tensor and the Green strain tensor for the bulk are expressed by the vectors $\{S\} = [S_{11}, S_{22}, S_{33}, S_{23}, S_{13}, S_{12}]$ and $\{\hat{E}\} = \{\hat{E}_{11}, \hat{E}_{22}, \hat{E}_{33}, 2\hat{E}_{23}, 2\hat{E}_{13}, 2\hat{E}_{12}\}$ respectively.

According to the constitutive relations in Eqs. (5.118) and (5.119), the matrix form $[C]$ of the polymer elastic tensor is given by

$$[C] = \begin{bmatrix} \lambda + 2\mu & \lambda & \lambda & 0 & 0 & 0 \\ \lambda & \lambda + 2\mu & \lambda & 0 & 0 & 0 \\ \lambda & \lambda & \lambda + 2\mu & 0 & 0 & 0 \\ 0 & 0 & 0 & \mu & 0 & 0 \\ 0 & 0 & 0 & 0 & \mu & 0 \\ 0 & 0 & 0 & 0 & 0 & \mu \end{bmatrix} \quad (5.137)$$

where λ and μ are the Lamé's constants of polymer matrix, and $\{S\} = [C]\{\hat{E}\}$.

Chapitre 5. Numerical modeling of the mechanical properties of 162 graphene reinforced nanocomposites

Similarly, defining the surface stress and strain tensors as vectors $\{S^s\} = \{S_{11}^s, S_{22}^s, S_{33}^s, S_{23}^s, S_{13}^s, S_{12}^s\}$ and $\{\hat{E}^s\} = \{\hat{E}_{11}^s, \hat{E}_{22}^s, \hat{E}_{33}^s, 2\hat{E}_{23}^s, 2\hat{E}_{13}^s, 2\hat{E}_{12}^s\}$ respectively, the surface stiffness matrix $[C^s]$ is expressed as :

$$[C^s] = \begin{bmatrix} (\lambda^s+2\mu^s)P_{11}^2 & \lambda^s P_{11}P_{22}+2\mu^s P_{12}^2 & \lambda^s P_{11}P_{33}+2\mu^s P_{13}^2 \\ \lambda^s P_{11}P_{22}+2\mu^s P_{12}^2 & (\lambda^s+2\mu^s)P_{22}^2 & \lambda^s P_{22}P_{33}+2\mu^s P_{23}^2 \\ \lambda^s P_{11}P_{33}+2\mu^s P_{13}^2 & \lambda^s P_{22}P_{33}+2\mu^s P_{23}^2 & (\lambda^s+2\mu^s)P_{33}^2 \\ \lambda^s P_{11}P_{23}+2\mu^s P_{12}P_{13} & (\lambda^s+2\mu^s)P_{22}P_{23} & (\lambda^s+2\mu^s)P_{23}P_{33} \\ (\lambda^s+2\mu^s)P_{11}P_{13} & \lambda^s P_{13}P_{22}+2\mu^s P_{12}P_{23} & (\lambda^s+2\mu^s)P_{13}P_{33} \\ (\lambda^s+2\mu^s)P_{11}P_{12} & (\lambda^s+2\mu^s)P_{12}P_{22} & \lambda^s P_{12}P_{33}+2\mu^s P_{13}P_{23} \\ \lambda^s P_{11}P_{23}+2\mu^s P_{12}P_{13} & (\lambda^s+2\mu^s)P_{11}P_{13} & (\lambda^s+2\mu^s)P_{11}P_{12} \\ (\lambda^s+2\mu^s)P_{22}P_{23} & \lambda^s P_{13}P_{22}+2\mu^s P_{12}P_{23} & (\lambda^s+2\mu^s)P_{12}P_{22} \\ (\lambda^s+2\mu^s)P_{23}P_{33} & (\lambda^s+2\mu^s)P_{13}P_{33} & \lambda^s P_{12}P_{33}+2\mu^s P_{13}P_{23} \\ \lambda^s P_{23}^2+\mu^s(P_{22}P_{33}+P_{23}^2) & \lambda^s P_{13}P_{23}+\mu^s(P_{13}P_{23}+P_{12}P_{33}) & \lambda^s P_{12}P_{23}+\mu^s(P_{13}P_{22}+P_{12}P_{23}) \\ \lambda^s P_{13}P_{23}+\mu^s(P_{13}P_{23}+P_{12}P_{33}) & \lambda^s P_{13}^2+\mu^s(P_{11}P_{33}+P_{13}^2) & \lambda^s P_{12}P_{13}+\mu^s(P_{11}P_{23}+P_{12}P_{13}) \\ \lambda^s P_{12}P_{23}+\mu^s(P_{13}P_{22}+P_{12}P_{23}) & \lambda^s P_{12}P_{13}+\mu^s(P_{11}P_{23}+P_{12}P_{13}) & \lambda^s P_{12}^2+\mu^s(P_{11}P_{22}+P_{12}^2) \end{bmatrix} \quad (5.138)$$

where λ^s and μ^s are the surface Lamé's constants of graphene and satisfying $\{S^s\} = [C^s]\{\hat{E}^s\}$. The surface deformation gradient $\mathbf{F}^s = \mathbf{F}\mathbf{P}$.

Using the above discretization scheme, and the definitions in Eq. (5.137)-(5.138), the linearized problem in Eq. (5.136) can be discreted as a system of algebraic equations as :

$$([K^b] + [K^s] + [K^c])\Delta\mathbf{u} = [R^b] + [R^s] + [R^c] \quad (5.139)$$

where $[K^b]$, $[K^s]$ and $[K^c]$ denote the bulk, graphene surface and interface stiffness matrix. $[R^b]$, $[R^s]$ and $[R^c]$ are the corresponding residual terms, and $\Delta\mathbf{u}$ is the incremental displacement field. The matrices $[K^b]$, $[K^s]$, $[K^c]$, $[R^b]$, $[R^s]$ and $[R^c]$ are defined by :

$$[K^b] = \int_{\Omega_0} ([\tilde{B}^b]^T[C][\tilde{B}^b] + [B^b]^T[S][B^b])dV \quad (5.140)$$

$$[K^s] = \int_{\Gamma_0} ([\tilde{B}^s]^T[C^s][\tilde{B}^s] + [B^s]^T[S^s][B^s])dS \quad (5.141)$$

$$[K^c] = \int_{\Gamma_0} [M^e]^T[T][M^e]dS \quad (5.142)$$

$$[R^b] = - \int_{\Omega_0} [\tilde{B}^b]^T\{S\}dV \quad (5.143)$$

$$[R^s] = - \int_{\Gamma_0} [\tilde{B}^s]^T\{S^s\}dS \quad (5.144)$$

$$[R^e] = - \int_{\Gamma_0} [M^e]^T \mathbf{t} ([\mathbf{u}_k]) dS. \quad (5.145)$$

In the equations above, $[B^b]$ is a matrix of shape functions derivatives for the bulk defined as :

$$[B^b] = \begin{bmatrix} \frac{\partial N_1}{\partial X_1} & 0 & 0 & \frac{\partial N_2}{\partial X_1} & 0 & 0 & \frac{\partial N_3}{\partial X_1} & 0 & 0 & \frac{\partial N_4}{\partial X_1} & 0 & 0 \\ \frac{\partial N_1}{\partial X_2} & 0 & 0 & \frac{\partial N_2}{\partial X_2} & 0 & 0 & \frac{\partial N_3}{\partial X_2} & 0 & 0 & \frac{\partial N_4}{\partial X_2} & 0 & 0 \\ \frac{\partial N_1}{\partial X_3} & 0 & 0 & \frac{\partial N_2}{\partial X_3} & 0 & 0 & \frac{\partial N_3}{\partial X_3} & 0 & 0 & \frac{\partial N_4}{\partial X_3} & 0 & 0 \\ 0 & \frac{\partial N_1}{\partial X_1} & 0 & 0 & \frac{\partial N_2}{\partial X_1} & 0 & 0 & \frac{\partial N_3}{\partial X_1} & 0 & 0 & \frac{\partial N_4}{\partial X_1} & 0 \\ 0 & \frac{\partial N_1}{\partial X_2} & 0 & 0 & \frac{\partial N_2}{\partial X_2} & 0 & 0 & \frac{\partial N_3}{\partial X_2} & 0 & 0 & \frac{\partial N_4}{\partial X_2} & 0 \\ 0 & \frac{\partial N_1}{\partial X_3} & 0 & 0 & \frac{\partial N_2}{\partial X_3} & 0 & 0 & \frac{\partial N_3}{\partial X_3} & 0 & 0 & \frac{\partial N_4}{\partial X_3} & 0 \\ 0 & 0 & \frac{\partial N_1}{\partial X_1} & 0 & 0 & \frac{\partial N_2}{\partial X_1} & 0 & 0 & \frac{\partial N_3}{\partial X_1} & 0 & 0 & \frac{\partial N_4}{\partial X_1} \\ 0 & 0 & \frac{\partial N_1}{\partial X_2} & 0 & 0 & \frac{\partial N_2}{\partial X_2} & 0 & 0 & \frac{\partial N_3}{\partial X_2} & 0 & 0 & \frac{\partial N_4}{\partial X_2} \\ 0 & 0 & \frac{\partial N_1}{\partial X_3} & 0 & 0 & \frac{\partial N_2}{\partial X_3} & 0 & 0 & \frac{\partial N_3}{\partial X_3} & 0 & 0 & \frac{\partial N_4}{\partial X_3} \end{bmatrix} \quad (5.146)$$

satisfying that

$$[\nabla_X(\mathbf{u}^e)] = [\nabla_{11}^e \ \nabla_{12}^e \ \nabla_{13}^e \ \nabla_{21}^e \ \nabla_{22}^e \ \nabla_{23}^e \ \nabla_{31}^e \ \nabla_{32}^e \ \nabla_{33}^e]^T = [B^b] \cdot \mathbf{u}^e \quad (5.147)$$

where \mathbf{u}^e is the displacement vector on each element defined as

$$\mathbf{u}^e = [u_1^x \ u_1^y \ u_1^z \ u_2^x \ u_2^y \ u_2^z \ u_3^x \ u_3^y \ u_3^z \ u_4^x \ u_4^y \ u_4^z]^T. \quad (5.148)$$

Then, $[\tilde{B}_I^b]$ is associated with the symmetric operation $\mathbf{F}^T \nabla_{\mathbf{X}}$ as

$$[\tilde{B}_I^b] = \begin{bmatrix} F_{11} \frac{\partial N_I}{X_1} & F_{21} \frac{\partial N_I}{X_1} & F_{31} \frac{\partial N_I}{X_1} \\ F_{12} \frac{\partial N_I}{X_2} & F_{22} \frac{\partial N_I}{X_2} & F_{32} \frac{\partial N_I}{X_2} \\ F_{13} \frac{\partial N_I}{X_3} & F_{23} \frac{\partial N_I}{X_3} & F_{33} \frac{\partial N_I}{X_3} \\ F_{12} \frac{\partial N_I}{X_3} + F_{13} \frac{\partial N_I}{X_2} & F_{22} \frac{\partial N_I}{X_3} + F_{23} \frac{\partial N_I}{X_2} & F_{32} \frac{\partial N_I}{X_3} + F_{33} \frac{\partial N_I}{X_2} \\ F_{11} \frac{\partial N_I}{X_3} + F_{13} \frac{\partial N_I}{X_1} & F_{21} \frac{\partial N_I}{X_3} + F_{23} \frac{\partial N_I}{X_1} & F_{31} \frac{\partial N_I}{X_3} + F_{33} \frac{\partial N_I}{X_1} \\ F_{11} \frac{\partial N_I}{X_2} + F_{12} \frac{\partial N_I}{X_1} & F_{21} \frac{\partial N_I}{X_2} + F_{22} \frac{\partial N_I}{X_1} & F_{31} \frac{\partial N_I}{X_2} + F_{32} \frac{\partial N_I}{X_1} \end{bmatrix} \quad (5.149)$$

therefore, $[\tilde{B}^b]$ can be described by the equation :

$$[\tilde{B}^b] = [F][B^b] \quad (5.150)$$

in which

$$[F] = \begin{bmatrix} F_{11} & 0 & 0 & F_{21} & 0 & 0 & F_{31} & 0 & 0 \\ 0 & F_{12} & 0 & 0 & F_{22} & 0 & 0 & F_{32} & 0 \\ 0 & 0 & F_{13} & 0 & 0 & F_{23} & 0 & 0 & F_{33} \\ 0 & F_{13} & F_{12} & 0 & F_{23} & F_{22} & 0 & F_{33} & F_{32} \\ F_{13} & 0 & F_{11} & F_{23} & 0 & F_{21} & F_{33} & 0 & F_{31} \\ F_{12} & F_{11} & 0 & F_{22} & F_{21} & 0 & F_{32} & F_{31} & 0 \end{bmatrix} \quad (5.151)$$

Besides, $[S]$ is a matrix defined by :

$$[S] = \begin{bmatrix} S_{11} & S_{12} & S_{13} & 0 & 0 & 0 & 0 & 0 & 0 \\ S_{21} & S_{22} & S_{23} & 0 & 0 & 0 & 0 & 0 & 0 \\ S_{31} & S_{32} & S_{33} & 0 & 0 & 0 & 0 & 0 & 0 \\ 0 & 0 & 0 & S_{11} & S_{12} & S_{13} & 0 & 0 & 0 \\ 0 & 0 & 0 & S_{21} & S_{22} & S_{23} & 0 & 0 & 0 \\ 0 & 0 & 0 & S_{31} & S_{32} & S_{33} & 0 & 0 & 0 \\ 0 & 0 & 0 & 0 & 0 & 0 & S_{11} & S_{12} & S_{13} \\ 0 & 0 & 0 & 0 & 0 & 0 & S_{21} & S_{22} & S_{23} \\ 0 & 0 & 0 & 0 & 0 & 0 & S_{31} & S_{32} & S_{33} \end{bmatrix} \quad (5.152)$$

and $\{S\} = [S_{11} \ S_{22} \ S_{33} \ S_{23} \ S_{13} \ S_{12}]$.

In addition, considering the surface operators, $[B_I^s]$ is associated with the surface gradient $\nabla_{\mathbf{X}}^s$ on node I and is expressed by

$$[B_I^s] = \begin{bmatrix} P_{11} \frac{\partial N_I}{X_1} + P_{12} \frac{\partial N_I}{X_2} + P_{13} \frac{\partial N_I}{X_3} & 0 & 0 \\ P_{12} \frac{\partial N_I}{X_1} + P_{22} \frac{\partial N_I}{X_2} + P_{23} \frac{\partial N_I}{X_3} & 0 & 0 \\ P_{13} \frac{\partial N_I}{X_1} + P_{23} \frac{\partial N_I}{X_2} + P_{33} \frac{\partial N_I}{X_3} & 0 & 0 \\ 0 & P_{11} \frac{\partial N_I}{X_1} + P_{12} \frac{\partial N_I}{X_2} + P_{13} \frac{\partial N_I}{X_3} & 0 \\ 0 & P_{12} \frac{\partial N_I}{X_1} + P_{22} \frac{\partial N_I}{X_2} + P_{23} \frac{\partial N_I}{X_3} & 0 \\ 0 & P_{13} \frac{\partial N_I}{X_1} + P_{23} \frac{\partial N_I}{X_2} + P_{33} \frac{\partial N_I}{X_3} & 0 \\ 0 & 0 & P_{11} \frac{\partial N_I}{X_1} + P_{12} \frac{\partial N_I}{X_2} + P_{13} \frac{\partial N_I}{X_3} \\ 0 & 0 & P_{12} \frac{\partial N_I}{X_1} + P_{22} \frac{\partial N_I}{X_2} + P_{23} \frac{\partial N_I}{X_3} \\ 0 & 0 & P_{13} \frac{\partial N_I}{X_1} + P_{23} \frac{\partial N_I}{X_2} + P_{33} \frac{\partial N_I}{X_3} \end{bmatrix}. \quad (5.153)$$

The other operator $(\mathbf{F}^s)^T \nabla_{\mathbf{X}}^s$ has the expression on node I as

$$(\mathbf{F}^s)^T \nabla_{\mathbf{X}}^s \mathbf{u}_I = [\tilde{B}_I^s] \mathbf{u}_I \quad (5.154)$$

where the matrix $[\tilde{B}_I^s]$ is described as

$$[\tilde{B}_I^s] = \begin{bmatrix} F_{11}^s[B_I^s]_{11} & F_{21}^s[B_I^s]_{11} & F_{31}^s[B_I^s]_{11} \\ F_{12}^s[B_I^s]_{21} & F_{22}^s[B_I^s]_{21} & F_{32}^s[B_I^s]_{21} \\ F_{13}^s[B_I^s]_{31} & F_{23}^s[B_I^s]_{31} & F_{33}^s[B_I^s]_{31} \\ F_{12}^s[B_I^s]_{31} + F_{13}^s[B_I^s]_{21} & F_{22}^s[B_I^s]_{31} + F_{23}^s[B_I^s]_{21} & F_{32}^s[B_I^s]_{31} + F_{33}^s[B_I^s]_{21} \\ F_{11}^s[B_I^s]_{31} + F_{13}^s[B_I^s]_{11} & F_{21}^s[B_I^s]_{31} + F_{23}^s[B_I^s]_{11} & F_{31}^s[B_I^s]_{31} + F_{33}^s[B_I^s]_{11} \\ F_{11}^s[B_I^s]_{21} + F_{12}^s[B_I^s]_{11} & F_{21}^s[B_I^s]_{21} + F_{22}^s[B_I^s]_{11} & F_{31}^s[B_I^s]_{21} + F_{32}^s[B_I^s]_{11} \end{bmatrix}. \quad (5.155)$$

Finally, $[S^s]$ and $\{S^s\}$ has the same form with the bulk terms as :

$$[S^s] = \begin{bmatrix} S_{11}^s & S_{12}^s & S_{13}^s & 0 & 0 & 0 & 0 & 0 & 0 \\ S_{21}^s & S_{22}^s & S_{23}^s & 0 & 0 & 0 & 0 & 0 & 0 \\ S_{31}^s & S_{32}^s & S_{33}^s & 0 & 0 & 0 & 0 & 0 & 0 \\ 0 & 0 & 0 & S_{11}^s & S_{12}^s & S_{13}^s & 0 & 0 & 0 \\ 0 & 0 & 0 & S_{21}^s & S_{22}^s & S_{23}^s & 0 & 0 & 0 \\ 0 & 0 & 0 & S_{31}^s & S_{32}^s & S_{33}^s & 0 & 0 & 0 \\ 0 & 0 & 0 & 0 & 0 & 0 & S_{11}^s & S_{12}^s & S_{13}^s \\ 0 & 0 & 0 & 0 & 0 & 0 & S_{21}^s & S_{22}^s & S_{23}^s \\ 0 & 0 & 0 & 0 & 0 & 0 & S_{31}^s & S_{32}^s & S_{33}^s \end{bmatrix} \quad (5.156)$$

and $\{S^s\} = [S_{11}^s \ S_{22}^s \ S_{33}^s \ S_{23}^s \ S_{13}^s \ S_{12}^s]$.

5.7 Weak electromechanic coupling

In this section, we describe a model to introduce a first mechanism of electromechanical coupling. Here the coupling is only weak, *i.e.* there is only an effect of the mechanics on the electric conduction problem. The coupling is due to the dependence of the effective conduction to the average distance between graphene sheets, because of the tunneling effect. Then, if large strains are prescribed, this distance might change and modify the electric field which in turns should modify the effective electric conductivity of the composite. In this section we will investigate these effects. Due to a lack of time, it was not possible to introduce stronger coupling, *e.g.* through damage related to high electric fields. This is reported to future studies and to the perspectives of this work.

5.7.1 Electrical percolation threshold

Firstly, we use the methodology proposed in [Lu 2017b] to investigate the influence of graphene volume fraction on the effective electric conductivity of graphene/ polymer nanocomposites as well as the percolation threshold. The length of the cubic RVE is 70 nm. The graphene sheets are square surfaces with a fixed size $15 \times 15 \text{ nm}^2$ and a thickness of 0.2 nm. Thus the aspect ratio of graphene is 75. The sheets are distributed randomly using a Markov-chain hard-plate algorithm (see in section 3.5.4).

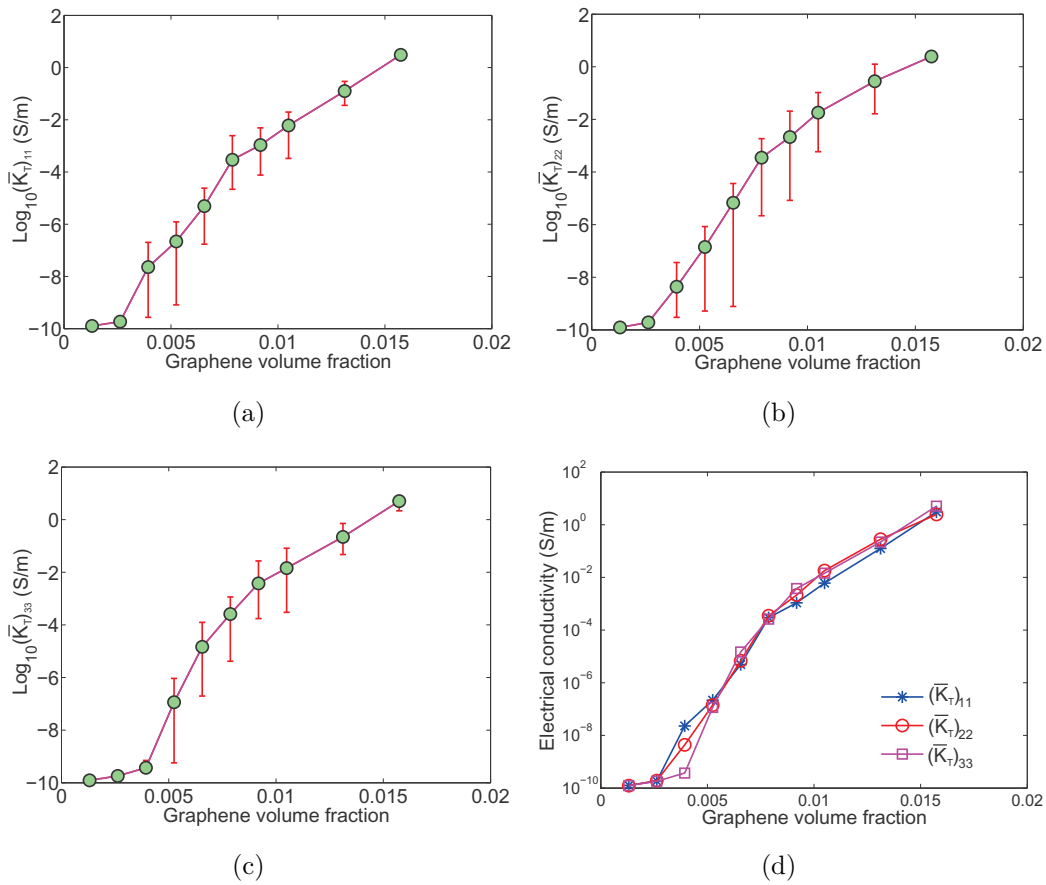


FIGURE 5.14 – Effective electrical conductivity of graphene reinforced nanocomposites as a function of graphene volume fraction. Barrier height between graphene and polymer matrix is set to be 0.17 eV, and graphene aspect ratio is 75. The applied electric field is 0.0025V/nm. (a) $(\overline{K}_T)_{11}$; (b) $(\overline{K}_T)_{22}$; (c) $(\overline{K}_T)_{33}$; (d) Comparison.

The barrier height between graphene and polymer matrix is taken as

$\Phi_0 = 0.17$ eV. Periodic boundary conditions are prescribed. The problem being nonlinear, the effective conductivity is the incremental one dependent on the intensity and history of the applied electric field, which is defined in Eq. (3.48). The examples are given for a fixed value $\bar{E}_1 = 0.0025$ V/nm.

The numerical results are provided in Fig. 5.14 for graphene reinforced nanocomposite with varying graphene volume fraction. Taking into account the tunnel effect, the numerical values of $(\bar{K}_T)_{11}$, $(\bar{K}_T)_{22}$ and $(\bar{K}_T)_{33}$ are plotted for each volume fraction as shown in Fig. 5.14 (a-c), where the average values are obtained for 30 realizations. An additional comparison among the electrical conductivities in the three main directions is shown in Fig. 5.14 (d). A sharp rise of conductivity of several orders of magnitude can be noticed at about 0.52 vol% where the mean value exceeds 10^{-8} S/m. Generally, the percolation threshold is the minimum filler content in the matrix which is characterized by a sharp rise of several magnitude in conductivity due to the formation of conductive network, and realizes a transition from insulator to conductor. Therefore, we estimate that the percolation threshold is about 0.52 vol% in this example.

5.7.2 Distance function at finite deformation

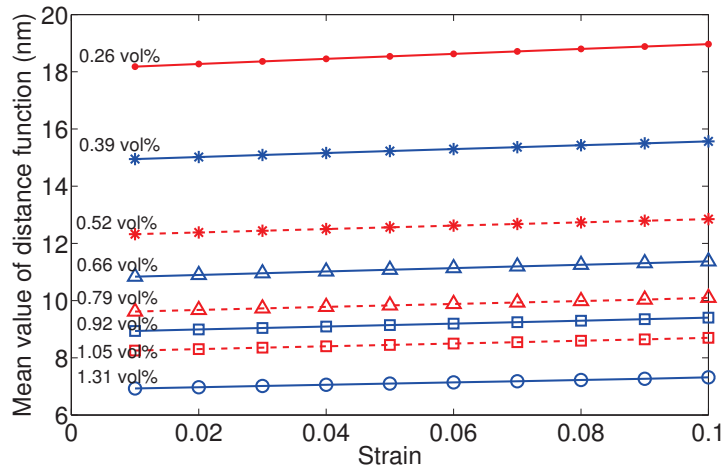


FIGURE 5.15 – Distance function of the nanocomposites as a function of the deformation at different graphene volume fraction.

For each graphene volume fraction, a microstructure is randomly defined within the RVE. Taking advantage of the mechanical modeling for the finite

**Chapitre 5. Numerical modeling of the mechanical properties of
168 graphene reinforced nanocomposites**

deformation of graphene reinforced nanocomposites, a series of deformation from 1% to 10% are applied along the X -direction on the RVE. The deformed microstructures are stored along with the increment of deformation according to the solution of displacement field affected by the cohesive interface. The local deformation in each microstructure leads to a various local distance function, which dominates the tunneling current between the graphene sheets, and therefore influences the effective electrical conductivity.

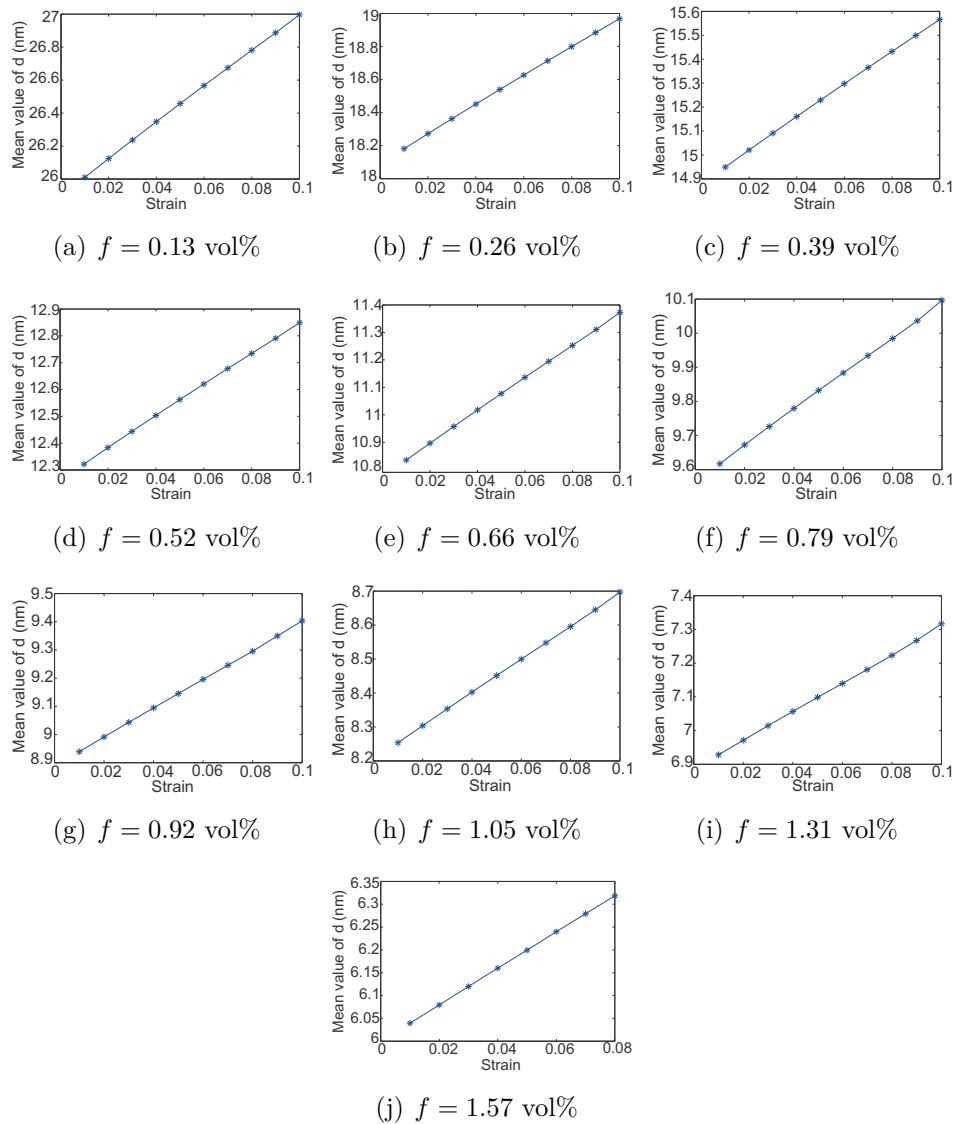


FIGURE 5.16 – Mean value of distance function at the deformation of 1%-10% along X direction for the nanocomposite with various graphene aspect ratio.

Given the distance function d on each nodes of the elements, we can obtain the new distance function d_e of each element by numerical integration in the elements. The average values of d_e as a function of the applied deformation for the RVEs with various graphene volume fraction are shown in Fig. 5.15

To better appreciate the evolution of the mean value of the distance function with respect to the strain, each curve of Fig. 5.15 is described individually in Fig. 5.16 (a-j), showing a linear evolution. It is obvious that the higher graphene volume fraction exhibits lower mean distance function, and can result in a modified effective electrical conductivity when the composite is stretched.

5.7.3 Evolution of electrical properties under stretching of the composite

Introducing the new distance function calculated after the mechanical deformation along the X - direction, the electrical conductivities at different effective strain are shown in Fig. 5.17. Focusing on the electrical conductivity along the direction of deformation $(\bar{K}_T)_{11}$, we can observe in Fig. 5.17 (a) that the mechanical deformation has little effect on the electrical conductivity of the nanocomposites when the graphene volume fraction is below the percolation threshold. When the graphene concentration is above the percolation threshold, the electrical conductivity $(\bar{K}_T)_{11}$ decreases along with the applied strain, but it should be noted that the nanocomposites remains conductor. However, if the graphene volume fraction is around the percolation threshold, a sharp decrease of the electrical conductivity can be seen when the nanocomposites is subjected to strain, which is regarded as a transition point from conductor to insulator. For instance, with 0.66 vol% graphene the transition point of the sample is 3%, and with 0.52 vol% graphene it is 10%. However, the deformation along X direction would not affect the electrical conductivities of the nanocomposites in the other two main directions $(\bar{K}_T)_{22}$ and $(\bar{K}_T)_{33}$, which can be seen from Fig. 5.17 (b-c).

We note that this drop in conductivity does not occur for each curve above a given volume fraction. This is due to the fact that the simulations for each volume fraction have been performed on a single realization, and that some configurations might be more favorable to this effect. It is interesting to note that in view of this effect, it is theoretically possible to design a composite which can go from conductor to insulator by varying the applied strain on the

system.

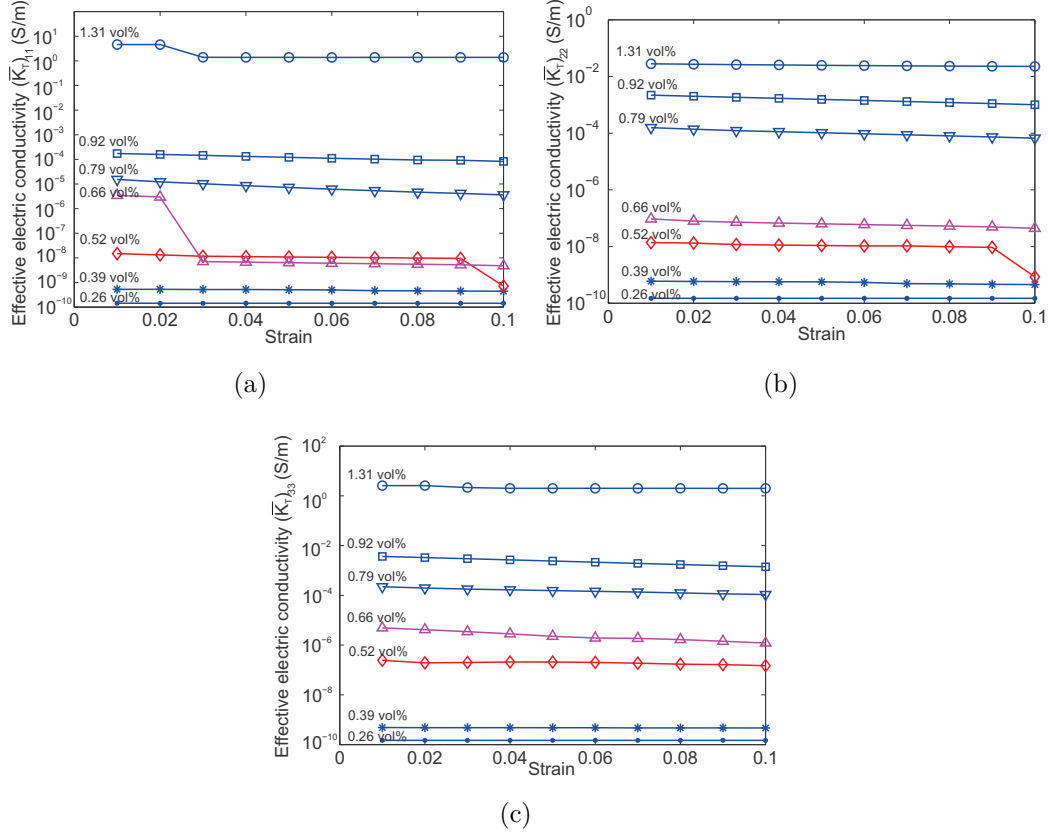


FIGURE 5.17 – Effective electrical conductivity of graphene reinforced nanocomposites as a function of the deformation for various graphene volume fraction. Barrier height between graphene and polymer matrix is set to be 0.17 eV, and graphene aspect ratio is 75. The applied electric field is 0.0025V/nm. (a) $(\bar{K}_T)_{11}$; (b) $(\bar{K}_T)_{22}$; (c) $(\bar{K}_T)_{33}$.

5.8 Conclusion

In this chapter, we have proposed a numerical modeling framework for predicting the effective stiffness of graphene reinforced nanocomposites, taking into account the interfacial behavior by cohesive zone model. First, the nonlinear cohesive law has been identified by molecular dynamics. Then, the nonlinear equations of the mechanical problem have been introduced and solved by FEM, where the graphene platelets are modeled by elastic imperfect surface model. The effective stiffness of the nanocomposites has been evaluated

numerically by homogenization. Applying the method to RVE computations of polymer/PE nanocomposites, we have estimated the effective stiffness of the composites as a function of graphene volume fraction. An increase of 30% of the Young's modulus has been observed when the graphene volume fraction reaches 1.5vol%. Compared with the numerical results neglecting the cohesive interface between graphene and polymer, we have observed that the interfacial interaction plays an important role in the microscopic mechanical properties of the nanocomposites.

Moreover, to evaluate the degradation of electrical performances with decohesion of graphene sheets under mechanical stress, we also extended the numerical model to finite deformation problem. The proposed model is demonstrated to predict the variation of percolation threshold under mechanical stress. Coupling both electrical and mechanical problems, it was shown that when the graphene volume fraction is around percolation threshold, the electrical conductivity may suffer a sharp decrease at a certain effective deformation, that is to say, the conducting nanocomposites transform to insulator above a critical strain and the percolation threshold increases. This effect might be exploited to design new materials going from insulator to conductor depending on the applied strain.

Conclusion and perspective

6.1 General conclusion

In the present thesis work, we have provided several contributions to the multiscale modeling of the electrical and mechanical properties of graphene reinforced nanocomposites, summarized as follows.

Firstly, a numerical modeling framework for predicting the effective electric conductivity in polymer/graphene nanocomposites has been provided, taking into account the tunneling effect. The approach is original as it is the first time to our best knowledge that the tunneling effect is modeled in a 3D continuum framework and embedded into finite elements computations. We have provided a modeling scheme in which the graphene sheets are modeled as highly imperfect interfaces to avoid meshing their thickness, and where the tunneling effect is introduced to modify the conductivity in the polymer matrix between close graphene sheets. A complete numerical FEM framework has been provided, and has been applied to 3D RVE of graphene-polymer nanocomposites. The analyses performed using this model on random distributions of graphene sheets for various volume fractions and polymer matrix parameters have allowed concluding on the effects of the respective microstructural parameters with respect to the effective electric properties of the composites, which are obtained by a numerical homogenization procedure.

The second contribution which is also not found in other studies, is the identification of the mechanical behavior of the complex interface between the graphene and the polymer matrix. Indeed, close to the graphene sheet, the polymer chains are confined and form an interphase of several Å where the density and mechanical properties differ from the bulk polymer. In addition, the cohesion between the graphene sheet and the surrounding polymer is weak, while the stiffness in the tangential direction of the graphene is very high. To model these complex interactions, we have proposed an imperfect

interface model in the continuum framework and have proposed a procedure based on MD simulations to evaluate the different coefficients of the model. The obtained continuum model is convenient to be included in finite element simulations, in order to avoid the full description of all atomistic details while preserving the right behavior.

The last contribution is an application of imperfect interface models involving both displacement jump and normal traction jump to random microstructures containing these interfaces, and extended to the finite strains context. This framework is then applied to graphene-polymer nanocomposite RVE to determine their effective incremental elastic tangent behavior and its sensibility to the microstructural parameters. Finally, we have combined this model with the electrical model defined in Chapter 3 to describe the weak electromechanical coupling which occurs at finite strains due to the modification of the critical distances between the graphene sheets during stretching and which affect the percolation. We have shown that this kind of material could theoretically go from conductor to insulator depending on the applied strain.

6.2 Perspectives

There are many potential extension and perspectives to this work, and many questions remain to be addressed.

First, we have chosen a simplified tunneling model, but such model does not imply higher temperature effects. Other models for high temperatures have been studied in the literature, like Fowler-Nordheim tunneling or direct tunneling for room temperature or Schottky emission and thermionic-field emission for high temperatures (see [Chiu 2014b]). Then, the developed models in this thesis could be extended to introduce temperature effects. Besides, according to the choice of different polymer matrix, some bulk-limited conduction mechanism associated with the trap energy level could also be taken into account.

The morphologies of graphene dispersion have been simplified in the presented work. However in practical applications, graphene sheets have much more complicated shapes and do not remain planar. More importantly, graphene sheets are difficult to disperse and usually for aggregates, which can

modify drastically the effective behavior, both regarding electrical and mechanical properties. In that context, several percolation threshold can occur [Wen 2007, Thongruang 2002]. Then, more realistic morphologies of nanostructures, with possibly several characteristic scales, should be characterized with appropriate experiments and introduce in the numerical models. This point should be handled in future studies.

Finally, conducting nanocomposites subjected to high electric currents could involve strong, nonlinear electromechanical coupling. For example, high electric current might cause damage due to electrical breakdown of the polymer matrix, which in turn could modify the electric conductivity related to tunneling effect of by modifying drastically the morphology of fillers. An example of crack propagation in polymer at high electric current is described in Fig. 6.1). A very exciting topic would then to study the damage and strength of such composites when subjected to high energy electric fields.

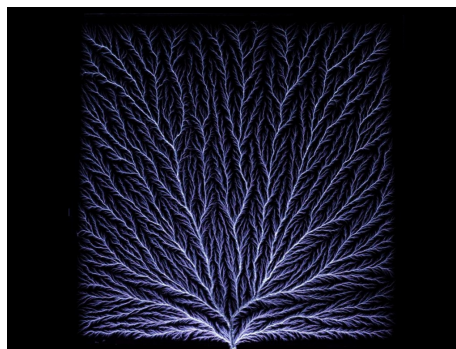


FIGURE 6.1 – Lichtenberg figure : A larger amount of electrical charge is injected into a specimen, which creates very dense dendritic discharges. [Engineering 2017].

Bibliographie

- [Achenbach 1989] J. D. Achenbach and H. Zhu. *Effect of interfacial zone on mechanical behavior and failure of fiber-reinforced composites*. Journal of the Mechanics and Physics of Solids, vol. 37, no. 3, pages 381–393, 1989. (Cited on page 85.)
- [Adamson 1967] A. W. Adamson and A. P. Gast. *Physical chemistry of surfaces*. 1967. (Cited on page 29.)
- [Admal 2010] N. C. Admal and E. B. Tadmor. *A unified interpretation of stress in molecular systems*. Journal of Elasticity, vol. 100, no. 1, pages 63–143, 2010. (Cited on pages 86, 92 and 101.)
- [Admal 2016a] N. C. Admal and E. B. Tadmor. *Material fields in atomistics as pull-backs of spatial distributions*. Journal of the Mechanics and Physics of Solids, vol. 89, pages 59–76, 2016. (Cited on pages 85, 86 and 101.)
- [Admal 2016b] N. C. Admal and E. B. Tadmor. *The non-uniqueness of the atomistic stress tensor and its relationship to the generalized Beltrami representation*. Journal of the Mechanics and Physics of Solids, vol. 93, pages 72–92, 2016. (Cited on pages 85, 86 and 101.)
- [Akhtar 2013] M. S. Akhtar, S. Kwon, F. J. Stadler and O. B. Yang. *High efficiency solid state dye sensitized solar cells with graphene–polyethylene oxide composite electrolytes*. Nanoscale, vol. 5, no. 12, pages 5403–5411, 2013. (Cited on page 36.)
- [Alexandre 2000] M. Alexandre and P. Dubois. *Polymer-layered silicate nanocomposites : preparation, properties and uses of a new class of materials*. Materials Science and Engineering : R : Reports, vol. 28, no. 1, pages 1–63, 2000. (Cited on page 27.)
- [Allaoui 2008] A. Allaoui, S. V. Hoa and M. D. Pugh. *The electronic transport properties and microstructure of carbon nanofiber/epoxy composites*. Composites Science and Technology, vol. 68, no. 2, pages 410 – 416, 2008. (Cited on pages 2, 38 and 219.)
- [An 2011] X. An, T. W. Butler, M. Washington, S. K. Nayak and S. Kar. *Optical and sensing properties of 1-pyrenecarboxylic acid-functionalized*

- graphene films laminated on polydimethylsiloxane membranes.* ACS Nano, vol. 5, no. 2, pages 1003–1011, 2011. (Cited on page 34.)
- [Andersen 1980] H. C. Andersen. *Molecular dynamics simulations at constant pressure and/or temperature.* The Journal of Chemical Physics, vol. 72, no. 4, pages 2384–2393, 1980. (Cited on page 90.)
- [Angmo 2013] D. Angmo and F. C. Krebs. *Flexible ITO-free polymer solar cells.* Journal of Applied Polymer Science, vol. 129, no. 1, pages 1–14, 2013. (Cited on page 36.)
- [Ansari 2009] S. Ansari and E. P. Giannelis. *Functionalized graphene sheet-Poly (vinylidene fluoride) conductive nanocomposites.* Journal of Polymer Science Part B : Polymer Physics, vol. 47, no. 9, pages 888–897, 2009. (Cited on page 76.)
- [Araby 2014] S. Araby, Q. Meng, L. Zhang, H. Kang, P. Majewski, Y. Tang and J. Ma. *Electrically and thermally conductive elastomer/graphene nanocomposites by solution mixing.* Polymer, vol. 55, no. 1, pages 201–210, 2014. (Cited on page 28.)
- [Arash 2014] B. Arash, Q. Wang and V. K. Varadan. *Mechanical properties of carbon nanotube/polymer composites.* Scientific Reports, vol. 4, page 6479, 2014. (Cited on pages 1, 83 and 219.)
- [Arash 2015] B. Arash, H. S. Park and T. Rabczuk. *Mechanical properties of carbon nanotube reinforced polymer nanocomposites : a coarse-grained model.* Composites Part B : Engineering, vol. 80, pages 92–100, 2015. (Cited on page 98.)
- [Arroyo 2002] M. Arroyo and T. Belytschko. *An atomistic-based finite deformation membrane for single layer crystalline films.* Journal of the Mechanics and Physics of Solids, vol. 50, no. 9, pages 1941–1977, 2002. (Cited on page 86.)
- [Arroyo 2004] M. Arroyo and T. Belytschko. *Finite crystal elasticity of carbon nanotubes based on the exponential Cauchy-Born rule.* Physical Review B, vol. 69, no. 11, page 115415, 2004. (Cited on page 86.)
- [Auhl 2003] R. Auhl, R. Everaers, G. S. Grest, K. Kremer and S. J. Plimpton. *Equilibration of long chain polymer melts in computer simulations.* The Journal of Chemical Physics, vol. 119, no. 24, pages 12718–12728, 2003. (Cited on page 97.)

- [Awad 2009] W. H. Awad, G. Beyer, D. Benderly, W. L. Ijdo, P. Songtipya, M. del Mar Jimenez-Gasco, E. Manias and C. A. Wilkie. *Material properties of nanoclay PVC composites*. *Polymer*, vol. 50, no. 8, pages 1857–1867, 2009. (Cited on page 26.)
- [Awasthi 2008] A. P. Awasthi, D. C. Lagoudas and D. C. Hammerand. *Modeling of graphene–polymer interfacial mechanical behavior using molecular dynamics*. *Modelling and Simulation in Materials Science and Engineering*, vol. 17, no. 1, page 015002, 2008. (Cited on pages 32 and 126.)
- [Ayachit 2015] U. Ayachit. *The paraview guide : A parallel visualization application*. Kitware, Inc., USA, 2015. (Cited on page 71.)
- [Baibarac 2009] M. Baibarac, I. Baltog and S. Lefrant. *Raman spectroscopic evidence for interfacial interactions in poly (bithiophene)/single-walled carbon nanotube composites*. *Carbon*, vol. 47, no. 5, pages 1389–1398, 2009. (Cited on page 30.)
- [Balandin 2008] A. A. Balandin, S. Ghosh, W. Bao, I. Calizo, D. Teweldebrhan, F. Miao and C. N. Lau. *Superior thermal conductivity of single-layer graphene*. *Nano Letters*, vol. 8, no. 3, pages 902–907, 2008. (Cited on pages 19 and 20.)
- [Bao 2012] W. S. Bao, S. A. Meguid, Z. H. Zhu and G. J. Weng. *Tunneling resistance and its effect on the electrical conductivity of carbon nanotube nanocomposites*. *Journal of Applied Physics*, vol. 111, 2012. (Cited on page 38.)
- [Barber 2003] A. H. Barber, S. R. Cohen and H. D. Wagner. *Measurement of carbon nanotube-polymer interfacial strength*. *Applied Physics Letters*, vol. 82, no. 23, pages 4140–4142, 2003. (Cited on pages 30 and 84.)
- [Barber 2004a] A. H. Barber, S. R. Cohen, S. K. and H. D. Wagner. *Interfacial fracture energy measurements for multi-walled carbon nanotubes pulled from a polymer matrix*. *Composites Science and Technology*, vol. 64, no. 15, pages 2283–2289, 2004. (Cited on pages 31 and 84.)
- [Barber 2004b] A. H. Barber, S. R. Cohen and H. D. Wagner. *Static and dynamic wetting measurements of single carbon nanotubes*. *Physical Review Letters*, vol. 92, no. 18, page 186103, 2004. (Cited on page 30.)

- [Barber 2005] A. H. Barber, S. R. Cohen and H. D. Wagner. *External and internal wetting of carbon nanotubes with organic liquids*. Physical Review B, vol. 71, no. 11, page 115443, 2005. (Cited on page 30.)
- [Barenblatt 1962] G. I. Barenblatt. *The mathematical theory of equilibrium cracks in brittle fracture*. Advances in Applied Mechanics, vol. 7, pages 55–129, 1962. (Cited on pages 126 and 132.)
- [Baschnagel 2000] J. Baschnagel, K. Binder, P. Doruker, A. A. Gusev, O. Hahn, K. Kremer, W. L. Mattice, F. Müller-Plathe, M. Murat, W. Paul, S. Santos, U. W. Suter and V. Tries. *Bridging the Gap Between Atomistic and Coarse-Grained Models of Polymers : Status and Perspectives*. Advances in Polymer Science, vol. 152, page 51, 2000. (Cited on page 99.)
- [Bassil 2005] A. Bassil, P. Puech, G. Landa, W. Bacsa, S. Barrau, P. Demont, C. Lacabanne, E. Perez, R. Bacsa and E. Flahaut. *Spectroscopic detection of carbon nanotube interaction with amphiphilic molecules in epoxy resin composites*. Journal of Applied Physics, vol. 97, no. 3, page 034303, 2005. (Cited on page 30.)
- [Bauhofer 2009] W. Bauhofer and J. Z. Kovacs. *A review and analysis of electrical percolation in carbon nanotube polymer composites*. Composites Science and Technology, vol. 69, no. 10, pages 1486–1498, 2009. (Cited on pages 38 and 65.)
- [Benveniste 1985] Y. Benveniste. *The effective mechanical behaviour of composite materials with imperfect contact between the constituents*. Mechanics of Materials, vol. 4, no. 2, pages 197–208, 1985. (Cited on page 85.)
- [Benveniste 1987] Y. Benveniste. *A new approach to the application of Mori-Tanaka's theory in composite materials*. Mechanics of Materials, vol. 6, no. 2, pages 147–157, 1987. (Cited on page 150.)
- [Benveniste 2001] Y. Benveniste and T. Miloh. *Imperfect soft and stiff interfaces in two-dimensional elasticity*. Mechanics of Materials, vol. 33, no. 6, pages 309–323, 2001. (Cited on page 128.)
- [Benveniste 2006a] Y. Benveniste. *A general interface model for a three-dimensional curved thin anisotropic interphase between two anisotropic media*. Journal of the Mechanics and Physics of Solids, vol. 54, pages 708–734, 2006. (Cited on pages 41 and 128.)

- [Benveniste 2006b] Y. Benveniste. *An $O(hN)$ interface model of a three-dimensional curved interphase in conduction phenomena*. In Proceedings of the Royal Society of London A : Mathematical, Physical and Engineering Sciences, volume 462, pages 1593–1617. The Royal Society, 2006. (Cited on page 41.)
- [Benveniste 2007] Y. Benveniste and G. Bau. *An interface model of a graded three-dimensional anisotropic curved interphase*. In Proceedings of the Royal Society of London A : Mathematical, Physical and Engineering Sciences, volume 463, pages 419–434. The Royal Society, 2007. (Cited on page 41.)
- [Benveniste 2013] Y. Benveniste. *Models of thin interphases and the effective medium approximation in composite media with curvilinearly anisotropic coated inclusions*. International Journal of Engineering Science, vol. 72, pages 140–154, 2013. (Cited on pages 2 and 220.)
- [Berber 2000] S. Berber, Y. K. Kwon and D. Tománek. *Unusually high thermal conductivity of carbon nanotubes*. Physical Review Letters, vol. 84, no. 20, page 4613, 2000. (Cited on page 19.)
- [Berendsen 1984] H. J. C. Berendsen, J. P. M. Postma, W. F. van Gunsteren, A. DiNola and J. R. Haak. *Molecular dynamics with coupling to an external bath*. The Journal of Chemical Physics, vol. 81, no. 8, pages 3684–3690, 1984. (Cited on pages 89, 90 and 99.)
- [Berger 2006] C. Berger, Z. Song, X. Li, X. Wu, N. Brown, C. Naud and D. Mayou, T. Li, J. Hass, A. N. Marchenkov, E. H. Conrad, P. N. First and W. A. der Heer. *Electronic confinement and coherence in patterned epitaxial graphene*. Science, vol. 312, no. 5777, pages 1191–1196, 2006. (Cited on page 9.)
- [Binder 1995] K. Binder. Monte carlo and molecular dynamics simulations in polymer science. Oxford University Press, 1995. (Cited on pages 97, 98 and 135.)
- [Blake 2008] P. Blake, P. D. Brimicombe, R. R. Nair, T. J. Booth, D. Jiang, F. Schedin, L. A. Ponomarenko, S. V. Morozov, H. F. Gleeson, E. W. Hill, A. K. Geim and K. S. Novoselov. *Graphene-based liquid crystal device*. Nano Letters, vol. 8, no. 6, pages 1704–1708, 2008. (Cited on page 19.)

- [Blakslee 1970] O. L. Blakslee, D. G. Proctor, E. J. Seldin, G. B. Spence and T. Weng. *Elastic constants of compression-annealed pyrolytic graphite*. Journal of Applied Physics, vol. 41, no. 8, pages 3373–3382, 1970. (Cited on page 17.)
- [Bolotin 2008a] K. I. Bolotin, K. J. Sikes, J. Hone, H. L. Stormer and P. Kim. *Temperature-dependent transport in suspended graphene*. Physical Review Letters, vol. 101, no. 9, page 096802, 2008. (Cited on page 16.)
- [Bolotin 2008b] K. I. Bolotin, K. J. Sikes, Z. Jiang, M. Klima, G. Fudenberg, J. Hone, P. Kim and H. L. Stormer. *Ultrahigh electron mobility in suspended graphene*. Solid State Communications, vol. 146, no. 9, pages 351–355, 2008. (Cited on page 16.)
- [Born 1940] M. Born. *On the stability of crystal lattices. I*. In Mathematical Proceedings of the Cambridge Philosophical Society, volume 36, pages 160–172. Cambridge University Press, 1940. (Cited on page 86.)
- [Bortz 2011] D. R. Bortz, E. G. Heras and I. Martin-Gullon. *Impressive fatigue life and fracture toughness improvements in graphene oxide/epoxy composites*. Macromolecules, vol. 45, no. 1, pages 238–245, 2011. (Cited on page 27.)
- [Bose 2011] S. Bose, N. H. Kim, T. Kuila, K. Lau and J. H. Lee. *Electrochemical performance of a graphene-polypyrrole nanocomposite as a supercapacitor electrode*. Nanotechnology, vol. 22, no. 29, page 295202, 2011. (Cited on page 36.)
- [Bövik 1994] P. Bövik. *On the modelling of thin interface layers in elastic and acoustic scattering problems*. The Quarterly Journal of Mechanics and Applied Mathematics, vol. 47, no. 1, pages 17–42, 1994. (Cited on pages 41 and 128.)
- [Brach 2017a] S. Brach, L. Dormieux, D. Kondo and G. Vairo. *Nanoporous materials with a general isotropic plastic matrix : Exact limit state under isotropic loadings*. International Journal of Plasticity, vol. 89, pages 1–28, 2017. (Cited on pages 2 and 220.)
- [Brach 2017b] S. Brach, L. Dormieux, D. Kondo and G. Vairo. *Strength properties of nanoporous materials : a 3-layered based non-linear homogenization approach with interface effects*. International Journal of Engineering Science, vol. 115, pages 28–42, 2017. (Cited on pages 1, 2, 219 and 220.)

- [Britnell 2013] L. Britnell, R. M. Ribeiro, A. Eckmann, R. Jalil, B. D. Belle, A. Mishchenko, Y. Kim, R. V. Gorbachev, T. Georgiou, S. V. Morozov, A. N. Grigorenko, A. K. Geim, C. Casiraghi, A. H. CastroNeto and K. S. Novoselov. *Strong light-matter interactions in heterostructures of atomically thin films*. *Science*, vol. 340, no. 6138, pages 1311–1314, 2013. (Cited on page 33.)
- [Bryning 2005] M. B. Bryning, M. F. Islam, J. M. Kikkawa and A. G. Yodh. *Very Low Conductivity Threshold in Bulk Isotropic Single-Walled Carbon Nanotube–Epoxy Composites*. *Advanced Materials*, vol. 17, no. 9, pages 1186–1191, 2005. (Cited on page 65.)
- [Buldum 2001] A. Buldum and J. P. Lu. *Contact resistance between carbon nanotubes*. *Physical Review B*, vol. 63, page 161403, 2001. (Cited on page 39.)
- [Cai 2009] D. Cai and M. Song. *A simple route to enhance the interface between graphite oxide nanoplatelets and a semi-crystalline polymer for stress transfer*. *Nanotechnology*, vol. 20, no. 31, page 315708, 2009. (Cited on page 83.)
- [Camacho 1996] G. T. Camacho and M. Ortiz. *Computational modelling of impact damage in brittle materials*. *International Journal of Solids and Structures*, vol. 33, no. 20-22, pages 2899–2938, 1996. (Cited on pages 126 and 133.)
- [Cashell 1981] E. M. Cashell, J. M. D. Coey, G. E. Wardell, V. J. McBrierty and D. C. Douglass. *dc electrical conduction in carbon black filled cis-polybutadiene*. *Journal of Applied Physics*, vol. 52, no. 3, pages 1542–1547, 1981. (Cited on page 73.)
- [Castañeda 1995] P. P. Castañeda and J. R. Willis. *The effect of spatial distribution on the effective behavior of composite materials and cracked media*. *Journal of the Mechanics and Physics of Solids*, vol. 43, no. 12, pages 1919–1951, 1995. (Cited on pages 38 and 69.)
- [Chatterjee 2012] S. Chatterjee, J. W. Wang, W. S. Kuo, N. H. Tai, C. Salzmann, W. L. Li, R. Hollertz, F. A. Nüesch and B. T. T. Chu. *Mechanical reinforcement and thermal conductivity in expanded graphene nanoplatelets reinforced epoxy composites*. *Chemical Physics Letters*, vol. 531, pages 6–10, 2012. (Cited on page 27.)

- [Chatzigeorgiou 2017] G. Chatzigeorgiou, F. Meraghni and A. Javili. *Generalized interfacial energy and size effects in composites*. Journal of the Mechanics and Physics of Solids, vol. 106, pages 257–282, 2017. (Cited on pages 84 and 113.)
- [Chen 2007] T. Chen, G. J. Dvorak and C. C. Yu. *Size-dependent elastic properties of unidirectional nano-composites with interface stresses*. Acta Mechanica, vol. 188, no. 1-2, pages 39–54, 2007. (Cited on pages 2 and 220.)
- [Chen 2008] H. Chen, Q. Xue, Q. Zheng, J. Xie and K. Yan. *Influence of nanotube chirality, temperature, and chemical modification on the interfacial bonding between carbon nanotubes and polyphenylacetylene*. The Journal of Physical Chemistry C, vol. 112, no. 42, pages 16514–16520, 2008. (Cited on page 32.)
- [Chen 2012] Y. Chen, Y. Qi, Z. Tai, X. Yan, F. Zhu and Q. Xue. *Preparation, mechanical properties and biocompatibility of graphene oxide/ultrahigh molecular weight polyethylene composites*. European Polymer Journal, vol. 48, no. 6, pages 1026–1033, 2012. (Cited on page 28.)
- [Chen 2015] Z. Chen, A. Umar, S. Wang, Y. Wang, T. Tian, Y. Shang, Y. Fan, Q. Qi, D. Xu and L. Jiang. *Supramolecular fabrication of multilevel graphene-based gas sensors with high NO₂ sensibility*. Nanoscale, vol. 7, no. 22, pages 10259–10266, 2015. (Cited on pages 33 and 34.)
- [Chiu 2012] F. C. Chiu and I. N. Huang. *Phase morphology and enhanced thermal/mechanical properties of polyamide 46/graphene oxide nano-composites*. Polymer Testing, vol. 31, no. 7, pages 953–962, 2012. (Cited on page 28.)
- [Chiu 2014a] F. C. Chiu. *A Review on Conduction Mechanisms in Dielectric Films*. Advances in Materials Science & Engineering, pages 1–18, 2014. (Cited on page 46.)
- [Chiu 2014b] F. C. Chiu. *A Review on Conduction Mechanisms in Dielectric Films*. Advances in Materials Science & Engineering, pages 1–18, 2014. (Cited on page 174.)
- [Chowdhury 2007] S. C. Chowdhury and T. Okabe. *Computer simulation of carbon nanotube pull-out from polymer by the molecular dynamics method*. Composites Part A : Applied Science and Manufacturing, vol. 38, no. 3, pages 747–754, 2007. (Cited on page 126.)

- [Cormier 2001] J. Cormier, J. M. Rickman and T. J. Delph. *Stress calculation in atomistic simulations of perfect and imperfect solids*. Journal of Applied Physics, vol. 89, no. 1, pages 99–104, 2001. (Cited on page 86.)
- [Das 2009] B. Das, K. E. Prasad, U. Ramamurty and C. N. R. Rao. *Nano-indentation studies on polymer matrix composites reinforced by few-layer graphene*. Nanotechnology, vol. 20, no. 12, page 125705, 2009. (Cited on page 25.)
- [Dauber-Osguthorpe 1988] P. Dauber-Osguthorpe, V. A. Roberts, D. J. Osguthorpe, J. W., M. Genest and A. T. Hagler. *Structure and energetics of ligand binding to proteins : Escherichia coli dihydrofolate reductase-trimethoprim, a drug-receptor system*. Proteins : Structure, Function, and Bioinformatics, vol. 4, no. 1, pages 31–47, 1988. (Cited on page 91.)
- [den Bosch 2006] M. J. Van den Bosch, P. J. G. Schreurs and M. G. D. Geers. *An improved description of the exponential Xu and Needleman cohesive zone law for mixed-mode decohesion*. Engineering Fracture Mechanics, vol. 73, no. 9, pages 1220–1234, 2006. (Cited on pages 134 and 135.)
- [den Bosch 2007] M. J. Van den Bosch, P. J. G. Schreurs and M. G. D. Geers. *A cohesive zone model with a large displacement formulation accounting for interfacial fibrillation*. European Journal of Mechanics-A/Solids, vol. 26, no. 1, pages 1–19, 2007. (Cited on pages 126 and 132.)
- [Dikin 2007] D. A. Dikin, S. Stankovich, E. J. Zimney, R. D. Piner, G. H. B. Dommett, G. Evmenenko, S. T. Nguyen and R. S. Ruoff. *Preparation and characterization of graphene oxide paper*. Nature, vol. 448, no. 7152, page 457, 2007. (Cited on page 18.)
- [Dresselhaus 1996] M. S. Dresselhaus, G. Dresselhaus and P. C. Eklund. *Science of fullerenes and carbon nanotubes : their properties and applications*. Academic Press, 1996. (Cited on page 30.)
- [Du 2005] F. Du, J. E. Fischer and K. I. Winey. *Effect of nanotube alignment on percolation conductivity in carbon nanotube/polymer composites*. Physical Review B, vol. 72, no. 12, page 121404, 2005. (Cited on pages 38 and 65.)
- [Du 2012] J. Du and H. M. Cheng. *The fabrication, properties, and uses of graphene/polymer composites*. Macromolecular Chemistry and Physics, vol. 213, no. 10-11, pages 1060–1077, 2012. (Cited on pages 20 and 37.)

- [Duan 2005a] H. L. Duan, J. Wang, Z. P. Huang and B. L. Karihaloo. *Eshelby formalism for nano-inhomogeneities*. In Proceedings of the Royal Society of London A : Mathematical, Physical and Engineering Sciences, volume 461, pages 3335–3353, 2005. (Cited on page 132.)
- [Duan 2005b] H. L. Duan, J. Wang, Z. P. Huang and B. L. Karihaloo. *Size-dependent effective elastic constants of solids containing nano-inhomogeneities with interface stress*. Journal of the Mechanics and Physics of Solids, vol. 53, no. 7, pages 1574–1596, 2005. (Cited on pages 1, 2, 85, 132, 219 and 220.)
- [Duan 2006] H. L. Duan, J. Wang, B. L. Karihaloo and Z. P. Huang. *Nanoporous materials can be made stiffer than non-porous counterparts by surface modification*. Acta Materialia, vol. 54, no. 11, pages 2983–2990, 2006. (Cited on pages 2 and 220.)
- [Dugdale 1960] D. S. Dugdale. *Yielding of steel sheets containing slits*. Journal of the Mechanics and Physics of Solids, vol. 8, no. 2, pages 100–104, 1960. (Cited on pages 126 and 132.)
- [Dujardin 1998] E. Dujardin, T. W. Ebbesen, A. Krishnan and M. M. J. Treacy. *Wetting of single shell carbon nanotubes*. Advanced Materials, vol. 10, no. 17, pages 1472–1475, 1998. (Cited on page 29.)
- [El-Kady 2013] M. F. El-Kady and R. B. Kaner. *Scalable fabrication of high-power graphene micro-supercapacitors for flexible and on-chip energy storage*. Nature Communications, vol. 4, page 1475, 2013. (Cited on page 33.)
- [Engineering 2017] Stoneridge Engineering. *What are Lichtenberg figures, and how do we make them ?* 2017. <http://www.capturedlightning.com/frames/lichtenbergs.html>. (Cited on page 175.)
- [Eshelby 1957] J. D. Eshelby. *The determination of the elastic field of an ellipsoidal inclusion, and related problems*. In Proceedings of the Royal Society of London A : Mathematical, Physical and Engineering Sciences, volume 241, pages 376–396. The Royal Society, 1957. (Cited on pages 70 and 150.)
- [Evans 1983] D. J. Evans. *Computer experiment for nonlinear thermodynamics of Couette flow*. The Journal of Chemical Physics, vol. 78, no. 6, pages 3297–3302, 1983. (Cited on page 89.)

- [Evans 1984] D. J. Evans and O. P. Morriss. *Non-Newtonian molecular dynamics*. Computer Physics Reports, vol. 1, no. 6, pages 297–343, 1984. (Cited on page 89.)
- [Fan 2015] Z. Fan, F. Gong, S. T. Nguyen and H. M. Duong. *Advanced multifunctional graphene aerogel-Poly (methyl methacrylate) composites : Experiments and modeling*. Carbon, vol. 81, pages 396–404, 2015. (Cited on page 38.)
- [Fang 2009] M. Fang, K. Wang, H. Lu, Y. Yang and S. Nutt. *Covalent polymer functionalization of graphene nanosheets and mechanical properties of composites*. Journal of Materials Chemistry, vol. 19, no. 38, pages 7098–7105, 2009. (Cited on pages 25 and 125.)
- [Fang 2010] M. Fang, Z. Zhang, J. Li, H. Zhang, H. Lu and Y. Yang. *Constructing hierarchically structured interphases for strong and tough epoxy nanocomposites by amine-rich graphene surfaces*. Journal of Materials Chemistry, vol. 20, no. 43, pages 9635–9643, 2010. (Cited on page 26.)
- [Farsad 2012] M. Farsad and F. J. Vernerey. *An XFEM-based numerical strategy to model mechanical interactions between biological cells and a deformable substrate*. International Journal for Numerical Methods in Engineering, vol. 92, no. 3, pages 238–267, 2012. (Cited on pages 2 and 220.)
- [Fornes 2003] T. D. Fornes and D. R. Paul. *Modeling properties of nylon 6/clay nanocomposites using composite theories*. Polymer, vol. 44, no. 17, pages 4993–5013, 2003. (Cited on page 27.)
- [Frankland 2003] S. J. V. Frankland, V. M. Harik, G. M. Odegard, D. W. Brenner and T. S. Gates. *The stress-strain behavior of polymer-nanotube composites from molecular dynamics simulation*. Composites Science and Technology, vol. 63, no. 11, pages 1655–1661, 2003. (Cited on page 117.)
- [Fuchs 2013] J. N. Fuchs. *Dirac fermions in graphene and analogues : magnetic field and topological properties*. arXiv preprint arXiv :1306.0380, 2013. (Cited on page 15.)
- [Fukushima 2006] H. Fukushima, L. T. Drzal, B. P. Rook and M. J. Rich. *Thermal conductivity of exfoliated graphite nanocomposites*. Journal of Thermal Analysis and Calorimetry, vol. 85, no. 1, pages 235–238, 2006. (Cited on page 28.)

- [Galpaya 2012] D. Galpaya, M. Wang, M. Liu, N. Motta, E. R. Waclawik and C. Yan. *Recent advances in fabrication and characterization of graphene-polymer nanocomposites*. Graphene, vol. 1, no. 2, pages 30–49, 2012. (Cited on pages 20 and 22.)
- [Gan 2012] X. Gan, H. Zhou, B. Zhu, X. Yu, Y. Jia, B. Sun, M. Zhang, X. Huang, J. Liu and T. Luo. *A simple method to synthesize graphene at 633K by dechlorination of hexachlorobenzene on Cu foils*. Carbon, vol. 50, no. 1, pages 306–310, 2012. (Cited on page 11.)
- [Gao 1995] J. Gao. *An efficient method of generating dense polymer model melts by computer simulation*. The Journal of Chemical Physics, vol. 102, no. 2, pages 1074–1077, 1995. (Cited on pages 97 and 99.)
- [Geers 2010] M. G. D. Geers, V. G. Kouznetsova and W. A. M. Brekelmans. *Multi-scale computational homogenization : Trends and challenges*. Journal of Computational and Applied Mathematics, vol. 7, pages 2175–2182, 2010. (Cited on page 52.)
- [Geers 2016] M. G. D. Geers and J. Yvonnet. *Multiscale Modeling of Microstructure-Property Relations*. MRS Bull., vol. 41(08), pages 610–616, 2016. (Cited on page 52.)
- [Geim 2007] A. K. Geim and K. S. Novoselov. *The rise of graphene*. Nature Materials, vol. 6, no. 3, pages 183–191, 2007. (Cited on pages 9 and 10.)
- [Geuzaine 2009] C. Geuzaine and J. F. Remacle. *Gmsh : A 3-D finite element mesh generator with built-in pre- and post-processing facilities*. International Journal for Numerical Methods in Engineering, vol. 79, no. 11, pages 1309–1331, 2009. (Cited on page 58.)
- [Giannelis 1996] E. P. Giannelis. *Polymer layered silicate nanocomposites*. Advanced Materials, vol. 8, no. 1, pages 29–35, 1996. (Cited on page 125.)
- [Glusker 1994] J. P. Glusker, M. Lewis and M. Rossi. *Crystal structure analysis for chemists and biologists*, volume 16. John Wiley & Sons, 1994. (Cited on page 93.)
- [Gojny 2006] F. H. Gojny, M. H. G. Wichmann, B. Fiedler, I. A. Kinloch, W. Bauhofer, A. H. Windle and K. Schulte. *Evaluation and identification of electrical and thermal conduction mechanisms in carbon nanotube/epoxy composites*. Polymer, vol. 47, no. 6, pages 2036 – 2045, 2006. (Cited on page 38.)

- [Gómez-Navarro 2008] C. Gómez-Navarro, M. Burghard and K. Kern. *Elastic properties of chemically derived single graphene sheets*. Nano Letters, vol. 8, no. 7, pages 2045–2049, 2008. (Cited on page 18.)
- [Gong 2010] L. Gong, I. A. Kinloch, R. J. Young, I. Riaz, R. Jalil and K. S. Novoselov. *Interfacial stress transfer in a graphene monolayer nanocomposite*. Advanced Materials, vol. 22, no. 24, pages 2694–2697, 2010. (Cited on page 83.)
- [Gou 2004] J. Gou, B. Minaie, B. Wang, Z. Liang and C. Zhang. *Computational and experimental study of interfacial bonding of single-walled nanotube reinforced composites*. Computational Materials Science, vol. 31, no. 3, pages 225–236, 2004. (Cited on page 126.)
- [Gou 2005] J. Gou, Z. Liang, C. Zhang and B. Wang. *Computational analysis of effect of single-walled carbon nanotube rope on molecular interaction and load transfer of nanocomposites*. Composites Part B : Engineering, vol. 36, no. 6, pages 524–533, 2005. (Cited on page 32.)
- [Gremaud 2016] G. Gremaud. Eulerian theory of newtonian deformable lattices-dislocation and disclination charges in solids. EPFL-BOOK-220175, 2016. (Cited on page 101.)
- [Grest 1986] G. S. Grest and K. Kremer. *Molecular dynamics simulation for polymers in the presence of a heat bath*. Physical Review A, vol. 33, no. 5, page 3628, 1986. (Cited on page 89.)
- [Grimaldi 2006] C. Grimaldi and I. Balberg. *Tunneling and nonuniversality in continuum percolation systems*. Physical Review Letters, vol. 96, no. 6, page 066602, 2006. (Cited on page 38.)
- [Gu 2008] S. T. Gu. *Contributions à la modélisation des interfaces imparfaites et à l'homogénéisation des matériaux hétérogènes*. PhD thesis, Université Paris-Est, 2008. (Cited on page 41.)
- [Gu 2011] S.T. Gu and Q.-C. He. *Interfacial discontinuity relations for coupled multifield phenomena and their application to the modeling of thin interphases as imperfect interfaces*. Journal of the Mechanics and Physics of Solids, vol. 59, no. 7, pages 1413–1426, 2011. (Cited on pages 39, 41, 50, 116 and 128.)
- [Gu 2016] J. Gu, X. Yang, Z. Lv, N. Li, C. Liang and Q. Zhang. *Functionalized graphite nanoplatelets/epoxy resin nanocomposites with high thermal*

- conductivity*. International Journal of Heat and Mass Transfer, vol. 92, pages 15–22, 2016. (Cited on page 28.)
- [Guessasma 2010] S. Guessasma, N. Benseddiq and D. Lourdin. *Effective Young's modulus of biopolymer composites with imperfect interface*. International Journal of Solids and Structures, vol. 47, no. 18, pages 2436–2444, 2010. (Cited on page 85.)
- [Guo 2012] F. Guo, G. Silverberg, S. Bowers, S. P. Kim, D. Datta, V. Shenoy and R. H. Hurt. *Graphene-based environmental barriers*. Environmental Science & Technology, vol. 46, no. 14, pages 7717–7724, 2012. (Cited on page 28.)
- [Guo 2013] W. Guo, C. Cheng, Y. Wu, Y. Jiang, J. Gao, D. Li and L. Jiang. *Bio-inspired two-dimensional nanofluidic generators based on a layered graphene hydrogel membrane*. Advanced Materials, vol. 25, no. 42, pages 6064–6068, 2013. (Cited on page 33.)
- [Gurtin 1975] M. E. Gurtin and A. Ian Murdoch. *A continuum theory of elastic material surfaces*. Archive for Rational Mechanics and Analysis, vol. 57, no. 4, pages 291–323, 1975. (Cited on pages 1, 127 and 219.)
- [Haggenmueller 2007] R. Haggenmueller, C. Guthy, J. R. Lukes, J. E. Fischer and K. I. Winey. *Single wall carbon nanotube/polyethylene nanocomposites : thermal and electrical conductivity*. Macromolecules, vol. 40, no. 7, pages 2417–2421, 2007. (Cited on page 65.)
- [Haley 2015] B. P. Haley, C. Li, N. Wilson, E. Jaramillo and A. Strachan. *Atomistic simulations of amorphous polymers in the cloud with Polymer-Modeler*. arXiv preprint arXiv :1503.03894, 2015. (Cited on page 99.)
- [Hamann 1988] C. Hamann, H. Burghardt and T. Frauenheim. *Electrical conduction mechanisms in solids*. Vch Pub, 1988. (Cited on page 46.)
- [Hardy 1982] R. J. Hardy. *Formulas for determining local properties in molecular-dynamics simulations : Shock waves*. The Journal of Chemical Physics, vol. 76, no. 1, pages 622–628, 1982. (Cited on pages 86 and 100.)
- [Hardy 2002] R. J. Hardy, S. Root and D. R. Swanson. *Continuum properties from molecular simulations*. In AIP Conference Proceedings, volume 620, pages 363–366, 2002. (Cited on page 100.)

- [Hashemi 2016] R. Hashemi and G. J. Weng. *A theoretical treatment of graphene nanocomposites with percolation threshold, tunneling-assisted conductivity and microcapacitor effect in AC and DC electrical settings*. Carbon, vol. 96, pages 474–490, 2016. (Cited on page 39.)
- [Hashin 1963] Z. Hashin and S. Shtrikman. *A variational approach to the theory of the elastic behaviour of multiphase materials*. Journal of the Mechanics and Physics of Solids, vol. 11, no. 2, pages 127–140, 1963. (Cited on pages 69 and 150.)
- [Hashin 1990] Z. Hashin. *Thermoelastic properties of fiber composites with imperfect interface*. Mechanics of Materials, vol. 8, no. 4, pages 333–348, 1990. (Cited on page 127.)
- [Hashin 1991] Z. Hashin. *Thermoelastic properties of particulate composites with imperfect interface*. Journal of the Mechanics and Physics of Solids, vol. 39, no. 6, pages 745–762, 1991. (Cited on page 127.)
- [Hashin 1992] Z. Hashin. *Extremum principles for elastic heterogenous media with imperfect interfaces and their application to bounding of effective moduli*. Journal of the Mechanics and Physics of Solids, vol. 40, no. 4, pages 767–781, 1992. (Cited on page 85.)
- [Hashin 2001] Z. Hashin. *Thin interphase/imperfect interface in conduction*. Journal of Applied Physics, vol. 89, no. 4, pages 2261–2267, 2001. (Cited on page 41.)
- [Hashin 2002] Z. Hashin. *Thin interphase/imperfect interface in elasticity with application to coated fiber composites*. Journal of the Mechanics and Physics of Solids, vol. 50, no. 12, pages 2509–2537, 2002. (Cited on pages 41 and 85.)
- [Hass 2008] J. Hass, W. A. De Heer and E. H. Conrad. *The growth and morphology of epitaxial multilayer graphene*. Journal of Physics : Condensed Matter, vol. 20, no. 32, page 323202, 2008. (Cited on page 10.)
- [He 2009] F. He, S. Lau, H. L. Chan and J. Fan. *High Dielectric Permittivity and Low Percolation Threshold in Nanocomposites Based on Poly(vinylidene fluoride) and Exfoliated Graphite Nanoplates*. Advanced Materials, vol. 21, no. 6, pages 710–715, 2009. (Cited on page 38.)
- [Heinz 2005] H. Heinz, H. Koerner, K. L. Anderson, R. A. Vaia and B. L. Farmer. *Force field for mica-type silicates and dynamics of octadecy-*

- lammonium chains grafted to montmorillonite*. Chemistry of Materials, vol. 17, no. 23, pages 5658–5669, 2005. (Cited on page 91.)
- [Hernández-Pérez 2010] A. Hernández-Pérez and F. Avilés. *Modeling the influence of interphase on the elastic properties of carbon nanotube composites*. Computational Materials Science, vol. 47, no. 4, pages 926–933, 2010. (Cited on page 84.)
- [Hoang 2015] M. T. Hoang, J. Yvonnet, A. Mitrushchenkov, G. Chambaud and H. L. Duan. *Size-dependent mechanical properties of axial and radial mixed AlN/GaN nanostructure*. Nanotechnology, vol. 26, no. 11, page 115703, 2015. (Cited on page 120.)
- [Holzapfel 2000] G. A. Holzapfel. *Nonlinear solid mechanics : A continuum approach for engineering*. Wiley, 2000. (Cited on page 157.)
- [Hoover 1985] W. G. Hoover. *Canonical dynamics : equilibrium phase-space distributions*. Physical Review A, vol. 31, no. 3, page 1695, 1985. (Cited on page 89.)
- [Hossain 2010] D. Hossain, M. A. Tschopp, D. K. Ward, J. L. Bouvard, P. Wang and M. F. Horstemeyer. *Molecular dynamics simulations of deformation mechanisms of amorphous polyethylene*. Polymer, vol. 51, no. 25, pages 6071–6083, 2010. (Cited on page 97.)
- [Hu 2008a] C. H. Hu, C. H. Liu, L. Z. Chen, Y. C. Peng and S. S. Fan. *Resistance-pressure sensitivity and a mechanism study of multiwall carbon nanotube networks/poly(dimethylsiloxane) composites*. Applied Physics Letters, vol. 93, no. 3, 2008. (Cited on page 38.)
- [Hu 2008b] N. Hu, Y. Karube, C. Yan, Z. Masuda and H. Fukunaga. *Tunneling effect in a polymer/carbon nanotube nanocomposite strain sensor*. Acta Materialia, vol. 56, no. 13, pages 2929 – 2936, 2008. (Cited on page 38.)
- [Hu 2013] K. Hu, M. K. Gupta, D. D. Kulkarni and V. V. Tsukruk. *Ultra-Robust Graphene Oxide-Silk Fibroin Nanocomposite Membranes*. Advanced Materials, vol. 25, no. 16, pages 2301–2307, 2013. (Cited on page 33.)
- [Huang 2007] Z. P. Huang and L. Sun. *Size-dependent effective properties of a heterogeneous material with interface energy effect : from finite deformation theory to infinitesimal strain analysis*. Acta Mechanica, vol. 190, no. 1-4, pages 151–163, 2007. (Cited on pages 2 and 220.)

- [Huang 2012] H. D. Huang, P. G. Ren, J. Chen, W. Q. Zhang, X. Ji and Z. M. Li. *High barrier graphene oxide nanosheet/poly (vinyl alcohol) nanocomposite films*. Journal of Membrane Science, vol. 409, pages 156–163, 2012. (Cited on page 28.)
- [Huy 1974] H. P. Huy and E. Sánchez-Palencia. *Phénomènes de transmission à travers des couches minces de conductivité élevée*. Journal of Mathematical Analysis and Applications, vol. 47, no. 2, pages 284–309, 1974. (Cited on page 40.)
- [Irving 1950] J. H. Irving and J. G. Kirkwood. *The statistical mechanical theory of transport processes. IV. The equations of hydrodynamics*. The Journal of Chemical Physics, vol. 18, no. 6, pages 817–829, 1950. (Cited on page 86.)
- [Israelachvili 2015] J. N. Israelachvili. *Intermolecular and surface forces*. Academic Press, 2015. (Cited on page 29.)
- [Jiang 2009a] J. W. Jiang, J. S. Wang and B. Li. *Young’s modulus of graphene : a molecular dynamics study*. Physical Review B, vol. 80, no. 11, page 113405, 2009. (Cited on page 83.)
- [Jiang 2009b] J. Y. Jiang, M. S. Kim, H. M. Jeong and C. M. Shon. *Graphite oxide/poly (methyl methacrylate) nanocomposites prepared by a novel method utilizing macroazoinitiator*. Composites Science and Technology, vol. 69, no. 2, pages 186–191, 2009. (Cited on pages 24 and 76.)
- [Kalaitzidou 2007] K. Kalaitzidou, H. Fukushima and L. T. Drzal. *Multifunctional polypropylene composites produced by incorporation of exfoliated graphite nanoplatelets*. Carbon, vol. 45, no. 7, pages 1446–1452, 2007. (Cited on page 28.)
- [Karayiannis 2002] N. C. Karayiannis, V. G. Mavrantzas and D. N. Theodorou. *A novel Monte Carlo scheme for the rapid equilibration of atomistic model polymer systems of precisely defined molecular architecture*. Physical Review Letters, vol. 88, no. 10, page 105503, 2002. (Cited on page 97.)
- [Khounlavong 2010] L. Khounlavong, V. Pryamitsyn and V. Ganesan. *Many-body interactions and coarse-grained simulations of structure of nanoparticle-polymer melt mixtures*. The Journal of Chemical Physics, vol. 133, no. 14, page 144904, 2010. (Cited on page 32.)

- [Kim 2009] K. S. Kim, Y. Zhao, H. Jang, S. Y. Lee, J. M. Kim, K. S. Kim, J. H. Ahn, P. Kim, J. Y. Choi and B. H. Hong. *Large-scale pattern growth of graphene films for stretchable transparent electrodes*. Nature, vol. 457, no. 7230, page 706, 2009. (Cited on page 33.)
- [Kim 2010] H. Kim, Y. Miura and C. W. Macosko. *Graphene/polyurethane nanocomposites for improved gas barrier and electrical conductivity*. Chemistry of Materials, vol. 22, no. 11, pages 3441–3450, 2010. (Cited on pages 24 and 25.)
- [Kim 2015] S. Y. Kim, Y. J. Noh and J. Yu. *Prediction and experimental validation of electrical percolation by applying a modified micromechanics model considering multiple heterogeneous inclusions*. Composites Science and Technology, vol. 106, pages 156–162, 2015. (Cited on page 70.)
- [Klarbring 1991] A. Klarbring. *Derivation of a model of adhesively bonded joints by the asymptotic expansion method*. International Journal of Engineering Science, vol. 29, no. 4, pages 493–512, 1991. (Cited on pages 40 and 128.)
- [Kobayashi 1980] S. Kobayashi, K. Maeda and S. Takeuchi. *Computer simulation of deformation of amorphous Cu₅₇Zr₄₃*. Acta Metallurgica, vol. 28, no. 12, pages 1641–1652, 1980. (Cited on page 95.)
- [Krauth 2006] W. Krauth. Statistical mechanics : algorithms and computations, volume 13. OUP Oxford, 2006. (Cited on page 56.)
- [Kremer 1990] K. Kremer and G. S. Grest. *Dynamics of entangled linear polymer melts : A molecular-dynamics simulation*. The Journal of Chemical Physics, vol. 92, no. 8, pages 5057–5086, 1990. (Cited on page 97.)
- [Krishnan 2008] S. Krishnan, E. Stefanakos and S. Bhansali. *Effects of dielectric thickness and contact area on current-voltage characteristics of thin film metal-insulator-metal diodes*. Thin Solid Films, vol. 516, no. 8, pages 2244 – 2250, 2008. (Cited on page 47.)
- [Kujawski 2010] M. Kujawski, J. D. Pearse and E. Smela. *Elastomers filled with exfoliated graphite as compliant electrodes*. Carbon, vol. 48, no. 9, pages 2409–2417, 2010. (Cited on page 24.)
- [Le-Quang 2010] H. Le-Quang, G. Bonnet and Q-C He. *Size-dependent Eshelby tensor fields and effective conductivity of composites made of*

- anisotropic phases with highly conducting imperfect interfaces*. Physical Review B, vol. 81, no. 6, page 064203, 2010. (Cited on pages 2 and 220.)
- [Lee 2007] H. K. Lee and S. H. Pyo. *Micromechanics-based elastic damage modeling of particulate composites with weakened interfaces*. International Journal of Solids and Structures, vol. 44, no. 25, pages 8390–8406, 2007. (Cited on page 85.)
- [Lee 2008] C. Lee, X. Wei, J. W. Kysar and J. Hone. *Measurement of the elastic properties and intrinsic strength of monolayer graphene*. Science, vol. 321, no. 5887, pages 385–388, 2008. (Cited on pages 17, 18 and 83.)
- [Lee 2017] H Cheun Lee, Wei-Wen Liu, Siang-Piao Chai, Abdul Rahman Mohamed, Azizan Aziz, Cheng-Seong Khe, N MS Hidayah and U Hashim. *Review of the synthesis, transfer, characterization and growth mechanisms of single and multilayer graphene*. RSC Advances, vol. 7, no. 26, pages 15644–15693, 2017. (Cited on page 13.)
- [Lefrant 2004] S. Lefrant, J. P. Buisson, J. Schreiber, O. Chauvet, M. Baibarac and I. Baltog. *Raman studies of carbon nanotubes and polymer nanotube composites*. Molecular Crystals and Liquid Crystals, vol. 415, no. 1, pages 125–132, 2004. (Cited on page 30.)
- [Leimkuhler 2009] B. Leimkuhler, E. Noorizadeh and F. Theil. *A gentle stochastic thermostat for molecular dynamics*. Journal of Statistical Physics, vol. 135, no. 2, pages 261–277, 2009. (Cited on page 89.)
- [Lemaitre 2006] A. Lemaitre and C. Maloney. *Sum Rules for the Quasi-Static and Visco-Elastic Response of Disordered Solids at Zero Temperature*. Journal of Statistical Physics, vol. 123, no. 2, pages 415–452, 2006. (Cited on pages 86 and 96.)
- [Li 2006] C. Li and T. W. Chou. *Multiscale modeling of compressive behavior of carbon nanotube/polymer composites*. Composites Science and Technology, vol. 66, no. 14, pages 2409–2414, 2006. (Cited on pages 1, 86 and 219.)
- [Li 2007] J. Li, P. C. Ma, W. S. Chow, C. K. To, B. Z. Tang and J. K. Kim. *Correlations between Percolation Threshold, Dispersion State, and Aspect Ratio of Carbon Nanotubes*. Advanced Functional Materials, vol. 17, no. 16, pages 3207–3215, 2007. (Cited on page 38.)

- [Li 2009a] C. C. Li, C. L. Lu, Y. T. Lin, B. Y. Wei and W. K. Hsu. *Creation of interfacial phonons by carbon nanotube–polymer coupling*. Physical Chemistry Chemical Physics, vol. 11, no. 29, pages 6034–6037, 2009. (Cited on page 31.)
- [Li 2009b] Q. Li, N. H. Kim, G. H. Yoo and J. H. Lee. *Positive temperature coefficient characteristic and structure of graphite nanofibers reinforced high density polyethylene/carbon black nanocomposites*. Composites Part B : Engineering, vol. 40, no. 3, pages 218 – 224, 2009. (Cited on page 37.)
- [Li 2010] S. S. Li, K. H. Tu, C. C. Lin, C. W. Chen and M. Chhowalla. *Solution-processable graphene oxide as an efficient hole transport layer in polymer solar cells*. ACS Nano, vol. 4, no. 6, pages 3169–3174, 2010. (Cited on page 36.)
- [Li 2011] Y. Li, Y. Liu, X. Peng, C. Yan, S. Liu and N. Hu. *Pull-out simulations on interfacial properties of carbon nanotube-reinforced polymer nanocomposites*. Computational Materials Science, vol. 50, no. 6, pages 1854–1860, 2011. (Cited on page 32.)
- [Li 2013] W. Li, A. Dichiara and J. Bai. *Carbon nanotube-graphene nanoplatelet hybrids as high-performance multifunctional reinforcements in epoxy composites*. Composites Science and Technology, vol. 74, pages 221–227, 2013. (Cited on pages 1, 37 and 219.)
- [Liang 2009a] J. Liang, Y. Huang, L. Zhang, Y. Wang, Y. Ma, T. Guo and Y. Chen. *Molecular-level dispersion of graphene into poly (vinyl alcohol) and effective reinforcement of their nanocomposites*. Advanced Functional Materials, vol. 19, no. 14, pages 2297–2302, 2009. (Cited on page 148.)
- [Liang 2009b] J. Liang, Y. Wang, Y. Huang, Y. Ma, Z. Liu, J. Cai, C. Zhang, H. Gao and Y. Chen. *Electromagnetic interference shielding of graphene/epoxy composites*. Carbon, vol. 47, no. 3, pages 922–925, 2009. (Cited on page 76.)
- [Liang 2009c] J. Liang, Y. Xu, Y. Huang, L. Zhang, Y. Wang, Y. Ma, F. Li, T. Guo and Y. Chen. *Infrared-triggered actuators from graphene-based nanocomposites*. The Journal of Physical Chemistry C, vol. 113, no. 22, pages 9921–9927, 2009. (Cited on page 25.)

- [Liao 2001] K. Liao and S. Li. *Interfacial characteristics of a carbon nanotube-polystyrene composite system*. Applied Physics Letters, vol. 79, no. 25, pages 4225–4227, 2001. (Cited on page 126.)
- [Lielens 1999] G. Lielens. *Micro-macro modeling of structured materials*. PhD thesis, Universite Catholique de Louvain, 1999. (Cited on page 150.)
- [Lier 2000] G. Van Lier, C. Van Alsenoy, V. Van Doren and P. Geerlings. *Ab initio study of the elastic properties of single-walled carbon nanotubes and graphene*. Chemical Physics Letters, vol. 326, no. 1, pages 181–185, 2000. (Cited on pages 17 and 83.)
- [Liu 2007] F. Liu, P. Ming and J. Li. *Ab initio calculation of ideal strength and phonon instability of graphene under tension*. Physical Review B, vol. 76, no. 6, page 064120, 2007. (Cited on page 17.)
- [Liu 2008a] N. Liu, F. Luo, H. Wu, Y. Liu, C. Zhang and J. Chen. *One-step ionic-liquid-assisted electrochemical synthesis of ionic-liquid-functionalized graphene sheets directly from graphite*. Advanced Functional Materials, vol. 18, no. 10, pages 1518–1525, 2008. (Cited on page 23.)
- [Liu 2008b] Y. J. Liu, N. Nishimura, D. Qian, N. Adachi, Y. Otani and V. Mokashi. *A boundary element method for the analysis of CNT/polymer composites with a cohesive interface model based on molecular dynamics*. Engineering Analysis with Boundary Elements, vol. 32, no. 4, pages 299–308, 2008. (Cited on page 126.)
- [Liu 2012] C. Liu, G. Hu and H. Gao. *Preparation of few-layer and single-layer graphene by exfoliation of expandable graphite in supercritical N₂/N-dimethylformamide*. The Journal of Supercritical Fluids, vol. 63, pages 99–104, 2012. (Cited on page 11.)
- [Liu 2013] H. Liu, T. Kuila, N. H. Kim, B. C. Ku and J. H. Lee. *In situ synthesis of the reduced graphene oxide–polyethyleneimine composite and its gas barrier properties*. Journal of Materials Chemistry A, vol. 1, no. 11, pages 3739–3746, 2013. (Cited on page 28.)
- [Liu 2015] J. T. Liu, S. T. Gu and Q.-C. He. *A computational approach for evaluating the effective elastic moduli of non-spherical particle reinforced composites with interfacial displacement and traction jumps*. International Journal for Multiscale Computational Engineering, vol. 13, no. 2, 2015. (Cited on pages 2 and 220.)

- [Liu 2016] Y. Liu, A. L. Hamon, P. Haghi-Ashtiani, T. Reiss, B. Fan, D. He and J. Bai. *Quantitative Study of Interface/Interphase in Epoxy/Graphene-based Nanocomposites by Combining STEM and EELS*. ACS Applied Materials & Interfaces, vol. 8, no. 49, pages 34151–34158, 2016. (Cited on pages 84 and 123.)
- [Loomis 2012] J. Loomis, B. King and B. Panchapakesan. *Layer dependent mechanical responses of graphene composites to near-infrared light*. Applied Physics Letters, vol. 100, no. 7, page 073108, 2012. (Cited on page 28.)
- [Lotya 2009] M. Lotya, Y. Hernandez, P. J. King, R. J. Smith, V. Nicolosi, L. S. Karlsson, F. M. Blighe, S. De, Z. Wang and I. T. McGovern. *Liquid phase production of graphene by exfoliation of graphite in surfactant/water solutions*. Journal of the American Chemical Society, vol. 131, no. 10, pages 3611–3620, 2009. (Cited on pages 11 and 19.)
- [Lu 2007] W. B. Lu, J. Wu, L. Y. Jiang, Y. Huang, K. C. Hwang and B. Liu. *A cohesive law for multi-wall carbon nanotubes*. Philosophical Magazine, vol. 87, no. 14-15, pages 2221–2232, 2007. (Cited on page 126.)
- [Lu 2017a] X. Lu, J. Yvonnet, F. Detrez and J. Bai. Submitted, 2017. (Cited on page 40.)
- [Lu 2017b] X. Lu, J. Yvonnet, F. Detrez and J. Bai. *Multiscale modeling of nonlinear electric conductivity in graphene-reinforced nanocomposites taking into account tunnelling effect*. Journal of Computational Physics, vol. 337, pages 116–131, 2017. (Cited on pages 40 and 166.)
- [Lutsko 1988] J. F. Lutsko. *Stress and elastic constants in anisotropic solids : molecular dynamics techniques*. Journal of Applied Physics, vol. 64, no. 3, pages 1152–1154, 1988. (Cited on page 86.)
- [Ma 2013] J. Ma, Q. Meng, A. Micheltore, N. Kawashima, Z. Izzuddin, C. Bengtsson and H. C. Kuan. *Covalently bonded interfaces for polymer/graphene composites*. Journal of Materials Chemistry A, vol. 1, no. 13, pages 4255–4264, 2013. (Cited on page 83.)
- [Maeda 1978] K. Maeda and S. Takeuchi. *Computer simulation of deformation in two-dimensional amorphous structures*. Physica Status Solidi (A), vol. 49, no. 2, pages 685–696, 1978. (Cited on page 95.)

- [Maeda 1981] K. Maeda and S. Takeuchi. *Atomistic process of plastic deformation in a model amorphous metal*. Philosophical Magazine A, vol. 44, no. 3, pages 643–656, 1981. (Cited on page 95.)
- [Maeno 2010] Y. Maeno, A. Ishikawa and Y. Nakayama. *Adhesive behavior of single carbon nanotubes*. Applied Physics Express, vol. 3, no. 6, page 065102, 2010. (Cited on page 29.)
- [Maity 2016] N. P. Maity, R. Maity, R. K. Thapa and S. Baishya. *A tunneling current density model for ultra thin HfO₂ high-k dielectric material based {MOS} devices*. Superlattices and Microstructures, vol. 95, pages 24 – 32, 2016. (Cited on page 47.)
- [Maloney 2004] C. Maloney and A. Lemaître. *Universal breakdown of elasticity at the onset of material failure*. Physical Review Letters, vol. 93, no. 19, page 195501, 2004. (Cited on pages 86 and 96.)
- [Maloney 2006] C. Maloney and A. Lemaître. *Amorphous systems in athermal, quasistatic shear*. Physical Review E, vol. 74, no. 1, page 016118, 2006. (Cited on pages 86 and 96.)
- [Mannoor 2012] M. S. Mannoor, H. Tao, J. D. Clayton, A. Sengupta, D. L. Kaplan, R. R. Naik, N. Verma, F. G. Omenetto and M. C. McAlpine. *Graphene-based wireless bacteria detection on tooth enamel*. Nature Communications, vol. 3, page 763, 2012. (Cited on page 33.)
- [Manta 2017] A. Manta, M. Gresil and C. Soutis. *Predictive Model of Graphene Based Polymer Nanocomposites : Electrical Performance*. Applied Composite Materials, vol. 24, no. 2, pages 281–300, 2017. (Cited on page 39.)
- [Martin-Gallego 2013] M. Martin-Gallego, M. M. Bernal, M. Hernandez, R. Verdejo and M. A. López-Manchado. *Comparison of filler percolation and mechanical properties in graphene and carbon nanotubes filled epoxy nanocomposites*. European Polymer Journal, vol. 49, no. 6, pages 1347–1353, 2013. (Cited on pages 2, 38, 148 and 219.)
- [Martínez-Orozco 2015] R. D. Martínez-Orozco, R. Antaño-López and V. Rodríguez-González. *Hydrogen-gas sensors based on graphene functionalized palladium nanoparticles : impedance response as a valuable sensor*. New Journal of Chemistry, vol. 39, no. 10, pages 8044–8054, 2015. (Cited on page 34.)

- [Martyna 1994] G. J. Martyna, D. J. Tobias and M. L. Klein. *Constant pressure molecular dynamics algorithms*. The Journal of Chemical Physics, vol. 101, no. 5, pages 4177–4189, 1994. (Cited on pages 90 and 99.)
- [Mayo 1990] S. L. Mayo, B. D. Olafson and W. A. Goddard. *DREIDING : a generic force field for molecular simulations*. Journal of Physical chemistry, vol. 94, no. 26, pages 8897–8909, 1990. (Cited on pages 91 and 135.)
- [Miller 2000] R. E. Miller and V. B. Shenoy. *Size-dependent elastic properties of nanosized structural elements*. Nanotechnology, vol. 11, no. 3, page 139, 2000. (Cited on page 120.)
- [Moniruzzaman 2006] M. Moniruzzaman and K. I. Winey. *Polymer nanocomposites containing carbon nanotubes*. Macromolecules, vol. 39, no. 16, pages 5194–5205, 2006. (Cited on page 125.)
- [Murdoch 1976] A. I. Murdoch. *A thermodynamical theory of elastic material interfaces*. The Quarterly Journal of Mechanics and Applied Mathematics, vol. 29, no. 3, pages 245–275, 1976. (Cited on page 127.)
- [Murdoch 1993] A. I. Murdoch and D. Bedeaux. *On the physical interpretation of fields in continuum mechanics*. International Journal of Engineering Science, vol. 31, no. 10, pages 1345–1373, 1993. (Cited on pages 86 and 100.)
- [Murdoch 2007] A. I. Murdoch. *A critique of atomistic definitions of the stress tensor*. Journal of Elasticity, vol. 88, no. 2, pages 113–140, 2007. (Cited on page 86.)
- [Murdoch 2012] A. I. Murdoch. *Physical foundations of continuum mechanics*. Cambridge University Press, 2012. (Cited on page 100.)
- [Mylvaganam 2004] K. Mylvaganam and L. C. Zhang. *Nanotube functionalization and polymer grafting : an ab initio study*. The Journal of Physical Chemistry B, vol. 108, no. 39, pages 15009–15012, 2004. (Cited on page 31.)
- [Nair 2008] R. R. Nair, P. Blake, A. N. Grigorenko, K. S. Novoselov, T. J. Booth, T. Stauber, N. M. R. Peres and A. K. Geim. *Fine structure constant defines visual transparency of graphene*. Science, vol. 320, no. 5881, pages 1308–1308, 2008. (Cited on pages 18 and 19.)

- [Namilae 2005] S. Namilae and N. Chandra. *Multiscale model to study the effect of interfaces in carbon nanotube-based composites*. Transactions of the ASME-H-Journal of Engineering Materials and Technology, vol. 127, no. 2, pages 222–232, 2005. (Cited on pages 1, 86, 126 and 219.)
- [Needleman 1987] A. Needleman. *A continuum model for void nucleation by inclusion debonding*. Journal of Applied Mechanics, vol. 54, no. 3, pages 525–531, 1987. (Cited on pages 126 and 133.)
- [Needleman 1990] A. Needleman. *An analysis of decohesion along an imperfect interface*. International Journal of Fracture, vol. 42, no. 1, pages 21–40, 1990. (Cited on page 133.)
- [Nie 2017] M. Nie, D. M. Kalyon, K. Pochiraju and F. T. Fisher. *A controllable way to measure the interfacial strength between carbon nanotube and polymer using a nanobridge structure*. Carbon, vol. 116, pages 510–517, 2017. (Cited on page 84.)
- [Ning 2013] N. Ning, W. Zhang, J. Yan, F. Xu, T. Wang, H. Su, C. Tang and Q. Fu. *Largely enhanced crystallization of semi-crystalline polymer on the surface of glass fiber by using graphene oxide as a modifier*. Polymer, vol. 54, no. 1, pages 303–309, 2013. (Cited on page 28.)
- [Noll 1955] W. Noll. *Die Herleitung der Grundgleichungen der Thermomechanik der Kontinua aus der statistischen Mechanik*. Journal of Rational Mechanics and Analysis, no. 4, pages 627–646, 1955. (Cited on page 86.)
- [Nosé 1984] S. Nosé. *A molecular dynamics method for simulations in the canonical ensemble*. Molecular Physics, vol. 52, no. 2, pages 255–268, 1984. (Cited on page 89.)
- [Novoselov 2004] K. S. Novoselov, A. K. Geim, S. V. Morozov, D. Jiang, Y. Zhang, S. V. Dubonos, I. V. Grigorieva and A. A. Firsov. *Electric field effect in atomically thin carbon films*. Science, vol. 306, no. 5696, pages 666–669, 2004. (Cited on pages 9 and 10.)
- [Novoselov 2005] K. S. Novoselov, A. K. Geim, S. V. Morozov, D. Jiang, M. I. Katsnelson, I. V. Grigorieva, S. V. Dubonos and A. A. Firsov. *Two-dimensional gas of massless Dirac fermions in graphene*. Nature, vol. 438, no. 7065, pages 197–200, 2005. (Cited on page 16.)

- [Novoselov 2007a] K. S. Novoselov and A. K. Geim. *The rise of graphene*. Nature materials, vol. 6, pages 183–191, 2007. (Cited on page 17.)
- [Novoselov 2007b] K. S. Novoselov, Z. Jiang, Y. Zhang, S. V. Morozov, H. L. Stormer, U. Zeitler, J. C. Maan, G. S. Boebinger, P. Kim and A. K. Geim. *Room-temperature quantum Hall effect in graphene*. Science, vol. 315, no. 5817, pages 1379–1379, 2007. (Cited on page 17.)
- [Nuriel 2005] S. Nuriel, L. Liu, A. H. Barber and H. D. Wagner. *Direct measurement of multiwall nanotube surface tension*. Chemical Physics Letters, vol. 404, no. 4, pages 263–266, 2005. (Cited on pages 29 and 30.)
- [Odegard 2005] G.M. Odegard, T. C. Clancy and T. S. Gates. *Modeling of the mechanical properties of nanoparticle/polymer composites*. Polymer, vol. 46, no. 2, pages 553–562, 2005. (Cited on pages 1, 86 and 219.)
- [Ohta 2006] T. Ohta, A. Bostwick, T. Seyller, K. Horn and E. Rotenberg. *Controlling the electronic structure of bilayer graphene*. Science, vol. 313, no. 5789, pages 951–954, 2006. (Cited on pages 9 and 16.)
- [Otten 2009] R. H. J. Otten and P. van der Schoot. *Continuum percolation of polydisperse nanofillers*. Physical Review Letters, vol. 103, no. 22, page 225704, 2009. (Cited on page 38.)
- [Pan 2011] Y. Pan, G. J. Weng, S. A. Meguid, W. S. Bao, Z. H. Zhu and A. M. S. Hamouda. *Percolation threshold and electrical conductivity of a two-phase composite containing randomly oriented ellipsoidal inclusions*. Journal of Applied Physics, vol. 110, no. 12, page 123715, 2011. (Cited on page 69.)
- [Pang 2010] H. Pang, T. Chen, G. Zhang, B. Zeng and Z. M. Li. *An electrically conducting polymer/graphene composite with a very low percolation threshold*. Materials Letters, vol. 64, no. 20, pages 2226 – 2229, 2010. (Cited on pages 24 and 37.)
- [Pang 2012] H. Pang, G. J. Zhong, Y. Wang, J. Z. Xu, Z. M. Li, J. Lei, C. Chen and X. Ji. *In-situ synchrotron x-ray scattering study on isothermal crystallization of ethylene-vinyl acetate copolymers containing a high weight fraction of carbon nanotubes and graphene nanosheets*. Journal of Polymer Research, vol. 19, no. 3, page 9837, 2012. (Cited on page 28.)
- [Park 2003] J. H. Park and S. C. Jana. *The relationship between nano-and micro-structures and mechanical properties in PMMA-epoxy-nanoclay*

- composites*. Polymer, vol. 44, no. 7, pages 2091–2100, 2003. (Cited on page 26.)
- [Park 2008] S. Park, K. S. Lee, G. Bozoklu, W. Cai, S. T. Nguyen and R. S. Ruoff. *Graphene oxide papers modified by divalent ions-enhancing mechanical properties via chemical cross-linking*. ACS Nano, vol. 2, no. 3, pages 572–578, 2008. (Cited on page 18.)
- [Park 2009a] O. K. Park, T. Jeevananda, N. H. Kim, S. Kim and J. H. Lee. *Effects of surface modification on the dispersion and electrical conductivity of carbon nanotube/polyaniline composites*. Scripta Materialia, vol. 60, no. 7, pages 551 – 554, 2009. (Cited on page 37.)
- [Park 2009b] S. Park, D. A. Dikin, S. T. Nguyen and R. S. Ruoff. *Graphene oxide sheets chemically cross-linked by polyallylamine*. The Journal of Physical Chemistry C, vol. 113, no. 36, pages 15801–15804, 2009. (Cited on page 18.)
- [Park 2009c] S. Park and R. S. Ruoff. *Chemical methods for the production of graphenes*. Nature Nanotechnology, vol. 4, no. 4, pages 217–224, 2009. (Cited on page 9.)
- [Parrinello 1980] M. Parrinello and A. Rahman. *Crystal structure and pair potentials : A molecular-dynamics study*. Physical Review Letters, vol. 45, no. 14, page 1196, 1980. (Cited on page 90.)
- [Parrinello 1981] M. Parrinello and A. Rahman. *Polymorphic transitions in single crystals : A new molecular dynamics method*. Journal of Applied Physics, vol. 52, no. 12, pages 7182–7190, 1981. (Cited on page 90.)
- [Perez 2008] M. Perez, O. Lame, F. Leonforte and J. L. Barrat. *Polymer chain generation for coarse-grained models using radical-like polymerization*. The Journal of Chemical Physics, vol. 128, no. 23, page 234904, 2008. (Cited on pages 97 and 99.)
- [Potts 2011] J. R. Potts, D. R. Dreyer, C. W. Bielawski and R. S. Ruoff. *Graphene-based polymer nanocomposites*. Polymer, vol. 52, no. 1, pages 5–25, 2011. (Cited on page 125.)
- [Prasai 2011] D. Prasai, K. Bolotin, J. Tuberquia, R. Harl and K. Jennings. *Graphene : Atomically thin protective coating*. Bulletin of the American Physical Society, vol. 56, 2011. (Cited on page 12.)

- [Qian 2000] D. Qian, E. C. Dickey, R. Andrews and T. Rantell. *Load transfer and deformation mechanisms in carbon nanotube-polystyrene composites*. Applied Physics Letters, vol. 76, no. 20, pages 2868–2870, 2000. (Cited on page 26.)
- [Qian 2010] H. Qian, A. Bismarck, E. S. Greenhalgh and M. S. P. Shaffer. *Carbon nanotube grafted silica fibres : Characterising the interface at the single fibre level*. Composites Science and Technology, vol. 70, no. 2, pages 393–399, 2010. (Cited on pages 29 and 30.)
- [Rafiee 2009] M. A. Rafiee, J. Rafiee, Z. Wang, H. Song, Z. Z. Yu and N. Koratkar. *Enhanced mechanical properties of nanocomposites at low graphene content*. ACS Nano, vol. 3, no. 12, pages 3884–3890, 2009. (Cited on pages 25, 83 and 125.)
- [Rafiee 2010] M. A. Rafiee, J. Rafiee, I. Srivastava, Z. Wang, H. Song, Z. Z. Yu and N. Koratkar. *Fracture and fatigue in graphene nanocomposites*. Small, vol. 6, no. 2, pages 179–183, 2010. (Cited on page 27.)
- [Rahman 2012] R. Rahman and P. Servati. *Effects of inter-tube distance and alignment on tunnelling resistance and strain sensitivity of nanotube/polymer composite films*. Nanotechnology, vol. 23, no. 5, page 055703, 2012. (Cited on pages 68 and 72.)
- [Rahmat 2011] M. Rahmat and P. Hubert. *Carbon nanotube-polymer interactions in nanocomposites : a review*. Composites Science and Technology, vol. 72, no. 1, pages 72–84, 2011. (Cited on page 32.)
- [Ramanathan 2008] T. Ramanathan, A. A. Abdala, S. Stankovich, D. A. Dikin, M. Herrera-Alonso, R. D. Piner, D. H. Adamson, H. C. Schniepp, X. R. R. S. Chen and R. S. Ruoff. *Functionalized graphene sheets for polymer nanocomposites*. Nature Nanotechnology, vol. 3, no. 6, pages 327–331, 2008. (Cited on pages 25, 26, 27 and 125.)
- [Rasheed 2006] A. Rasheed, H. G. Chae, S. Kumar and M. D. Dadmun. *Polymer nanotube nanocomposites : Correlating intermolecular interaction to ultimate properties*. Polymer, vol. 47, no. 13, pages 4734–4741, 2006. (Cited on page 30.)
- [Reddy 2006] C. D. Reddy, S. Rajendran and K. M. Liew. *Equilibrium configuration and continuum elastic properties of finite sized graphene*. Nanotechnology, vol. 17, no. 3, page 864, 2006. (Cited on page 17.)

- [Roy 2001] Y. A. Roy and R. H. Dodds. *Simulation of ductile crack growth in thin aluminum panels using 3-D surface cohesive elements*. International Journal of Fracture, vol. 110, no. 1, pages 21–45, 2001. (Cited on page 135.)
- [Ruan 2011] G. Ruan, Z. Sun, Z. Peng and J. M. Tour. *Growth of graphene from food, insects, and waste*. ACS Nano, vol. 5, no. 9, pages 7601–7607, 2011. (Cited on page 11.)
- [Samoletov 2007] A. A. Samoletov, C. P. Dettmann and M. A. J. Chaplain. *Thermostats for "slow" configurational modes*. Journal of Statistical Physics, vol. 128, no. 6, pages 1321–1336, 2007. (Cited on page 89.)
- [Sanchez-Palencia 1970] E. Sanchez-Palencia. *Comportement limite d'un probleme de transmissiona travers une plaque faiblement conductrice*. Comptes Rendus de l'Académie des Sciences-Series I-Mathematics, vol. 270, pages 1026–1028, 1970. (Cited on page 40.)
- [Sandler 2003] J. K. W. Sandler, J. E. Kirk, I. A. Kinloch, M. S. P. Shaffer and A. H. Windle. *Ultra-low electrical percolation threshold in carbon-nanotube-epoxy composites*. Polymer, vol. 44, no. 19, pages 5893–5899, 2003. (Cited on page 38.)
- [Satti 2010] A. Satti, P. Larpent and Y. Gun'ko. *Improvement of mechanical properties of graphene oxide/poly (allylamine) composites by chemical crosslinking*. Carbon, vol. 48, no. 12, pages 3376–3381, 2010. (Cited on page 83.)
- [Schwartz 2013] G. Schwartz, B. C. Tee, . Mei, A. L. Appleton, D. H. Kim, H. Wang and Z. Bao. *Flexible polymer transistors with high pressure sensitivity for application in electronic skin and health monitoring*. Nature Communications, vol. 4, page 1859, 2013. (Cited on page 34.)
- [Seidel 2006] G. D. Seidel and D. C. Lagoudas. *Micromechanical analysis of the effective elastic properties of carbon nanotube reinforced composites*. Mechanics of Materials, vol. 38, no. 8, pages 884–907, 2006. (Cited on page 84.)
- [Shahil 2012] K. M. F. Shahil and A. A. Balandin. *Thermal properties of graphene and multilayer graphene : Applications in thermal interface materials*. Solid State Communications, vol. 152, no. 15, pages 1331–1340, 2012. (Cited on page 33.)

- [Sharma 2003] P. Sharma, S. Ganti and N. Bhate. *Effect of surfaces on the size-dependent elastic state of nano-inhomogeneities*. Applied Physics Letters, vol. 82, no. 4, pages 535–537, 2003. (Cited on page 85.)
- [Sharma 2004] P. Sharma and S. Ganti. *Size-dependent Eshelby’s tensor for embedded nano-inclusions incorporating surface/interface energies*. Journal of Applied Mechanics, vol. 71, no. 5, pages 663–671, 2004. (Cited on pages 2 and 220.)
- [Shen 2011] B. Shen, W. Zhai, C. Chen, D. Lu, J. Wang and W. Zheng. *Melt blending in situ enhances the interaction between polystyrene and graphene through π - π stacking*. ACS Applied Materials & Interfaces, vol. 3, no. 8, pages 3103–3109, 2011. (Cited on page 29.)
- [Shenoy 2002] V. B. Shenoy. *Size-dependent rigidities of nanosized torsional elements*. International Journal of Solids and Structures, vol. 39, no. 15, pages 4039–4052, 2002. (Cited on pages 1, 85 and 219.)
- [Shenoy 2005] V.B. Shenoy. *Atomistic calculations of elastic properties of metallic fcc crystal surfaces*. Physical Review B, vol. 71, no. 9, page 094104, 2005. (Cited on pages 2, 86, 120 and 220.)
- [Shinoda 2004] W. Shinoda, M. Shiga and M. Mikami. *Rapid estimation of elastic constants by molecular dynamics simulation under constant stress*. Physical Review B, vol. 69, no. 13, page 134103, 2004. (Cited on page 99.)
- [Shtein 2015] M. Shtein, R. Nadiv, M. Buzaglo, K. Kahil and O. Regev. *Thermally Conductive Graphene-Polymer Composites : Size, Percolation, and Synergy Effects*. Chemistry of Materials, vol. 27, no. 6, pages 2100–2106, 2015. (Cited on page 37.)
- [Shukla 2009] A. Shukla, R. Kumar, J. Mazher and A. Balan. *Graphene made easy : High quality, large-area samples*. Solid State Communications, vol. 149, no. 17, pages 718–721, 2009. (Cited on page 10.)
- [Simeoni 2005] M. Simeoni, C. De Luca, S. Picozzi, S. Santucci and B. Delley. *Interaction between zigzag single-wall carbon nanotubes and polymers : A density-functional study*. The Journal of Chemical Physics, vol. 122, no. 21, page 214710, 2005. (Cited on page 31.)
- [Simmons 1963] J. G. Simmons. *Electric Tunnel Effect between Dissimilar Electrodes Separated by a Thin Insulating Film*. Journal of Applied

- Physics, vol. 34, no. 9, pages 2581–2590, 1963. (Cited on pages 39 and 47.)
- [Simmons 1971] J. G. Simmons. *Conduction in thin dielectric films*. Journal of Physics D : Applied Physics, vol. 4, no. 5, page 613, 1971. (Cited on page 46.)
- [Somani 2006] P. R. Somani, S. P. Somani and M. Umeno. *Planer nano-graphenes from camphor by CVD*. Chemical Physics Letters, vol. 430, no. 1, pages 56–59, 2006. (Cited on page 11.)
- [Sommer 2010] J. U. Sommer and C. Luo. *Molecular dynamics simulations of semicrystalline polymers : crystallization, melting, and reorganization*. Journal of Polymer Science Part B : Polymer Physics, vol. 48, no. 21, pages 2222–2232, 2010. (Cited on pages 97 and 135.)
- [Song 2012] Z. Song, T. Xu, M. L. Gordin, Y. B. Jiang, I. T. Bae, Qi. Xiao, H. Zhan, J. Liu and D. Wang. *Polymer-graphene nanocomposites as ultrafast-charge and-discharge cathodes for rechargeable lithium batteries*. Nano Letters, vol. 12, no. 5, pages 2205–2211, 2012. (Cited on pages 1 and 219.)
- [Spitalsky 2010] Z. Spitalsky, D. Tasis, K. Papagelis and C. Galiotis. *Carbon nanotube Polymer composites : Chemistry, processing, mechanical and electrical properties*. Progress in Polymer Science, vol. 35, no. 3, pages 357–401, 2010. (Cited on page 37.)
- [Srivastava 2017] A. Srivastava and D. Kumar. *A continuum model to study interphase effects on elastic properties of CNT/GS-nanocomposite*. Materials Research Express, vol. 4, no. 2, page 025036, 2017. (Cited on page 84.)
- [Stankovich 2006] S. Stankovich, D. A. Dikin, G. H. B. Dommett, K. M. Kohlhaas¹, E. J. Zimney¹, E. A. Stach, R. D. Piner, S. T. Nguyen and R. S. Ruoff. *Graphene-based composite materials*. Nature, vol. 442, no. 7100, pages 282–286, 2006. (Cited on pages 22, 24, 60, 70, 76 and 79.)
- [Starr 2002] F. W. Starr, T. B. Schrøder and S. C. Glotzer. *Molecular dynamics simulation of a polymer melt with a nanoscopic particle*. Macromolecules, vol. 35, no. 11, pages 4481–4492, 2002. (Cited on page 32.)
- [Steurer 2009] Peter Steurer, Rainer Wissert, Ralf Thomann and Rolf Mülhaupt. *Functionalized graphenes and thermoplastic nanocomposites*

- based upon expanded graphite oxide*. Macromolecular rapid communications, vol. 30, no. 4-5, pages 316–327, 2009. (Cited on pages 22, 24 and 25.)
- [Strus 2008] M. C. Strus, L. Zalamea, A. Raman, R. B. Pipes, C. V. Nguyen and E. A. Stach. *Peeling force spectroscopy : exposing the adhesive nanomechanics of one-dimensional nanostructures*. Nano Letters, vol. 8, no. 2, pages 544–550, 2008. (Cited on pages 30 and 31.)
- [Sun 1998] H. Sun. *COMPASS : an ab initio force-field optimized for condensed-phase applications overview with details on alkane and benzene compounds*. The Journal of Physical Chemistry B, vol. 102, no. 38, pages 7338–7364, 1998. (Cited on page 91.)
- [Sun 2010a] X. Sun, P. Ramesh, M. E. Itkis, E. Bekyarova and R. C. Haddon. *Dependence of the thermal conductivity of two-dimensional graphite nanoplatelet-based composites on the nanoparticle size distribution*. Journal of Physics : Condensed Matter, vol. 22, no. 33, page 334216, 2010. (Cited on page 28.)
- [Sun 2010b] Z. Sun, Z. Yan, J. Yao, E. Beitler, Y. Zhu and J. M. Tour. *Growth of graphene from solid carbon sources*. Nature, vol. 468, no. 7323, page 549, 2010. (Cited on page 11.)
- [Sze 2006] S. M. Sze and K. K. Ng. *Physics of semiconductor devices*. John wiley & sons, 2006. (Cited on page 73.)
- [Tadmor 2011] E. B. Tadmor and R. E. Miller. *Modeling materials : continuum, atomistic and multiscale techniques*. Cambridge University Press, 2011. (Cited on page 92.)
- [Tang 2005] H. Tang, A. Acharya and S. Saigal. *Directional dependence of crack growth along the interface of a bicrystal with symmetric tilt boundary in the presence of gradient effects*. Mechanics of Materials, vol. 37, no. 5, pages 593–606, 2005. (Cited on page 135.)
- [Tang 2010] T. T. Tang, Y. Zhang, C. H. Park, B. Geng, C. Girit, Z. Hao, M. C. Martin, A. Zettl, M. F. Crommie and S. G. Louie. *A tunable phonon–exciton Fano system in bilayer graphene*. Nature Nanotechnology, vol. 5, no. 1, pages 32–36, 2010. (Cited on page 9.)
- [Tang 2013] L. C. Tang, Y. J. Wan, D. Yan, Y. B. Pei, L. Zhao, Y. B. Li, L. B. Wu, J. X. Jiang and G. Q. Lai. *The effect of graphene dispersion*

- on the mechanical properties of graphene/epoxy composites*. Carbon, vol. 60, pages 16–27, 2013. (Cited on page 83.)
- [Tanguy 2002] A. Tanguy, J. P. Wittmer, F. Leonforte and J. L. Barrat. *Continuum limit of amorphous elastic bodies : A finite-size study of low-frequency harmonic vibrations*. Physical Review B, vol. 66, no. 17, page 174205, 2002. (Cited on pages 86 and 96.)
- [Terrones 2011] M. Terrones, O. Martín, M. González, J. Pozuelo, B. Serrano, J. C. Cabanelas, S. M. Vega-Díaz and J. Baselga. *Interphases in Graphene Polymer-based Nanocomposites : Achievements and Challenges*. Advanced Materials, vol. 23, no. 44, pages 5302–5310, 2011. (Cited on page 83.)
- [Thongruang 2002] W. Thongruang, R. J. Spontak and C. M. Balik. *Bridged double percolation in conductive polymer composites : an electrical conductivity, morphology and mechanical property study*. Polymer, vol. 43, no. 13, pages 3717–3725, 2002. (Cited on page 175.)
- [Tibbetts 2007] G. G. Tibbetts, M. L. Lake, K. L. Strong and B. P. Rice. *A review of the fabrication and properties of vapor-grown carbon nanofiber/polymer composites*. Composites Science and Technology, vol. 67, pages 1709 – 1718, 2007. (Cited on page 37.)
- [Tkalya 2010] E. Tkalya, M. Ghislandi and A. Alekseev, C. Koning and J. Loos. *Latex-based concept for the preparation of graphene-based polymer nanocomposites*. Journal of Materials Chemistry, vol. 20, no. 15, pages 3035–3039, 2010. (Cited on page 24.)
- [Tkalya 2014] E. Tkalya, M. Ghislandi, R. Otten, M. Lotya, A. Alekseev, P. van der Schoot, J. Coleman, G. de With and C. Koning. *Experimental and Theoretical Study of the Influence of the State of Dispersion of Graphene on the Percolation Threshold of Conductive Graphene/Polystyrene Nanocomposites*. ACS Applied Materials & Interfaces, vol. 6, no. 17, pages 15113–15121, 2014. (Cited on page 69.)
- [Torquato 2013] S. Torquato. Random heterogeneous materials : microstructure and macroscopic properties, volume 16. Springer Science & Business Media, 2013. (Cited on page 56.)
- [Torres-Sánchez 2016] A. Torres-Sánchez, J. M. Vanegas and M. Arroyo. *Geometric derivation of the microscopic stress : A covariant central force*

- decomposition*. Journal of the Mechanics and Physics of Solids, vol. 93, pages 224–239, 2016. (Cited on page 86.)
- [Tran 2008] M. Q. Tran, J. T. Cabral, M. S. P. Shaffer and A. Bismarck. *Direct measurement of the wetting behavior of individual carbon nanotubes by polymer melts : The key to carbon nanotube- polymer composites*. Nano Letters, vol. 8, no. 9, pages 2744–2750, 2008. (Cited on pages 29 and 30.)
- [Tserpes 2017] K. I. Tserpes, A. Chanteli and I. S. Floros. *Prediction of yield strength of MWCNT/PP nanocomposite considering the interphase and agglomeration*. Composite Structures, vol. 168, pages 657–662, 2017. (Cited on page 84.)
- [Tvergaard 1992] V. Tvergaard and J. W. Hutchinson. *The relation between crack growth resistance and fracture process parameters in elastic-plastic solids*. Journal of the Mechanics and Physics of Solids, vol. 40, no. 6, pages 1377–1397, 1992. (Cited on page 133.)
- [Tvergaard 1993] V. Tvergaard and J. W. Hutchinson. *The influence of plasticity on mixed mode interface toughness*. Journal of the Mechanics and Physics of Solids, vol. 41, no. 6, pages 1119–1135, 1993. (Cited on page 126.)
- [Vacatello 2001] M. Vacatello. *Monte Carlo simulations of polymer melts filled with solid nanoparticles*. Macromolecules, vol. 34, no. 6, pages 1946–1952, 2001. (Cited on page 97.)
- [Vadukumpully 2011] S. Vadukumpully, J. Paul, N. Mahanta and S. Valiyaveetil. *Flexible conductive graphene/poly (vinyl chloride) composite thin films with high mechanical strength and thermal stability*. Carbon, vol. 49, no. 1, pages 198–205, 2011. (Cited on pages 28 and 37.)
- [Vaia 1995] R. A. Vaia, S. Vasudevan, W. Krawiec, L. G. Scanlon and E. P. Giannelis. *New polymer electrolyte nanocomposites : Melt intercalation of poly (ethylene oxide) in mica-type silicates*. Advanced Materials, vol. 7, no. 2, pages 154–156, 1995. (Cited on page 125.)
- [Verdejo 2008] R. Verdejo, F. Barroso-Bujans, M. A. Rodriguez-Perez, J. A. de Saja and M. A. Lopez-Manchado. *Functionalized graphene sheet filled silicone foam nanocomposites*. Journal of Materials Chemistry, vol. 18, no. 19, pages 2221–2226, 2008. (Cited on page 25.)

- [Verdejo 2011] R. Verdejo, M. M. Bernal, L. J. Romasanta and M. A. Lopez-Manchado. *Graphene filled polymer nanocomposites*. Journal of Materials Chemistry, vol. 21, no. 10, pages 3301–3310, 2011. (Cited on pages 1, 23, 83 and 219.)
- [Wan 2005] H. Wan, F. Delale and L. Shen. *Effect of CNT length and CNT-matrix interphase in carbon nanotube (CNT) reinforced composites*. Mechanics Research Communications, vol. 32, no. 5, pages 481–489, 2005. (Cited on page 84.)
- [Wan 2012] C. Wan and B. Chen. *Reinforcement and interphase of polymer/graphene oxide nanocomposites*. Journal of Materials Chemistry, vol. 22, no. 8, pages 3637–3646, 2012. (Cited on page 83.)
- [Wang 2011] J. Wang, Z. Huang, H. Duan, S. Yu, X. Feng, G. Wang, W. Zhang and T. Wang. *Surface stress effect in mechanics of nanostructured materials*. Acta Mechanica Solida Sinica, vol. 24, no. 1, pages 52–82, 2011. (Cited on pages 1 and 219.)
- [Wang 2014a] J. Wang, X. Zhao, J. Li, X. Kuang, Y. Fan, G. Wei and Z. Su. *Electrostatic assembly of peptide nanofiber–biomimetic silver nanowires onto graphene for electrochemical sensors*. ACS Macro Letters, vol. 3, no. 6, pages 529–533, 2014. (Cited on page 34.)
- [Wang 2014b] T. Wang, G. Liang, L. Yuan and A. Gu. *Unique hybridized graphene and its high dielectric constant composites with enhanced frequency stability, low dielectric loss and percolation threshold*. Carbon, vol. 77, pages 920–932, 2014. (Cited on page 37.)
- [Wang 2014c] Y. Wang, G. J. Weng, S. A. Meguid and A. M. Hamouda. *A continuum model with a percolation threshold and tunneling-assisted interfacial conductivity for carbon nanotube-based nanocomposites*. Journal of Applied Physics, vol. 115, no. 19, page 193706, 2014. (Cited on page 38.)
- [Wang 2014d] Z. Wang, J. Zhu, X. Y. Jin, W. Q. Chen and C. Zhang. *Effective moduli of ellipsoidal particle reinforced piezoelectric composites with imperfect interfaces*. Journal of the Mechanics and Physics of Solids, vol. 65, pages 138–156, 2014. (Cited on page 85.)
- [Wang 2015] Y. Wang, J. W. Shan and G. J. Weng. *Percolation threshold and electrical conductivity of graphene-based nanocomposites with filler*

- agglomeration and interfacial tunneling*. Journal of Applied Physics, vol. 118, no. 6, page 065101, 2015. (Cited on page 39.)
- [Wang 2016] J. Wang, S. Yu, S. Luo, B. Chu, R. Sun and C. P. Wong. *Investigation of nonlinear I-V behavior of CNTs filled polymer composites*. Materials Science and Engineering : B, vol. 206, pages 55–60, 2016. (Cited on pages 24, 38 and 72.)
- [Wei 2006] C. Wei. *Adhesion and reinforcement in carbon nanotube polymer composite*. Applied Physics Letters, vol. 88, no. 9, page 093108, 2006. (Cited on page 32.)
- [Wei 2009] T. Wei, G. Luo, Z. Fan, . Zheng, J. Yan, C. Yao, W. Li and C. Zhang. *Preparation of graphene nanosheet/polymer composites using in situ reduction-extractive dispersion*. Carbon, vol. 47, no. 9, pages 2296–2299, 2009. (Cited on page 37.)
- [Weiner 1981] J. H. Weiner. *Hellmann-Feynman theorem, elastic moduli, and the Cauchy relations*. Physical Review B, vol. 24, no. 2, page 845, 1981. (Cited on page 86.)
- [Wen 2007] S. Wen and D. D. L. Chung. *Double percolation in the electrical conduction in carbon fiber reinforced cement-based materials*. Carbon, vol. 45, no. 2, pages 263–267, 2007. (Cited on page 175.)
- [Wen 2014] J. Wen, Y. Jiang, Y. Yang and S. Li. *Conducting polymer and reduced graphene oxide Langmuir-Blodgett films : a hybrid nanostructure for high performance electrode applications*. Journal of Materials Science : Materials in Electronics, vol. 25, no. 2, pages 1063–1071, 2014. (Cited on page 36.)
- [Weng 1984] G. J. Weng. *Some elastic properties of reinforced solids, with special reference to isotropic ones containing spherical inclusions*. International Journal of Engineering Science, vol. 22, no. 7, pages 845–856, 1984. (Cited on pages 69 and 150.)
- [Weng 1990] G. J. Weng. *The theoretical connection between Mori-Tanaka's theory and the Hashin-Shtrikman-Walpole bounds*. International Journal of Engineering Science, vol. 28, no. 11, pages 1111–1120, 1990. (Cited on pages 69 and 150.)
- [Wittmer 2002] J. P. Wittmer, A. Tanguy, J. L. Barrat and L. Lewis. *Vibrations of amorphous, nanometric structures : When does continuum*

- theory apply?* EPL (Europhysics Letters), vol. 57, no. 3, page 423, 2002. (Cited on pages 86 and 96.)
- [Woltornist 2015] S. J. Woltornist, J. M. Y. Carrillo, T. O. Xu, A. V. Dobrynin and D. H. Adamson. *Polymer/Pristine Graphene Based Composites : From Emulsions to Strong, Electrically Conducting Foams*. Macromolecules, vol. 48, no. 3, pages 687–693, 2015. (Cited on page 37.)
- [Xia 2017a] X. Xia, Y. Wang, Z. Zhong and G. J. Weng. *A frequency-dependent theory of electrical conductivity and dielectric permittivity for graphene-polymer nanocomposites*. Carbon, vol. 111, pages 221 – 230, 2017. (Cited on pages 38 and 39.)
- [Xia 2017b] X. Xia, Z. Zhong and G. J. Weng. *Maxwell-Wagner-Sillars mechanism in the frequency dependence of electrical conductivity and dielectric permittivity of graphene-polymer nanocomposites*. Mechanics of Materials, vol. 109, pages 42–50, 2017. (Cited on page 39.)
- [Xin 2011] F. Xin and L. Li. *Decoration of carbon nanotubes with silver nanoparticles for advanced CNT/polymer nanocomposites*. Composites Part A : Applied Science and Manufacturing, vol. 42, no. 8, pages 961–967, 2011. (Cited on page 26.)
- [Xu 1994] X. P. Xu and A. Needleman. *Numerical simulations of fast crack growth in brittle solids*. Journal of the Mechanics and Physics of Solids, vol. 42, no. 9, pages 1397–1434, 1994. (Cited on page 126.)
- [Xu 2009] Y. Xu, Y. Wang, J. Liang, Y. Huang, Y. Ma, X. Wan and Y. Chen. *A hybrid material of graphene and poly (3,4-ethyldioxythiophene) with high conductivity, flexibility, and transparency*. Nano Research, vol. 2, no. 4, pages 343–348, 2009. (Cited on page 37.)
- [Xu 2010] Z. Xu and C. Gao. *In situ polymerization approach to graphene-reinforced nylon-6 composites*. Macromolecules, vol. 43, no. 16, pages 6716–6723, 2010. (Cited on page 26.)
- [Xu 2015] S. Xu, C. Li, H. Li, M. Li, C. Qu and B. Yang. *Carbon dioxide sensors based on a surface acoustic wave device with a graphene-nickel-L-alanine multilayer film*. Journal of Materials Chemistry C, vol. 3, no. 16, pages 3882–3890, 2015. (Cited on page 34.)
- [Yan 2010] J. Yan, T. Wei, B. Shao, F. Ma, Z. Fan, M. Zhang, C. Zheng, Y. Shang, W. Qian and F. Wei. *Electrochemical properties of graphene*

- nanosheet/carbon black composites as electrodes for supercapacitors*. Carbon, vol. 48, no. 6, pages 1731–1737, 2010. (Cited on page 35.)
- [Yan 2012] J. Yan, G. Qi, J. Cao, Y. Luo, W. Yang, B. Xie and M. Yang. *Study on amino-functionalized graphene oxide/poly (methyl methacrylate) nanocomposites*. Chemistry Letters, vol. 41, no. 7, pages 683–685, 2012. (Cited on page 27.)
- [Yang 2011] S. Y. Yang, W. N. Lin, Y. L. Huang, H. W. Tien, J. Y. Wang, C. C. M. Ma, S. M. Li and Y. S. Wang. *Synergetic effects of graphene platelets and carbon nanotubes on the mechanical and thermal properties of epoxy composites*. Carbon, vol. 49, no. 3, pages 793–803, 2011. (Not cited.)
- [Yang 2013] S. Yang, S. Yu, J. M. Ryu J. and Cho, W. Kyoung, D. S. Han and M. Cho. *Nonlinear multiscale modeling approach to characterize elastoplastic behavior of CNT/polymer nanocomposites considering the interphase and interfacial imperfection*. International Journal of Plasticity, vol. 41, pages 124–146, 2013. (Cited on page 84.)
- [Yousefi 2012] N. Yousefi, M. M. Gudarzi, Q. Zheng, S. H. Aboutalebi, F. Sharif and J. K. Kim. *Self-alignment and high electrical conductivity of ultralarge graphene oxide-polyurethane nanocomposites*. Journal of Materials Chemistry, vol. 22, no. 25, pages 12709–12717, 2012. (Cited on page 65.)
- [Yousefi 2013] N. Yousefi, M. M. Gudarzi, Q. Zheng, X. Lin, X. Shen, J. Jia, F. Sharif and J. K. Kim. *Highly aligned, ultralarge-size reduced graphene oxide/polyurethane nanocomposites : mechanical properties and moisture permeability*. Composites Part A : Applied Science and Manufacturing, vol. 49, pages 42–50, 2013. (Cited on pages 25 and 26.)
- [Yvonnet 2008a] J. Yvonnet, Q.-C. He and C. Toulemonde. *Numerical modeling of the effective conductivities of composites with arbitrarily shaped inclusions and highly conducting interface*. Composites Science and Technology, vol. 68, no. 13, pages 2818 – 2825, 2008. (Cited on pages 39 and 50.)
- [Yvonnet 2008b] J. Yvonnet, H. Le. Quang and Q. C. He. *An XFEM/level set approach to modelling surface/interface effects and to computing the size-dependent effective properties of nanocomposites*. Computational

- Mechanics, vol. 42, no. 1, pages 119–131, 2008. (Cited on pages 1, 2, 41, 85, 219 and 220.)
- [Yvonnet 2011] J. Yvonnet, A. Mitrushchenkov, G. Chambaud and Q.-C. He. *Finite element model of ionic nanowires with size-dependent mechanical properties determined by ab initio calculations*. Computer Methods in Applied Mechanics and Engineering, vol. 200, no. 5, pages 614–625, 2011. (Cited on pages 1, 2, 85, 86, 219 and 220.)
- [Yvonnet 2012] J. Yvonnet, A. Mitrushchenkov, G.e Chambaud, Q.-C. He and S.-T. Gu. *Characterization of surface and nonlinear elasticity in wurtzite ZnO nanowires*. Journal of Applied Physics, vol. 111, no. 12, page 124305, 2012. (Cited on pages 2, 86 and 220.)
- [Zaman 2011] I. Zaman, T. T. P. Thanh, H. C. Kuan, Q. Meng, L. T. B. La, L. Luong, O. Youssf and J. Ma. *Epoxy/graphene platelets nanocomposites with two levels of interface strength*. Polymer, vol. 52, no. 7, pages 1603–1611, 2011. (Cited on page 83.)
- [Zang 2015] Y. Zang, F. Zhang, C. Di and D. Zhu. *Advances of flexible pressure sensors toward artificial intelligence and health care applications*. Materials Horizons, vol. 2, no. 2, pages 140–156, 2015. (Cited on pages 34 and 35.)
- [Zeng 2011] X. Zeng, X. Xu, P. M. Shenai and E. Kovalev, C. Baudot, N. Mathews and Y. Zhao. *Characteristics of the Electrical Percolation in Carbon Nanotubes/Polymer Nanocomposites*. The Journal of Physical Chemistry C, vol. 115, no. 44, pages 21685–21690, 2011. (Cited on pages 2, 38 and 219.)
- [Zhang 2004] Q. Zhang and L. A. Archer. *Monte Carlo simulation of structure and nanoscale interactions in polymer nanocomposites*. The Journal of Chemical Physics, vol. 121, no. 21, pages 10814–10824, 2004. (Cited on pages 32 and 33.)
- [Zhang 2005] Y. Zhang, Y. W. Tan, H. L. Stormer and P. Kim. *Experimental observation of quantum Hall effect and Berry's phase in graphene*. arXiv preprint cond-mat/0509355, 2005. (Cited on page 17.)
- [Zhang 2010a] H. Zhang, W.e Zheng, Q. Yan, Y. Yang, J. Wang, Z. Lu, G. Ji and Z. Yu. *Electrically conductive polyethylene terephthalate/graphene nanocomposites prepared by melt compounding*. Polymer, vol. 51, no. 5, pages 1191–1196, 2010. (Cited on pages 70, 79 and 80.)

- [Zhang 2010b] K. Zhang, L. L. Zhang, X. S. Zhao and J. Wu. *Graphene/polyaniline nanofiber composites as supercapacitor electrodes*. Chemistry of Materials, vol. 22, no. 4, pages 1392–1401, 2010. (Cited on page 36.)
- [Zhang 2012a] H. B. Zhang, W. G. Zheng, Q. Yan, Z. G. Jiang and Z. Z. Yu. *The effect of surface chemistry of graphene on rheological and electrical properties of polymethylmethacrylate composites*. Carbon, vol. 50, no. 14, pages 5117–5125, 2012. (Cited on page 23.)
- [Zhang 2012b] X. Zhang, X. Fan, C. Yan, H. Li, Y. Zhu, X. Li and L. Yu. *Interfacial microstructure and properties of carbon fiber composites modified with graphene oxide*. ACS Applied Materials & Interfaces, vol. 4, no. 3, pages 1543–1552, 2012. (Cited on page 84.)
- [Zhang 2013a] H. L. Zhang, X. L. Wei, Y. Zang, J. Y. Cao, S. Liu, X. P. He, Q. Chen, Y. T. Long, J. Li and G. R. Chen. *Fluorogenic probing of specific recognitions between sugar ligands and glycoprotein receptors on cancer cells by an economic graphene nanocomposite*. Advanced Materials, vol. 25, no. 30, pages 4097–4101, 2013. (Cited on page 29.)
- [Zhang 2013b] W. Zhang, M. Yi, Z. Shen, X. Zhao, X. Zhang and S. Ma. *Graphene-reinforced epoxy resin with enhanced atomic oxygen erosion resistance*. Journal of Materials Science, vol. 48, no. 6, pages 2416–2423, 2013. (Cited on page 28.)
- [Zhang 2013c] W. Zhang, B. Zhao, Z. He, X. Zhao, H. Wang, S. Yang, H. Wu and Y. Cao. *High-efficiency ITO-free polymer solar cells using highly conductive PEDOT : PSS/surfactant bilayer transparent anodes*. Energy & Environmental Science, vol. 6, no. 6, pages 1956–1964, 2013. (Cited on page 36.)
- [Zhang 2014] G. Zhang, L. A. Moreira, T. Stuehn, K. C. Daoulas and K. Kremer. *Equilibration of high molecular weight polymer melts : a hierarchical strategy*. ACS Macro Letters, vol. 3, no. 2, pages 198–203, 2014. (Cited on page 98.)
- [Zhang 2015] L. L. Zhang, J. Jasa, G. Gazonas, A. Jérusalem and M. Negahban. *Extracting continuum-like deformation and stress from molecular dynamics simulations*. Computer Methods in Applied Mechanics and Engineering, vol. 283, pages 1010–1031, 2015. (Cited on page 86.)

- [Zhao 2010] X. Zhao, Q. Zhang, D. Chen and P. Lu. *Enhanced mechanical properties of graphene-based poly (vinyl alcohol) composites*. *Macromolecules*, vol. 43, no. 5, pages 2357–2363, 2010. (Cited on page 83.)
- [Zhao 2011] X. Zhao and L. Ye. *Structure and properties of highly oriented polyoxymethylene/multi-walled carbon nanotube composites produced by hot stretching*. *Composites Science and Technology*, vol. 71, no. 10, pages 1367–1372, 2011. (Cited on page 30.)
- [Zhao 2015] H. Zhao and J. Bai. *Highly Sensitive Piezo-Resistive Graphite Nanoplatelet-Carbon Nanotube Hybrids/Polydimethylsilicone Composites with Improved Conductive Network Construction*. *ACS Applied Materials & Interfaces*, vol. 7, no. 18, pages 9652–9659, 2015. PMID : 25898271. (Cited on page 37.)
- [Zhao 2016] W. Zhao, J. Kong, H. Liu, Q. Zhuang, J. Gu and Z. Guo. *Ultra-high thermally conductive and rapid heat responsive poly (benzobisoxazole) nanocomposites with self-aligned graphene*. *Nanoscale*, vol. 8, no. 48, pages 19984–19993, 2016. (Cited on page 28.)
- [Zheng 2013] Q. Zheng, G. Fang, F. Cheng, H. Lei, P. Qin and C. Zhan. *Low-temperature solution-processed graphene oxide derivative hole transport layer for organic solar cells*. *Journal of Physics D : Applied Physics*, vol. 46, no. 13, page 135101, 2013. (Cited on page 36.)
- [Zhu 2007] R. Zhu, E. Pan and A. K. Roy. *Molecular dynamics study of the stress-strain behavior of carbon-nanotube reinforced Epon 862 composites*. *Materials Science and Engineering : A*, vol. 447, no. 1, pages 51–57, 2007. (Cited on page 117.)
- [Zhu 2013] L. Zhu, X. Zhao, Y. Li, X. Yu, C. Li and Q. Zhang. *High-quality production of graphene by liquid-phase exfoliation of expanded graphite*. *Materials Chemistry and Physics*, vol. 137, no. 3, pages 984–990, 2013. (Cited on page 11.)

ANNEXE A

Résumé

Les nanocomposites graphène/polymère ont récemment attiré une attention croissante en raison de leurs performances électrique et mécanique, comme le montrent de récentes études [Song 2012, Arash 2014, Verdejo 2011, Li 2013]. Bien que de nombreuses expériences aient été menées pour étudier ces nouveaux matériaux, les mécanismes à l'échelle nanométrique ne sont pas encore bien compris et leurs relations avec les propriétés effectives restent indéterminées. Dans ce contexte, les méthodologies multi-échelles impliquant des simulations aux échelles atomistique, nanométrique, micrométrique et macroscopique peuvent nous aider à résoudre ce problème. Les simulations numériques à l'échelle atomique permettent de comprendre certains phénomènes qui ne sont pas accessibles à l'expérimentation ainsi que d'analyser l'influence des différents paramètres. La combinaison de ces simulations dans une démarche d'homogénéisation numérique est un pas en avant pour étudier l'influence des constituants nanométriques sur les propriétés effectives [Namilae 2005, Li 2006, Odegard 2005].

Il a été démontré expérimentalement que les propriétés macroscopiques des nanocomposites renforcés avec du graphène ne proviennent pas seulement des propriétés des constituants purs, matrice et feuillets de graphène, mais aussi des mécanismes physiques spécifiques à l'échelle nanoscopique, tels que :

- des effets de surface et/ou d'interfaces [Shenoy 2002, Duan 2005b, Gurtin 1975, Yvonnet 2008b, Yvonnet 2011, Wang 2011] ;
- des effets liés aux interphases, dont la modélisation dans le régime non-linéaire est récente [Brach 2017b] ;
- l'«effet tunnel», qui est un phénomène purement quantique permettant aux électrons de franchir des barrières isolantes très minces de quelques nanomètres entre deux conducteurs [Allaoui 2008, Martin-Gallego 2013, Zeng 2011]. L'effet tunnel est à l'origine de valeurs inattendues de conductivité électrique pour de très faibles fractions volumiques de charges.

L'incorporation de certains de ces mécanismes nanométriques dans des schémas d'homogénéisation a été proposée dans le cas de l'élasticité de surface en [Sharma 2004, Duan 2005b, Duan 2006, Benveniste 2013] et étendu aux phénomènes non linéaires dans [Brach 2017a, Brach 2017b] par exemple. Ces approches analytiques se limitent à certaines classes de phénomènes et à des géométries simples, comme les particules sphéroïdales [Huang 2007, Le-Quang 2010], ou les nanofibres [Chen 2007]. Pour des formes plus complexes et des distributions quelconques de nano-charges, il est nécessaire d'utiliser des approches d'homogénéisation numériques et robustes [Yvonnet 2008b, Liu 2015, Farsad 2012].

Dans une approche multi-échelles, les paramètres matériaux doivent être identifiés. Or certains de ces paramètres, comme les paramètres de surface ou d'interface ne sont pas accessibles expérimentalement. Donc ils doivent être évalués à l'aide de simulations atomistiques [Shenoy 2005, Yvonnet 2011, Yvonnet 2012]. Il n'y a que peu de travaux qui traitent de l'identification des propriétés d'interface.

Les défis à relever pour avoir des modèles multi-échelles prédictifs et efficaces des nanocomposites de graphène, qui ont été étudiés dans cette thèse, sont :

- Développer un modèle continu non-linéaire du comportement électrique prenant en compte l'effet tunnel ;
- Caractériser les propriétés mécaniques des interphases et interfaces en considérant les interactions atomiques, c'est-à-dire identifier la raideur élastique de l'interphase et de l'interface ;
- Développer des procédures efficaces d'homogénéisation numérique prenant en compte les phénomènes nanométriques susmentionnés pour prédire les propriétés électriques et mécaniques effectives des nanocomposites renforcés de graphène.

L'objectif de ce travail de doctorat est de répondre à ces différentes questions scientifiques.

Le plan du manuscrit est le suivant :

Le chapitre 2 présente une brève introduction aux nanocomposites à base de graphène, en spécifiant entre autres la cristallographie, les propriétés et les méthodes de synthèse du graphène ainsi que les propriétés et les applications des nano-composites renforcés avec du graphène.

Dans le chapitre 3, un cadre de modélisation numérique est proposé pour

évaluer la conductivité électrique effective des composites polymères renforcés avec des feuillets de graphène, en introduisant l'effet tunnel. Une formulation d'éléments finis non-linéaire et une méthodologie numérique pour modéliser les effets non-locaux induits par l'effet tunnel sont introduits. De plus, pour éviter de mailler les feuilles de graphène dans leur épaisseur, un modèle de surface hautement conductrice est utilisé. La conductivité effective est ensuite évaluée à partir de Volume Élémentaire Représentatifs (VER) contenant des feuilles de graphène distribuées aléatoirement. Enfin, l'ensemble des outils développés est utilisé pour analyser la sensibilité des propriétés électriques effectives par rapport aux propriétés des constituants et de la répartition des renforts de graphène.

Dans le chapitre 4, une méthodologie basée sur la procédure de Murdoch-Hardy est utilisée pour construire les champs continus de déplacement, de déformation, de contrainte et de propriétés élastiques au niveau l'interphase graphène/polymère à partir des résultats de simulations atomistiques de dynamique moléculaire (DM). Deux modèles continus sont identifiés : l'un contient à la fois la feuille de graphène modélisée par une interface imparfaite et l'interphase induite par l'évolution de la densité et de la conformation des chaînes de polymère au voisinage d'une feuille de graphène ; et l'autre où la feuille de graphène et l'interphase sont intégrées dans un modèle équivalent d'interface imparfaite.

Au chapitre 5, les propriétés mécaniques non-linéaires effectives des nanocomposites graphène-polymère sont évaluées à partir d'une extension du précédent modèle d'interface imparfaite au cadre des transformations finies. Des simulations de DM sont utilisées pour identifier le comportement non-linéaire de l'interface entre le graphène et le polymère. Les propriétés mécaniques effectives du nanocomposite sont évaluées à l'aide d'un schéma d'homogénéisation numérique incrémental. De plus, un exemple préliminaire de couplage faible entre les phénomènes électriques et mécaniques est présenté.

Titre : Modélisation électro-mécanique multi-échelle des nanocomposites graphène/polymère

Mots clés : nanocomposites polymères-graphènes, interphase, multi-échelle, méthode des éléments finis, méthode de dynamique moléculaire, Procédure Murdoch-Hardy, homogénéisation non-linéaire, effet tunnel

Résumé : Cette étude porte sur le développement de modèles et de méthodes numériques pour prédire les propriétés électriques et mécaniques des nanocomposites polymères/graphènes.

Dans une première partie, un modèle non-linéaire de conduction électrique prenant en compte l'effet tunnel est introduit pour déterminer la conductivité effective de ces nanocomposites au travers d'une procédure d'homogénéisation numérique. Celle-ci, basée sur une formulation éléments finis a mis en évidence l'influence des paramètres microstructuraux sur la conductivité effective au travers d'une étude statistique.

Ensuite, un modèle atomistique de l'interface polymère/graphène a été proposé pour valuer les propriétés de l'interface et de l'interphase. Les champs de contrainte et de déplacement

ont été identifiés par une extension de la procédure d'Hardy-Murdoch à partir des simulations de mécanique moléculaire. À l'aide de ces champs, un modèle élastique continue avec des interfaces imparfaites a été identifié et comparé aux résultats des simulations de mécanique moléculaire.

Finalement, le modèle atomistique a permis d'identifier un modèle de zone cohésive non-linéaire pour modéliser la décohésion à l'interface polymère/graphène. Une procédure d'homogénéisation numérique par la méthode des éléments finis a été introduite pour estimer les propriétés mécaniques effectives dans le cadre des transformations finies. Les microstructures déformées ont été utilisées dans le modèle électrocinétique pour déterminer l'impact de la décohésion interfaciale sur la conductivité effective.

Title : Multi-scale electro-mechanical modeling of graphene/polymer nanocomposites

Keywords : Graphene-polymer nanocomposites, interphase, multi-scale, finite element method, molecular dynamics method, Murdoch-Hardy procedure, nonlinear homogenization, tunneling effect

Abstract : This work contributes to developing numerical methodologies for predicting the electrical and mechanical properties of graphene/polymer nanocomposites, which can provide a better view for the design of new materials.

First, a nonlinear electrical conduction model taking into account the tunneling effect is introduced to determine the effective conductivity of the graphene/polymer nanocomposites through a numerical homogenization procedure. The influences of barrier height and microstructural parameters on the conductivity were demonstrated.

Then, to characterize the properties of interphases and interfaces, we employed the Murdoch-Hardy procedure combined with the molecular dynamics method to study the mechanical properties of the graphene/polymer

nanocomposites. The stiffness tensor components of the interphase, interface and bulk polymer region are identified. Based on these fields, a continuous elastic model with imperfect interface has been identified and compared with the results of molecular dynamics simulations.

Finally, the atomistic model was used to identify a nonlinear cohesive zone model to simulate the decohesion at the interface of polymer and graphene. A numerical homogenization procedure by finite element method was introduced to estimate the effective mechanical properties in the framework of the finite strains. The proposed mechanical modeling is finally extended to the finite strain problem to predict the evolution of percolation threshold under tension within the proposed electrical model.

